Université Paris-Sud

Faculté des sciences d'Orsay

Mémoire d'habilitation à diriger des recherches
Inversion et régularisation

Jean–François GIOVANNELLI

Groupe Problèmes Inverses
Laboratoire des Signaux et Systèmes (CNRS – Supélec – UPS)
Supélec, Plateau de Moulon, 91192 Gif–sur–Yvette Cedex, France

Soutenance le 12 décembre 2005, devant le jury constitué de :

Mme	Laure	BLANC-FÉRAUD	Rapporteure
M.	Patrick	FLANDRIN	Président et examinateur
M.	François	GOUDAIL	Examinateur
Mme	Isabelle	MAGNIN	Rapporteure
M.	Ali	MOHAMMAD-DJAFARI	Examinateur
Mme	Sylvie	ROQUES	Rapporteure

Table des matières

Structure du document

Ce document décrit mes activités de recherche au sein du Groupe Problèmes Inverses du Laboratoire des Signaux et Systèmes (CNRS – Supélec – UPS), depuis une dizaine d'années. Il est divisé en trois parties.

1. La première partie présente un bilan quantitatif. Elle démarre par un court *curriculum vitæ* (page 9) qui résume l'ensemble de mes activités. Elle se poursuit par un unique chapitre (page 11) qui décrit les aspects factuels et quantitatifs de mon dossier : encadrement doctoral, collaborations, publications. La liste des publications elle-même est à la page 17. Il se termine par quelques éléments sur mes activités d'enseignement.
2. La seconde partie concerne le contenu scientifique et elle est divisée en quatre chapitres.
   - Le premier (page 25) positionne le travail par rapport à l'existant et en propose une synthèse dans une perspective historique.
   - Le second (page 31) donne un résumé détaillé qui s'appuie sur les publications annexées.
   - Le troisième (page 43) présente mes perspectives de recherches.
   - Le quatrième (page 49) contient les références bibliographiques de l'ensemble du document (il reprend les références de la liste de publication).
3. La dernière partie (de la page 59 à la fin) reproduit dix publications de revue (parues ou en révision). Elles sont représentatives de l'ensemble de mes travaux.

Première partie

Curriculum vitæ et bilan quantitatif

État civil

Jean–François GIOVANNELLI
Laboratoire des Signaux et Systèmes
Supélec, Plateau de Moulon, 91192 Gif–sur–Yvette, Cedex
Tél. : 01 69 85 17 39
Mél. : giova@lss.supelec.fr
Web : www.lss.supelec.fr/perso/giovannelli/

Né le 31 mars 1966
Nationalité française
Vivant maritalement
Deux enfants

Cursus

2004 - 05 : En délégation au CNRS au L2S.

Depuis 1997 : Maître de conférences à l'UPS en 61e section, affecté au L2S.

1997 (6 mois) : Chercheur des Laboratoires de Recherche Fondamentale de la Société L'ORÉAL.

1995 - 97 : ATER à l'UPS puis post-doctorant au L2S.

1991 - 95 : Thèse de Doctorat en traitement du signal au L2S et monitorat à l'UPS.

1990 : Ingénieur en Électronique, ENSEA.

Recherche

Thèmes de recherche (détails partie II, page 23)

- Problèmes inverses mal-posés, régularisation, approches bayésiennes.
- Caractérisation spectrale, synthèse de Fourier, déconvolution.
- Imagerie médicale, astronomique, aéroportée et satellitaire, surveillance industrielle.

Publications (détails page 17)

- Douze articles dans des revues internationales avec comité de lecture.
- Vingt-deux communications de congrès, quatre chapitres d'ouvrages.
- Un logiciel déposé.

Encadrement (détails page 11)

- Participation à l'encadrement de cinq thèses : Aurélien HAZART (*depuis 2004*), Gilles ROCHEFORT (*soutenue en 2005*), Vincent SAMSON (*soutenue en 2002*), Redha BOUBERTAKH (*soutenue en 2002*), Philippe CIUCIU (*soutenue en 2000*).

Responsabilité de collaborations (détails page 13)

- Trois collaborations académiques : Observatoire de Paris (*depuis 2000*), Institut d'Astrophysique Spatiale (*1998-2003*), Unité INSERM d'Imagerie Médicale Quantitative (*depuis 1992*).
- Quatre collaborations contractuelles : Société L'ORÉAL (*en cours de démarrage*), EDF (*depuis 2001*), ONÉRA (*depuis 1999*), CEA (*en 1998*).

Divers

- Responsable du Groupe Problèmes Inverses, *depuis 2003* (quatre permanents, sept thésards).
- Titulaire d'un contrat d'encadrement doctoral et de recherche, *depuis 1999*.
- Relecteur auprès de : IEEE Trans. on Signal Processing, on Image Processing, on Geoscience and Remote Sensing, on Aerospace and Electronic Systems, Signal Processing, Astronomy & Astrophysics (dix-sept articles au total).
- Membre du Conseil de laboratoire du L2S (*2000-04*).
- Membre des CS-61 à l'UPS (*2000-03*) et CS-37 / 61 / 63 à l'Université de Paris 13 (*2001-03*).
- Participation à l'organisation d'un Workshop : MAXENT 2000.
- Forte implication dans la définition de la politique informatique du L2S.

Chapitre 1

Bilan quantitatif

Cette partie présente sommairement mon implication dans l'encadrement de thèses et dans diverses collaborations. Elle présente également la liste de mes publications, à la page 17. La dernière section donne quelques éléments sur mes activités d'enseignement.

1.1 Encadrement doctoral

A des degrés divers, je me suis impliqué dans l'encadrement de *cinq thésards* : quatre ont soutenu et un est à mi-parcours. Pour chacun, je précise ci-dessous quelques éléments concernant le contexte, les pourcentages d'encadrement, les publications communes et la situation actuelle.

1.1.1 Analyse spectrale haute résolution

J'ai coencadré, à hauteur de 20% avec Jérôme IDIER, la thèse de Philippe CIUCIU intitulée « *Méthodes markoviennes en estimation spectrale non paramétrique. Applications en imagerie radar Doppler* » [24] et soutenue en octobre 2000. Le jury était composé de :

- Gilles AUBERT,
- Guy DEMOMENT,
- Patrick FLANDRIN (Rapporteur),
- Jean-Jacques FUCHS (Rapporteur),
- Jérôme IDIER,
- Daniel MULLER.

Le travail est consacré à l'analyse spectrale haute résolution, en particulier dans les situations défavorables où très peu de données sont disponibles. Il est spécifiquement dédié au cas où le spectre recherché est constitué d'un ensemble de raies superposé à un fond continu et à la séparation de composantes large bande / bande étroite.

Ce travail a donné lieu à la publication de deux articles de revue. Le premier (dont je suis coauteur) concernant les aspects méthodologiques [32] est paru aux *Transactions on Signal Processing des IEEE* (annexé à la page 107). Le second est consacré à des aspects spécifiquement algorithmiques [26] pour lesquels je ne suis pas impliqué. Le travail a également donné lieu à plusieurs communications

de congrès [30, 29, 31]. Les premiers travaux ont été réalisés en collaboration avec la Société THOMSON et nous sommes coauteurs d'un rapport de contrat [25]. Des résultats partiels ont également été présentés au Colloque Jeunes Chercheurs Alain Bouissy [27] et à une journée du GDR-ISIS [28].

Philippe CIUCIU est aujourd'hui chercheur au Service Hospitalier Frédéric Joliot du CEA à Orsay.

1.1.2 Synthèse de Fourier et IRM

J'ai coencadré, à hauteur de 50% avec Alain HERMENT la thèse de Redha BOUBERTAKH intitulée « *Synthèse de Fourier régularisée : cas des données incomplètes et application à l'*IRM *cardiaque rapide* » [11] et soutenue en novembre 2002 devant le jury constitué de :

- Jacques BITTOUN,
- Isabelle BLOCH (Rapporteur),
- Jean–François GIOVANNELLI,
- Alain HERMENT,
- Ali MOHAMMAD–DJAFARI,
- Françoise PEYRIN (Rapporteur).

Je suis entièrement responsable de l'encadrement concernant les aspects méthodologiques et algorithmiques relatifs à la reconstruction d'images. Les résultats obtenus ont été publiés dans deux papiers de conférence [13, 14] et un article va paraître dans la revue *Signal Processing* [12] (et annexé à la page 173).

Redha BOUBERTAKH est actuellement en stage post-doctoral au Kings College, à Londres.

1.1.3 Imagerie de points brillants sur fond nuageux

En 2000, j'ai obtenu un agrément de la part de l'Université me confiant la direction scientifique de la thèse de Vincent SAMSON que j'ai coencadrée à 40 % avec Frédéric CHAMPAGNAT. Le manuscrit [120] est intitulé « *Approche régularisée pour la détection d'objets ponctuels dans une séquence d'images* » et concerne l'imagerie haute résolution de points brillants sur fond nuageux. Le doctorant a soutenu en décembre 2002 devant le jury composé de :

- Patrick BOUTHEMY (Rapporteur),
- Frédéric CHAMPAGNAT,
- Guy DEMOMENT,
- Jean–François GIOVANNELLI,
- Claude JAUFFRET,
- Philippe RÉFRÉGIER (Rapporteur).

Vincent SAMSON a présenté ses premiers résultats au Colloque Jeunes Chercheurs Alain Bouissy [123] et dans deux rapports intermédiaires [121, 124]. Les résultats obtenus ont donné lieu à la publication de deux papiers de conférence [122, 125] et d'un papier de revue [126] dans *Applied Optics* (reproduit à la page 133).

Vincent SAMSON a ensuite effectué un séjour post-doctoral à l'INRIA à Rennes et il est actuellement ingénieur de la société EADS-Astrium à Toulouse.

1.1.4 Super-résolution et séquences d'images

En 2002-2005, j'ai participé à hauteur de 10%, avec Frédéric CHAMPAGNAT (pour 60 %) et Guy LE BESNERAIS (pour 30 %) à l'encadrement de la thèse de Gilles ROCHEFORT consacrée à la reconstruction d'image haute résolution à partir d'une séquence d'images. Le manuscrit est intitulé « *Amélioration de la résolution de séquences d'images. Applications aux capteurs aéroportés* » [115] et la soutenance a eu lieu en mai 2005 devant le jury :

- Lydiane AGRANIER,
- Laure BLANC-FÉRAUD (Rapporteur),
- Patrick BOUTHEMY (Rapporteur),
- Frédéric CHAMPAGNAT,
- Guy DEMOMENT,
- Jean–François GIOVANNELLI.

La première partie du travail est synthétisée dans un rapport interne [116]. Un article [117] reprenant l'ensemble du travail est en révision pour publication dans les *Transactions on Image Processing des IEEE* ; il est reproduit à la page 157.

Grâce aux compétences acquises pendant son travail de thèse, Gilles ROCHEFORT a été embauché par la Société RealEyes3D qui développe et commercialise des logiciels de traitement d'images pour les appareils photos numériques des téléphones portables. La société a obtenu le soutien de l'ANVAR à l'embauche d'un jeune docteur sur un poste à forte coloration recherche technologique et innovation.

1.1.5 Identification de sources de pollutions

Depuis début 2004, j'encadre la thèse d'Aurélien HAZART, consacrée à l'« *identification de sources de pollutions à partir de mesures de concentrations dans la nappe phréatique* », en collaboration avec la R&D d'EDF (Laurence CHATELLIER et Stéphanie DUBOST). Pour cela, j'ai également obtenu un agrément de la part de l'Université me confiant la direction scientifique du travail de thèse. Le travail du doctorant (suite à son stage de DEA [83]) est bien engagé : il a réalisé une large étude bibliographique [81, 82] et une étude technique précise concernant les indéterminations spécifiques rencontrées. La première partie de son travail est parue sous la forme d'une communication [84] au GRETSI en septembre 2005.

1.2 Collaborations académiques et industrielles

Cette section décrit les collaborations que j'ai prises en charge. Elles sont d'envergures différentes et entrent toutes dans mes thèmes de recherche scientifique.

1.2.1 Imagerie médicale

Depuis très longtemps, l'équipe (et notamment Guy DEMOMENT) développe de nombreux travaux en collaboration avec Alain HERMENT, directeur de recherche à l'INSERM. Pour ma part, le travail en commun a démarré avec mes travaux de thèse et j'ai pris la responsabilité de la collaboration depuis mon recrutement en 1997. Elle concerne l'imagerie médicale et plus précisément l'échographie Doppler dans un premier temps, puis l'imagerie par résonance magnétique (IRM).

Une large partie de nos travaux communs concerne la *caractérisation spectrale*. Cette collaboration a été concrétisée, notamment, par l'animation d'un Work-Package au sein du Consortium Européen DOLPHINS (Doppler Linear Processing for Hydraulics and Imagery New System). Sur le sujet, nous avons coencadré Christophe BERTHOMIER, étudiant en post-doctorat, et avons publié nos résultats communs dans un article de la revue *Ultrasound in Medicine and Biology* [6].

Ces dernières années, notre contribution concerne essentiellement l'IRM et donc, du point de vue du traitement des données, les problèmes de *synthèse de Fourier*. C'est sur ce thème que nous avons coencadré la thèse de Redha BOUBERTAKH évoquée précédemment. Dans ce contexte, nous avons conjointement répondu à un appel d'offre INSERM-STIC et obtenu le financement d'un ingénieur pour six mois : nous avons ainsi recruté Boris MATROT de février à juillet 2003. Son travail a concerné spécifiquement les problèmes de *déroulage de phase en 2D* rencontrés en IRM cardio-vasculaire pour l'imagerie des flux sanguins.

L'Unité INSERM à laquelle appartient Alain HERMENT a été recréée récemment : il s'agit maintenant de l'unité INSERM U.678, Laboratoire d'Imagerie Fonctionnelle (LIF). Notre collaboration se développe dans ce nouveau contexte.

1.2.2 Imagerie en astronomie

Imagerie infrarouge et modèle non-linéaire

En 1997, avec Jérôme IDIER, nous avons initié une collaboration avec Alain ABERGEL et Alain COULAIS, de l'Institut d'Astrophysique Spatiale de l'UPS. Ce travail a concerné initialement l'inversion de modèles non-linéaires pour les détecteurs infrarouges des caméras ISOCAM et ISOPHOT embarquées dans le satellite ISO de l'Agence Spatiale Européenne. Nous avons coencadré plusieurs stages et nous avons plusieurs communications de congrès en commun [34, 33, 35], citées dans plusieurs autres communications [99, 93, 42, 97, 49].

La collaboration s'est avérée particulièrement fructueuse : j'ai porté avec Alain ABERGEL un projet de recrutement pour développer notre collaboration. Nous avons obtenu – par une procédure du *Bonus Qualité Recherche* – qu'un poste de Maître de conférences soit mis au concours en 2003, en section 34 / 61. Grâce à une large publicité, nous avons eu vingt-six candidats, en avons retenu dix pour une audition et en avons finalement classé cinq. Nous accueillons Thomas RODET depuis septembre 2003. Il a pris en charge cette collaboration qui se développe fortement et dont je suis aujourd'hui largement désengagé. Les activités portent encore sur l'imagerie infrarouge mais plus particulièrement sur le traitement des données du satellite SPITZER lancé en août 2003. La collaboration se développe également vers l'inversion de données tomographiques issues du satellite STEREO.

Radio-interférométrie et synthèse de Fourier

En 2002, Alain COULAIS a été recruté à l'Observatoire de Paris et je développe naturellement ma collaboration avec lui. Nous nous intéressons essentiellement aux problèmes de reconstruction d'images pour des instruments existants (radio-héliographe de Nançay, avec Alain KERDRAON) et des instruments en projet (interféromètre ALMA, SKA). Notre travail concerne maintenant la *synthèse de Fourier pour la radio-interférométrie* : il s'agit d'un problème de synthèse de Fourier ou de déconvolution, avec contrainte de positivité et éventuellement contrainte de support. Notre contribution est spécifique au cas où la carte recherchée est la superposition d'un ensemble de points brillants sur un fond homogène. Nous avons présenté nos travaux à l'occasion d'un séminaire invité à l'observatoire

de Nançay [63] et un article [65] vient de paraître dans la revue *Astronomy & Astrophysics* (reproduit à la page 143). Nous présentons aussi une version courte au GRETSI 2005 [64]. L'outil développé est en cours d'intégration au logiciel d'exploitation scientifique du NRH et nous travaillons à la publication de nos codes IDL / GDL et Matlab / Octave.

1.2.3 Imagerie haute résolution : aéroportée et satellitaire

Depuis 1999, je mène une collaboration suivie avec Frédéric CHAMPAGNAT et Guy LE BESNERAIS, ingénieurs de recherche à l'ONÉRA au sein de l'Unité Traitement d'Images du Département Traitement de l'Information et Modélisation. Nos travaux communs concernent l'*imagerie haute résolution* et plus précisément l'amélioration de la résolution spatiale d'images à partir d'une séquence observée, dans un contexte aéroporté ou satellitaire en optique visible ou en infrarouge. Sur un plan méthodologique, il s'agit de problème de *déconvolution* / *sur-résolution* / *séparation* et de *super-résolution*. Une partie des développements communs sera industrialisée dans les années à venir. C'est dans ce contexte que se situent les thèses de Vincent SAMSON et Gilles ROCHEFORT évoquées précédemment. En plus des publications avec les deux thésards [117, 126], le travail a donné lieu à deux rapports [61, 62].

1.2.4 Contrôle et surveillance industriels

Cette partie concerne une collaboration avec la division R&D d'EDF à Chatou. Plus précisément, je collabore avec le Département Optimisation des Performances des Process et son groupe Systèmes Dynamiques et Traitement de l'Information (anciennement Traitements Avancés de l'Information). La collaboration implique (ou a impliqué) plusieurs personnes : Laurence CHÂTELLIER, Stéphanie DUBOST, Arnaud FOURNIGUET, Stéphane GAUTIER, Pierre PEUREUX, Lionel ROBILLARD. Ces travaux se sont présentés sous la forme de trois contrats de collaboration d'envergures différentes.

1. En 2001 (trois mois) : surveillance vibratoire des arbres de rotors des groupes turbo-alternateurs. Du point de vue du traitement, il s'agit de problèmes d'*analyse spectrale haute résolution*, éventuellement adaptative.
2. Depuis fin 2002 : *localisation spatiale et temporelle de sources de pollutions* potentielles autour des centrales nucléaires de production d'électricité. Il s'agit d'un problème de *déconvolution - interpolation* et le travail se déroule sous la forme du coencadrement de la thèse d'Aurélien HAZART, évoquée précédemment.
3. Depuis juin 2005, notre collaboration se développe encore sur le thème de la *reconstruction 3D* à partir de radiographies en faible nombre (tomographie). Je suis impliqué dans ce développement mais c'est Ali MOHAMMAD–DJAFARI qui assure la majeure partie du travail. Dans ce cadre nous accueillons Lionel ROBILLARD (Ingénieur Chercheur EDF) en visite dans l'équipe. Cette étude vise à améliorer la méthode de reconstruction existante pour obtenir un meilleur dimensionnement des défauts.

Ces travaux communs entrent dans le cadre de la convention de collaboration EDF-R&D / Supélec-L2S pour les développements en traitement du signal et des images (Contrat N°EP-1105, signé le 6 novembre 2001). Je suis le correspondant pour le L2S du comité d'animation technique et nous prévoyons un élargissement à d'autres activités.

1.2.5 Caractérisation des tissus de la peau

Depuis début 2005, je conduis une collaboration avec la Société L'ORÉAL (équipe d'Imagerie Quantitative des Laboratoires de Recherche Avancée, département Sciences de la Matière) concernant la caractérisation des tissus de la peau par *tomographie optique cohérente* et notamment la mesure de l'épaisseur du *stratum corneum*. Brièvement, il s'agit d'un travail de *déconvolution impulsionnelle positive* réalisé grâce à des modèles *a priori* de mélanges de gaussiennes tronquées et Bernoulli-gaussiens tronqués. Le travail a été en partie réalisé par Loïc SIMON au cours de son stage de magistère [129] et les idées développées sont très voisines de celles proposées par [102].

Au préalable, les travaux développés en échographie Doppler pendant ma thèse avaient trouvé des débouchés pour la caractérisation acoustique des tissus de la peau : en 1993, j'ai participé à une première collaboration avec la Société L'ORÉAL consacrée au problème de la mesure de l'atténuation acoustique des tissus de la peau. Nous avons deux publications en commun [74, 90] dans des congrès internationaux.

1.2.6 Restauration des spectres sur les micro-systèmes

La collaboration évoquée ici est en cours de démarrage à l'automne 2005. Le travail repose sur des méthodes de *déconvolution et restauration de spectres* pour l'identification d'espèces moléculaires dans un échantillon biologique, grâce à des micro-systèmes. Il se déroulera en grande partie au Département Micro-Technologies pour la Biologie et la Santé au CEA à Grenoble, en collaboration avec Pierre GRANGEAT sous la forme du coencadrement d'un étudiant en thèse, Grégory STRUBEL, que nous venons de recruter.

Les domaines d'application de tels micro-systèmes couvrent la recherche génétique, médicale et pharmaceutique mais aussi les contrôles sanitaires, la protection de l'environnement, la lutte contre le bio-terrorisme. Par exemple, ces travaux pourraient accélérer la définition d'antibiotiques ciblés pour le traitement des maladies infectieuses ou l'optimisation des chimiothérapies du cancer.

1.2.7 Miscellanées

Par ailleurs, j'ai participé à quatre autres collaborations plus anciennes.

- En 1994, 95 et 96, j'ai participé à trois collaborations avec la Société THOMSON concernant la *caractérisation temps-fréquence en temps court* qui, après un travail complémentaire de synthèse, ont débouché sur une publication [73] dans les *IEEE Transactions on Geoscience and Remote Sensing* en 2001 (reproduite à la page 95).
- En 1999, j'ai mené avec Jérôme IDIER un travail en collaboration avec Grégoire PICHENOT, CEA (Institut de Protection et de Sûreté Nucléaire, Département de Protection de la Santé de l'Homme et de Dosimétrie) consacré à l'*inversion de données en spectrométrie de neutrons*. Ce travail, plus ponctuel, s'est déroulé sous la forme d'une prestation de service. Je le classe plutôt dans un volet « diffusion de l'information scientifique » de mes activités, il ne s'agit pas *stricto sensu* d'une collaboration de recherche au sens où elle ne débouche pas sur des développements scientifiques nouveaux en traitement du signal. Cela dit, elle est très enrichissante et me paraît faire partie des missions d'un enseignant chercheur. Les résultats sont rapportés dans [70].

1.3 Liste de publications

Je suis coauteur de *douze articles* dans des revues internationales avec comité de lecture (pour moitié aux IEEE), ce qui représente une moyenne de 1,1 article par an entre 1995 et 2005. A ces articles parus, s'ajoutent un article à paraître et un article en révision. Je suis également auteur ou coauteur de quatre chapitres d'ouvrages et vingt-deux communications de congrès avec comité de lecture et actes (dont treize congrès internationaux). J'ai participé à la rédaction d'un ouvrage collectif [87] (coordonné par Jérôme IDIER) qui a été l'occasion de synthétiser nos travaux et d'affirmer leur place dans le contexte de la recherche en traitement des signaux et des images. L'équipe a également fait paraître plusieurs documents collectifs de synthèse sur le sujet [39, 40, 38, 105]. Je suis aussi auteur ou coauteur de sept rapports de contrat. La liste complète de mes publications est fournie ci-dessous.

Je suis également porteur d'un projet de dépôt d'un logiciel : GPAC (Gradient à Pas Adaptatif avec Corrections). Il s'agit d'un code Matlab qui met en œuvre un algorithme d'optimisation particulièrement adapté à des critères multivariés fonctions d'un grand nombre de variables : un algorithme de descente à pas adaptatif utilisant les caractéristiques du premier ordre (gradient) et n'utilisant pas d'information du second ordre (hessien ou approximations du hessien). Diverses directions de descente sont proposées (gradient simple, gradient conjugué, corrections de Vignes et de la bissectrice) et différentes techniques d'adaptation du pas de descente sont disponibles (dichotomie et interpolations).

Les publications sont présentées dans l'ordre chronologique et par catégorie. Les références surmontées d'une étoile* concernent strictement mon travail de thèse.

Articles de revues internationales avec comité de lecture

Les références [2], [4], [5], [6], [8], [10], [11] et [12] sont annexées (à partir de la page 59).

[1]* A. Herment et **J.-F. Giovannelli**, « An adaptive approach to computing the spectrum and mean frequency of Doppler signals », *Ultrasonic Imaging*, vol. 27, pp. 1–26, 1995.

[2]* **J.-F. Giovannelli**, G. Demoment et A. Herment, « A Bayesian method for long AR spectral estimation : a comparative study », *IEEE Transactions on Ultrasonics Ferroelectrics and Frequency Control*, vol. 43, n°2, pp. 220–233, mars 1996.

[3]* A. Herment, **J.-F. Giovannelli**, G. Demoment, B. Diebold et A. Delouche, « Improved characterization of non–stationary flows using a regularized spectral analysis of ultrasound Doppler signals », *Journal de Physique III*, vol. 7, n°10, pp. 2079–2102, octobre 1997.

[4] J. Idier et **J.-F. Giovannelli**, « Structural stability of least squares prediction methods », *IEEE Transactions on Signal Processing*, vol. 46, n°11, pp. 3109–3111, novembre 1998.

[5] **J.-F. Giovannelli** et J. Idier, « Bayesian interpretation of periodograms », *IEEE Transactions on Signal Processing*, vol. 49, n°7, pp. 1988–1996, juillet 2001.

[6] P. Ciuciu, J. Idier et **J.-F. Giovannelli**, « Regularized estimation of mixed spectra using a circular Gibbs-Markov model », *IEEE Transactions on Signal Processing*, vol. 49, n°10, pp. 2201–2213, octobre 2001.

[7] C. Berthomier, A. Herment, **J.-F. Giovannelli**, G. Guidi, L. Pourcelot et B. Diebold, « Multigate Doppler signal analysis using 3-D regularized long AR modeling », *Ultrasound in Medicine and Biology*, vol. 27, n°11, pp. 1515–1523, 2001.

[8] **J.-F. Giovannelli**, J. Idier, G. Desodt et D. Muller, « Regularized adaptive long autoregressive spectral analysis », *IEEE Transactions on Geoscience and Remote Sensing*, vol. 39, n°10, pp. 2194–2202, octobre 2001.

[9] A. Mohammad-Djafari, **J.-F. Giovannelli**, G. Demoment et J. Idier, « Regularization, maximum entropy and probabilistic methods in mass spectrometry data processing problems », *Int. Journal of Mass Spectrometry*, vol. 215, n°1-3, pp. 175–193, avril 2002.

[10] **J.-F. Giovannelli**, J. Idier, R. Boubertakh et A. Herment, « Unsupervised frequency tracking beyond the Nyquist limit using Markov chains », *IEEE Transactions on Signal Processing*, vol. 50, n°12, pp. 1–10, décembre 2002.

[11] V. Samson, F. Champagnat et **J.-F. Giovannelli**, « Point target detection and subpixel position estimation in optical imagery », *Applied Optics*, vol. 43, n°2, *Special Issue on Image processing for EO sensors*, pp. 257–263, janvier 2004.

[12] **J.-F. Giovannelli** et A. Coulais, « Positive deconvolution for superimposed extended source and point sources. », *Astronomy and Astrophysics*, vol. 439, pp. 401–412, 2005.

Articles à paraître ou en révision

Les deux références sont annexées (à partir de la page 157).

[1] R. Boubertakh, **J.-F. Giovannelli**, A. De Cesare et A. Herment, « Regularized reconstruction of MR images from sparse acquisitions », à paraître dans *Signal Processing*, janvier 2004.

[2] G. Rochefort, F. Champagnat, G. Le Besnerais et **J.-F. Giovannelli**, « Super-resolution from a sequence of undersampled images under affine motion », en révision dans *IEEE Transactions on Image Processing*, février 2005.

Participation à des ouvrages

[1]* A. Herment, C. Pellot et **J.-F. Giovannelli**, « Application of regularisation methods to cardiovascular imaging », in *Proceedings of IEEE EMBS–Satellite workshop on medical image processing : from pixel to structure*, Y. Goussard, Ed., Montréal, Québec, Canada, septembre 1997, pp. 27–55, Édition de l'École Polytechnique de Montréal.

[2] G. Demoment, J. Idier, **J.-F. Giovannelli** et A. Mohammad-Djafari, « Problèmes inverses en traitement du signal et de l'image », vol. TE 5 235 de *Traité Télécoms*, pp. 1–25. Techniques de l'Ingénieur, Paris, 2001.

[3] G. Le Besnerais, **J.-F. Giovannelli** et G. Demoment, « Filtrage inverse et méthodes linéaires en déconvolution », in *Approche bayésienne pour les problèmes inverses*, J. Idier, Ed., Paris, 2001, pp. 81–114, Traité IC2, Série traitement du signal et de l'image, Hermès.

[4] **J.-F. Giovannelli** et A. Herment, « Caractérisation spectrale en vélocimétrie doppler ultrasonore », in *Approche bayésienne pour les problèmes inverses*, J. Idier, Ed., Paris, 2001, pp. 271–295, Traité IC2, Série traitement du signal et de l'image, Hermès.

Communications dans des congrès avec comité de lecture et actes

[1]* **J.-F. Giovannelli**, A. Herment et G. Demoment, « A Bayesian approach to ultrasound Doppler spectral analysis », in *Proceedings of International Ultrasonics Symposium*, Baltimore, MD, USA, octobre 1993, vol. 3, pp. 538–541.

[2]⋆ **J.-F. Giovannelli**, A. Herment et G. Demoment, « Vélocimétrie Doppler ultrasonore : approche classique ou approche régularisée ? », in *Actes du 14 e colloque GRETSI*, Juan-les-Pins, septembre 1993, vol. 1, pp. 555–558.

[3]⋆ **J.-F. Giovannelli** et G. Demoment, « A statistical study of a regularized method for long autoregressive spectral estimation », in *Proceedings of the International Conference on Acoustic, Speech and Signal Processing*, Minneapolis, MN, USA, avril 1993, vol. 4, pp. 137–140.

[4]⋆ A. Herment, G. Demoment et **J.-F. Giovannelli**, « Adaptive estimation of the spectrum and mean frequency of Doppler signals », in *Proceedings of International Ultrasonics Symposium*, Cannes, novembre 1994, vol. 3, pp. 1717–1720.

[5]⋆ **J.-F. Giovannelli**, J. Idier, B. Querleux, A. Herment et G. Demoment, « Maximum likelihood and maximum a posteriori estimation of Gaussian spectra. Application to attenuation measurement and color Doppler velocimetry », in *Proceedings of International Ultrasonics Symposium*, Cannes, novembre 1994, vol. 3, pp. 1721–1724.

[6]⋆ J. Idier, **J.-F. Giovannelli** et B. Querleux, « Bayesian time-varying AR spectral estimation for ultrasound attenuation measurement in biological tissues », in *Proceedings of the Section on Bayesian Statistical Science*, Alicante, Espagne, 1994, pp. 256–261, American Statistical Association.

[7] A. Herment, E. Mousseaux, **J.-F. Giovannelli**, J. Idier, O. Jolivet et J. Bittoun, « Improved robustness of MR velocity mapping by using a spatial regularized estimation of flow patterns », in *Fourth scientific meeting of the International Society for Magnetic Resonance in Medicine*, New York, NY, USA, avril 1996, vol. 2, p. 1288.

[8] A. Herment, E. Mousseaux, **J.-F. Giovannelli**, J. Idier, J. Bittoun et O. Jolivet, « MR velocity mapping : Improvement of noise robustness by using a regularized estimation of flow patterns », in *Computer Assisted Radiology*, Paris, juin 1996, vol. 1124, pp. 116–120.

[9] A. Herment, **J.-F. Giovannelli**, E. Mousseaux, J. Idier, A. De Cesare et J. Bittoun, « Regularized estimation of flow patterns in MR velocimetry », in *Proceedings of the International Conference on Image Processing*, Lausanne, Suisse, septembre 1996, pp. 291–294.

[10] J. Idier, **J.-F. Giovannelli** et P. Ciuciu, « Interprétation régularisée des périodogrammes et extensions non quadratiques », in *Actes du 16 e colloque GRETSI*, Grenoble, septembre 1997, pp. 695–698.

[11] J. Idier et **J.-F. Giovannelli**, « Stabilité structurelle des méthodes de prédiction linéaire », in *Actes du 16 e colloque GRETSI*, Grenoble, septembre 1997, pp. 543–546.

[12] P. Ciuciu, J. Idier et **J.-F. Giovannelli**, « Analyse spectrale non paramétrique haute résolution », in *Actes du 17 e colloque GRETSI*, Vannes, septembre 1999, pp. 721–724.

[13] P. Ciuciu, J. Idier et **J.-F. Giovannelli**, « Markovian high resolution spectral analysis », in *Proceedings of the International Conference on Acoustic, Speech and Signal Processing*, Phoenix, AZ, USA, mars 1999, pp. 1601–1604.

[14] R. Boubertakh, A. Herment, **J.-F. Giovannelli** et A. De Cesare, « MR image reconstruction from sparse data and spiral trajectories », in *Magnetic Resonance Materials in Physics Biology and Medicine*, Paris, septembre 2000, 17th Annual meeting of the European Society for Magnetic Resonance in Medicine and Biology, vol. 11–Sup. 1, p. 85.

[15] A. Coulais, B. Fouks, **J.-F. Giovannelli**, A. Abergel et J. See, « Transient response of IR detectors used in space astronomy : what we have learned from ISO satellite », in *Procedings of* SPIE

4131-42, Infrared Spaceborne Remote Sensing, M. Strojnik et B. Andresen, Eds., San Diego, CA, USA, juillet 2000, vol. VIII, pp. 205–217.

[16] A. Coulais, F. Balleux, A. Abergel, **J.-F. Giovannelli** et J. See, « Correction par bloc des transitoires de la caméra infrarouge ISOPHOT C-100 avec un modèle non linéaire dissymétrique », in *Actes du 18 e colloque GRETSI*, Toulouse, septembre 2001.

[17] P. Ciuciu, J. Idier et **J.-F. Giovannelli**, « Estimation spectrale régularisée de fouillis et de cibles en imagerie radar Doppler », in *Actes du 18 e colloque GRETSI*, Toulouse, septembre 2001.

[18] V. Samson, F. Champagnat et **J.-F. Giovannelli**, « Détection d'objets ponctuels sur fond de clutter », in *Actes du 18 e colloque GRETSI*, Toulouse, France, septembre 2001.

[19] V. Samson, F. Champagnat et **J.-F. Giovannelli**, « Detection of point objects with random subpixel location and unknown amplitude », in *PSIP'2003*, Grenoble, France, janvier 2003.

[20] A. Coulais, J. Malaizé, **J.-F. Giovannelli**, T. Rodet, A. Abergel, B. Wells, P. Patrashin, H. Kaneda et B. Fouks, « Non-linear transient models and transient corrections methods for IR low-background photo-detectors », in *ADASS-13*, Strasbourg, octobre 2003.

[21] A. Hazart, **J.-F. Giovannelli**, S. Dubost et L. Chatellier, « Pollution de milieux poreux : identifiabilité et identification de modèles paramétriques de sources », in *Actes du 20 e colloque GRETSI*, Louvain-la-Neuve, Belgique, septembre 2005.

[22] **J.-F. Giovannelli** et A. Coulais, « Déconvolution avec contraintes de positivité et de support : sources ponctuelles sur source étendue », in *Actes du 20 e colloque GRETSI*, Louvain-la-Neuve, Belgique, septembre 2005.

Autres communications

[1] J. Idier, P. Ciuciu et **J.-F. Giovannelli**, « Analyse spectrale à temps court et périodogrammes non quadratiques », Palaiseau, janvier 1998, CMAPX, École Polytechnique.

[2] P. Ciuciu, J. Idier et **J.-F. Giovannelli**, « Nouveaux estimateurs du spectre de puissance », in *Colloque Jeunes Chercheurs Alain Bouissy*, Orsay, mars 1998.

[3] P. Ciuciu, J. Idier et **J.-F. Giovannelli**, « Analyse spectrale non paramétrique à haute résolution », Paris, décembre 1999, GDR-PRC ISIS, GT1.

[4] R. Boubertakh, A. Herment, **J.-F. Giovannelli** et A. De Cesare, « Reconstruction d'images IRM à partir de données incomplètes », in *Forum des Jeunes Chercheurs en Génie Biologique et Médical*, Tours, juin 2000, pp. 52–53.

[5] V. Samson, F. Champagnat et **J.-F. Giovannelli**, « Détection d'objets ponctuels sur fond nuageux en imagerie satellitaire », in *Colloque Jeunes Chercheurs Alain Bouissy*, Orsay, France, février 2001.

[6] G. Demoment, J. Idier, **J.-F. Giovannelli** et A. Mohammad-Djafari, « Restauration et reconstruction d'image », in *Le traitement d'image à l'aube du XXIe siècle*, Paris, mars 2002, Journées d'études SEE, pp. 45–56.

[7] **J.-F. Giovannelli** et A. Coulais, « Inversion de données interférométriques : cas des images à toutes les échelles spatiales », Nançay, novembre 2003, Premier atelier "Projets et R & D en Radioastronomie".

Rapports de contrats

[1]⋆ **J.-F. Giovannelli** et J. Idier, « Mesure de l'atténuation acoustique de la peau. Étude de faisabilité », Rapport de contrat (confidentiel) CNRS–Société L'ORÉAL, GPI–L2S, 1993.

[2]⋆ **J.-F. Giovannelli** et J. Idier, « Caractérisation spectrale du fouillis de radar Doppler. Méthodes autorégressives adaptatives régularisées », Rapport de contrat (confidentiel) CNRS–Société THOMSON, GPI–L2S, 1994.

[3] **J.-F. Giovannelli** et J. Idier, « Une nouvelle approche non–paramétrique de l'imagerie radar Doppler », Rapport de contrat (confidentiel) CNRS–Société THOMSON, GPI–L2S, 1995.

[4] P. Ciuciu, **J.-F. Giovannelli** et J. Idier, « Analyse spectrale post–moderne. Application aux signaux radars », Rapport de contrat (confidentiel) CNRS–Société THOMSON, GPI–L2S, 1997.

[5] **J.-F. Giovannelli** et J. Idier, « Méthodes et algorithmes d'inversion de données en spectrométrie de neutrons : analyse bibliographique prospective. », Rapport de contrat (confidentiel) SUPÉLEC–CEA, GPI–L2S, 1999.

[6] **J.-F. Giovannelli**, « Détection d'objets ponctuels en mouvement dans une séquence d'images », Rapport de contrat ONÉRA, convention N° F/10.646/DA-CDES, GPI–L2S, décembre 2002.

[7] **J.-F. Giovannelli**, « Débruitage impulsionnel : approche non-supervisée », Rapport (n°2) de contrat ONÉRA, convention N° F/10.646/DA-CDES, GPI–L2S, février 2004.

Rapports internes

[1] V. Samson, F. Champagnat et **J.-F. Giovannelli**, « Détection d'objets ponctuels en mouvement dans une séquence d'images : une approche régularisée », rapport technique 1/04005 DTIM, ONÉRA, février 2001.

[2] **J.-F. Giovannelli** et A. Herment, « Gaussian regularization for 2D frequency unaliasing and phase unwrapping », rapport technique, GPI–L2S, 2001.

[3] V. Samson, F. Champagnat et **J.-F. Giovannelli**, « Modèles d'estimation d'objets ponctuels dans une séquence d'images sur fond corrélé », rapport technique 1/06768 DTIM, ONÉRA, mai 2002.

[4] **J.-F. Giovannelli** et A. Herment, « Convex regularization for high resolution MRI from aliased low frequency data », rapport technique, GPI–L2S, septembre 2002.

[5] G. Rochefort, F. Champagnat, G. Le Besnerais et **J.-F. Giovannelli**, « Techniques de super-résolution et extension du modèle de formation d'images », rapport technique 1/06766 DTIM, ONÉRA, octobre 2003.

[6] A. Hazart, S. Dubost, S. Gautier et **J.-F. Giovannelli**, « Estimation de la distribution d'une pollution à partir de mesures dans la nappe phréatique », Rapport de stage du DEA-TIS 2002-2003, EDF / GPI–L2S, Gif-sur-Yvette, septembre 2003.

Thèse

[1]⋆ **J.-F. Giovannelli**, *Estimation de caractéristiques spectrales en temps court. Application à l'imagerie Doppler*, Thèse de Doctorat, Université de Paris-Sud, Orsay, février 1995.

1.4 Enseignement et formation

Cette section décrit mes activités d'enseignement. Elles concernent le *traitement du signal et de l'image* en général et pour une plus petite partie les *problèmes inverses et la reconstruction d'images*.

Charge à l'Université Paris-Sud — Mes enseignements à l'Université Paris-Sud se déroulent en 2e et 3e cycle, dans la filière en EEA, sous la forme de cours magistraux pour 50%, de travaux dirigés pour 20% et de travaux pratiques pour 30%.

- Je suis en particulier responsable du cours de *signaux et systèmes linéaires* de la licence en EEA. J'ai rédigé un recueil d'exercices variés, aussi souvent que possible motivés par des considérations physiques réelles (radars, optique, propagation, *etc*).
- J'ai proposé un cours de *reconstruction et restauration de signaux et d'images* dans le DESS-SE pour lequel j'ai rédigé un polycopié.
- J'ai proposé une vingtaine de nouveaux sujets de TP, TE, TER et stages. A chaque fois, je m'attache à bâtir les sujets autour d'applications pratiques et basées sur des signaux réels.
- Par ailleurs, je me suis impliqué dans la mise en place du schéma LMD, en particulier la définition des nouveaux contenus en lien avec les matières connexes.

Vacations en formation continue à Supélec — En dehors de l'Université, j'ai l'opportunité de participer régulièrement à trois sessions de formation continue dispensées par Supélec et destinées à des ingénieurs (pour un volume annuel moyen de 10 heures environ). La première est une session générale consacrée au traitement du signal et mon intervention (en alternance avec Guy DEMOMENT) introduit le *filtrage de Kalman*. La seconde concerne plus spécifiquement le filtrage adapté et nous y présentons également une intervention à propos de filtrage de Kalman. La troisième traite de *techniques d'inversion de mesures* et mon intervention concerne (1) le cadre linéaire et gaussien, (2) le cas non-gaussien et convexe et (3) un exemple synthétique lié à la caractérisation spectrale et temps-fréquence des signaux.

Vacations en DEA — Elles se sont déroulées d'une part à Créteil et d'autre part à Lyon.

- Le cours de *restauration et reconstruction d'images* du DEA de Génie biologique et médical de l'Université de Paris XII dans l'option Signaux et Images en médecine m'a été proposé en décembre 1997. Malgré l'importance de ma charge d'enseignement à l'UPS, j'ai jugé opportun de l'accepter. J'y présente les rudiments de restauration et reconstruction d'images médicales : tomographie, échographie, imagerie par résonance magnétique, *etc*.
- Par ailleurs, j'interviens pour une séance de cours de 4 heures dans le module *problèmes inverses* du DEA Images et systèmes à Lyon (INSA de Lyon, École Centrale de Lyon, Université Claude Bernard Lyon 1) concernant la *déconvolution gaussienne « à la Hunt »*.

École d'été d'analyse numérique et d'informatique — Les Écoles d'été d'analyse numérique et d'informatique (CEA – EDF – INRIA) s'adressent à un public de chercheurs et d'ingénieurs. Leur objectif est de fournir un cours complet et actualisé dans un domaine choisi de l'analyse numérique et de l'informatique, de faire le point sur l'état d'avancement des sujets et de confronter les expériences des auditeurs. La session de juin 2000 (du 15 au 20) a été consacrée à l'analyse d'images et s'est déroulée au centre d'étude du Bréau. J'y ai présenté un cours concernant également la *déconvolution gaussienne et la méthode Hunt* et une séance de travaux pratiques associée.

Deuxième partie

Bilan scientifique qualitatif

Chapitre 2

Perspective historique et synthèse

2.1 Point de vue inverse

Depuis plusieurs décennies, les « techniques numériques » ont envahi un grand nombre de domaines et s'appuient sur une discipline encore relativement jeune : le traitement du signal. Sa vocation est essentiellement de construire des méthodes et des algorithmes qui fournissent une valeur pour un paramètre physique d'intérêt (noté x) lorsqu'on leur injecte un jeu de données (noté y). Les domaines concernés sont évidemment très nombreux, en particulier tous ceux qui traitent des données expérimentales.

Bien souvent, la réalité physique en jeu peut être décrite (au moins en première approximation) par des équations linéaires : depuis les équations de Maxwell jusqu'à la loi d'Ohm en passant par la notion de filtrage en électronique, les modèles sous-jacents sont linéaires. Ainsi, on est amené à manipuler les outils mathématiques associés : transformation linéaire, convolution, transformée de Fourier, *etc*.

Par ailleurs, la « réalité terrain » n'étant décrite que de manière imparfaite par les équations de la physique et les systèmes de mesure étant eux aussi imparfaits, on est en général amené à prendre en compte des incertitudes (de mesure et de modélisation). Un outil mathématique particulièrement adapté pour cela est la théorie des signaux aléatoires.

A ce stade, on est capable, dans une certaine mesure, de décrire le phénomène physique en jeu ainsi que les incertitudes auxquelles il est soumis. En somme, étant donnés les paramètres physiques, on sait décrire les données observées : on dispose d'un *modèle direct*

$$y = Hx + b\,. \tag{2.1}$$

Cela dit, le travail du traitement du signal n'est pas terminé : son objet est au contraire de partir des données observées y pour remonter aux paramètres physiques x qui en sont l'origine, c'est-à-dire de réaliser une opération d'inversion. On parle de *problèmes inverses* et le plus souvent, ils sont *mal-posés* : les données sont insuffisantes pour construire une solution acceptable. Face à ces difficultés, les méthodes de *régularisation* permettent d'intégrer des informations sur les objets observés pour compléter les informations apportées par les données.

2.2 Quelques éléments historiques

2.2.1 Approches quadratiques et solutions linéaires

Historiquement, les premières méthodes de régularisation sont quadratiques (L_2) et on peut leur donner une interprétation en terme d'analyse à l'ordre deux ou de processus gaussien. On peut ainsi les faire remonter aux années 50 avec le filtrage de Wiener et aux années 60 avec le filtrage et le lissage de Kalman. Dans les deux cas, les solutions sont régularisées et le point de vue est bayésien au sens où les quantités inconnues sont modélisées par des signaux aléatoires.

Au début des années 60, les travaux de Phillips, Twomey et Tikhonov [113, 136, 133] sont explicitement consacrés à la régularisation par pénalisation (toujours quadratique) et leur point de vue est plus déterministe. Leurs contributions arrivent à maturité au milieu des années 70 avec l'ouvrage de Tikhonov [134] dans un cadre continu et celui de Andrews et Hunt [4] dans un cadre discret.

La méthodologie repose sur un critère J comprenant deux types de termes :

1. un terme d'adéquation aux données : en général un terme de moindres carrés bâti sur le modèle direct (2.1),
2. un (ou plusieurs) terme(s) de pénalisation quadratique $\mathcal{P}(x)$ adressant seulement les paramètres inconnus.

Le critère s'écrit alors :

$$J(x) = \|y - Hx\|^2 \; + \; \lambda \, \mathcal{P}(x) \, ,$$

où le paramètre de régularisation λ (hyperparamètre) pondère l'influence relative de chacun des termes. La solution proposée est alors définie comme minimiseur de ce critère :

$$\widehat{x} = \arg\min_x J(x) \, .$$

Les solutions ainsi construites sont linéaires vis-à-vis des données et elles allient simplicité de mise en œuvre, efficacité algorithmique et robustesse. Elles sont pertinentes pour des signaux et des images réguliers ; cependant, pour des signaux ou des images présentant des impulsions ou des ruptures (c'est-à-dire régulier, mais par morceaux uniquement) la pénalisation quadratique s'avère insatisfaisante : elle a un effet de lissage global et ne permet pas de préserver ou détecter des discontinuités ou impulsions.

Remarque 1 — *Ces outils méthodologiques s'interprètent dans le cadre de la théorie de l'estimation bayésienne et exploitent des modèles probabilistes a priori gaussiens (indépendants ou à corrélation markovienne le plus souvent). Les premières extensions développées et décrites sommairement dans la section suivante reposent sur ce point de vue bayésien.*

2.2.2 Variables cachées et détection d'événements rares

Pour dépasser les limitations des approches linéaires, à la fin des années 70 et au début des années 80, plusieurs auteurs introduisent des variables binaires cachées (*i.e.*, non observées) modélisant des événements rares : apparition d'impulsions ou de contours.

– Geman & Geman [56] introduisent des modèles markoviens pixels-contours propices à la production de zones homogènes séparées par des contours réguliers : la loi *a priori* probabilise à la fois le champ des pixels et un processus de lignes interactives.

– Kormylo & Mendel [104] introduisent des modèles Bernoulli-gaussiens blancs, favorisant l'apparition d'impulsions en faible nombre dans un signal essentiellement nul : la loi *a priori* probabilise à la fois l'amplitude et l'apparition d'impulsions.

Ces travaux, fondateurs, introduisent des modèles très riches, permettant de décrire plus finement les signaux et les images recherchés et de réaliser une opération de *détection* de contours ou d'impulsions simultanée à l'inversion.

Dans un cadre déterministe, [9, 110, 108] utilisent aussi un processus caché binaire permettant de localiser des ruptures et d'interrompre le lissage ou la pénalisation. Cependant, les variables cachées sont ici découplées : seul le nombre de ruptures est pénalisé et pas leur position relative. En termes de pénalisation, le potentiel est une quadratique tronquée L_2-L_0 : il est quadratique (L_2) autour de l'origine pénalisant fermement les petites fluctuations et constant (L_0) à partir d'un certain seuil autorisant ainsi l'apparition de contours ou d'impulsions marquées. D'autres potentiels non convexes de la forme L_2-L_0 ou concaves, ont été considérés [54, 57, 55], mais sans introduire explicitement de variable de ligne. On peut cependant faire un lien entre ces potentiels et des variables de lignes non-interactives à valeurs continues (et non plus binaires) [55, 23, 88, 8].

Ces approches posent toutefois des difficultés d'ordre algorithmique. Les critères J ainsi construits peuvent posséder des minima locaux, en grand nombre dans certains cas. La charge calculatoire pour les optimiser devient alors beaucoup plus importante, et parfois sans garantie d'obtenir le minimum global. A cet inconvénient s'ajoute aussi celui de l'instabilité et de la non-continuité de la solution obtenue [15, 127, 96, 131].

2.2.3 Cas convexe et préservation d'événements rares

D'autres approches ont été développées depuis et en particulier celles fondées sur des potentiels *convexes* mais non quadratiques comme la fonction de Huber ou la fonction hyperbolique [23, 88]. Ces potentiels sont dits L_2-L_1 : ils demeurent quadratiques (L_2) autour de l'origine, pénalisant toujours les petites fluctuations, et linéaire (L_1) à partir d'un certain seuil, autorisant ainsi la préservation de ruptures ou d'impulsions.

Dans ce cadre, les constructions de [54, 55] ont débouché sur deux algorithmes : ARTHUR et LEGEND [23] développés au Laboratoire I3S. Ils ont ensuite été complétés par des travaux du Groupe Problèmes Inverses [88]. L'analyse bayésienne des variables duales [22], plus récente, est aussi instructive et inspirera une partie des perspectives proposées.

Remarque 2 — *Les propriétés de stricte convexité et de différentiabilité sont cruciales en pratique pour le critère. En effet, sous ces hypothèses [15],*

1. *le critère possède un minimiseur unique, ce qui permet de définir proprement une estimée ;*
2. *celle-ci est continue par rapport aux données et aux hyperparamètres ;*
3. *une large classe d'algorithmes classiques est disponible pour la calculer.*

Notons cependant que la non-continuité des estimées vis à vis des données est un desiderata *dans les problèmes de détection ou de segmentation.*

Les contributions reposant sur ces pénalisations convexes sont nombreuses car elles constituent un compromis intéressant entre coût de calcul et préservation des discontinuités éventuelles. Mes travaux s'appuient largement sur ces contributions.

2.3 Synthèse des travaux

Du point de vue des thèmes académiques, mes centres d'intérêt ont évolué au cours de la dernière décennie. La problématique centrale de mon travail de thèse [60] (1991-1995) concerne la caractérisation spectrale, en temps court. Ce thème recouvre plusieurs problèmes clés en traitement du signal : l'analyse spectrale, l'analyse temps-fréquence et l'estimation de moments spectraux. Ce thème a continué d'exister dans mes activités jusqu'en 2000. En parallèle, à partir de 1998, j'ai commencé à diversifier mes activités, passant naturellement de l'analyse spectrale (vue comme un problème de synthèse de Fourier) à la synthèse de Fourier elle-même et dans un second temps à son problème dual : la déconvolution. Ces trois thèmes sont successivement résumés au chapitre suivant :

1. caractérisation spectrale (§ 3.1, p. 31),
2. synthèse de Fourier (§ 3.2, p. 35),
3. déconvolution (§ 3.3, p. 38).

Ces activités sont essentiellement motivées par des applications que l'on peut regrouper naturellement sous le terme d'*imagerie*. L'application initiale de mon travail de thèse est l'échographie Doppler pour des applications médicales et repose sur la caractérisation spectrale de signaux. Ces travaux en caractérisation spectrale ont ensuite trouvé des débouchés dans d'autres domaines comme l'imagerie des tissus (mesure de l'atténuation acoustique des tissus de la peau, en 1993) et le traitement de signaux issus de radars Doppler (surveillance des turbulences atmosphériques, sur la période 1994-2000). Les développements que j'ai proposé ensuite en synthèse de Fourier et déconvolution ont également trouvé des applications en imagerie médicale (par IRM, en 1998-2002) mais aussi en imagerie astronomique (par interférométrie en 1998-2005) et satellitaire / aéroportée (visible et infrarouge, en 1999-2005).

Malgré la diversité des thèmes et des applications, mes activités présentent une double spécificité :

1. en termes de problèmes abordés : je m'intéresse aux *problèmes inverses mal-posés*.
2. en termes méthodologiques : j'aborde ces problèmes avec les outils de la *régularisation*.

Le caractère mal-posé est dû au manque d'informations fournies par les données à propos des objets imagés. Dans les problèmes qui m'intéressent les composantes hautes fréquences des objets imagés sont fortement atténuées, absentes ou même repliées dans les données observées, les données sont en faible quantité et / ou faiblement informatives, ou encore fortement sous-échantillonnées.

Le travail réalisé prend en compte des informations *a priori* ou introduit des hypothèses sur les objets recherchés, pour compenser, au moins partiellement, le manque d'informations apportées par les données. Il s'appuie pour cela sur des méthodes de régularisation, non seulement par pénalisation comme évoqué précédemment mais aussi par contrainte et paramétrisation (ou des combinaisons de ces trois formes).

1. *Paramétrisation*, afin de structurer les solutions. La modélisation des spectres monochromatiques ou gaussiens (voir § 3.1.3, p. 34) de même que la modélisation des sources de pollutions (voir § 1.1.5, p. 13) entrent dans ce cadre.
2. *Contraintes*, qui interdisent les solutions indésirables et limitent les espaces de solutions. Un exemple typique est la positivité des images recherchées en astronomie (voir § 3.2.2, p. 35).
3. *Pénalisation* des solutions indésirables. L'ensemble du travail réalisé exploite cette forme dans le cas convexe. Il exploite deux types de pénalisation qui permettent de se prononcer sur le

caractère *a priori* corrélé ou non corrélé des objets recherchés et qui se codent comme somme de fonctions potentiels adressant les pixels.

– (3-a) : des termes d'interactions entre pixels voisins favorisant un objet régulier

$$\mathcal{P}_{\mathrm{c}}(\boldsymbol{x}) = \sum_{p \sim q} \phi_{\mathrm{c}}\left[x_q - x_p\right] \tag{2.2}$$

où $\sim$ symbolise la relation de voisinage entre pixels.

– (3-b) : des termes séparables favorisant un objet impulsionnel.

$$\mathcal{P}_{\mathrm{s}}(\boldsymbol{x}) = \sum \phi_{\mathrm{s}}\left[x_p\right] \ . \tag{2.3}$$

Ces termes rappellent indépendamment les pixels à zéro et favorisent ainsi les cartes quasi-nulles et présentant quelques impulsions.

D'un point de vue stochastique, les premiers sont des champs markoviens et les seconds des bruits blancs. Une partie de ma contribution repose sur la superposition de ces deux composantes (bi-modèle), en analyse spectrale (voir § 3.1.2, p. 33), en imagerie satellitaire (voir § 3.3.1, p. 38) et en imagerie pour l'astronomie (voir § 3.2.2, p. 35). D'un point de vue stochastique, le modèle n'est ni blanc, ni markovien.

2.3.1 Une contribution : bi-modèle

Plus précisément, ce « bi-modèle » est dédié à l'estimation d'objets possédant une composante impulsionnelle superposée à une composante régulière. L'objet recherché est alors modélisé comme la somme de deux composantes : $x = x_{\mathrm{e}} + x_{\mathrm{p}}$. Cette forme fait apparaître de nouvelles indéterminations puisqu'il s'agit d'estimer maintenant deux objets au lieu d'un, toujours à partir du même jeu de données y. Cependant, cette modélisation permet d'introduire de manière explicite des informations caractéristiques sur chacune des cartes par l'intermédiaire des deux modèles *a priori* : un terme interactif du type (2.2) pour la carte x_{e} et un terme séparable du type (2.3) pour la carte x_{p}.

Nous avons proposé ce « bi-modèle », en 1996 avec Jérôme IDIER, pour l'estimation de raies superposées à un fond homogène en analyse spectrale. Je l'ai ensuite exploité en déconvolution pour l'imagerie de points brillants sur un fond nuageux. Dans les deux cas, le travail repose sur des termes de pénalisation convexe du type L_2-L_1 pour chacune des deux composantes x_{e} et x_{p}. J'ai ensuite enrichi et complété ces travaux en introduisant

– des contraintes de positivité et de support,
– une spécificité L_2+L_1 : un terme L_2-corrélé pour la composante régulière x_{e} (*i.e.*, ϕ_{c} est quadratique) et un terme L_1-séparable pour la composante impulsionnelle x_{p} (*i.e.*, ϕ_{d} est linéaire), au lieu de deux termes L_2-L_1.

Ces idées ont débouché notamment sur une contribution en déconvolution / séparation, synthétisée en un article [65] paru dans la revue *Astronomy & Astrophysics* (et reproduit à la page 143).

2.3.2 Une contribution : inversion de repliement spectral

Une autre spécificité du travail réalisé concerne l'extrapolation spectrale incluant une éventuelle opération d'inversion de repliement spectral. On la trouve naturellement dans ma contribution à la

poursuite de moments spectraux au-delà de la limite de repliement. On la trouve également dans le volet synthèse de Fourier et déconvolution. De manière synthétique, on peut dire que dans les trois cas on inverse (au moins partiellement) le repliement en s'appuyant sur un modèle d'observation qui inclut ce repliement.

- Dans le cas de l'imagerie visible ou infrarouge, le système de mesure est construit à la fois sur l'optique et sur l'intégration-échantillonnage que réalise chaque élément de capteur CCD.
- Dans le cas de la synthèse de Fourier (et en interférométrie et en IRM) c'est le caractère parcellaire du remplissage du plan de Fourier qui induit un phénomène de repliement ou de quasi-repliement.
- Plus simplement, dans le cas de la poursuite de moments spectraux, c'est l'échantillonnage qui produit une indétermination sur la bande de fréquence initialement occupée par les signaux.

Chapitre 3

Résumés

Ce chapitre résume successivement les trois thèmes de recherche : caractérisation spectrale (§ 3.1, p. 31), synthèse de Fourier (§ 3.2, p. 35) et déconvolution (§ 3.3, p. 38). Au fur et à mesure des développements plusieurs perspectives spécifiques à chaque thème sont évoquées.

3.1 Caractérisation spectrale

Les méthodes d'inversion de données développées ne sont pas limitées aux problèmes inverses *stricto sensu* puisque, pour ma part, je m'intéresse à la caractérisation spectrale des signaux. Ce thème fait suite à mes travaux de thèse et de post-doctorat et a constitué le fil conducteur d'une partie de mes activités. Ce terme de caractérisation spectrale recouvre plusieurs problèmes clés en traitement du signal :

- l'analyse spectrale [66, 32, 71],
- l'analyse temps-fréquence [73],
- l'estimation de moments spectraux [72].

Ces questions présentent un enjeu crucial dans plusieurs domaines : caractérisation des flux sanguins par échographie Doppler ultrasonore [74, 85, 6] ou par résonance magnétique [86], caractérisation acoustique des tissus biologiques [90, 74], radars de surveillance des turbulences atmosphériques [25, 73].

Outre le fait que les paramètres d'intérêt sont de type spectraux, l'ensemble des problèmes traités possède une caractéristique commune : le nombre très réduit de données disponibles (entre quatre et seize !) pour estimer ces paramètres. A ce défaut d'information peut s'ajouter une indétermination supplémentaire : la nature discrète des données et les contraintes expérimentales sur la fréquence d'échantillonnage laissent indéterminée la bande de fréquence effectivement occupée par les signaux. Il s'agit alors d'inverser un repliement spectral dans un contexte temps court.

Le manque d'informations fournies par les observations induit de fortes incertitudes sur les paramètres cherchés, s'ils sont estimés sur la seule base de ces observations. La démarche adoptée consiste alors à prendre en compte des informations *a priori* sur la structure des objets recherchés (spectres, nappes temps-fréquence, *etc*) pour compenser, au moins partiellement, le manque d'informations apportées par les données.

3.1.1 Modèle autorégressif

Dans le cadre de l'analyse spectrale autorégressive, la démarche standard consiste à :

1. déterminer un ordre pour le modèle utilisé en optimisant un critère tel que celui d'Akaïke qui pénalise les ordres élevés et assure ainsi de manière indirecte une certaine régularité spectrale ;
2. minimiser un critère de moindres carrés pour estimer les paramètres AR eux-mêmes.

Malheureusement, dans nos situations le nombre de données est très réduit et ce schéma présente deux limitations. D'une part les méthodes de détermination d'ordre sont instables [137] et d'autre part le modèle que l'on peut estimer est d'ordre trop faible pour décrire des spectres variés. Nous adoptons alors l'approche introduite par Kitagawa & Gersch [94] qui pose le problème de manière radicalement différente : la notion de douceur spectrale est intégrée au sein même du critère d'estimation sous la forme d'une pénalisation.

Dans le cadre de l'analyse spectrale adaptative, il existe de nombreux algorithmes : moindres carrés à fenêtres glissantes, moindres carrés à oubli exponentiel et de nombreuses variantes. Ces algorithmes présentent le défaut déjà mentionné ci-dessus pour l'aspect spectral mais un nouveau défaut s'ajoute avec la dimension temporelle. Ces méthodes introduisent une idée de continuité temporelle dans les nappes temps-fréquence de manière détournée, par le biais de la taille d'une fenêtre de lissage ou par un paramètre d'oubli. Qui plus est, il n'existe pas de méthode de réglage automatique de ces paramètres.

Kitagawa & Gersch [95] proposent de prendre en compte la notion de régularité temporelle dans le formalisme du filtrage de Kalman, mais indépendamment de la notion de douceur spectrale. Dans le but d'intégrer simultanément la douceur spectrale et la continuité temporelle, nous réalisons une synthèse originale de leurs deux propositions. Nous construisons un critère cohérent afin de prendre en compte simultanément les deux informations. Comme dans [95], un lisseur de Kalman permet de calculer son minimum.

Dans les deux cas, les méthodes développées sont entièrement automatiques : le réglage du compromis entre les données et les informations de continuité est obtenu par maximum de vraisemblance marginale ou par validation croisée. Les résultats sont présentés, entre autres dans deux publications dans les *IEEE Transactions on Geoscience and Remote Sensing* [73] (reproduite à la page 95) et *IEEE Transactions on Ultrasonics Ferroelectrics Frequency Control* [66]. Ce dernier est cité à plusieurs reprises, en particulier au CREATIS : [46, 76, 45]. Nous avons par ailleurs étudié la stabilité des systèmes associés : ce travail est publié dans [89] (reproduit à la page 77) et cité dans [100].

La méthodologie a été adaptée au problème de mesure de l'atténuation acoustique des tissus de la peau (collaboration avec la Société L'ORÉAL, évoquée au § 1.2.5, p. 16) et au traitement de signaux issus de radars Doppler (collaboration avec la Société THOMSON, décrite au § 1.2.7, p. 16). Nous montrons une précision accrue dans la caractérisation des structures imagées [67, 90, 68, 73]. Une version modifiée de ces algorithmes a été développée en échographie Doppler en collaboration avec Alain HERMENT (collaboration décrite au § 1.2.1, p. 13) et publiée dans *Ultrasound in Medicine and Biology* [6].

Perspectives — Les méthodes exposées précédemment sont robustes et adaptées à la prise en compte d'informations de régularité spectrale et temporelle. Cependant, dans certaines situations comme l'imagerie de turbulences atmosphériques, la brutale apparition d'un front de précipitations

induit une rupture temporelle dans la nappe temps-fréquence qui n'est pas restituée correctement par des méthodes convexes. Je propose de développer des méthodes adaptées à ces situations en exploitant des modèles à ruptures [9, 50, 36].

3.1.2 Modèle de Fourier

Les travaux concernant les modèles AR présentés précédemment sont fondés sur la prise en compte d'information de régularité spectrale ; l'objectif du travail présenté ici est au contraire de laisser apparaître des composantes hautes résolutions tout en conservant une douceur globale. Il s'agit d'une situation usuelle : le spectre recherché comporte un fond à variation lente auquel peuvent se superposer des composantes quasi-monochromatiques.

Un tel travail dans le cadre de l'analyse spectrale AR s'avère délicat car les termes de régularisation pénalisent les coefficients AR et pas directement la forme des spectres. C'est pourquoi nous avons choisi de travailler à partir du modèle de Fourier *i.e.*, la juxtaposition d'un grand nombre de raies d'amplitudes inconnues $\boldsymbol{a} \in \mathbb{C}^P$. Le problème se ramène alors à celui de la synthèse de Fourier où le nombre d'amplitudes souhaitées est largement plus grand que le nombre de données : le problème est fortement indéterminé.

Nous montrons que l'introduction de modèles *a priori* gaussiens, corrélés ou blancs, permet d'interpréter les techniques de périodogramme standard : fenêtrage et « bourrage de zéros ». Ces résultats sont originaux et publiés dans les *IEEE Transactions on Signal Processing* [71] (reproduit à la page 83). En particulier, sa section IV bâtit une interprétation bayésienne dans un contexte fonctionnel en terme de moyenne *a posteriori*, là où une interprétation en terme de maximum *a posteriori* n'est pas possible. Ce travail est cité par [141] paru dans le *Journal of the Royal Statistical Society*.

Par ailleurs, ces résultats donnent un éclairage nouveau aux techniques de périodogramme et à leur faible pouvoir de résolution. Ils débouchent directement sur des méthodes résolvantes fondées sur des modèles *a priori* non-gaussiens. Dans cette classe de modèles, pour des raisons de coût de calcul, nous nous limitons aux modèles à potentiels convexes. Ce travail est développé dans la thèse de Philippe CIUCIU évoquée au § 1.1.1, p. 11.

Afin de prendre en compte les caractéristiques des spectres recherchés (composante régulière plus composantes quasi-monochromatiques), nous introduisons un « bi-modèle » particulièrement adapté : $\boldsymbol{a} = \boldsymbol{a}^{\mathrm{l}} + \boldsymbol{a}^{\mathrm{e}}$.

- Le premier terme, piloté par un modèle markovien associé à des potentiels $R_{\mathrm{l}}(|a^{\mathrm{l}}_{p+1}| - |a^{\mathrm{l}}_{p}|)$, assure la *douceur spectrale* de la composante large bande.
- Le second, piloté au contraire par un terme séparable de potentiel $R_{\mathrm{e}}(|a^{\mathrm{e}}_{p}|)$ autorise les *composantes résolues*.

Cette idée de « bi-modèle » *i.e.*, d'objets ponctuels superposés à un fond régulier, est par ailleurs à la base du travail de la thèse de Vincent SAMSON (présentée au § 1.1.3, p. 12 et détaillée au § 3.3.1, p. 38). Cette idée est également un élément central de mes travaux récents en imagerie pour l'astronomie (présentés au § 1.2.2, p. 14 et développés au § 3.2.2, p. 35).

Sur un problème d'estimation de spectre de largeur très faible nous obtenons un gain spectaculaire en terme de résolution spectrale et de réjection des lobes secondaires confirmant ainsi les résultats déjà proposés par [119]. Sur un problème de recherche de spectre régulier, nous réduisons fortement la variabilité (sans introduire de biais notable) et mettons en évidence un gain en précision

de l'ordre de 40%. Enfin et surtout sur un problème « mixte » de recherche de composantes quasi-monochromatiques dans un fond relativement homogène, nous traitons le fameux exemple de Kay & Marple [92] : nous mettons en évidence une capacité fortement accrue à restituer simultanément les deux types de composantes et à les séparer. Ces résultats ont été présentés dans deux communications de congrès [30, 29] et dans un article aux *IEEE Transactions on Signal Processing* [32] (reproduit à la page 107). La communication [30] est citée à plusieurs reprises ([17, 16, 18]).

3.1.3 Modèles gaussien et monochromatique

Le troisième volet concernant la caractérisation spectrale traite de la poursuite de fréquence moyenne et de largeur spectrale, dans un contexte présentant deux difficultés : la première tient au fait que les signaux mesurés sont de très courte durée et la seconde tient au fait que la bande de fréquence initialement occupée par les signaux est inconnue. Il s'agit alors d'inverser un repliement spectral dans un contexte temps court.

La faiblesse du nombre de données disponibles rend les méthodes classiques inefficaces et nous analysons leurs limitations sous l'angle de la théorie de l'estimation, en exploitant un modèle monochromatique et un modèle gaussien pour les spectres. L'une ou l'autre de ces hypothèses permet de mettre en évidence une vraisemblance périodique dans la direction des fréquences moyennes, qui traduit les indéterminations sur la bande de fréquence initialement occupée par les signaux.

Une partie de mes travaux de thèse [74, 60] constitue une réponse novatrice à cette question. L'introduction d'une chaîne de Markov pour les paramètres spectraux permet de prendre en compte un certain degré de continuité du profil de fréquence recherché afin de compenser, dans un certaine mesure, le manque d'informations apportées par les données. Cette idée conduit à un critère dont le minimum est obtenu par l'algorithme de Viterbi.

Après ma thèse, je me suis intéressé au réglage automatique des paramètres de la méthode *i.e.*, l'estimation des hyperparamètres. J'ai encadré, avec Jérôme IDIER, le stage de DEA de Redha BOUBERTAKH et nous avons adapté un algorithme itératif de type EM [5, 103] permettant de maximiser, au moins localement, la vraisemblance des paramètres [10]. La méthode obtenue est alors entièrement non-supervisée.

Les résultats sont spectaculaires : on a une très forte réduction des variabilités sans introduction de biais notable, en même temps qu'un suivi robuste de la fréquence, y compris au-delà de la limite de Shannon. Ce travail a fait l'objet d'une publication dans les *IEEE Transactions on Signal Processing* [72] (reproduite à la page 121). Le papier est cité dans [19]. L'intérêt et l'efficacité de la méthode développée ont été démontrés sur des signaux synthétiques et réels dans le cadre de la vélocimétrie Doppler ultrasonore et en imagerie par résonance magnétique [74, 86].

Perspectives — Cela dit, le travail restant à réaliser est important : il s'agit de l'extension en 2 et 3D [58], cruciale du point de vue des applications. Sur ce point, le passage d'une chaîne de Markov à un champ de Markov permet sans difficulté d'étendre à 2D ou même 3D le critère construit en 1D mais le problème d'optimisation devient beaucoup plus complexe et il n'existe pas d'algorithme efficace. Le travail récent de [41] pourra constituer un point de départ pour le développement de l'extension multidimensionnelle.

3.2 Synthèse de Fourier

Dans les problèmes envisagés ici, les données observées sont constituées d'une partie seulement de la transformée de Fourier bruitée de l'objet recherché : le modèle direct est une transformée de Fourier tronquée bruitée. Selon les modalités, les données sont disponibles sur des domaines différents, sur des grilles cartésiennes ou non. Parmi les applications on peut citer l'imagerie en astronomie par interférométrie et l'imagerie médicale par résonance magnétique mais aussi la tomographie à rayons X, ...

L'étape d'inversion est un problème dit de *synthèse de Fourier* et sa difficulté majeure tient à la troncature. Elle est souvent forte, les informations dans le domaine de Fourier sont très incomplètes et en particulier l'observation des hautes fréquences est souvent inexistante. Le modèle direct, linéaire à bruit additif, est de rang déficient puisque le nombre de données est inférieur au nombre de pixels. En conséquence, il existe une infinité d'objets compatibles avec tout jeu de données. La sélection d'une solution passe donc par la prise en compte d'informations *a priori* sur la carte recherchée.

3.2.1 Synthèse de Fourier, analyse spectrale et bi-modèle

Dans cette section, entre le travail réalisé en analyse spectrale (vue comme un problème de synthèse de Fourier) et déjà détaillé au § 3.1.2, p. 33.

3.2.2 Contrainte de positivité et de support

Le point de départ de ce travail est un problème d'interférométrie radio pour l'observation du soleil qui pose un problème de synthèse de Fourier largement abordé dans la communauté de l'astronomie. On pourra consulter [130] qui propose un tour d'horizon intéressant. Notre contribution est centrée sur le cas où la carte inconnue (1) est positive et respecte un support connu et (2) se présente comme la somme de deux composantes.

- Une carte de *sources ponctuelles* essentiellement nulle avec quelques valeurs importantes. C'est une composante large bande, occupant l'ensemble du domaine de Fourier. Elle est naturellement décrite par une loi séparable et notre choix s'est porté sur la loi exponentielle qui présente plusieurs avantages. Elle permet de conserver un critère quadratique. Elle favorise les pixels nuls, grâce à un potentiel minimum et à dérivée strictement positive à l'origine. Elle possède une queue plus lourde que la gaussienne, favorisant ainsi l'apparition d'événements plus rares.
- Une carte spatialement *étendue*, plutôt régulière et occupant essentiellement les basses fréquences. Le champ choisi pour la décrire est naturellement corrélé et notre choix s'est tourné vers le cas gaussien, ce qui permet de conserver un critère quadratique.

Cette démarche fait apparaître de nouvelles indéterminations puisqu'il s'agit d'estimer maintenant deux cartes, toujours à partir d'un seul jeu de données. Cependant, elle permet d'introduire de manière explicite des informations caractéristiques de chacune des cartes par l'intermédiaire de deux lois *a priori* adaptées.

Remarque 3 — *Contrairement à une idée fausse qui semble pourtant répandue et tenace, la carte des sources ponctuelles n'est pas une composante haute fréquence et elle s'étend sur l'ensemble de l'espace de Fourier. Ainsi, les deux cartes possèdent des composantes aux basses fréquences.*

Du point de vue bayésien, la capacité à séparer les deux composantes repose sur le choix des lois *a priori* pour chacune des deux. Ces choix se distinguent par deux caractères : la dépendance et la forme de la loi.

- Le modèle est séparable et la queue est lourde pour la carte impulsionnelle.
- Le modèle est corrélé et gaussien pour la carte étendue.

La démarche adoptée débouche sur une loi *a posteriori* dont le potentiel est quadratique et différentiable sur $\mathbb{R}_+^N$. En pratique, le couple de carte solution s'obtient numériquement par l'optimisation d'un critère quadratique sous contrainte linéaire. Nous avons envisagé plusieurs options algorithmiques [111, 7, 59] garantissant l'obtention de l'unique minimiseur et vous avons retenu un algorithme de lagrangien augmenté. Il est particulièrement adapté à notre situation et permet de tirer parti de la structure pour le calcul explicite et par FFT de certaines solutions intermédiaires. Il n'est pas décrit ici et on pourra consulter la section V de [65] (reproduit à la page 143) pour avoir plus de détails.

Remarque 4 — *Une pratique bien ancrée dans une partie de la communauté astro consiste à reconvoluer les cartes obtenues par le « lobe propre » (e.g., lobe gaussien ajusté à la réponse impulsionnelle). L'idée consiste à dégrader la résolution des cartes reconstruites jusqu'à la résolution naturelle des données. Tel n'est pas le cas ici.*

Nous proposons des premiers résultats de traitement de données réelles et simulées sur un cas délicat : le mélange de structures issues de la convolution de la réponse instrument riche en lobes secondaires et des deux types de sources (ponctuelle et étendue). Il s'agit d'un cas très complexe à démêler et l'expérience des astronomes sur ces données est que les méthodes existantes ne parviennent pas du tout à démêler les contributions. Nous montrons pourtant qu'avec la méthode proposée les effets de l'instrument sont largement inversés, la séparation des deux composantes est assurée et chacune des deux est clairement déconvoluée. Bien sûr, la positivité et les supports sont également respectés.

La reconstruction de la carte des sources étendues est très satisfaisante, car les erreurs sont désormais en deçà de 5%, alors qu'avec des techniques alternatives, on les estimait entre 7 et 10% (et à partir de données sans source ponctuelle). Les sources ponctuelles sont elles aussi bien reconstruites : positions, amplitudes, largeurs et rapports de flux sont restitués de manière fidèle. Nous mettons également en évidence le caractère haute résolution de la méthode mais qui reste encore à quantifier plus précisément. Dans le cas simulé présenté, les sources sont correctement séparées alors qu'elles ne le sont pas dans les données.

Ce travail résulte de la collaboration avec Alain COULAIS (Observatoire de Paris), déjà présentée au § 1.2.2, p. 14. Nous avons présenté nos travaux à l'occasion d'un séminaire invité à l'observatoire de Nançay [63] et un article [65] va paraître dans la revue *Astronomy & Astrophysics* (reproduit à la page 143). Nous présentons aussi une version courte au GRETSI 2005 [64]. L'outil développé est en cours d'intégration au logiciel préparant à l'exploitation scientifique des observations du radiohéliographe de Nançay. Par ailleurs nous travaillons à la mise en ligne de nos codes IDL / GDL et Matlab / Octave.

3.2.3 Données irrégulières

Une troisième contribution concerne le cas des données acquises sur une grille irrégulière. La technique usuelle travaille en deux temps :

1. interpoler / extrapoler et ré-échantillonner les données pour compléter le domaine de Fourier sur un maillage cartésien,
2. calculer la transformée de Fourier inverse (rapide) des données complétées.

Cette technique, plus rapide, est cependant limitée en résolution. De plus, il est difficile d'analyser le lien entre les différents interpolateurs et l'information introduite indirectement sur l'objet recherché. Afin d'améliorer la qualité des estimées, notre approche consiste à prendre en compte les données avec leur localisation exacte dans le plan de Fourier. Le modèle direct est alors une transformée de Fourier discrète (TFD) irrégulière, non calculable par FFT. Les résultats sont également très intéressants puisqu'on montre une forte capacité à inverser un repliement spectral. Sur un plan algorithmique, nous proposons un schéma de calcul nécessitant deux calculs de TFD seulement, au lieu de plusieurs centaines par une approche standard [12].

Ce travail s'est déroulé en collaboration avec Alain HERMENT (évoquée au § 1.2.1, p. 13) et dans le cadre de la thèse de Redha BOUBERTAKH décrite au § 1.1.2, p. 12. Les résultats sont en cours de publication dans un article à paraître dans la revue *Signal Processing* [12] (reproduit à la page 173).

Perspectives en synthèse de Fourier — Elles se présentent en trois points.

- Les aspects 3.2.1 et 3.2.2 sont bâtis pour une grille cartésienne, 3.2.2 est limité à des critères quadratiques et 3.2.3 est limité à un contexte non-contraint et « mono-modèle ». Une partie des perspectives repose sur la synthèse de ces travaux dans un cadre plus général : données irrégulières, pénalisation convexe, forme « bi-modèle » et prise en compte de la positivité et d'un support. Ces travaux pourraient avoir des retombées dans d'autres modalités d'imagerie (tomographie, spectroscopie).
- Par ailleurs, la caractérisation des estimateurs obtenus me paraît être un élément important et manquant aux travaux existants. Deux études me paraissent importantes :
  1. une étude quantitative de la capacité de notre approche bi-modèle à séparer effectivement deux composantes,
  2. une étude de l'influence de la positivité et d'un support sur la résolution des images obtenues et l'inversion d'un éventuel repliement spectral.
- Le troisième volet de ces perspectives concerne l'IRM et doit se dérouler en collaboration avec Alain HERMENT (collaboration déjà évoquée précédemment, au § 1.2.1, p. 13), à l'occasion d'un séjour de trois mois que je vais effectuer dans son laboratoire. Il repose sur une *géométrie d'acquisition radiale* : les données IRM sont acquises sur des segments de droites dans un format typique de la tomographie. Or, les méthodes et algorithmes sans ré-échantillonnage évoqués précédemment présentent l'avantage d'être exploitables quelle que soit la trajectoire d'acquisition, nous pourrons donc les exploiter. Les premières applications visées sont (i) les mesures de flux sanguins dans le cœur et l'aorte, (ii) les mesures de vitesse de l'air pour l'étude de la perfusion pulmonaire (Helium hyperpolarisé) nécessitant toutes les deux des acquisitions rapides.

3.3 Déconvolution : haute résolution et séquence d'images

Dans cette dernière section du chapitre, le contexte est celui de l'imagerie à partir d'une séquence d'images aériennes ou satellitaires en optique visible ou en infrarouge. Dans ce cadre, la résolution naturelle des données est essentiellement liée au système d'observation composé d'une optique et de capteurs. Un tel système, en première approximation, est décrit par une relation de convolution spatiale continue entre le signal bidimensionnel y recueilli en sortie du capteur à l'instant t et l'intensité lumineuse x du champ incident en entrée :

$$y(u, v, t) = (h * x)(u, v, t) + b(u, v, t)\,. \tag{3.1}$$

La fonction h désigne la réponse impulsionnelle du système « optique plus capteur » et le terme additif b représente les erreurs de mesure et de modélisation. La séquence d'images numériques mesurées provient de la discrétisation temporelle et spatiale de y.

3.3.1 Imagerie sur fond nuageux

Il s'agit dans cette partie de localiser précisément ou de réhausser des points brillants sur un fond nuageux structuré et bruité dans une séquence d'images.

- *Aspects spatiaux*. Le caractère passe-bas des capteurs limite la résolution. Ainsi, un objet ponctuel peut impressionner plusieurs capteurs et la tache image est très variable suivant sa position sub-pixellique (effet de phasage). Par ailleurs, le dimensionnement de l'ensemble induit un certain repliement spectral. Ce point nous a conduit naturellement à développer un traitement approprié incluant le repliement et le phasage.
- *Aspects temporels*. La cadence d'acquisition des vues est au contraire suffisamment rapide pour que la déformation du fond nuageux entre deux images soit négligeable. Cependant, la stabilisation du système d'observation est imparfaite ce qui induit de petites variations de la ligne de visée. Ce point nous a conduit à l'utilisation d'un modèle de translation pure entre deux images consécutives du fond.

Nous formulons ainsi le problème comme un problème inverse avec une dimension déconvolution, une dimension séparation et une dimension inversion de repliement spectral. Le travail intègre le modèle global de formation des données (3.1), la spécificité « bi-modèle » et repose sur les approches classiques de la régularisation par pénalisation convexe.

La contribution repose sur trois éléments :

- la modélisation (au moins partielle) de la physique des détecteurs qui intègre le repliement et le phasage ;
- l'exploitation des propriétés spatiales distinguant le fond nuageux et les objets ponctuels qui est la clé de la séparation des deux contributions ;
- enfin, l'exploitation de l'ensemble des informations spatio-temporelles ce qui permet de tirer parti de la forte redondance temporelle des images.

L'approche préconisée consiste à inverser le modèle sur des grilles spatiales de résolution supérieure à celle des données ce qui permet de dépasser la résolution naturelle des données.

Les résultats mènent à une triple conclusion. (1) Ils conduisent à relativiser l'intérêt de détections sub-pixelliques : le gain par rapport au filtre adapté est faible et l'utilisation d'une approche sur-résolue ne paraît pas justifiée, compte-tenu de la surcharge calculatoire. (2) En ce qui concerne la localisation elle-même, nous avons au contraire montré des gains encourageants. Une étude plus poussée de la qualité des estimateurs sur des données réalistes nous semble indiquée : sensibilité au bruit et surtout à sa structure, à l'instrumentation en général (optique, capteur, échantillonnage). (3) L'intérêt majeur de ce travail sur la sur-résolution concerne l'imagerie du fond. Les résultats sont très encourageants et mettent en évidence un apport capital dans un traitement multi-images en présence de repliement. Le gain en performance est ici au contraire suffisant pour justifier son utilisation pratique. Deux aspects essentiels restent cependant à étudier : le réglage des paramètres et la sensibilité au défilement des cibles.

Cette partie du travail fait l'objet d'un article dans le *Special Issue on Image processing for EO sensors* de la revue *Applied Optics* [126] et reproduit à la page 133.

Perspectives — Dans un premier temps, nous envisageons d'affiner les modèles utilisés pour décrire les cibles, le fond et le mouvement inter-images.

- *Cibles ponctuelles*. Il s'agit de favoriser d'avantage les cartes nulles presque partout et présentant des impulsions parcimonieuses à rehausser ou détecter. On pourrait s'appuyer sur au moins trois types de modèles : (1) les modèles L_1 préconisés par [1, 2, 3] (voir aussi [53]), (2) les potentiels non-convexes L_2-L_0 tels que la quadratique tronquée [9] ou encore (3) les modèles impulsionnels Poisson-gaussiens [43, 44] ou Bernoulli-gaussiens [21, 20] explicitement ponctuel.
- *Fond nuageux*. Il s'agit là de favoriser d'avantage les zones homogènes séparées par des contours francs et réguliers. Plusieurs options sont également envisageables, notamment [88] qui ouvre la possibilité d'introduire des interactions entre variables de lignes tout en restant dans un cadre convexe.
- *Aspects temporels et mouvement*. Il s'agit d'affiner le modèle de mouvement ou de déformation du fond nuageux. Un travail a déjà été réalisé sur cette question avec la thèse de Gilles ROCHEFORT (évoquée au § 1.1.4, p. 13), dans un contexte un peu différent mais qui pourrait avoir des retombées pour les problèmes abordés ici. Il est décrit plus en détail ci-dessous au § 3.3.2.

3.3.2 Sur-résolution et séquences d'images

Le travail présenté ici fait suite au travail présenté dans la section précédente et concerne l'amélioration de la résolution spatiale d'images. Il s'agit d'exploiter une séquence d'images observées (dite de basse résolution, BR) pour construire une image de plus haute résolution (dite sur-résolue, SR). L'amélioration de la résolution repose naturellement sur une opération d'extrapolation spectrale, rendue possible par la présence

- de repliement spectral résultant de l'acquisition des données et
- de mouvements sub-pixelliques dans la séquence d'images.

L'inversion du repliement repose sur l'inversion d'un modèle direct décrivant de manière réaliste et précise ces deux éléments. Notre contribution concerne ce modèle direct.

Nous modélisons la fonction de transfert optique, l'intégration sur le capteur et le mouvement, proprement échantillonnés. Le modèle utilisé est celui évoqué précédemment Eq. (3.1), auquel s'est ajouté le mouvement. Sur ce sujet, l'analyse de l'existant permet de dégager deux groupes d'approches, selon la place donnée à la transformation géométrique résultant du mouvement et à son approximation numérique.

1. Le mouvement est pris en compte après l'optique (*i.e.*, sur l'image BR), dans un format dit de Schultz et Stevenson [128].

2. Le mouvement est pris en compte à la plus haute résolution (*i.e.*, sur l'image SR), dans un format dit de Elad et Feuer [47, 48]. Ce format se décline lui-même sous deux formes : avec interpolation d'ordre 0 (plus proche voisin) et d'ordre 1 (bilinéaire).

Les premières évaluations sont réalisées en terme de contribution d'un pixel SR à un élément détecteur et comparées à la contribution exacte obtenue par intégration numérique intensive. Les résultats mettent en évidence l'impact de l'interpolation (plus proche voisin, bilinéaire), du facteur de surrésolution (3 ou 5) et du mouvement (rotations et rapprochements divers). Nous montrons que la seconde approche, dans sa forme bilinéaire, est plus complexe à exploiter mais plus fidèle à la réalité. Elle présente cependant des limites que nous avons bien identifiées pour des forts rapprochements et des fortes rotations. La suite du travail concerne le développement d'une extension véritablement dédiée aux mouvements affines.

Notre effort a ainsi porté sur la prise en compte de ce mouvement, et par là, la construction de l'image à indice continu subissant le mouvement, *i.e.*, l'aspect interpolation. Nous abordons la question de l'interpolation en nous appuyant sur les techniques d'approximation au sens de L_2 et une base de fonctions b-spline. Le modèle direct ainsi construit est une extension du modèle Elad et Feuer adapté aux mouvements affines.

Remarque 5 — *Pour un mouvement en translation, avec des fonctions de bases rectangulaires, la meilleure approximation au sens L_2 est donnée par l'interpolation bilinéaire.*

Sur un plan pratique, les développements s'appuient sur la décomposition de la transformation 2D en une succession de transformations élémentaires 1D de type cisaillement et bénéficient de résultats récents concernant les b-splines [138, 139], permettant le calcul exact et efficace des coefficients optimaux.

Une première évaluation, fondée sur les calculs de contributions des pixels SR au détecteur, montre clairement l'apport de la méthode notamment dans le cas de rotations et de rapprochements importants. Nous évaluons également le modèle direct complet et montrons un gain de 10 dB environ par rapport à la proposition de Elad et Feuer. Des résultats comparatifs sont effectués sur divers exemples d'images et de mouvements, en rapprochement faible, fort ou variable par morceaux. Les résultats obtenus confirment l'intérêt du travail réalisé. Nous montrons que la méthode proposée, dans le cas d'une pénalisation convexe et avec contrainte de positivité conduit à une amélioration notable des performances pour des mouvements en rapprochement et rotation. Cette amélioration est d'autant plus visible que les images sont contrastées.

Ces résultats ont été synthétisés sous la forme d'un article actuellement en révision pour publication dans les *IEEE Transactions on Image Processing* [117] (reproduit à la page 157).

Perspectives — Elles se déclinent ici en deux volets.

- Un prolongement naturel de ce travail serait d'étendre les procédés de SR à des modèles de mouvement plus complexes. Dans ce sens, nous avons mis en œuvre une approche affine par morceaux ; celle-ci reste toutefois limitée. Une approche SR pour des mouvements paramétriques par morceaux peut constituer une étape avant de considérer une représentation 3D de la scène. Pour ces situations, il est notamment possible de prendre en compte des transformations géométriques plus importantes et de natures différentes. Par exemple, il est envisageable de traiter le cas de la transformation homographique, mais cela nécessite une nouvelle transformation élémentaire qui ne peut plus être un simple cisaillement.
- Les domaines d'application de la SR sont très vastes, au delà du domaine visé initialement. Ils peuvent notamment inclure la conversion de vidéos de résolution standard vers des résolutions plus élevées bénéficiant d'un traitement multi-images. De plus, il est courant de procéder à des retouches sur de vieux films (élimination de rayures, débruitage, *etc*) ; l'amélioration de résolution pourrait faire partie de ces traitements.

Chapitre 4

Perspectives : aspects non-supervisés

Une partie des perspectives de recherche est présentée au fur et à mesure des développements dans le chapitre précédent. Un volet concerne la caractérisation spectrale et ses dérivées : il s'agit de détection de ruptures temporelles en analyse temps-fréquence proposée au § 3.1.1, p. 32 et de déroulage de phase évoqué au § 3.1.3, p. 34. Les perspectives concernant la synthèse de Fourier sont exposées au § 3.2.3, p. 37. Les extensions du volet haute-résolution et sur-résolution sont présentées aux § 3.3.1, p. 39 et § 3.3.2, p. 41.

Une importante partie des perspectives concerne naturellement la suite et la fin de la thèse présentée au § 1.1.5, p. 13 consacrée à l'identification de sources de pollutions ainsi que la thèse présentée au § 1.2.6, p. 16 qui doit démarrer à propos de restauration de spectres.

Le présent chapitre ne revient pas sur ces perspectives et se focalise sur la question plus transversale de l'estimation des hyperparamètres.

4.1 Introduction

Les solutions régularisées décrites au chapitre précédent nécessitent en effet le réglage d'hyperparamètres : ils gèrent le compromis entre les différents termes des critères (dans une lecture déterministe) et pilotent les lois *a priori* pour le bruit et les objets (dans une lecture bayésienne). De très nombreuses contributions sont consacrées à la question de l'estimation de ces paramètres : elles proposent et comparent diverses approches (voir par exemple [75, 135, 79, 132, 80, 52, 60]). Ce type d'approche est exploité dans mes travaux en caractérisation spectrale : en analyse spectrale, en analyse temps-fréquence (voir § 3.1.1, p. 32 et § 3.1.2, p. 33) et en poursuite de moments spectraux (voir § 3.1.3, p. 34). La méthodologie reposant sur la maximisation de vraisemblance marginale est probablement la plus puissante puisque formellement elle est envisageable pour une large classe de problèmes et de lois *a priori*. Dans le cas à deux dimensions (ou plus) et d'une loi *a priori* corrélée (champ de Markov, en général), la méthodologie se heurte cependant à une difficulté majeure : la fonction de partition des champs *a priori* n'est pas connue de manière explicite. On pourra consulter [140, Part.VI], [98, Ch.7] ou [87, Ch.8] par exemple.

Le travail envisagé propose une classe particulière de champs toroïdaux composites : les cliques et les pixels sont en nombre égal et en contrepartie la fonction de partition est explicite et simple. Une attention particulière sera portée au cas des potentiels L_2-L_1. Le travail s'inspire largement de trois contributions.

1. Les contributions de Hunt à la déconvolution débouchant [4] sur les approximations circulantes et les modèles toroïdaux permettant une mise en œuvre rapide tirant partie des algorithmes de FFT.

2. La proposition de Geman et Yang [55] initialement introduite dans le but d'alléger la charge calculatoire des algorithmes de recuit simulé. Leur contribution est double.

   – Ils introduisent des variables auxiliaires pour ramener le problème du tirage d'un champ corrélé et non-gaussien à celui du tirage d'un champ corrélé et gaussien et d'un champ séparable.

   – Par ailleurs, ils s'appuient sur les modèles toroïdaux pour ramener le problème du tirage d'un champ gaussien corrélé à celui du tirage d'un champ gaussien blanc suivi d'une FFT.

3. La dernière source d'inspiration est due à Champagnat et Idier [22] et à leur analyse bayésienne notamment en terme de « *Location Mixture of Gaussian* ».

Remarque 6 — *Les travaux de Jalobeanu [91] s'inspirent également de ceux de Geman et Yang [55] et Hunt [4], mais ils ne débouchent pas sur un champ possédant une fonction de partition explicite.*

4.2 Une famille de champs corrélés avec partition explicite

4.2.1 Notations

On travaille sur des images $P \times P$, réelles ou complexes, possédant $N = P^2$ pixels, représentées sous forme matricielle. On note a_{pq} l'élément générique de la matrice $\boldsymbol{A}$, $N_2(\boldsymbol{A}) = \sum |\, a_{pq} \,|^2$ le carré de sa norme et $\overset{\circ}{\boldsymbol{A}}$ sa FFT-2D. Cette transformée est normalisée : la relation de Parseval s'écrit $N_2(\boldsymbol{A}) = N_2(\overset{\circ}{\boldsymbol{A}})$ et la moyenne empirique des pixels est $\sum a_{pq}/N = \overset{\circ}{a}_{00}$. Les symboles $\star$ et $*$ représentent respectivement la convolution circulante et le produit élément par élément de deux matrices. Si $\boldsymbol{F}$ représente un filtre circulant et $\boldsymbol{X}$ un objet en entrée, la sortie s'écrit $\boldsymbol{Y} = \boldsymbol{F} \star \boldsymbol{X}$ et on a $\overset{\circ}{\boldsymbol{Y}} = \overset{\circ}{\boldsymbol{F}} * \overset{\circ}{\boldsymbol{X}}$. Si $\overset{\circ}{f}_{pq} \neq 0$ pour tout p, q, le filtre associé est inversible.

Le champ aléatoire proposé est caractérisé par une matrice $\boldsymbol{F}$ et il est composé de deux variables : une variable pixel notée $\mathcal{X}$ et une variable auxiliaire notée $\mathcal{B}$. Sa loi jointe pour $(\mathcal{X}, \mathcal{B})$ est définie par la loi de $\mathcal{X}|\mathcal{B}$ d'une part et par la loi de $\mathcal{B}$ d'autre part. La première est gaussienne corrélée et $\boldsymbol{B}$ en paramètre la moyenne et la seconde est séparable.

4.2.2 Champ gaussien toroïdal pour $\mathcal{X}|\mathcal{B}$

Considérons deux matrices $\boldsymbol{B}$ et $\boldsymbol{F}$ avec $\overset{\circ}{f}_{pq} \neq 0$ pour tout p, q et le champ gaussien toroïdal possédant une densité paramétrée sous la forme :

$$f_{\mathcal{X}|\mathcal{B}}\left[\boldsymbol{X}|\boldsymbol{B}\right] = K^{-1}_{\mathcal{X}|\mathcal{B}} \, \exp - \left[\overline{r}_{\mathrm{d}} \, N_2(\boldsymbol{F} \star \boldsymbol{X} - \boldsymbol{B})\right]/2 \,, \tag{4.1}$$

où $\overline{r}_{\mathrm{d}} > 0$ est une variance inverse. Dans le domaine de Fourier, le potentiel est séparable :

$$\begin{aligned} N_2(\boldsymbol{F} \star \boldsymbol{X} - \boldsymbol{B}) &= N_2\left(\mathring{\boldsymbol{F}} * \mathring{\boldsymbol{X}} - \mathring{\boldsymbol{B}}\right) \\ &= \sum_{pq} |\, \mathring{f}_{pq}\, \mathring{x}_{pq} - \mathring{b}_{pq}\,|^2 \\ &= \sum_{pq} |\, \mathring{f}_{pq}|^2\, |\, \mathring{x}_{pq} - \mathring{b}_{pq}/\mathring{f}_{pq}\,|^2 \end{aligned}$$

ce qui a trois conséquences essentielles pour la suite des développements.

1. La loi de $\mathring{\mathcal{X}}$ est séparable et chaque $\mathring{X}_{pq}$ est gaussien de moyenne $\mathring{b}_{pq}/\mathring{f}_{pq}$ et de variance inverse $\overline{r}_{\mathrm{d}}|\mathring{f}_{pq}|^2$. En conséquence, l'échantillonnage de $\mathcal{X}$ se ramène à l'échantillonnage d'un bruit blanc gaussien suivi d'une FFT-2D.
2. Le changement de variable $\overline{\mathcal{X}} = \boldsymbol{F} \star \mathcal{X}$ est inversible et $\overline{\mathcal{X}}$ est blanc et homogène : chaque $\overline{X}_{pq}$ est gaussien de moyenne b_{pq} et de variance inverse $\overline{r}_{\mathrm{d}}$.
3. La fonction de partition est explicite et indépendante de $\boldsymbol{B}$:

$$K_{\mathcal{X}|\mathcal{B}}^{-1} = \overline{r}_{\mathrm{d}}^{\,N/2} \;\; (2\pi)^{-N/2} \prod |\mathring{f}_{pq}|\,. \tag{4.2}$$

Remarque 7 — *La construction proposée est implicitement limitée : le nombre de cliques est égal au nombre de pixels. En contre partie, la partition $K_{\mathcal{X}|\mathcal{B}}$ est indépendante de $\boldsymbol{B}$.*

4.2.3 Champ composite

On introduit alors un champ séparable et homogène pour les variables auxiliaires $\mathcal{B}$ possédant une densité $f_{\mathcal{B}}\,[\boldsymbol{B}]$, produit des $f_B\,[\,b_{pq}\,]$. La densité jointe s'écrit $f_{\mathcal{X},\mathcal{B}}\,[\boldsymbol{X}, \boldsymbol{B}] = f_{\mathcal{X}|\mathcal{B}}\,[\boldsymbol{X}|\boldsymbol{B}]\, f_{\mathcal{B}}\,[\boldsymbol{B}]$ et la loi marginale s'obtient en intégrant les variables auxiliaires :

$$f_{\mathcal{X}}\,[\boldsymbol{X}] = \int_{\mathbb{R}^N} f_{\mathcal{X}|\mathcal{B}}\,[\boldsymbol{X}|\boldsymbol{B}]\, f_{\mathcal{B}}\,[\boldsymbol{B}]\;\mathrm{d}\boldsymbol{B}\,.$$

On fait ainsi apparaître un produit de convolution séparable :

$$\begin{aligned} f_{\mathcal{X}}\,[\boldsymbol{X}] &= K_{\mathcal{X}|\mathcal{B}}^{-1} \int_{\mathbb{R}^N} f_{\mathcal{B}}\,[\boldsymbol{B}]\;\exp - [\,\overline{r}_{\mathrm{d}}\, N_2(\boldsymbol{F} \star \boldsymbol{X} - \boldsymbol{B})\,]\,/2\;\;\mathrm{d}\boldsymbol{B} \\ &= K_{\mathcal{X}|\mathcal{B}}^{-1} \prod_{pq} \int_{\mathbb{R}} f_B\,[\,b_{pq}\,]\;\exp - \left[\,\overline{r}_{\mathrm{d}}\;(\overline{x}_{pq} - b_{pq})^2\,\right]/2\;\;\mathrm{d}b_{pq} \end{aligned}$$

Une partie du travail pourra être consacrée à l'étude des conditions d'existence de ce champ. Une autre partie pourra être consacrée à l'étude des propriétés du potentiel associé : convexité, limites, symétries,...

4.2.4 Cas Laplace pour les variables auxiliaires

Cette section est dédiée au cas de variables auxiliaires sous une densité de Laplace suggérée par [22]. On l'écrit sous la forme :

$$f_{\mathcal{B}}\,[\boldsymbol{B}] = K_{\mathcal{B}}^{-1} \;\; \exp\left[-\,\overline{r}_{\mathrm{b}}\, N_1(\boldsymbol{B})\,/2\right]\,, \tag{4.3}$$

où $\overline{r}_{\mathrm{b}} > 0$ est un paramètre d'échelle, $N_1(\boldsymbol{B}) = \sum |b_{pq}|$ et avec $K_{\mathcal{B}}^{-1} = [\overline{r}_{\mathrm{b}}/4]^N$. D'après (4.1) et (4.3), la densité jointe pour $(\mathcal{X}, \mathcal{B})$ prend la forme

$$f_{\mathcal{X},\mathcal{B}}\,[\boldsymbol{X}, \boldsymbol{B}] = K_{\mathcal{X},\mathcal{B}}^{-1}\ \exp - [\,\overline{r}_{\mathrm{d}}\, N_2(\boldsymbol{F} \star \boldsymbol{X} - \boldsymbol{B})\ + \overline{r}_{\mathrm{b}}\, N_1(\boldsymbol{B})\,]\,/2\,, \tag{4.4}$$

et sa fonction de partition est explicite : $K_{\mathcal{X},\mathcal{B}} = K_{\mathcal{X}|\mathcal{B}}\, K_{\mathcal{B}}$. La loi marginale pour $\mathcal{X}$ fait apparaître la convolution monodimensionnelle d'une densité gaussienne et d'une densité laplacienne :

$$f_{\mathcal{X}}\,[\boldsymbol{X}] = K_{\mathcal{X},\mathcal{B}}^{-1} \prod_{pq} \int_{\mathbb{R}} \exp - \left[\,\overline{r}_{\mathrm{d}}\ (\overline{x}_{pq} - b_{pq})^2\ + \overline{r}_{\mathrm{b}}\,|b_{pq}|\,\right]/2\ \mathrm{d}b_{pq}$$

qui fait alors apparaître la fonction potentiel φ :

$$f_{\mathcal{X}}\,[\boldsymbol{X}] = K_{\mathcal{X},\mathcal{B}}^{-1}\ \exp - \left[\,\sum_{pq} \varphi(\overline{x}_{pq})\,\right]/2\,.$$

de type L_2-L_1, qui s'explicite à partir de la fonction erfc.

Exemple 1 *(voir figure 4.1) — Considérons le cas où le champ est basé sur un filtre laplacien de support* 3×3*, défini par* $[0\,,1\,,0\,;\,1\,,-4\,,1\,;\,0\,,1\,,0]$ *et représenté par la matrice* $\boldsymbol{D}$*. A la fréquence nulle, on a un coefficient nul : on introduit alors un paramètre supplémentaire* $\varepsilon > 0$ *pour caractériser la moyenne et on pose* $\boldsymbol{F}_\varepsilon = \boldsymbol{D} + \varepsilon$*. On peut écrire la fonction de partition du champ joint :*

$$K_{\mathcal{X},\mathcal{B}}^{-1} = \delta\ \varepsilon\ \overline{r}_{\mathrm{d}}^{\,N/2}\ \overline{r}_{\mathrm{b}}^{\,N}\,, \quad \textit{avec}\ \ \delta = (32\pi)^{-N/2} \prod_{(p,q)\neq(0,0)} |\overset{\circ}{d}_{pq}|\,.$$

Si $\varepsilon = 0$ *le champ n'est pas normalisable et les cliques sont formées des 4 plus proches voisins. Si* $\varepsilon \neq 0$*, le champ est bien normalisable et chaque clique s'étend sur l'ensemble de l'image (et il ne s'agit plus à proprement parler de champ de Markov).*

Nous proposons ainsi un champ *a priori* particulier corrélé à potentiel convexe, L_2-L_1, avec sa fonction de partition. A notre connaissance, il s'agit d'une contribution originale et ce champ pourrait permettre de développer une méthode de déconvolution non supervisée efficace, décrite sommairement dans la section suivante. Il est bien sûr possible de simplifier le problème et de traiter la question du débruitage, du réhaussement de contours ou de l'estimation des paramètres du champ directement observé.

4.3 Déconvolution non supervisée

Nous envisageons ici le problème de la déconvolution non supervisée. On note respectivement $\boldsymbol{Y}$, $\boldsymbol{X}$, $\boldsymbol{H}$ et $\boldsymbol{N}$ les données observées, l'objet inconnu, la matrice de convolution et le bruit. Avec les notations adoptées, l'équation de convolution s'écrit : $\boldsymbol{Y} = \boldsymbol{H} \star \boldsymbol{X} + \boldsymbol{N}$.

Dans le cadre bayésien, la solution est définie à partir d'une loi *a posteriori* fondée sur des choix de lois *a priori* pour le bruit, l'objet et éventuellement pour les hyperparamètres.

- Le travail proposé sera en priorité dédié au cas classique du bruit blanc gaussien centré. Notons $\overline{r}_{\mathrm{n}}$ sa variance inverse.
- La loi pour l'objet est définie dans la partie précédente. Dans sa version jointe en $(\mathcal{X}, \mathcal{B})$ la densité est donnée par (4.4) et elle est pilotée par les deux paramètres $\overline{r}_{\mathrm{d}}$ et $\overline{r}_{\mathrm{b}}$.

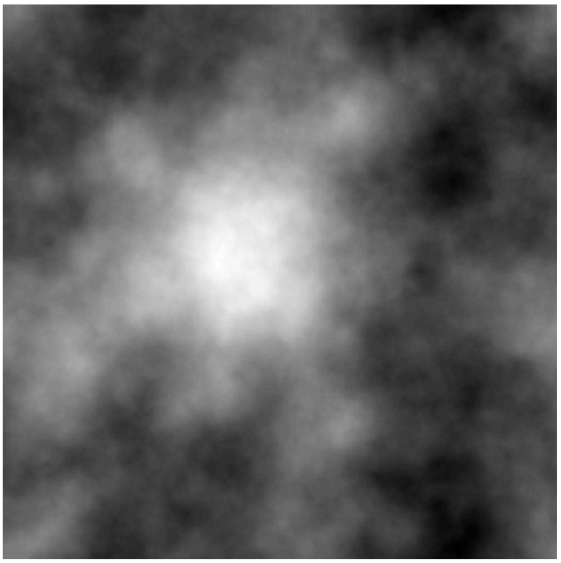

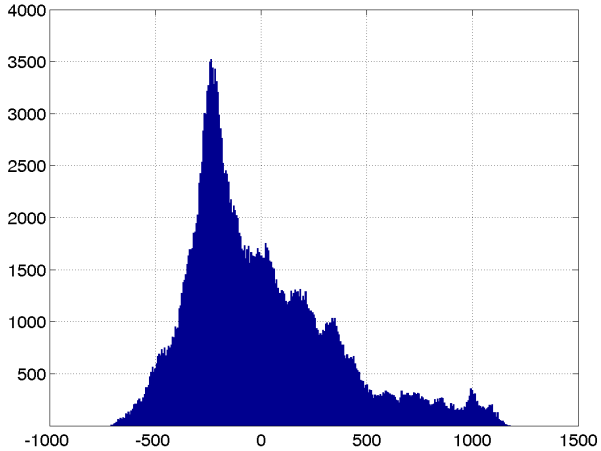

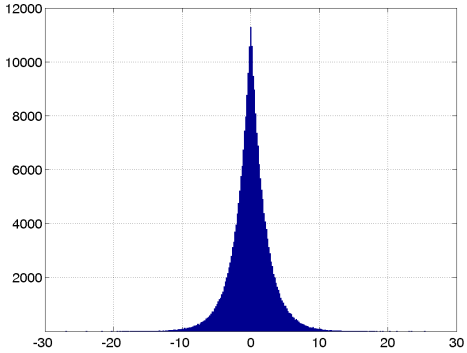

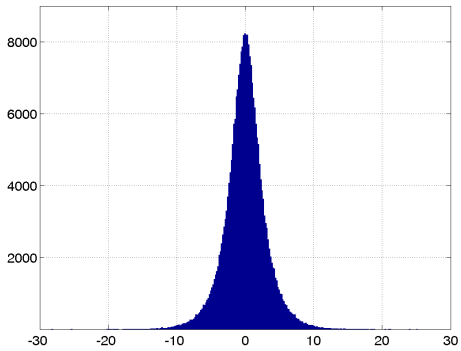

FIG. 4.1 – En haut : réalisation du champ *a priori* ($\varepsilon = \overline{r}_{\mathrm{d}} = \overline{r}_{\mathrm{b}} = 1$). Au milieu : histogramme des pixels. En bas : histogrammes des variables auxiliaires B (à gauche) et histogramme des $\overline{X}$ (à droite).

– Il est également possible d'introduire une loi pour les hyperparamètres $\boldsymbol{r}_\varepsilon = [\boldsymbol{r}, \varepsilon] = [\overline{r}_\mathrm{n}, \overline{r}_\mathrm{d}, \overline{r}_\mathrm{b}, \varepsilon]$. Ce pourra être une loi Gamma par exemple ou le cas limite de la mesure uniforme sur $\mathbb{R}_+$ pour $\overline{r}_\mathrm{b}$, $\overline{r}_\mathrm{d}$ et $\overline{r}_\mathrm{n}$ (permettant de ne pas se prononcer *a priori* sur leur valeur). Au contraire, le paramètre ε caractérisant le niveau moyen de l'image pourra être considéré comme un paramètre de nuisance. La stratégie pourra consister à l'intégrer hors du problème sous une mesure *a priori* de Dirac (permettant de ne pas se prononcer *a priori* sur la valeur moyenne de l'image).

On pourra alors ainsi construire la loi jointe pour $(\mathcal{Y}, \mathcal{X}, \mathcal{B}, \mathcal{R}_\mathcal{E})$ et en déduire la loi *a posteriori* totale pour l'ensemble des paramètres inconnus $(\mathcal{X}, \mathcal{B}, \mathcal{R})$ connaissant les données observées $\mathcal{Y}$. Il sera alors possible d'approcher la moyenne *a posteriori* par des techniques usuelles d'échantillonnage stochastique [114, 140] : on échantillonne successivement les variables auxiliaires, l'objet et les hyperparamètres conditionnellement aux autres variables.

– **Échantillonnage des variables auxiliaires**. L'échantillonnage des variables auxiliaires est le plus délicat mais doit pouvoir se faire de manière directe en inversant la fonction de répartition de $\mathcal{B}|\mathcal{X}$ (explicite à partir de la fonction ierf).
– **Échantillonnage de l'objet**. L'objet conditionnellement aux autres quantités est gaussien toroïdal. Son échantillonnage se ramène donc à l'échantillonnage d'un bruit blanc gaussien suivi d'une FFT-2D.
– **Échantillonnage des hyperparamètres**. Chacun des paramètres $\overline{r}_\mathrm{n}$, $\overline{r}_\mathrm{d}$ et $\overline{r}_\mathrm{b}$ suit une loi γ de paramètres connus, que l'on sait échantillonner aisément.

Ces trois étapes permettent ainsi de construire des échantillons de la « *loi a posteriori totale* » (pour l'objet, les variables auxiliaires et les hyperparamètres) et d'en déduire une approximation empirique de la moyenne *a posteriori*.

Au moins une approche concurrente pourra être étudiée : fondée sur la vraisemblance marginale plutôt que *a posteriori*. Une partie du « travail de marginalisation » devra être réalisée analytiquement et on peut déjà affirmer que certaines des intégrales peuvent être explicitées [77, p.337] à partir des *parabolic cynlinder functions* [77, p.1064]. Cela autorisera le développement d'un algorithme EM et d'un algorithme SEM, intermédiaire.

4.4 Plus long terme

A plus long terme, le travail envisagé pourrait s'étendre à des problèmes d'inversion linéaires en dehors de la déconvolution. La méthodologie introduite demeure valide et la modification à apporter concerne l'échantillonnage de l'objet $\mathcal{X}$. Il reste gaussien mais l'échantillonnage n'est plus possible globalement par FFT. Les techniques d'échantillonage de Gibbs pourraient alors constituer un outil adapté mais les temps de calculs en seraient allongés, peut-être de manière rédhibitoire. Pour les problèmes non linéaires, la loi pour $\mathcal{X}$ n'est plus gaussienne et une étude au cas par cas serait requise.

Concernant le champ *a priori*, d'autres lois pour les variables auxiliaires sont bien sûr envisageables. La méthodologie reste ici encore valide mais la difficulté concerne alors l'échantillonnage des variables auxiliaires $\mathcal{B}$. L'échantillonnage par inversion de la fonction de partition pourra s'avérer impossible ; cependant, des algorithmes d'échantillonnage par réjection ou de type Hastings-Metropolis pourraient permettre de lever cette difficulté.

Chapitre 5

Bibliographie

[1] S. Alliney, « Digital filters as absolute norm regularizers », *IEEE Transactions on Signal Processing*, vol. 40, n°6, pp. 1548–1562, juin 1992.

[2] S. Alliney, « Digital filters as absolute norm regularizers », *IEEE Transactions on Medical Imaging*, vol. 12, n°2, pp. 173–181, 1993.

[3] S. Alliney et S. A. Ruzinsky, « An algorithm for the minimization of mixed l_1 and l_2 norms with application to Bayesian estimation », *IEEE Transactions on Signal Processing*, vol. 42, n°3, pp. 618–627, mars 1994.

[4] H. C. Andrews et B. R. Hunt, *Digital Image Restoration*, Prentice-Hall, Englewood Cliffs, NJ, USA, 1977.

[5] L. E. Baum, T. Petrie, G. Soules et N. Weiss, « A maximization technique occuring in the statistical analysis of probabilistic functions of Markov chains », *Annals of Mathematical Statistics*, vol. 41, n°1, pp. 164–171, 1970.

[6] C. Berthomier, A. Herment, J.-F. Giovannelli, G. Guidi, L. Pourcelot et B. Diebold, « Multigate Doppler signal analysis using 3-D regularized long AR modeling », *Ultrasound in Medicine and Biology*, vol. 27, n°11, pp. 1515–1523, 2001.

[7] D. P. Bertsekas, *Nonlinear programming*, Athena Scientific, Belmont, MA, USA, 2nd edition, 1999.

[8] M. J. Black et A. Rangarajan, « On the unification of line processes, outlier rejection, and robust statistics with applications in early vision », *International Journal of Computer Vision*, vol. 19, n°1, pp. 57–91, 1996.

[9] A. Blake et A. Zisserman, *Visual reconstruction*, The MIT Press, Cambridge, MA, USA, 1987.

[10] R. Boubertakh, « Chaînes de Markov en poursuite de fréquence. Application à la vélocimétrie ultrasonore et IRM », Rapport de stage de DEA, GPI–L2S, Gif-sur-Yvette, septembre 1998.

[11] R. Boubertakh, *Synthèse de Fourier régularisée : cas des données incomplètes et application à l'*IRM *cardiaque rapide*, Thèse de Doctorat, Université de Paris–Sud, Orsay, novembre 2002.

[12] R. Boubertakh, J.-F. Giovannelli, A. De Cesare et A. Herment, « Regularized reconstruction of MR images from sparse acquisitions », en révision dans *Signal Processing*, janvier 2004.

[13] R. Boubertakh, A. Herment, J.-F. Giovannelli et A. De Cesare, « MR image reconstruction from sparse data and spiral trajectories », in *Magnetic Resonance Materials in Physics Biology and Medicine*, Paris, septembre 2000, 17th Annual meeting of the European Society for Magnetic Resonance in Medicine and Biology, vol. 11–Sup. 1, p. 85.

[14] R. Boubertakh, A. Herment, J.-F. Giovannelli et A. De Cesare, « Reconstruction d'images IRM à partir de données incomplètes », in *Forum des Jeunes Chercheurs en Génie Biologique et Médical*, Tours, juin 2000, pp. 52–53.

[15] C. A. Bouman et K. D. Sauer, « A generalized Gaussian image model for edge-preserving MAP estimation », *IEEE Transactions on Image Processing*, vol. 2, n°3, pp. 296–310, juillet 1993.

[16] M. Çetin et W. Karl, « Superresolution and edge-preserving reconstruction of complex-valued synthetic aperture radar images », in *Proceedings of the International Conference on Image Processing*, Vancouver, Canada, septembre 2000, vol. 1, pp. 701–704.

[17] M. Çetin et W. Karl, « Feature-enhanced synthetic aperture radar image formation based on nonquadratic regularization », *IEEE Transactions on Image Processing*, vol. 10, n°4, pp. 623–631, avril 2001.

[18] M. Çetin, D. M. Malioutov et A. S. Willsky, « A variational technique for source localization based on sparse signal reconstruction perspective », in *Proceedings of the International Conference on Acoustic, Speech and Signal Processing*, Orlando, USA, mai 2002, vol. 3, pp. 2965–2968.

[19] V. Cevher et J. H. McClellan, « General direction-of-arrival tracking with acoustic nodes », *IEEE Transactions on Signal Processing*, vol. 53, n°1, pp. 1–12, janvier 2005.

[20] F. Champagnat, Y. Goussard et J. Idier, « Unsupervised deconvolution of sparse spike trains using stochastic approximation », *IEEE Transactions on Signal Processing*, vol. 44, n°12, pp. 2988–2998, décembre 1996.

[21] F. Champagnat et J. Idier, « Deconvolution of sparse spike trains accounting for wavelet phase shifts and colored noise », in *Proceedings of the International Conference on Acoustic, Speech and Signal Processing*, Minneapolis, MN, USA, 1993, pp. 452–455.

[22] F. Champagnat et J. Idier, « A connection between half-quadratic criteria and EM algorithm », *IEEE Signal Processing Letters*, vol. 11, n°9, pp. 709–712, septembre 2004.

[23] P. Charbonnier, L. Blanc-Féraud, G. Aubert et M. Barlaud, « Deterministic edge-preserving regularization in computed imaging », *IEEE Transactions on Image Processing*, vol. 6, n°2, pp. 298–311, février 1997.

[24] P. Ciuciu, *Méthodes markoviennes en estimation spectrale non paramétrique. Applications en imagerie radar Doppler*, Thèse de Doctorat, Université de Paris–Sud, Orsay, octobre 2000.

[25] P. Ciuciu, J.-F. Giovannelli et J. Idier, « Analyse spectrale post–moderne. Application aux signaux radars », Rapport de contrat (confidentiel) CNRS–Société THOMSON, GPI–L2S, 1997.

[26] P. Ciuciu et J. Idier, « A Half-Quadratic block-coordinate descent method for spectral estimation », *Signal Processing*, vol. 82, n°7, pp. 941–959, juillet 2002.

[27] P. Ciuciu, J. Idier et J.-F. Giovannelli, « Nouveaux estimateurs du spectre de puissance », in *Colloque Jeunes Chercheurs Alain Bouissy*, Orsay, mars 1998.

[28] P. Ciuciu, J. Idier et J.-F. Giovannelli, « Analyse spectrale non paramétrique à haute résolution », Paris, décembre 1999, GDR-PRC ISIS, GT1.

[29] P. Ciuciu, J. Idier et J.-F. Giovannelli, « Analyse spectrale non paramétrique haute résolution », in *Actes du 17 e colloque GRETSI*, Vannes, septembre 1999, pp. 721–724.

[30] P. Ciuciu, J. Idier et J.-F. Giovannelli, « Markovian high resolution spectral analysis », in *Proceedings of the International Conference on Acoustic, Speech and Signal Processing*, Phoenix, AZ, USA, mars 1999, pp. 1601–1604.

[31] P. Ciuciu, J. Idier et J.-F. Giovannelli, « Estimation spectrale régularisée de fouillis et de cibles en imagerie radar Doppler », in *Actes du 18 e colloque GRETSI*, Toulouse, septembre 2001.

[32] P. Ciuciu, J. Idier et J.-F. Giovannelli, « Regularized estimation of mixed spectra using a circular Gibbs-Markov model », *IEEE Transactions on Signal Processing*, vol. 49, n°10, pp. 2201–2213, octobre 2001.

[33] A. Coulais, F. Balleux, A. Abergel, J.-F. Giovannelli et J. See, « Correction par bloc des transitoires de la caméra infrarouge ISOPHOT C-100 avec un modèle non linéaire dissymétrique », in *Actes du 18 e colloque GRETSI*, Toulouse, septembre 2001.

[34] A. Coulais, B. Fouks, J.-F. Giovannelli, A. Abergel et J. See, « Transient response of IR detectors used in space astronomy : what we have learned from ISO satellite », in *Procedings of* SPIE *4131-42, Infrared Spaceborne Remote Sensing*, M. Strojnik et B. Andresen, Eds., San Diego, CA, USA, juillet 2000, vol. VIII, pp. 205–217.

[35] A. Coulais, J. Malaizé, J.-F. Giovannelli, T. Rodet, A. Abergel, B. Wells, P. Patrashin, H. Kaneda et B. Fouks, « Non-linear transient models and transient corrections methods for IR low-background photo-detectors », in *ADASS-13*, Strasbourg, octobre 2003.

[36] A. De Cesare, *Algorithmes rapides de restauration des signaux : application à l'imagerie médicale*, Thèse de Doctorat, Université de Paris-Sud, Orsay, février 1996.

[37] G. Demoment, « Image reconstruction and restoration : Overview of common estimation structure and problems », *IEEE Transactions on Acoustics, Speech and Signal Processing*, vol. ASSP-37, n°12, pp. 2024–2036, décembre 1989.

[38] G. Demoment, « Problèmes inverses en traitement du signal et de l'image », in *Voies nouvelles pour l'analyse des données en sciences de l'univers*, J.-P. Rozelot et A. Bijaoui, Eds., Les Ulis, 2002, vol. 12, pp. 3–34, EDP Sciences.

[39] G. Demoment, J. Idier, J.-F. Giovannelli et A. Mohammad-Djafari, « Problèmes inverses en traitement du signal et de l'image », vol. TE 5 235 de *Traité Télécoms*, pp. 1–25. Techniques de l'Ingénieur, Paris, 2001.

[40] G. Demoment, J. Idier, J.-F. Giovannelli et A. Mohammad-Djafari, « Restauration et reconstruction d'image », in *Le traitement d'image à l'aube du XXIe siècle*, Paris, mars 2002, Journées d'études SEE, pp. 45–56.

[41] J. M. B. Dias et Leitão, « The $\mathbb{Z}\pi M$ algorithm : a method for interferometric image reconstruction in SAR/SAS », *IEEE Transactions on Image Processing*, vol. 11, n°4, pp. 408–422, avril 2002.

[42] H. Dole, « ISO and the cosmic infrared background », in *Exploiting the ISO Data Archive - Infrared Astronomy in the Internet Age (Invited Review Talk)*, Siguenza, Espagne, juin 2002, Gry, C. et al. Eds, ESA SP-511.

[43] F. Dublanchet, P. Duvaut et J. Idier, *Complex sinusoid analysis by Bayesian deconvolution of the discrete Fourier transform*, pp. 323–328, Maximum Entropy and Bayesian Methods. Kluwer Academic Publ., Santa Fe, NM, USA, K. Hanson edition, 1995.

[44] F. Dublanchet, J. Idier et P. Duvaut, « Direction-of-arrival and frequency estimation using Poisson-Gaussian modeling », in *Proceedings of the International Conference on Acoustic, Speech and Signal Processing*, Munich, Allemagne, avril 1997, pp. 3501–3504.

[45] I. Dydenko, D. Friboulet, J. M. Gorce, J. D'hooge, B. Bijnens et I. Magnin, « Towards ultrasound cardiac image segmentation based on the radiofrequency signal », *Medical Image Analysis*, vol. 7, pp. 353–367, 2003.

[46] I. Dydenko, D. Friboulet et I. Magnin, « Introducing spectral estimation for boundary detection in echography radiofrequency images », in *Functional Imaging and Modeling of the Heat (FIMH'01)*, Helsinki (Finland), 2001, pp. 24–31.

[47] M. Elad et A. Feuer, « Restoration of a single superresolution image from several blurred, noisy, and undersampled measured images », *IEEE Transactions on Image Processing*, vol. 6, n°12, pp. 1646–1658, décembre 1997.

[48] M. Elad et A. Feuer, « Superresolution restoration of an image sequence : Adaptive filtering approach », *IEEE Transactions on Image Processing*, vol. 8, n°3, pp. 387–395, mars 1999.

[49] M. Ern, D. Offermann, P. Preusse, K. U. Grossmann et J. Oberheide, « Calibration procedures and correction of detector signal relaxations for the CRISTA infrared satellite instrument », *Applied Optics*, vol. 42, n°9, pp. 1594–1609, mars 2003.

[50] M. Fayolle, *Modélisation unilatérale composite pour la restauration d'images*, Thèse de Doctorat, Université de Paris-Sud, Orsay, octobre 1998.

[51] J. A. Fessler, H. Erdoğan et W. B. Wu, « Exact distribution of edge-preserving MAP estimators for linear signal models witth gaussian measurement noise », *IEEE Transactions on Image Processing*, vol. 9, n°6, pp. 1049–1055, juin 2000.

[52] N. Fortier, G. Demoment et Y. Goussard, « GCV and ML methods of determining parameters in image restoration by regularization : Fast computation in the spatial domain and experimental comparison », *Journal of Visual Communication and Image Representation*, vol. 4, n°2, pp. 157–170, juin 1993.

[53] J.-J. Fuchs, « An inverse problem approach to robust regression », in *Proceedings of the International Conference on Acoustic, Speech and Signal Processing*, Phoenix, AZ, USA, mars 1999, pp. 1908–1911, IEEE.

[54] D. Geman et G. Reynolds, « Constrained restoration and the recovery of discontinuities », *IEEE Transactions on Pattern Analysis and Machine Intelligence*, vol. 14, n°3, pp. 367–383, mars 1992.

[55] D. Geman et C. Yang, « Nonlinear image recovery with half-quadratic regularization », *IEEE Transactions on Image Processing*, vol. 4, n°7, pp. 932–946, juillet 1995.

[56] S. Geman et D. Geman, « Stochastic relaxation, Gibbs distributions, and the Bayesian restoration of images », *IEEE Transactions on Pattern Analysis and Machine Intelligence*, vol. 6, n°6, pp. 721–741, novembre 1984.

[57] S. Geman, D. McClure et D. Geman, « A nonlinear filter for film restoration and other problems in image processing », *CVGIP : Graphical Models and Image Processing*, vol. 54, n°4, pp. 281–289, juillet 1992.

[58] D. C. Ghiglia et M. D. Pritt, *Two-Dimensional Phase Unwrapping*, Interscience. John Wiley, 1998.

[59] J. C. Gilbert, *Optimisation Différentiable : Théorie et Algorithmes*, Notes de cours. INRIA, Rocquencourt, 1999.

[60] J.-F. Giovannelli, *Estimation de caractéristiques spectrales en temps court. Application à l'imagerie Doppler*, Thèse de Doctorat, Université de Paris-Sud, Orsay, février 1995.

[61] J.-F. Giovannelli, « Détection d'objets ponctuels en mouvement dans une séquence d'images », Rapport de contrat ONÉRA, convention N° F/10.646/DA-CDES, GPI–L2S, décembre 2002.

[62] J.-F. Giovannelli, « Débruitage impulsionnel : approche non-supervisée », Rapport (n°2) de contrat ONÉRA, convention N° F/10.646/DA-CDES, GPI–L2S, février 2004.

[63] J.-F. Giovannelli et A. Coulais, « Inversion de données interférométriques : cas des images à toutes les échelles spatiales », Nançay, novembre 2003, Premier atelier "Projets et R & D en Radioastronomie".

[64] J.-F. Giovannelli et A. Coulais, « Déconvolution avec contraintes de positivité et de support : sources ponctuelles sur source étendue », in *Actes du 20e colloque GRETSI*, Louvain-la-Neuve, Belgique, septembre 2005.

[65] J.-F. Giovannelli et A. Coulais, « Positive deconvolution for superimposed extended source and point sources. », *Astronomy and Astrophysics*, vol. 439, pp. 401–412, 2005.

[66] J.-F. Giovannelli, G. Demoment et A. Herment, « A Bayesian method for long AR spectral estimation : a comparative study », *IEEE Transactions on Ultrasonics Ferroelectrics and Frequency Control*, vol. 43, n°2, pp. 220–233, mars 1996.

[67] J.-F. Giovannelli et J. Idier, « Mesure de l'atténuation acoustique de la peau. Étude de faisabilité », Rapport de contrat (confidentiel) CNRS–Société L'ORÉAL, GPI–L2S, 1993.

[68] J.-F. Giovannelli et J. Idier, « Caractérisation spectrale du fouillis de radar Doppler. Méthodes autorégressives adaptatives régularisées », Rapport de contrat (confidentiel) CNRS–Société THOMSON, GPI–L2S, 1994.

[69] J.-F. Giovannelli et J. Idier, « Une nouvelle approche non–paramétrique de l'imagerie radar Doppler », Rapport de contrat (confidentiel) CNRS–Société THOMSON, GPI–L2S, 1995.

[70] J.-F. Giovannelli et J. Idier, « Méthodes et algorithmes d'inversion de données en spectrométrie de neutrons : analyse bibliographique prospective. », Rapport de contrat (confidentiel) SUPÉLEC–CEA, GPI–L2S, 1999.

[71] J.-F. Giovannelli et J. Idier, « Bayesian interpretation of periodograms », *IEEE Transactions on Signal Processing*, vol. 49, n°7, pp. 1988–1996, juillet 2001.

[72] J.-F. Giovannelli, J. Idier, R. Boubertakh et A. Herment, « Unsupervised frequency tracking beyond the Nyquist limit using Markov chains », *IEEE Transactions on Signal Processing*, vol. 50, n°12, pp. 1–10, décembre 2002.

[73] J.-F. Giovannelli, J. Idier, G. Desodt et D. Muller, « Regularized adaptive long autoregressive spectral analysis », *IEEE Transactions on Geoscience and Remote Sensing*, vol. 39, n°10, pp. 2194–2202, octobre 2001.

[74] J.-F. Giovannelli, J. Idier, B. Querleux, A. Herment et G. Demoment, « Maximum likelihood and maximum a posteriori estimation of Gaussian spectra. Application to attenuation measurement and color Doppler velocimetry », in *Proceedings of International Ultrasonics Symposium*, Cannes, novembre 1994, vol. 3, pp. 1721–1724.

[75] G. H. Golub, M. Heath et G. Wahba, « Generalized cross-validation as a method for choosing a good ridge parameter », *Technometrics*, vol. 21, n°2, pp. 215–223, mai 1979.

[76] J. M. Gorce, D. Friboulet, I. Dydenko, J. D'hooge, B. Bijnens et I. Magnin, « Processing radiofrequency ultra-sound images : a robust method for local spectral features estimation by a spatially regularized parametric approach », *IEEE Transactions on Ultrasonics Ferroelectrics and Frequency Control*, vol. 49, n°12, pp. 1704–1719, décembre 2002.

[77] I. S. Gradshteyn et I. M. Ryzhik, *Table of integrals, series, and products*, Academic Press, Inc., 4-th edition, 1980.

[78] P. J. Green, « Bayesian reconstructions from emission tomography data using a modified EM algorithm », *IEEE Transactions on Medical Imaging*, vol. 9, n°1, pp. 84–93, mars 1990.

[79] P. Hall et D. M. Titterington, « Common structure of techniques for choosing smoothing parameter in regression problems », *Journal of the Royal Statistical Society B*, vol. 49, n°2, pp. 184–198, 1987.

[80] P. Hansen, « Analysis of discrete ill-posed problems by means of the L-curve », *SIAM Review*, vol. 34, pp. 561–580, 1992.

[81] A. Hazart, « Etude bibliographiques sur l'inversion du transport de polluant dans la nappe phréatique », Rapport interne, EDF / GPI–L2S, 2004.

[82] A. Hazart et S. Dubost, « Indétermination du terme source de l'équation de transport de polluant », Rapport interne, EDF / GPI–L2S, 2005.

[83] A. Hazart, S. Dubost, S. Gautier et J.-F. Giovannelli, « Estimation de la distribution d'une pollution à partir de mesures dans la nappe phréatique », Rapport de stage du DEA-TIS 2002-2003, EDF / GPI–L2S, Gif-sur-Yvette, septembre 2003.

[84] A. Hazart, J.-F. Giovannelli, S. Dubost et L. Chatellier, « Pollution de milieux poreux : identifiabilité et identification de modèles paramétriques de sources », in *Actes du 20e colloque GRETSI*, Louvain-la-Neuve, Belgique, septembre 2005.

[85] A. Herment, J.-F. Giovannelli, G. Demoment, B. Diebold et A. Delouche, « Improved characterization of non–stationary flows using a regularized spectral analysis of ultrasound Doppler signals », *Journal de Physique III*, vol. 7, n°10, pp. 2079–2102, octobre 1997.

[86] A. Herment, J.-F. Giovannelli, E. Mousseaux, J. Idier, A. De Cesare et J. Bittoun, « Regularized estimation of flow patterns in MR velocimetry », in *Proceedings of the International Conference on Image Processing*, Lausanne, Suisse, septembre 1996, pp. 291–294.

[87] J. Idier, Ed., *Approche bayésienne pour les problèmes inverses*, Traité IC2, Série traitement du signal et de l'image, Hermès, Paris, 2001.

[88] J. Idier, « Convex half-quadratic criteria and interacting auxiliary variables for image restoration », *IEEE Transactions on Image Processing*, vol. 10, n°7, pp. 1001–1009, juillet 2001.

[89] J. Idier et J.-F. Giovannelli, « Structural stability of least squares prediction methods », *IEEE Transactions on Signal Processing*, vol. 46, n°11, pp. 3109–3111, novembre 1998.

[90] J. Idier, J.-F. Giovannelli et B. Querleux, « Bayesian time-varying AR spectral estimation for ultrasound attenuation measurement in biological tissues », in *Proceedings of the Section on Bayesian Statistical Science*, Alicante, Espagne, 1994, pp. 256–261, American Statistical Association.

[91] A. Jalobeanu, L. Blanc-Féraud et J. Zerubia, « Estimation d'hyperparamètres pour la restauration d'images satellitaires par une méthode MCMCML », rapport de recherche 3469, INRIA, Sophia Antipolis, août 1998.

[92] S. M. Kay et S. L. Marple, « Spectrum analysis – a modern perspective », *Proceedings of the IEEE*, vol. 69, n°11, pp. 1380–1419, novembre 1981.

[93] D. Kester, « Memory effects and their correction in SWS Si:Ga detectors », in *The Calibration Legacy of the ISO Mission*, ISO Data Centre, ESA-VILSPA, Espagne, février 2001.

[94] G. Kitagawa et W. Gersch, « A smoothness priors long AR model method for spectral estimation », *IEEE Transactions on Automatic and Control*, vol. 30, n°1, pp. 57–65, janvier 1985.

[95] G. Kitagawa et W. Gersch, « A smoothness priors time-varying AR coefficient modeling of nonstationary covariance time series », *IEEE Transactions on Automatic and Control*, vol. 30, n°1, pp. 48–56, janvier 1985.

[96] H. R. Künsch, « Robust priors for smoothing and image restoration », *Annals of the Institute of Statistical Mathematics*, vol. 46, n°1, pp. 1–19, 1994.

[97] C. Lari, M. Vaccari, G. Rodighiero, D. Fadda, C. Gruppioni, F. Pozzi, A. Franceschini et G. Zamorani, « The Lari method for ISO-CAM/PHOT data reduction and analysis », in *Exploiting the ISO Data Archive - Infrared Astronomy in the Internet Age*, Siguenza, Espagne, juin 2002, Gry, C. et al. Eds.

[98] S. Z. Li, *Markov Random Field Modeling in Image Analysis*, Springer-Verlag, Tokyo, 2001.

[99] C. Lloyd, « The effects of the detector transient response on LWS data », in *The Calibration Legacy of the ISO Mission*, ISO Data Centre, ESA-VILSPA, Espagne, février 2001.

[100] R. Lopez-Valcarce et S. Dasgupta, « A new proof for the stability of equation-error models », *IEEE Signal Processing Letters*, vol. 6, n°6, pp. 148–150, juin 1999.

[101] J. L. Marroquin, S. K. Mitter et T. A. Poggio, « Probabilistic solution of ill-posed problems in computational vision », *J. Amer. Stat. Assoc.*, vol. 82, pp. 76–89, 1987.

[102] V. Mazet, J. Idier et D. Brie, « Déconvolution impulsionnelle positive myope », in *Actes du 20e colloque GRETSI*, Louvain-la-Neuve, Belgique, septembre 2005.

[103] G. J. McLachlan et T. Krishnan, *The EM Algorithm and Extensions*, Wiley series in probability and statistics. John Wiley and Sons, Inc., 1997.

[104] J. M. Mendel, *Optimal Seismic Deconvolution*, Academic Press, New York, NY, USA, 1983.

[105] A. Mohammad-Djafari, J.-F. Giovannelli, G. Demoment et J. Idier, « Regularization, maximum entropy and probabilistic methods in mass spectrometry data processing problems », *Int. Journal of Mass Spectrometry*, vol. 215, n°1-3, pp. 175–193, avril 2002.

[106] L. Mugnier, T. Fusco et J.-M. Conan, « MISTRAL : a myopic edge-preserving image restoration method, with application to astronomical adaptive-optics-corrected long-exposure images », *Journal of the Optical Society of America*, vol. 21, n°10, pp. 1841–1854, octobre 2004.

[107] M. Nikolova, « Estimées localement fortement homogènes », *Compte-rendus de l'académie des sciences*, vol. t. 325, pp. 665–670, 1997.

[108] M. Nikolova, « Markovian reconstruction using a GNC approach », *IEEE Transactions on Image Processing*, vol. 8, n°9, pp. 1204–1220, septembre 1999.

[109] M. Nikolova, « Local strong homogeneity of a regularized estimator », *SIAM Journal of Applied Mathematics*, vol. 61, n°2, pp. 633–658, 2000.

[110] M. Nikolova, J. Idier et A. Mohammad-Djafari, « Inversion of large-support ill-posed linear operators using a piecewise Gaussian MRF », *IEEE Transactions on Image Processing*, vol. 7, n°4, pp. 571–585, avril 1998.

[111] J. Nocedal et S. J. Wright, *Numerical Optimization*, Series in Operations Research. Springer Verlag, New York, 2000.

[112] J. A. O'Sullivan, « Roughness penalties on finite domains », *IEEE Transactions on Image Processing*, vol. 4, n°9, pp. 1258–1268, septembre 1995.

[113] D. L. Phillips, « A technique for the numerical solution of certain integral equation of the first kind », *J. Ass. Comput. Mach.*, vol. 9, pp. 84–97, 1962.

[114] C. Robert, *Méthodes de Monte-Carlo par chaînes de Markov*, Economica, Paris, 1996.

[115] G. Rochefort, *Amélioration de la résolution de séquence d'images. Application aux capteurs aéroportés.*, Thèse de Doctorat, Université de Paris–Sud, Orsay, mars 2005.

[116] G. Rochefort, F. Champagnat, G. Le Besnerais et J.-F. Giovannelli, « Techniques de super-résolution et extension du modèle de formation d'images », rapport technique 1/06766 DTIM, ONÉRA, octobre 2003.

[117] G. Rochefort, F. Champagnat, G. Le Besnerais et J.-F. Giovannelli, « Super-resolution from a sequence of undersampled images under affine motion », en révision dans *IEEE Transactions on Image Processing*, février 2005.

[118] L. Rudin, S. Osher et C. Fatemi, « Nonlinear total variation based noise removal algorithm », *Physica D*, vol. 60, pp. 259–268, 1992.

[119] M. D. Sacchi, T. J. Ulrych et C. J. Walker, « Interpolation and extrapolation using a high-resolution discrete Fourier transform », *IEEE Transactions on Signal Processing*, vol. 46, n°1, pp. 31–38, janvier 1998.

[120] V. Samson, *Approche régularisée pour la détection d'objets ponctuels en mouvement dans une séquence d'images*, Thèse de Doctorat, Université de Paris–Sud, Orsay, décembre 2002.

[121] V. Samson, F. Champagnat et J.-F. Giovannelli, « Détection d'objets ponctuels en mouvement dans une séquence d'images : une approche régularisée », rapport technique 1/04005 DTIM, ONÉRA, février 2001.

[122] V. Samson, F. Champagnat et J.-F. Giovannelli, « Détection d'objets ponctuels sur fond de clutter », in *Actes du 18e colloque GRETSI*, Toulouse, France, septembre 2001.

[123] V. Samson, F. Champagnat et J.-F. Giovannelli, « Détection d'objets ponctuels sur fond nuageux en imagerie satellitaire », in *Colloque Jeunes Chercheurs Alain Bouissy*, Orsay, France, février 2001.

[124] V. Samson, F. Champagnat et J.-F. Giovannelli, « Modèles d'estimation d'objets ponctuels dans une séquence d'images sur fond corrélé », rapport technique 1/06768 DTIM, ONÉRA, mai 2002.

[125] V. Samson, F. Champagnat et J.-F. Giovannelli, « Detection of point objects with random subpixel location and unknown amplitude », in *PSIP'2003*, Grenoble, France, janvier 2003.

[126] V. Samson, F. Champagnat et J.-F. Giovannelli, « Point target detection and subpixel position estimation in optical imagery », *Applied Optics*, vol. 43, n°2, *Special Issue on Image processing for EO sensors*, pp. 257–263, janvier 2004.

[127] K. D. Sauer et C. A. Bouman, « A local update strategy for iterative reconstruction from projections », *IEEE Transactions on Signal Processing*, vol. 41, n°2, pp. 534–548, février 1993.

[128] R. R. Schultz et R. L. Stevenson, « Extraction of high-resolution frames from video sequences », *IEEE Transactions on Image Processing*, vol. 5, n°6, pp. 996–1011, juin 1996.

[129] L. Simon, « Déconvolution impulsionnelle positive : application à la tomographie de la peau. », Rapport de stage, GPI–L2S, Gif-sur-Yvette, juillet 2005.

[130] J.-L. Starck, E. Pantin et F. Murtagh, « Deconvolution in astronomy : a review », *Publication of the Astronomical Society of the Pacific*, vol. 114, pp. 1051–1069, octobre 2002.

[131] R. L. Stevenson, B. E. Schmitz et E. J. Delp, « Discontinuity preserving regularization of inverse visual problems », *IEEE Transactions on Systems, Man and Cybernetics*, vol. 24, n°3, pp. 455–4469, mars 1994.

[132] A. Thompson, J. C. Brown, J. W. Kay et D. M. Titterington, « A study of methods of choosing the smoothing parameter in image restoration by regularization », *IEEE Transactions on Pattern Analysis and Machine Intelligence*, vol. PAMI-13, n°4, pp. 326–339, avril 1991.

[133] A. Tikhonov, « Regularization of incorrectly posed problems », *Soviet. Math. Dokl.*, vol. 4, pp. 1624–1627, 1963.

[134] A. Tikhonov et V. Arsenin, *Solutions of Ill-Posed Problems*, Winston, Washington, DC, USA, 1977.

[135] D. M. Titterington, « Common structure of smoothing techniques in statistics », *International Statistical Review*, vol. 53, n°2, pp. 141–170, 1985.

[136] S. Twomey, « On the numerical solution of Fredholm integral equations of the first kind by the inversion of the linear system produced by quadrature », *J. ACM*, vol. 10, pp. 97–101, 1963.

[137] T. J. Ulrych et R. W. Clayton, « Time series modelling and maximum entropy », *Physics of the Earth and Planetary Interiors*, vol. 12, pp. 188–200, 1976.

[138] M. Unser, A. Aldroubi et M. Eden, « B-Spline signal processing : Part I—Theory », *IEEE Transactions on Signal Processing*, vol. 41, n°2, pp. 821–833, février 1993.

[139] M. Unser, A. Aldroubi et M. Eden, « B-Spline signal processing : Part II—Efficient design and applications », *IEEE Transactions on Signal Processing*, vol. 41, n°2, pp. 834–848, février 1993.

[140] G. Winkler, *Image Analysis, Random Fields and Markov Chain Monte Carlo Methods*, Springer Verlag, Berlin, Allemagne, 2003.

[141] P. J. Wolfe, S. J. Godsill et W.-J. Wee-Jing Ng, « Bayesian variable selection and regularization for time-frequency surface estimation », *Journal of the Royal Statistical Society B*, vol. 66, n°3, pp. 575–589, août 2004.

Troisième partie

Publications annexées

J.-F. Giovannelli, G. Demoment et A. Herment, « A Bayesian method for long AR spectral estimation : a comparative study », *IEEE Transactions on Ultrasonics Ferroelectrics and Frequency Control*, vol. 43, n°2, pp. 220–233, mars 1996.

220 IEEE TRANSACTIONS ON ULTRASONICS, FERROELECTRICS, AND FREQUENCY CONTROL, VOL. 43, NO. 2, MARCH 1996

A Bayesian Method for Long AR Spectral Estimation: A Comparative Study

Jean-François Giovannelli, Guy Demoment, and Alain Herment

Abstract— **In this paper, we address the problem of smooth power spectral density estimation of zero-mean stationary Gaussian processes when only a short observation set is available for analysis. The spectra are described by a long autoregressive model whose coefficients are estimated in a Bayesian regularized least squares (RLS) framework accounting for the spectral smoothness *prior*. The critical computation of the trade-off parameters is addressed using both maximum likelihood (ML) and generalized cross-validation (GCV) criteria in order to automatically tune the spectral smoothness. The practical interest of the method is demonstrated by a computed simulation study in the field of Doppler spectral analysis. In a Monte Carlo simulation study with a known spectral shape, investigation of quantitative indexes such as bias and variance, but also quadratic, logarithmic, and Kullback distances shows interesting improvements with respect to the usual least squares method, whatever the window data length and the signal-to-noise ratio (SNR).**

I. Introduction

THE SPECTRAL estimation problem has been extensively studied because of its obvious practical importance as well as its theoretical interest. Literature on the spectral estimation problem is abundant and varied since this problem arises in very different branches of engineering and applied physics: nondestructive testing, attenuation measurements, Doppler velocimetry, etc. This paper deals with the particular situation when only a short set of data is available for spectral estimation and when the spectra are known to be smooth in some sense. This paper's objective is to obtain improvement in terms of resolution of fine details of analyzed structure by processing very short windows.

The well-known periodogram is the most popular spectral estimation approach for two reasons. The first one is the computational efficiency of the fast Fourier transform (FFT) algorithm which simplifies real time applications. The second reason is its good performance when sufficient data are available. Unfortunately, when the window data length decreases, the bias and variance of the periodogram both increase, to which the literature often refers [1]–[3]. Many variations of the periodogram are also described in the literature: windowed, averaged periodograms, etc. The conclusion of the study of these methods is that the bias of this estimator can be reduced if an increase in variance is accepted, and vice versa, but bias and variance cannot be reduced simultaneously. Hence, such a method is unusable in the particular situation when only a very short set of data is available for spectral estimation.

Parametric spectral estimation methods have gained attention as potentially interesting tools in the last two decades. They allow the improvement of the statistical properties of spectral estimators with respect to the Fourier-based methods. Estimation of the parameters of ARMA and MA models needs the resolution of a set of nonlinear equations, whereas the AR parameters estimates can be calculated by solving a set of linear ones. Moreover, algorithms, such as Levinson's, used to solve this set of equations are computationally efficient. When the AR modeling assumption is valid, spectral estimates are less biased and have lower variability than the Fourier-based ones. For these reasons, the AR method became the most popular approach to parametric spectral estimation [1]–[3]. However, as often noticed in the literature, two facts make this method less statistically reliable for a shorter observation vector. The first fact is the instability of techniques used to determine the model order, especially for short sets of data. The second fact is that the conventional least squares framework leads to a parsimonious parametric model (i.e., small number of parameters with respect to large number of data), which cannot be a good replica of the true power spectral density.

The Bayesian method used within the scope of this paper helps to alleviate this problem. The basic idea of this approach, introduced by Kitagawa and Gersch [4], is to take into account the spectral smoothness assumption in the estimation method. Such a Bayesian method is free from the parsimony principle, and allows the reliable estimation of N parameters from only N observations. Hence, this method enables the estimation of the PSD in a broader class of spectra and the description of various spectral shapes.

The paper is organized as follows. In Section II, the problem of spectral estimation of a zero-mean stationary Gaussian process is summarized, with particular attention paid to its connection to AR modelization and estimation strategy. After a short description of the Bayesian approach to parameter estimation, Section III is devoted to the presentation of the Bayesian spectral analysis method. Special attention is paid to the problem of automatic estimation of the trade-off parameters in Section IV. Section V and VI are respectively devoted to simulation methodology and description of results obtained in

Manuscript received October 18, 1994; revised September 20, 1995.

J.-F. Giovannelli and G. Demoment are with the Laboratoire des Signaux et Systèmes (CNRS–SUPÉLEC–UPS), 91192 Gif-sur-Yvette, Cedex, France (e-mail: giova@lss.supelec.fr).

A. Herment is with INSERM U66, Imagerie Biomédicale Morphologique et Fonctionnelle, Hôpital Pitié, 75634 Paris, Cedex 13, France.

Publisher Item Identifier S 0885-3010(96)01754-6.

the field of Doppler velocimetry. Finally, conclusions are presented in Section VII as well as points still to be investigated.

II. Conventional AR Parameter Estimation

A. The Spectral Estimation Problem

The problem of spectral estimation is to determine the spectral content of a random process based on a finite number of observations. Mathematically, the spectral content is the PSD of a discrete-time second-order stationary process and is defined as

$$S_x(f) = \sum_{-\infty}^{+\infty} r(k) \exp(-2i\pi f k),$$

where $r(k)$ are the correlation lags of the process.

Our field of interest is the case of real zero-mean stationary Gaussian N-dimensional observation vector $\boldsymbol{x} = [x_1, x_2, \cdots, x_N]^t$. Hence, the probability density function for such a vector is

$$\begin{aligned} f_{X|\theta}(\boldsymbol{x}|\boldsymbol{\theta}) &= f_{X|R}(\boldsymbol{x}|R) \\ &= (2\pi)^{-N/2}(\det R)^{-1/2} \exp\left(-\tfrac{1}{2}\boldsymbol{x}^t R^{-1}\boldsymbol{x}\right), \end{aligned} \quad (1)$$

where the Toeplitz positive covariance matrix R is parameterized by an N-dimensional parameter vector $\boldsymbol{\theta}$ which may be equivalently chosen as N correlation lags, N reflection coefficients, or $N-1$ autoregressive parameters and the noise power.

The density given by (1), seen as a function of $\boldsymbol{\theta}$, is the likelihood of $\boldsymbol{\theta}$, denoted $L(\boldsymbol{\theta})$ and gathers all the information provided by the data. Since $L(\boldsymbol{\theta})$ is a function of the N-dimensional parameter $\boldsymbol{\theta}$, it is important to note that the spectral estimation problem requires estimation of $\boldsymbol{\theta}$ i.e., estimation of N coefficients from N observations.

B. Maximum Likelihood (ML) and Least Squares Estimation

A common approach to the parameter estimation problem is the ML approach, but the likelihood given by (1) is nonlinear with respect to $\boldsymbol{\theta}$ due to the nonlinear dependence of R with respect to $\boldsymbol{\theta}$ and to the presence of the determinant and inverse of R. Several techniques [5], [6] were proposed in order to maximize $L(\boldsymbol{\theta})$ with respect to $\boldsymbol{\theta}$, but such a nonlinear optimization problem is impractical for real-time applications. In order to avoid this problem, a particular choice for $\boldsymbol{\theta}$ and an approximation of the likelihood are achieved, leading to a computationally efficient estimator. Generally, $\boldsymbol{\theta}$ is chosen as the AR coefficients $\boldsymbol{a} = [a_1, a_2, \cdots, a_{N-1}]^t$, and as long as the PSD is not sharply peaked, as in our case by hypothesis, an approximate expression for the likelihood is

$$\begin{aligned} f_{X|A}(\boldsymbol{x}|\boldsymbol{a}) &= (2\pi\sigma_u^2)^{-N/2} \\ &\quad \cdot \exp\left(-\frac{1}{2\sigma_u^2}(\boldsymbol{x} - X\boldsymbol{a})^t(\boldsymbol{x} - X\boldsymbol{a})\right) \end{aligned} \quad (2)$$

(see [2, p. 185]). The data vector $\boldsymbol{x}$ and the data matrix X (also called observation vector $\boldsymbol{x}$ and observation matrix X) are designed in the classical manner [2], [3] as follows:

$$\boldsymbol{x} = \begin{bmatrix} x_1 \\ x_2 \\ x_3 \\ x_4 \\ \vdots \\ x_N \\ 0 \\ \vdots \\ 0 \\ 0 \\ 0 \end{bmatrix}, \quad X = \begin{bmatrix} 0 & 0 & \cdots & 0 \\ x_1 & 0 & \cdots & 0 \\ x_2 & x_1 & \cdots & 0 \\ x_3 & x_2 & \cdots & 0 \\ & & \ddots & \\ x_{N-1} & x_{N-2} & x_2 & x_1 \\ x_N & x_{N-1} & & x_2 \\ & \ddots & & \\ 0 & \cdots & x_{N-1} & x_{N-2} \\ 0 & \cdots & x_N & x_{N-1} \\ 0 & \cdots & 0 & x_N \end{bmatrix}. \quad (3)$$

Equation (2) clearly shows that the maximization of the AR parameter approximated likelihood is equivalent to the minimization of the usual least squares criterion [2], [3]

$$Q_0(\boldsymbol{a}) = (\boldsymbol{x} - X\boldsymbol{a})^t(\boldsymbol{x} - X\boldsymbol{a}). \quad (4)$$

The explicit expression for the minimizer of this criterion, the least squares estimate, is well known

$$\begin{aligned} \hat{\boldsymbol{a}}_{LS} &= \arg\min Q_0(\boldsymbol{a}) \\ &= (X^t X)^{-1} X^t \boldsymbol{x}. \end{aligned} \quad (5)$$

C. Short Time Case

As pointed out above, the signal is parameterized by N parameters, thus estimation of N autoregressive coefficients from N observations is desirable. In such a situation, least squares estimation techniques lead to a large variance and results in many spurious spectral peaks, hence even if the solution has small bias, it yields to an unacceptable spectra. An alternative is possible to alleviate the conflict between long model and least squares methods: on the one hand, the usual approach gives up the very first idea of estimating N coefficients, on the other hand, Kitagawa and Gersch [4] propose to abandon the usual least squares principle.

As already mentioned, the first solution is often adopted. In order to reduce the estimation variance and avoid spurious peaks, in a least squares framework, the model order is drastically reduced, for instance, to one-third or one-quarter of the observation vector length. Such an approach is efficient when enough data are available, but fails for a short data set because the model is then too poor to describe a wide class of spectra.

Our approach is on the opposite method, and we propose to adopt the second solution: our criterion is a modified version of the least squares, and we go on estimating a long model. Estimation of N parameters from N observations is an ill-posed problem which suffers from a lack of information to infer N AR parameters from N data. Literature about these problems is abundant and varied since they arise in almost every branch of engineering and applied physics [7]. The resolution of ill-posed

problems needs the use of the regularization concept, i.e., the introduction of prior information in the solution. The Bayesian framework provides an attractive and coherent framework to deal with these problems. This standpoint is developed in the next section.

III. Bayesian Approach to Spectral Estimation

A. Theoretical Background

In a Bayesian framework, introduction of prior information in the solution involves a change in the estimation criterion: instead of maximizing a likelihood of the parameter, the posterior likelihood is maximized, which contains information provided by the observations (via the likelihood) and by the *a priori* assumption about the expected solution (via the prior law). This compound criterion incorporates both "data-based knowledge" and "prior knowledge" about $\boldsymbol{\theta}$ [4], [7].

The first problem to address is the choice of a prior probability density $f_\Theta(\boldsymbol{\theta})$ for the vector $\boldsymbol{\theta}$. This density is supposed to contain the prior knowledge about the expected solution (see Section III-B). The information provided by the data is introduced through the conditional density for the observations, $f_{X|\Theta}(\boldsymbol{x}|\boldsymbol{\theta})$. Finally, the Bayes rule combines data and prior in the posterior density for $\boldsymbol{\theta}$

$$f_{\Theta|X}(\boldsymbol{\theta}|\boldsymbol{x}) = \frac{f_{X|\Theta}(\boldsymbol{x}|\boldsymbol{\theta}) f_\Theta(\boldsymbol{\theta})}{f_X(\boldsymbol{x})}. \tag{6}$$

In a strict Bayesian sense, (6) yields the solution to the problem since it gathers all the information about the AR coefficients. However, the need of one spectrum implies the choice of an estimator, and a popular choice is the maximum *a posteriori* (MAP). This punctual estimator is defined as the maximizer of the posterior density

$$\hat{\boldsymbol{\theta}}_{\mathrm{MAP}} = \arg\max f_{\Theta|X}(\boldsymbol{\theta}|\boldsymbol{x}).$$

The computation of this solution requires values for remaining parameters, called the hyperparameters, (parameters of the prior law, noise variance, etc.) which balance the solution between the data and the prior. The crucial problem of tuning the compromise between the fidelity to the data and the fidelity to the prior knowledge is addressed in Section IV.

B. Spectrum Smoothness Prior

The aim of this section is to design a prior law for the AR coefficients, modeling the PSD smoothness and leading to an easily computable solution.

The choice of a particular class of prior law is first driven by the need for a real-time computable estimation. This constraint leads to the consideration of the class of Gaussian prior

$$f_A(\boldsymbol{a}) = (2\pi)^{N/2} \det R_a^{-1/2} \exp\left(-\tfrac{1}{2}\, \boldsymbol{a}^t R_a^{-1} \boldsymbol{a}\right), \tag{7}$$

where the smoothness information about the PSD is introduced via the prior correlation R_a. Hence the objective of the followings is to find such a prior correlation.

The power spectral density for an AR process is [2]

$$S_x(f) = \frac{\sigma_u^2}{\left|1 - \sum_{k=1}^{p} a_k e^{2j\pi fk}\right|^2}, \tag{8}$$

which can be rewritten

$$S_x(f) = \frac{\sigma_u^2}{|1 - A(f)|^2}, \quad \text{with} \quad A(f) = \sum_{k=1}^{p} a_k e^{2j\pi fk}. \tag{9}$$

When the PSD is known to be smooth, Kitagawa and Gersch [4] proposed to constrain the PSD variations, i.e., to penalize its high variations. They consider the kth derivative of $A(f)$ defined in (9) in order to measure the PSD variations. Averaging the squared modulus of this derivative over the whole reduced frequency domain, they define the PSD kth smoothness by

$$D_k = \int_0^1 \left| \frac{\partial^k}{\partial f^k} A(f) \right|^2 df. \tag{10}$$

After elementary algebra, Kitagawa and Gersch showed in [4] that

$$D_k \propto \boldsymbol{a}^t \Delta_k \boldsymbol{a}, \tag{11}$$

where the Δ_k matrix, called the kth smoothness matrix, is defined by

$$\Delta_k = \begin{bmatrix} 1^{2k} & 0 & 0 & \cdots & 0 \\ 0 & 2^{2k} & 0 & \cdots & 0 \\ 0 & 0 & 3^{2k} & \cdots & 0 \\ & & & \ddots & \\ 0 & 0 & 0 & \cdots & p^{2k} \end{bmatrix}.$$

A small value of D_k means a small value of the averaged kth derivative of $A(f)$, hence a rather smooth PSD. At the limit, if $D_k = 0$, then $\boldsymbol{a} = 0$ and $S_x(f) = C^{te}$ over the whole frequency domain, i.e., the PSD estimate is completely flat. On the contrary, a large value of D_k implies strong variations of $A(f)$, hence a peaky PSD.

The covariance matrix R_a is designed from the kth order smoothness matrix Δ_k through the following:

$$R_a^{-1} = \frac{\lambda}{\sigma_u^2} \Delta_k.$$

The Gaussian prior defined in (7) with covariance R_a^{-1} favors smooth over peaked spectra.

C. Posterior Law and MAP Estimate

Section II shows that the approximated likelihood $f_{X|A}(\boldsymbol{x}|\boldsymbol{a})$ for the AR coefficients is built up as given in (2). The previous section gives a prior law $f_A(\boldsymbol{a})$ for the AR coefficients in (7). The posterior probability density function for $\boldsymbol{a}$ is then derived by applying the Bayes rule (6)

$$f_{A|X}(\boldsymbol{a}|\boldsymbol{x}) = \frac{f_{X|A}(\boldsymbol{x}|\boldsymbol{a}) f_A(\boldsymbol{a})}{f_X(\boldsymbol{x})}. \tag{12}$$

The denominator of (12), $f_X(\boldsymbol{x})$, being independent from $\boldsymbol{a}$, contributes nothing more than a normalizing constant K. Elementary algebra leads to the posterior law

$$f_{A|X}(\boldsymbol{a}|\boldsymbol{x}) = K \exp -\frac{1}{2\sigma_u^2} Q(\boldsymbol{a}), \tag{13}$$

where $Q(\boldsymbol{a})$ is given by

$$Q(\boldsymbol{a}) = (\boldsymbol{x} - X\boldsymbol{a})^t(\boldsymbol{x} - X\boldsymbol{a}) + \lambda \boldsymbol{a}^t \Delta_k^{-1} \boldsymbol{a} \tag{14}$$

and called the regularized least squares (RLS) criterion.

Since both the prior law $f_A(\boldsymbol{a})$ and the conditional law $f_{X|A}(\boldsymbol{x}|\boldsymbol{a})$ are Gaussian, and the model is linear, the posterior density is also Gaussian. Hence the choice of an estimator is no longer crucial: the MAP, the posterior mean, etc., are strictly equal. The MAP estimator $\hat{\boldsymbol{a}}_{\mathrm{MAP}}$ is defined as the posterior probability density maximizer, or equivalently as the minimizer of the RLS criterion $Q(\boldsymbol{a})$ of (14)

$$\begin{aligned} \hat{\boldsymbol{a}}_{\mathrm{RLS}} &= \hat{\boldsymbol{a}}_{\mathrm{MAP}} \\ &= \arg\max f_{A|X}(\boldsymbol{a}|\boldsymbol{x}) \\ &= \arg\min Q(\boldsymbol{a}). \end{aligned} \tag{15}$$

Since the problem is linear and Gaussian, we still have an explicit expression for its minimum

$$\hat{\boldsymbol{a}}_{\mathrm{RLS}} = (X^tX + \lambda\Delta_k)^{-1} X^t \boldsymbol{x}. \tag{16}$$

The crucial parameter λ, called the regularization parameter, balances between the prior and data-based solutions; the question of its estimation is addressed in Section IV.

D. Quadratic Regularization Interpretation

This section is devoted to the interpretation of this method in terms of quadratic regularization, outside the Bayesian framework.

The regularized criterion of (14) is composite. On the one hand, its first term is the data-based criterion $Q_0(\boldsymbol{a}) = (\boldsymbol{x} - X\boldsymbol{a})^t(\boldsymbol{x} - X\boldsymbol{a})$, on the other hand, its second term $Q_\infty(\boldsymbol{a}) = \boldsymbol{a}^t\Delta_k\boldsymbol{a}$ is a prior criterion. Combining these two criteria, the proposed criterion incorporates both the prior and data-based criteria

$$\begin{aligned} Q(\boldsymbol{a}) &= Q_0(\boldsymbol{a}) + \lambda Q_\infty(\boldsymbol{a}) \\ &= (\boldsymbol{x} - X\boldsymbol{a})^t(\boldsymbol{x} - X\boldsymbol{a}) + \lambda \boldsymbol{a}^t \Delta_k \boldsymbol{a}. \end{aligned} \tag{17}$$

As in the usual least squares case, an expression is available for the minimizer of this criterion

$$\hat{\boldsymbol{a}}_{\mathrm{RLS}} = \arg\min Q(\boldsymbol{a}) \tag{18}$$

$$= (X^tX + \lambda\Delta_k)^{-1} X^t \boldsymbol{x}. \tag{19}$$

For λ small enough ($\lambda = 0$ at the limit), the criterion reduces to the usual least squares case, $Q(\boldsymbol{a}) = Q_0(\boldsymbol{a})$, and the usual least squares solution is found: $\hat{\boldsymbol{a}} = \boldsymbol{a}_0 = (X^tX)^{-1}X^t\boldsymbol{x}$. For λ large enough ($\lambda = \infty$ at the limit), the criterion becomes the prior one $Q(\boldsymbol{a}) = Q_\infty(\boldsymbol{a})$, and the prior solution is found: $\hat{\boldsymbol{a}} = \boldsymbol{a}_\infty = 0$ so the PSD estimate is constant over the whole frequency domain.

Between the two extreme "prior-based" and "data-based" solutions, an acceptable solution must still be found. Therefore, the crucial parameter λ which gives a convenient solution has to be estimated from the data. The following section is devoted to this fundamental problem.

IV. Hyperparameter Estimation

The method described above in (16) requires values for three hyperparameters σ_u^2, λ, and k. The parameter σ_u^2 is a scaling factor while the two other parameters design the spectral shape. The parameter λ is of major importance for the spectral shape, so our study is focused on its estimation. On the contrary, the smoothness order is of lower influence and is usually fixed to $k = 1$ [its influence is nevertheless evaluated in Section VI-C1)].

The problem of hyperparameters estimation is the most delicate problem in regularization approaches, and has been extensively studied [8]–[12]. Numerous techniques have been proposed and compared in these papers and two approaches seem to be of great interest. The first strategy is founded on ML and allows estimation of both σ_u^2 and λ. The second strategy, called generalized cross validation (GCV), provides an alternative to λ estimation. The aim of this section is to give a brief overview of the different possible methods, and especially ML and GCV which are both implemented in the simulation study in Section VI.

A. Maximum Likelihood

We first investigate methods directly derived from the Bayesian framework. One of the interests of this framework is to provide coherent techniques to estimate the hyperparameters.

The parameters of interest are the noise variance and AR parameters, but the hyperparameter λ may be considered as a nuisance parameter. In a strict Bayesian framework, λ's integration out of the estimation problem may be desirable. Such a calculus may be driven with a Jeffreys prior [13], $f_\Lambda(\lambda) = 1/\lambda$ for instance, but the calculus is out of the scope of this article. However, it may be mentioned that this approach leads to a nonlinear criterion on $\boldsymbol{a}$, and consequently to an untractable method as far as real-time applications are concerned.

A second approach consists of estimating both the hyperparameters and AR parameters in the same pattern: the maximization of the joint probability density function, called the generalized likelihood

$$GL(\boldsymbol{a}, \lambda, \sigma_u^2) = f_{X,A}(\boldsymbol{x}, \boldsymbol{a}|\lambda, \sigma_u^2),$$

simultaneously over all the AR parameters $\boldsymbol{a}$, λ, and σ_u^2. It can be shown that for this kind of problem (linear and Gaussian), the solution is degenerated and leads to $\lambda = 0$ or $\sigma_u^2 = 0$.

The most commonly employed technique consists of maximizing the marginal likelihood obtained by integrating the AR parameters out of the problem

$$f_X(\boldsymbol{x}|\lambda, \sigma_u^2) = \int_a f_{X,A}(\boldsymbol{x}, \boldsymbol{a})\, d\boldsymbol{a} \tag{20}$$

$$= \int_a f_{X|A}(\boldsymbol{x}|\boldsymbol{a}) f_A(\boldsymbol{a})\, d\boldsymbol{a}. \tag{21}$$

In [4], Kitagawa and Gersch showed that the hyperparameter likelihood is

$$\begin{aligned} L(\lambda, \sigma_u^2) &= f_X(\boldsymbol{x}|\lambda, \sigma_u^2) \\ &= (2\pi\sigma_u^2)^{-N/2}(\det \Delta_k)^{1/2}\lambda^{N/2} \\ &\quad \cdot (\det(M_1))^{1/2} \exp -\frac{1}{2\sigma_u^2}\boldsymbol{x}^t(I - M_2)\boldsymbol{x}, \end{aligned} \tag{22}$$

with M_1 and M_2 given by

$$M_1 = X^t X + \lambda\Delta_k \tag{23}$$

$$M_2 = X^t(X^t X + \lambda\Delta_k)^{-1}X = X^t M_1^{-1} X. \tag{24}$$

The hyperparameters λ and σ_u^2 are finally chosen as the maximizers $\hat{\lambda}$ and $\hat{\sigma}_u^2$ of the likelihood with respect to λ and σ_u^2

$$(\hat{\lambda}, \hat{\sigma}_u^2) = \arg\max f_X(\boldsymbol{x}|\lambda, \sigma_u^2),$$

or equivalently, the minimizer of the opposite of the logarithm of the likelihood, namely the antilog-likelihood (ALL)

$$(\hat{\lambda}, \hat{\sigma}_u^2) = \arg\min -\log f_X(\boldsymbol{x}|\lambda, \sigma_u^2).$$

Such a maximization is a 2-D optimization problem, but can be explicitly optimized with respect to $\hat{\sigma}_u^2$ as shown below.

1) σ_u^2 Estimation: The ML estimate for σ_u^2 is derived from (22) by nullifying its derivative with respect to σ_u^2, and gives the usual empirical estimate for the noise variance

$$\hat{\sigma}_u^2 = \frac{1}{N}\boldsymbol{x}^t(I - M_2)\boldsymbol{x}. \tag{25}$$

It should be stressed that this expression is an explicit λ function through the M_2 dependence with λ.

2) λ Estimation: Replacing (21) into the likelihood obtained in (22), one can easily obtain the following for the ALL:

$$\mathrm{ALL}(\lambda) = -\log(\det(M_1)) + N\log(\lambda) + \log(\boldsymbol{x}^t(I - M_2)\boldsymbol{x}).$$

The hyperparameter λ is then chosen as the ALL minimizer

$$\hat{\lambda} = \lambda_{ML} = \arg\min \mathrm{ALL}(\lambda).$$

B. Generalized Cross Validation (GCV)

The previous methods are nondeterministic by nature since they are derived from the Bayesian framework. This section is devoted to a deterministic method, namely the GCV, derived from the quadratic regularization interpretation presented in Section III-D. In the class of deterministic solutions for hyperparameters estimation, the very first idea, called λ_χ or λ_{RESID} (see [11]) is based on the probability density function of the residual sum of the squares $Q_0(\boldsymbol{a})$. Since the signal is Gaussian and the model is linear, the residual sum of the squares follows a χ_N^2 distribution

$$Q_0(\boldsymbol{a}) \sim \chi_N^2 \sigma_u^2.$$

This motivates the choice of λ_χ as the solution of

$$Q_0(\boldsymbol{a}) = N\sigma_u^2$$

since $N\sigma_u^2$ is the expected value of the residual distribution. This method has been popular throughout the history of regularization techniques, but in practical cases when $\boldsymbol{a}$ is replaced by $\hat{\boldsymbol{a}}$, the residual sum of the squares does not exactly follow a χ_N^2 distribution.

In order to overcome this obstacle, Thompson *et al.* [11] proposed a better approximation of the distribution of the residual sum of the squares. They introduced an equivalent degree of freedom (EDF) for the residual $N' = N - \mathrm{Tr}\{M_2\}$, and proposed a λ estimation called λ_{EDF} as the solution of

$$Q_0(\boldsymbol{a}) = \mathrm{Tr}\{I - M_2\}\sigma_u^2.$$

The properties of these estimators have been examined and their performances compared in [8], [10], and [11]. It has been reported that these two techniques, especially the first one, substantially overregularize the solution. Moreover, they absolutely require the knowledge of the noise variance, and have been reported as interesting only if the exact noise variance (or a very good estimate of it) is available.

The cross validation (CV) criterion [9] is an estimate of the MSE, calculated from the data only. The basic principle is very simple and consists of removing one observation x_i from the data, and predicting it on the basis of the regularized solution obtained from the remaining data. The difference between the true and predicted data yields an error, and averaging the prediction errors over all the removed data leads to an approximate MSE. This error is a function of λ, called the cross-validation criterion

$$\mathrm{CV}(\lambda) = ||M(I - M_2)\boldsymbol{x}||,$$

where M is a diagonal matrix with the ith diagonal element $1/(1 - a_{ii})$, a_{ii} being the iith entry of M_2. The minimum of this criterion should give a good value of the hyperparameters. In fact, we shall not minimize CV, but a modified version of it called GCV. This criterion does not differ greatly from the CV, presents more pleasant properties [9], and takes the form

$$\mathrm{GCV}(\lambda) = \frac{||(I - M_2)\boldsymbol{x}||}{\mathrm{Tr}\{I - M_2\}}.$$

λ is chosen as λ_{GCV}, the minimizer of this criterion with respect to λ

$$\hat{\lambda} = \hat{\lambda}_{\mathrm{GCV}} = \arg\min \mathrm{GCV}(\lambda).$$

Since the GCV criterion is a function of λ only, this strategy represents an alternative to λ estimation, but does not allow simultaneous estimation of σ_u^2. The noise power estimate remains the usual estimate given (25) for ML strategy.

V. Methodology of the Simulation Study

A theoretical comparative study between the performances of the proposed and usual least squares methods is strongly desirable, but is a very difficult task because of the lack of an explicit expression for $\hat{\lambda}$. Theoretical results are available only for small $\hat{\lambda}$ values and in the GCV case [9], [11], but such small values are out of the domain of interest in our practical case. Therefore, a comparative simulated study is required. By Monte Carlo experiments [14], statistical results have been obtained in the following way: a large amount of signals have been simulated, and for each of them the

PSD has been estimated from the different methods and in different conditions. Then, assuming that the large number law is applicable, by averaging these estimates, several estimation characteristics were obtained.

A. Measures of Error and Assessment of Performance

1) PSD Estimation Performance Measurement: We now present different classes of comparison measures investigated to compare estimation methods.

a) Bias, variance, and mean square error: The first statistical characteristic is the bias $B(f)$ which characterizes the mean difference between the estimation expectation $E(f)$ and the true value $S_x(f)$. The second characteristic is the standard deviation $SD(f)$, i.e., the square root of the estimation variance $V(f)$. It quantifies the mean variability of the estimate around its expected value $E(f)$. Finally, the MSE, $\mathrm{MSE}\,(f) = B(f)^2 + V(f)$, integrating both bias and variance was also used.

b) Integrated performance index: As these quantities are functions of frequency, a qualitative and visual criterion is the only possibility for comparing the different estimation methods over the whole frequency domain. In order to avoid this difficulty, as proposed in [15], three indexes integrating the frequency dependence have been used: the integrated bias (IB), the integrated variance (IV), and the integrated mean square error (IMSE). They are calculated by integrating respectively the bias, variance, and MSE over the whole frequency domain.

c) Logarithmic distance: The second class of index consists of a measure of the mean dissimilarity between the true and estimated log-spectrum. We first define the log-distance (LD) between the true and estimated PSD

$$\mathrm{LD}\,(f) = [\log S_x(f) - \log \hat{S}_x(f)]^2.$$

Since it is also a function of frequency, it is helpful to build an integrated index

$$\mathrm{ILD} = \int_{-1/2}^{1/2} \mathrm{LD}\,(f)\, df,$$

which is a distance between the true and estimated log-PSD. A global statistical index considers the mean ILD (MILD) under the true probability distribution and takes the following form:

$$\mathrm{MILD} = E\{\mathrm{ILD}\}.$$

d) Kullback distance: The third comparison criterion is entropic. The Kullback dissimilarity measure is the entropy of the true probability distribution with respect to the estimated, and is defined by

$$\mathrm{KD}\,(f_t, f_e) = E_{f_t}\left\{\frac{f_e(x)}{f_t(x)}\right\},$$

where f_t and f_e are, respectively, the true and estimated probability distribution of the process. In our study, since the processes are Gaussian, the Kullback distance is

$$KD(f_t, f_e) = -\tfrac{1}{2}\left(N + \log\det R_e^{-1}R_t - \mathrm{Tr}\,\{R_e^{-1}R_t\}\right).$$

Then, the error measure is the mean Kullback distance (MKD)

$$\mathrm{MKD} = E_{f_t}\{K(f_t, f_e)\}.$$

2) λ Estimation Performances Measurement: In order to assess and compare the different methods of estimation for the hyperparameters, the first step is to determine a reference, and this is done in the following way. As the true PSD is known in our simulation study, the "true" λ can be evaluated as λ_{IMSE}, the minimizer of the IMSE defined in the previous section. Such a λ_{IMSE} is not an actual estimate since it requires the knowledge the true PSD and a large amount of simulated signal. Nevertheless, it is an interesting reference in order to assess the two actually practicable methods i.e., ML and GCV (which estimate the hyperparameters from a single signal realization and, of course, without knowing the true PSD). This λ_{IMSE} will be considered as the true λ value in order to evaluate bias B_λ, variance V_λ, and MSE MSE_λ.

B. Theoretical Spectrum and Simulated Signals

1) Choice of a Field of Application: On the one hand, the studied method concerns several fields of application, such as nondestructive testing, attenuation measurements, Doppler imaging, etc., and on the other hand, a simulation study requires the choice of a spectral shape and simulation model related to the considered application. Among the applications, we have made the choice of ultrasonic Doppler velocimetry, because it is one of the most difficult problems for several reasons:

1) Ultrasonic Doppler signals are known to be very complex and difficult to analyze since they are the results of a highly complex nonlinear backscattering phenomenon [16].
2) In ultrasound Doppler velocimetry, important variations of the signal-to-noise ratio (SNR) during the cardiac cycle are observed (the SNR falls down during diastole due to the clutter rejection filter).
3) The reduction of window data length is crucial in order to perform a more time-resolvant analysis of rapidly varying nonstationary flows, as pointed out by several authors, e.g., [17]–[19].

In Doppler spectral analysis, a seminal paper by Vaitkus *et al.* [20] compares numerous spectral estimation methods, parametric or not parametric. Comparison of several indexes, including IMSE for these methods, has indicated a slight superiority for the least squares AR method, especially for low SNR, while keeping an efficient computational cost. Our study follows that of Vaitkus *et al.*, and its objective is to show that the RLS AR methods achieve a new improvement with respect to the least squares AR methods. Particular attention will be paid to improvement in time resolution of fine details of the rapidly varying flow by processing very short windows.

2) Choice of Simulation Model and Spectral Shape: In order to perform a simulation study, two other choices are required: the first deals with spectral shape and the second concerns simulations of signals with the chosen PSD.

a) Spectral shape: A currently used spectral shape (see Fig. 1) is proposed in [21] and closely approximates the PSD seen around the peak systole under normal flow conditions in a carotid artery. This shape is used by several authors and seems to be recognized as a typical spectral shape [15], [22].

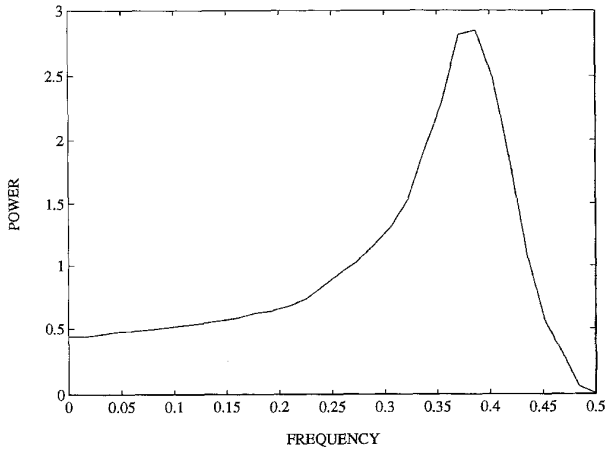

Fig. 1. Theoretical power spectral density approximating that typically seen around peak systole, used for simulated signals.

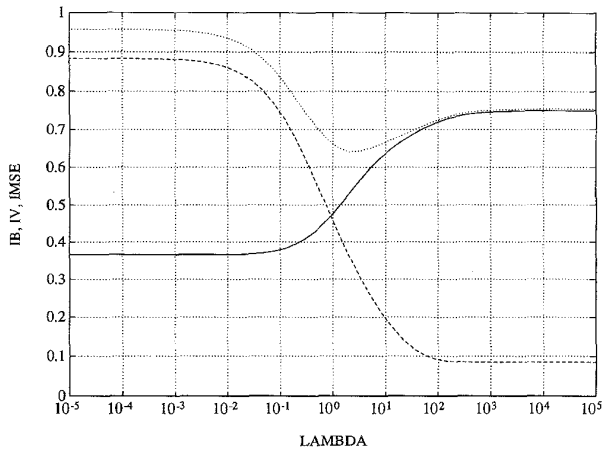

Fig. 2. Integrated bias (solid line), integrated variance (dashed line), and IMSE (dotted line) as a function of λ.

b) Simulation model: In a detailed study of the backscattered ultrasound from blood insonated by a continuous monochromatic wave, Mo and Cobbold in [21] showed that, under acceptable assumptions, the Doppler signal $x(t)$ is a zero-mean stationary Gaussian process.

Mo and Cobbold proposed the following simulation model [23] derived from their previously mentioned [21] physical study, and which can be assumed to faithfully reproduce the complex physical nature of the real signals. The chosen PSD function $S_x(f)$ shown in Fig. 1 is sampled on a fine frequency grid and each sample is multiplied by a χ^2 random variable. The square root of each obtained variable is multiplied by a uniformly distributed complex phase term, and finally an inverse Fourier transform yields to the simulated signal $x(n)$. It can be shown that $x(n)$ is a zero-mean stationary Gaussian process having the given PSD $S_x(f)$.

c) Simulated signals: The simulation model and the DSP described above have been used to generate 500 signals of 256 samples from the theoretical PSD shown in Fig. 1 in the same manner as [15] and [22]. The following study was made from 16–256 of these samples in order to compare the methods for different window data lengths. The effect of an additive Gaussian white noise on the estimation has also been investigated for an SNR from -30 to 30 dB.

VI. Results and Discussion

In this simulation study, particular attention is paid to the case in which 16 samples are observed with an SNR of 20 dB. In this situation, both λ (Section VI-A) and PSD estimation properties (Section VI-B) are investigated. Complementary results are given in Section VI-C1), VI-C2), and VI-C3) which investigate the influence of smoothness order, window data length, and SNR.

A. λ Estimation Properties

In this section, a study of λ estimation properties is presented in the case of 16 samples with an SNR of 20 dB and first smoothness order. We first find out the best λ value in

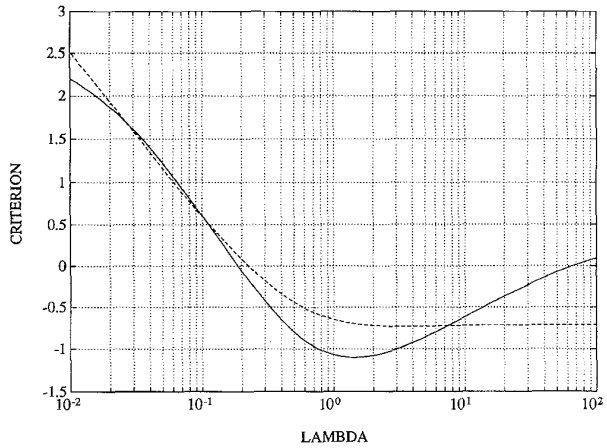

Fig. 3. The two λ estimation criteria obtained from Sig1: GCV (solid line) and ALL (dashed line).

Section VI-A1), then we compare the two estimation methods within each other and with the best λ value in Section VI-A2).

1) Determination of λ_{IMSE}*:* Simulations were made on a logarithmic grid of 100 values from $\lambda = 10^{-5}$ to $\lambda = 10^5$, and the indexes IB, IV, and IMSE are presented in Fig. 2.

For λ small enough ($\lambda < 10^{-3}$), the solution is not regularized, i.e., no prior knowledge is introduced. It is equivalent to say that the least squares solution is found, i.e., the solution is entirely based on data. Therefore, as expected, the statistical properties are still those pointed out in Section II: even if the estimation is low biased, the strong variance leads to unreliable results.

At the other extreme, for λ high enough ($\lambda > 10^3$), the solution is infinitely regularized, i.e., almost no data are taken into account in the estimation. It is equivalent to say that the solution is entirely prior based, i.e., the estimated spectrum is completely smooth and constant over the whole frequency domain. Therefore, as expected, the statistical properties of the estimation are opposite: the estimation has a very low variance, but the very strong bias leads to unusable results. Between these two extreme situations, IMSE shows a mini-

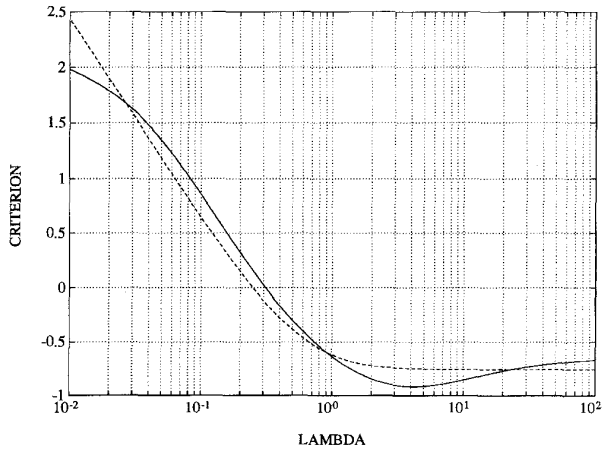

Fig. 4. The two λ estimation criteria obtained from Sig2: GCV (solid line) and ALL (dashed line).

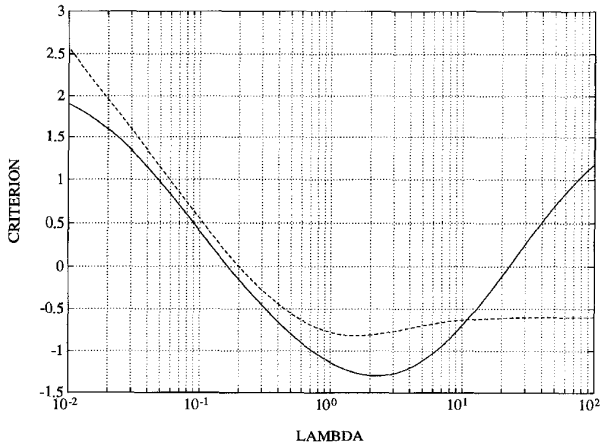

Fig. 5. The two λ estimation criteria obtained from Sig3: GCV (solid line) and ALL (dashed line).

mum IMSE $= 0.64$ for $\lambda_{\mathrm{IMSE}} = 2.02$. This value $\lambda_{\mathrm{IMSE}} = 2.02$ is assumed to be the true value of λ in the following comparisons.

2) Comparison of the λ Estimates: As mentioned above, in practical cases, λ must be estimated from each signal, and of course without knowing the actual PSD. Such a value is now sought by computing the two criteria (ALL and GCV) on a logarithmic grid of 100 values between 10^{-2} and 10^{2}. In order to understand the characteristics of the λ estimation methods presented in Section IV, we first describe results obtained from three particular signals, and in a second step, we provide statistical characteristics.

a) Estimation from typical signal realizations: First, as an example, Figs. 3, 4, and 5 show typical forms of the two estimation criteria: ALL [ALL (λ)] and GCV [GCV (λ)] for three particular signals, referred to as Sig1, Sig2, and Sig3. For Sig1 and Sig3, one can observe a minimum for each criterion (see Table I). On the contrary, for Sig2, one can see that the ALL has no minimum or, equivalently, the minimum is rejected to $\lambda = \infty$ ($\lambda = 100$ in our simulation).

TABLE I
λ ESTIMATION FROM THE GIVEN SIGNAL SIG1, SIG2, AND SIG3, USING THE TWO ESTIMATION METHODS: ML AND GCV

	$\hat{\lambda}_{ML}$	$\hat{\lambda}_{GCV}$
Sig1	3.51	1.39
Sig2	100	4.23
Sig3	1.52	2.21

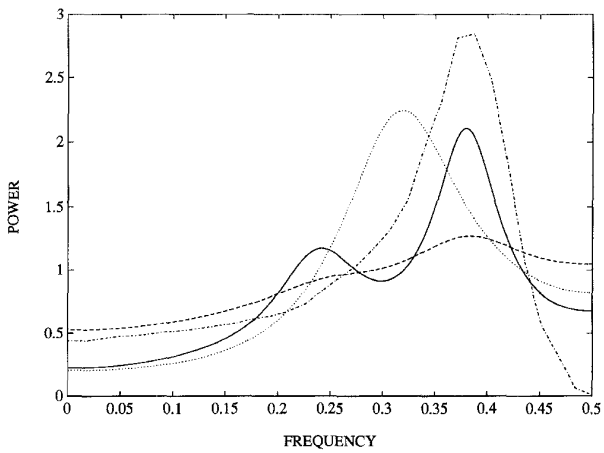

Fig. 6. Comparison of the two practicable regularized methods [$\hat{\lambda} = \lambda_{\mathrm{GCV}}$ (solid line) and $\hat{\lambda} = \lambda_{\mathrm{ML}}$ (dashed line)] and the usual least squares method (dotted line) from Sig1. The theoretical power spectral density is also plotted (dash-dot line).

The corresponding estimated spectra are given in Figs. 6, 7, and 8. As expected, for high $\hat{\lambda}$ values, the PSD estimate is smooth, at the limit for infinite $\hat{\lambda}$ values ($\hat{\lambda} = 100$ is large enough in our simulations) the PSD is entirely smooth and constant over the whole frequency domain. On the contrary, for smaller $\hat{\lambda}$ values, the PSD estimate is not smooth.

For some signal realizations (Sig2, for instance), the estimated regularization parameter is $\lambda = \infty$, so the regularized PSD estimate is constant over the whole frequency domain. It is important to note that at the same time, for these particular signal realizations, the least squares solution is also unreliable. When information is almost absent from the measured signal (for Sig2, for instance), the least squares solution yields a PSD estimate, which is completely different from the true PSD and presents almost any shape. In such cases, as there is so little information in the measured signal, the regularized solution leads to the prior solution, i.e., a flat spectrum. It is a noticeable advantage of the regularized method: when there is not enough information in the signal, instead of giving anything as a PSD estimate, which is the usual approach, a fixed ultrasmooth solution (regularized) is given. In this sense, it is an argument in favor of the regularized method that it can discriminate between informative and uninformative data.

b) Statistical characteristics: Averaged results for the 500 simulated signals are now presented. For each simulated signal, the criteria have been computed and the two λ

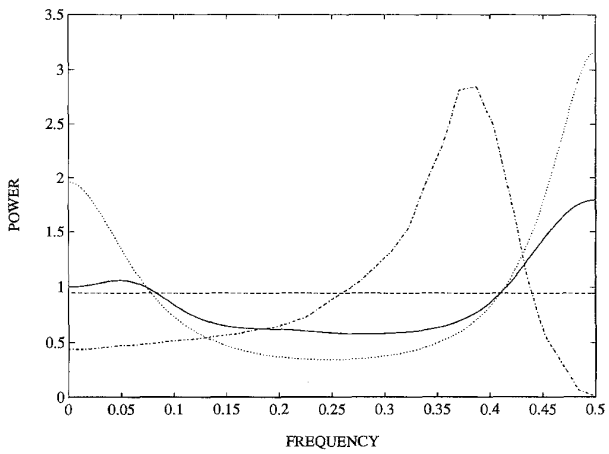

Fig. 7. Comparison of the two practicable regularized methods [$\hat{\lambda} = \lambda_{\mathrm{GCV}}$ (solid line) and $\hat{\lambda} = \lambda_{\mathrm{ML}}$ (dashed line)] and the usual least squares method (dotted line) from Sig2. The theoretical power spectral density is also plotted (dash-dot line).

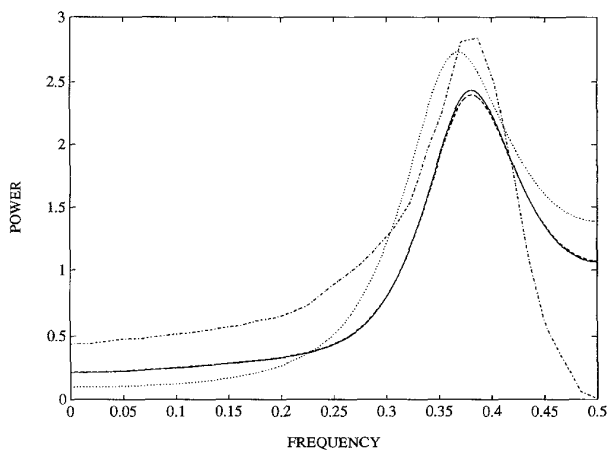

Fig. 8. Comparison of the two practicable regularized methods [$\hat{\lambda} = \lambda_{\mathrm{GCV}}$ (solid line) and $\hat{\lambda} = \lambda_{\mathrm{ML}}$ (dashed line)] and the usual least squares method (dotted line) from Sig3. The theoretical power spectral density is also plotted (dash-dot line).

estimates $(\hat{\lambda}_{\mathrm{ML}}, \hat{\lambda}_{\mathrm{GCV}})$ have been calculated. Fig. 9 shows the $\hat{\lambda}$ repartition for the two estimation methods.

As mentioned above for some signal realizations, the criteria may have no minimum (or equivalently, the minimum is rejected to $\lambda = \infty$). One can see that from the 500 simulated signals, the proportion of criteria without minimum is 30% when using the ML estimation criterion and 25% when using the GCV criterion. The GCV estimation procedure seems to be more robust, and in this sense is the best one.

In order to give a more accurate analysis, we eliminate the case of criterion without minimum from the results given here. The indexes of interest given in Table II can then be calculated. Table II gives the $\hat{\lambda}$ expected value, bias, standard deviation, and mean square error assuming that λ_{IMSE} is the true value.

These results first show that both the ML and GCV methods overestimate the parameter λ several times and, as a direct consequence, oversmooth the estimated spectra. This point needs

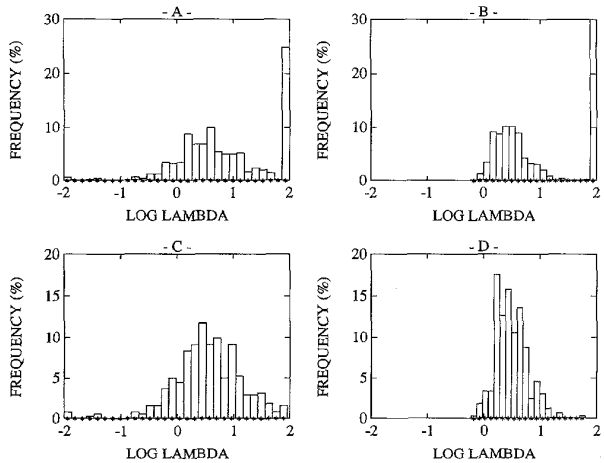

Fig. 9. Histogram of $\hat{\lambda}$. (a) GCV criterion, (b) ML, as obtained from the computations, (c) GCV criterion, and (d) ML, after elimination of the infinite values.

TABLE II
λ ESTIMATION STATISTICAL PROPERTIES FOR THE TWO METHODS: ML AND GCV

	$\hat{\lambda}_{ML}$	$\hat{\lambda}_{GCV}$
Expectation	3.93	8.12
Bias	1.91	6.10
Standard Deviation	2.12	3.66
Mean Square Error	2.85	7.11

to be made precise. Although the regularization parameter is overestimated, it remains in the correct range, i.e., around the minimum of the IMSE presented in Fig. 2.

Moreover, since the IMSE is slowly varying around its minimum, the error is rather indifferent to the variations of λ as long as it remains in the correct decade (here between 1 and 10). The slowly varying character of the error with respect to λ is a strong argument for the robustness of the estimation method. Finally, one of the interests of the estimation method is to automatically find the range of the IMSE minimum without knowing the true spectrum, using one signal only.

Now comparing ML and GCV, the results of Table II also show that the ML method overestimates λ slightly less than the GCV method, hence there is less oversmoothing of the estimated spectra. From this point of view, one can say that the ML estimation procedure seems to be the best one.

A definitive comparison of the two λ estimation methods is given in terms of recovering the spectrum, by comparing the PSD estimation performances (see Section VI-B).

B. PSD Estimation Performances

In order to give an assessment of an improvement with respect to the usual least squares solution, we will first find out the AR order giving the least error in Section VI-B1), and then we will show that the regularized method yields better

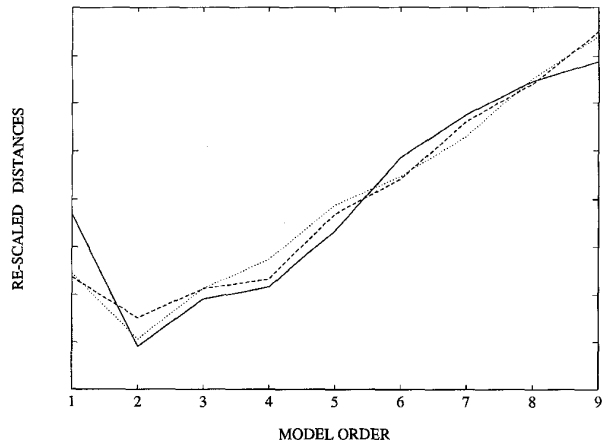

Fig. 10. Kullback distance (solid line), logarithmic distance (dashed line), and IMSE (dotted line) as a function of AR order.

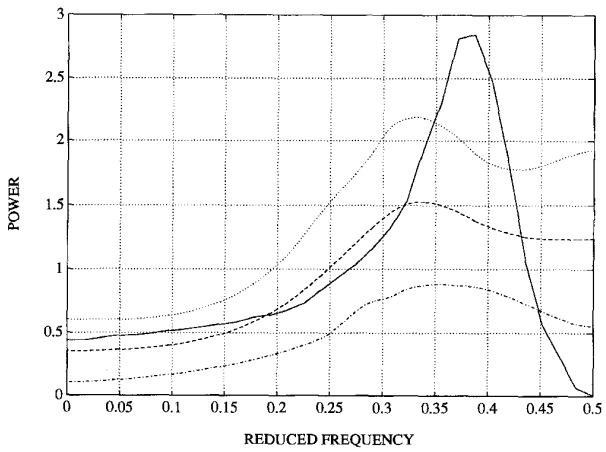

Fig. 11. Best selected usual least squares solution. Actual DSP (solid line), estimator expectation $E(f)$ (dashed line), $E(f) + SD(f)$ (dotted line), and $E(f) - SD(f)$ (dash-dotted line).

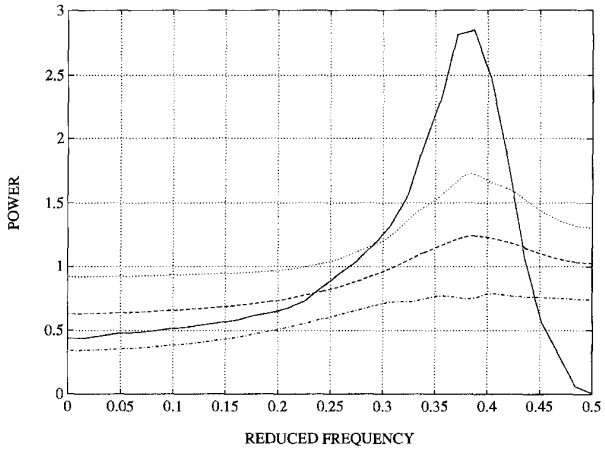

Fig. 12. Regularized least squares solution with λ_{ML}. Actual DSP (solid line), estimator expectation $E(f)$ (dashed line), $E(f)+SD(f)$ (dotted line), and $E(f) - SD(f)$ (dash-dotted line).

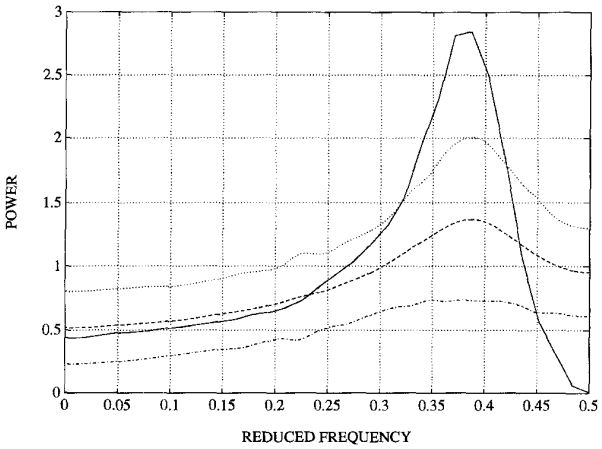

Fig. 13. Regularized least squares solution with λ_{GCV}. Actual DSP (solid line), estimator expectation $E(f)$ (dashed line), $E(f)+SD(f)$ (dotted line), and $E(f) - SD(f)$ (dash-dotted line).

results in Section VI-B2). The main point of the study is to make a comparison between the usual least squares solution (knowing the best order) and the regularized solution (without knowing the best regularization parameter).

1) Best Least Squares Model Order Selection: Since the problem of automatic choice for the model order is a difficult one, especially for a short data set, an exhaustive study has been performed and the best order has selected in the following manner.

For each possible order ($p = 1$ to 16), the three indexes IMSE, MKD, and MILD have been calculated and results are given in Fig. 10. Among all the possible orders p, the order $p_0 = 2$ minimizes the three indexes. Hence, the usual least squares solution with any model order selection criterion cannot give better results than $p = 2$. In this sense, the second-order AR model is the best for least squares estimation methods.

2) Assessment of an Improvement of Performance with Respect to the Best Least Squares Solution: We now present a comparison between the best usual least squares PSD estimation method ($p = 2$) and the regularized method. In the same way as previously, $\hat{S}_x(f)$ has been calculated using the regularized method with the two practicable λ estimation criteria (ML and GCV), and for the first smoothness order. As an example with particular signals, Sig1, Sig2, and Sig3, Figs. 6, 7, and 8 show the estimated PSD.

TABLE III
IMSE, MILD, MKD FOR THE THREE METHODS: LEAST SQUARES (LS), RLS WITH MAXIMUM LIKELIHOOD (ML), AND GCV FOR λ ESTIMATION

	LS	RLS (ML)	RLS (GCV)
IMSE	0.75	0.69	0.68
MILD	1.01	0.86	0.87
MKD	3.12	2.25	2.23

Mean estimate $E(f)$ and variability $E(f) \pm SD(f)$ are shown in Figs. 11, 12, and 13, respectively, for the best usual

TABLE IV
IB, IV, AND IMSE USING THE REGULARIZED SOLUTION FOR THREE SMOOTHNESS ORDERS (ZERO, ONE, AND TWO) AND WITH THE TWO λ ESTIMATION METHODS

	$k=0$		$k=1$		$k=2$	
	ML	GCV	ML	GCV	ML	GCV
IB	0.68	0.59	0.61	0.56	0.31	0.55
IV	0.24	0.38	0.30	0.38	0.66	0.43
IMSE	0.71	0.70	0.69	0.68	0.72	0.70

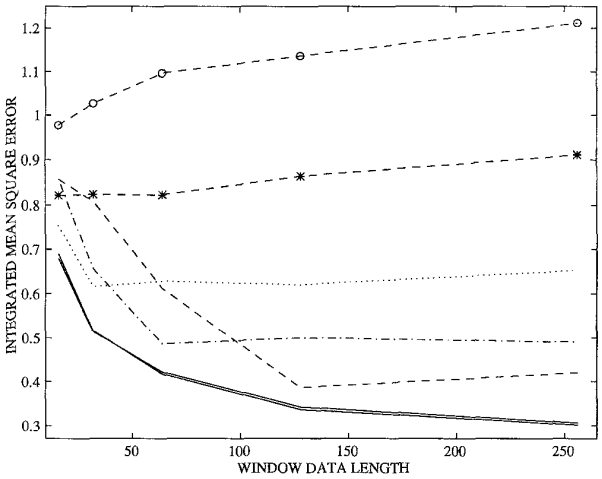

Fig. 14. IMSE for different model orders as a function of window data length. Least squares solution with $P = N/2$ (circle line), $P = N/4$ (star line), $P = N/8$ (dotted line), $P = N/16$ (dash-dotted line), and $P = N/32$ (dashed line). RLS solution with $\hat{\lambda} = \hat{\lambda}_{\mathrm{ML}}$ and $\hat{\lambda} = \hat{\lambda}_{\mathrm{GCV}}$ (solid lines almost coincident; see Table V for details).

least squares criterion and the regularized criterion with the two practicable λ estimation methods. The integrated indexes are reported in Table III for better readability.

The same indexes obtained from the regularized methods with the two λ estimation methods are shown to be smaller than those obtained for the best least squares solution defined in Section VI-B1). Since advantage has been given to the least squares method in the preliminary study giving $p = 2$ as the best model order, it appears that the proposed regularized method gives better statistical results than the usual least squares method.

Comparing GCV and ML estimation methods, one can see from Table III and from Figs. 12 and 13 that the two methods for hyperparameter estimation behave almost identically with a slight advantage to the GCV method. More accurate conclusions about the comparison between ML and GCV methods are difficult to draw on the basis of this result.

C. Influence of the Analysis Parameters

In the previous study, the smoothness order was fixed at one, the window data length at 16 samples, and the SNR at 20 dB. From this situation, we are now successively varying

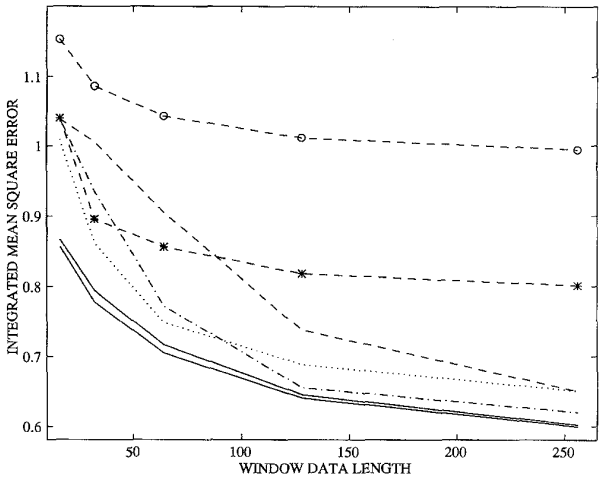

Fig. 15. MILD for different model order as a function of window data length. Least squares solution with $P = N/2$ (circle line), $P = N/4$ (star line), $P = N/8$ (dotted line), $P = N/16$ (dash-dotted line), and $P = N/32$ (dashed line). RLS solution with $\hat{\lambda} = \hat{\lambda}_{\mathrm{ML}}$ and $\hat{\lambda} = \hat{\lambda}_{\mathrm{GCV}}$ (solid lines almost coincident; see Table VI for details).

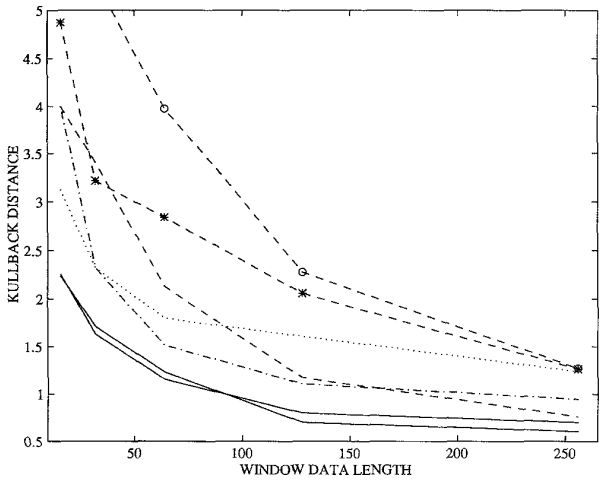

Fig. 16. MKD for different model order as a function of window data length. Least squares solution with $P = N/2$ (circle line), $P = N/4$ (star line), $P = N/8$ (dotted line), $P = N/16$ (dash-dotted line), and $P = N/32$ (dashed line). RLS solution with $\hat{\lambda} = \hat{\lambda}_{\mathrm{ML}}$ and $\hat{\lambda} = \hat{\lambda}_{\mathrm{GCV}}$ (solid lines almost coincident; see Table VII for details).

one of the three parameters (smoothness order, window data length, and SNR) while keeping the two others constant.

1) Smoothness Order: Influence of the smoothness order has been investigated and Table IV gives results for zero, one, and two smoothness orders. This table shows that the first smoothness prior gives very slightly better performances in terms of IMSE. On the other hand, results show low sensitivity to this parameter and the error index remains smaller than the best least squares index.

2) Data Window Length: In a first step, for several window data lengths ($N = 16, 32, \cdots, 256$), the estimations $\hat{S}_x(f)$ have been calculated using the usual least squares solution with several AR orders p ($p = N/2, N/4, \cdots, N/16$), and the three indexes IMSE, MILD, and MKD have been computed. Figs. 14, 15, and 16 show the curves corresponding to the

TABLE V
IMSE AS A FUNCTION OF THE WINDOW DATA LENGTH. NUMERICAL RESULTS OF FIG. 14

	RLS		LS				
N	λ_{GCV}	λ_{ML}	$p = N/2$	$p = N/4$	$p = N/8$	$p = N/16$	$p = N/32$
16	0.68	0.69	0.98	0.82	0.75	0.86	0.86
32	0.51	0.52	1.03	0.82	0.62	0.66	0.81
64	0.42	0.42	1.10	0.82	0.63	0.49	0.61
128	0.34	0.34	1.14	0.86	0.62	0.50	0.39
256	0.31	0.30	1.21	0.91	0.65	0.49	0.42

TABLE VI
MILD AS A FUNCTION OF THE WINDOW DATA LENGTH. NUMERICAL RESULTS OF FIG. 15

	RLS		LS				
N	λ_{GCV}	λ_{ML}	$p = N/2$	$p = N/4$	$p = N/8$	$p = N/16$	$p = N/32$
16	0.86	0.87	1.15	1.04	1.01	1.04	1.04
32	0.78	0.79	1.09	0.90	0.86	0.93	1.01
64	0.70	0.72	1.04	0.86	0.75	0.77	0.90
128	0.64	0.65	1.01	0.82	0.69	0.66	0.74
256	0.60	0.60	0.99	0.80	0.65	0.62	0.65

TABLE VII
MKD AS A FUNCTION OF THE WINDOW DATA LENGTH. NUMERICAL RESULTS OF FIG. 16

	RLS		LS				
N	λ_{GCV}	λ_{ML}	$p = N/2$	$p = N/4$	$p = N/8$	$p = N/16$	$p = N/32$
16	2.25	2.23	7.90	4.87	3.12	4.00	4.00
32	1.63	1.71	5.31	3.21	2.32	2.32	3.41
64	1.15	1.23	3.98	2.84	1.80	1.51	2.13
128	0.80	0.70	2.28	2.06	1.61	1.11	1.17
256	0.70	0.60	1.27	1.26	1.23	0.95	0.76

different AR orders as a function of the window data length, while Tables V, VI, and VII show the corresponding numerical results.

In a second step, the same indexes have been computed from the same simulated signals and window data lengths, but using the regularized solution with $\hat{\lambda} = \hat{\lambda}_{\mathrm{GCV}}$ and $\hat{\lambda} = \hat{\lambda}_{\mathrm{ML}}$. Results are also presented in Figs. 14, 15, and 16, and in numerical form in Tables V, VI, and VII.

From the results presented in the figures and tables, one can observe that in any case, the RLS solution gives the least error with a slight advantage over the GCV method.

From another standpoint, for given performances, e.g., IMSE $= 0.4$ (respectively, 0.5), the usual method requires $N = 128$ (respectively, 64) data, while the regularized method can achieve the same performance from only $N = 64$ (respectively, 32) data. Hence the proposed method can achieve more resolution along the time axis of rapidly varying nonstationary flow.

3) Signal-to-Noise Ratio: For several SNR's from -30 to 30 dB from 16 samples of the 500 simulated signals, estimations of $S_x(f)$ have been calculated using the best usual least squares solution and using the two RLS solutions (with $\hat{\lambda}_{\mathrm{ML}}$

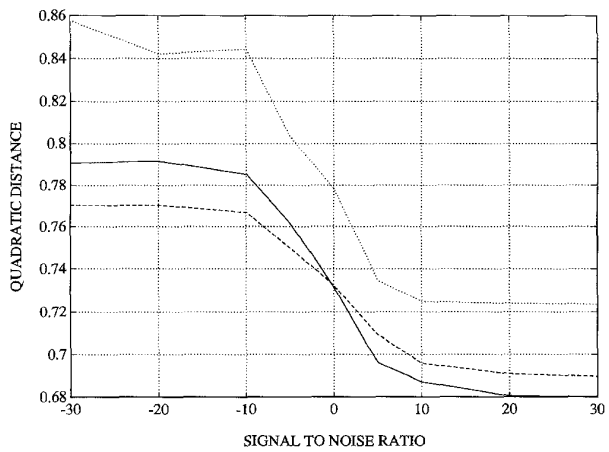

Fig. 17. IMSE as a function of SNR. Usual least squares solution (dotted line), regularized solution and λ_{GCV} (solid line), and regularized solution and λ_{ML} (dashed line).

and $\hat{\lambda}_{\mathrm{GCV}}$). The IMSE indexes are shown in Fig. 17. From the simulations results, it can be seen that for each SNR, the regularized solution yields better estimation qualities in terms of IMSE. Moreover, slightly better performance for the ML method for a negative SNR, and better performances for the GCV method for a positive SNR can be seen.

From another point of view, Fig. 17 shows that the performance of the regularized method for any positive SNR is better than or equivalent to the best performance of the least squares method (obtained with SNR = 30 dB), indicating an important gain in terms of SNR.

For given performances (e.g., IMSE = 0.76), the regularized method enables the exploitation of signals corrupted down to −5 dB, while the usual method cannot accept an SNR lower than +3 dB. Hence a gain on noise power (here, 8 dB) is achieved and allows a deeper flow analysis.

VII. Conclusions

We have addressed the problem of spectral estimation of a zero-mean stationary Gaussian process when only a short span of data is available for analysis (down to 16 observations). In such a situation, usual AR estimation strategies, such as ML or least squares, enforce the estimation of a parsimonious model which precludes the description of a large class of PSD. The Bayesian approach presented here and initially proposed by Kitagawa and Gersch [4] alleviates this limitation since it admits the robust estimation of long AR parameter vectors (typically 16 parameters from 16 observations).

We have performed a large simulation study in order to compare performances with respect to those of the usual method. We have compared two estimation methods of the fundamental regularization parameter: ML and GCV methods in terms of recovering a known PSD. The conclusion of this study is that the GCV method performs slightly better than the ML method. Nevertheless, this result should be taken with caution since the difference observed is very slender.

A statistical comparison of the presented Bayesian method versus the usual method has been achieved in different situations, varying the data span length and the SNR. The performances have been measured using various indexes: quadratic, logarithmic, and Kullback distances. The simulations confirm and extend the results of Kitagawa and Gersch in different situations and using new performance measures. The result is that the Bayesian method with automatic tuning of the hyperparameters yields better indexes than the usual least squares method, whatever the model order. The conclusion is then in favor of the Bayesian approach, at least for the class of signals within the scope of this paper. Nevertheless, we believe that as long as a spectral smoothness information is available for estimation, the presented method is able to provide better results than the nonregularized method.

Acknowledgment

The authors wish to thank J. Idier for numerous and helpful discussions. They are also grateful to Mr. Grün and Mrs. Groen for their expert editorial assistance.

References

[1] S. M. Kay and S. L. Marple, "Spectrum analysis—A modern perspective," *Proc. IEEE*, vol. 69, pp. 1380–1419, 1981.
[2] S. M. Kay, *Modern Spectral Analysis*. Englewood Cliffs, NJ: Prentice-Hall, 1988.
[3] S. L. Marple, *Digital Spectral Analysis with Applications*. Englewood Cliffs, NJ: Prentice-Hall, 1987.
[4] G. Kitagawa and W. Gersch, "A smoothness priors long AR model method for spectral estimation," *IEEE Trans. Automat. Contr.*, vol. AC-30, pp. 57–65, 1985.
[5] S. M. Kay, "Recursive maximum likelihood estimation of autoregressive processes," *IEEE Trans. Acoust., Speech, Signal Processing*, vol. ASSP-21, pp. 56–65, 1983.
[6] D. T. Pham, "Maximum likelihood estimation of the autoregressive model by relaxation on the reflection coefficients," *IEEE Trans. Signal Processing*, vol. SP-36, pp. 1363–1367, 1988.
[7] G. Demoment, "Image reconstruction and restoration: Overview of common estimation structure and problems," *IEEE Trans. Acoust., Speech, Signal Processing*, vol. 37, pp. 2024–2036, 1989.
[8] N. Fortier, G. Demoment, and Y. Goussard, "Comparison of GCV and ML methods of determining parameters in image restoration by regularisation," *J. Visual Commun. Image Representation*, vol. 4, pp. 157–170, 1993.
[9] G. H. Golub, M. Heath, and G. Wahba, "Generalized cross-validation as a method for choosing a good ridge parameter," *Technometrics*, vol. 21, pp. 215–223, 1979.
[10] P. Hall and D. M. Titterington, "Common structure of techniques for choosing smoothing parameter in regression problems," *J. Roy. Statist. Soc. B*, vol. 49, pp. 184–198, 1987.
[11] A. Thompson, J. C. Brown, J. W. Kay, and D. M. Titterington, "A study of methods of choosing the smoothing parameter in image restoration by regularization," *IEEE Trans. Pattern Anal. Machine Intell.*, vol. 13, pp. 326–339, 1991.
[12] D. M. Titterington, "Common structure of smoothing techniques in statistics," *Int. Satist. Rev.*, vol. 53, pp. 141–170, 1985.
[13] E. T. Jaynes, "Prior probabilities," *IEEE Trans. Syst. Sci. Cybernetics*, vol. SSC-4, pp. 227–241, 1968.
[14] Y. A. Shreider, *The Monte Carlo Method*, vol. 87. New York: Pergamon, 1966.
[15] P. J. Vaitkus and R. S. C. Cobbold, "A comparative study and assessment of Doppler ultrasound spectral estimation techniques. Part II: Method and results," *Ultrasound Med. Biol.*, vol. 14, pp. 673–688, 1988.
[16] B. A. J. Angelsen, "A theoretical study of the scattering of ultrasound from blood," *IEEE Trans. Biomed. Eng.*, vol. BME-27, pp. 61–67, 1980.
[17] R. I. Kitney and D. P. Giddens, "Analysis of blood flow velocity waveforms by phase shift averaging and autoregressive spectral estimation," *J. Biomed. Eng.*, vol. 105, pp. 398–401, 1983.
[18] H. E. Talhami and R. I. Kitney, "Maximum likelihood frequency tracking of the audio pulsed Doppler ultrasound signal using a Kalman filter," *Ultrasound Med. Biol.*, vol. 14, pp. 599–609, 1988.

[19] Z. Guo, J.-G. Durand, and H. C. Lee, "Comparison of time-frequency distribution techniques for analysis of simulated Doppler ultrasound signals of the femoral artery," *IEEE Trans. Biomed. Eng.*, vol. 41, pp. 332–342, 1994.
[20] P. J. Vaitkus and R. S. C. Cobbold, "A comparative study and assessment of Doppler ultrasound spectral estimation techniques. Part I: Estimation methods," *Ultrasound Med. Biol.*, vol. 14, pp. 661–672, 1988.
[21] L. Y. L. Mo and R. S. C. Cobbold, "Speckle in continuous wave Doppler ultrasound spectra: A simulation study," *IEEE Trans. Ultrason., Ferroelect., Freq. Contr.*, vol. UFFC-33, pp. 747–753, 1986.
[22] T. Loupas and W. N. McDicken, "Low-order complex AR models for mean and maximum frequency estimation in the context of Doppler color flow mapping," *IEEE Trans. Ultrason., Ferroelect., Freq. Contr.*, vol. 37, pp. 590–601, 1990.
[23] L. Y. L. Mo and R. S. C. Cobbold, "A stochastic model of the backscattered Doppler ultrasound from blood," *IEEE Trans. Ultrason., Ferroelect., Freq. Contr.*, vol. UFFC-33, pp. 20–27, 1986.

Jean-François Giovannelli was born in Béziers, France, in 1966. He graduated from the École Nationale Supérieure de l'Électronique et de ses Applications, in 1990. He received the Doctorat degree in physics at the Laboratoire des Signaux et Systèmes, Université de Paris-Sud, Orsay, in 1995. He is presently with the Laboratoire des Signaux et Systèmes as a Postdoctoral Student. He is interested in the Bayesian method for inverse problems in signal and image processing, mainly in the field of spectral estimation.

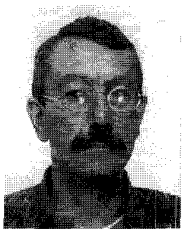

Guy Demoment was born in France, in 1948. He graduated from the École Supérieure d'Électricité, in 1970, and received the Doctorat d'État degree in physics from the Université de Paris-Sud, Orsay, in 1977.

From 1971 to 1977 he was with the Service des Mesures de l'École Supérieure d'Électricité. From 1977 to 1988 he was with the Centre National de la Recherche Scientifique, assigned to the Laboratoire des Signaux et Systèmes. He is presently a Professor in the Department of Physics at the Université de Paris-Sud, Orsay. After some works on biological system modeling, his interests shifted toward inverse problems in signal and image processing.

Dr. Demoment is a member of AF5.5 and SRV.

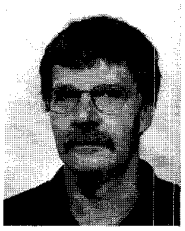

Alain Herment was born in Paris, France, in 1948. He graduated from ISEP Engineering School of Paris, in 1971. He received the Doctorat d'État degree in physics, in 1984.

Initially, he worked as an Engineer at the Centre National de la Recherche Scientifique. In 1977 he commenced a career as a Researcher at the Institut National pour la Santé et la Recherche Médicale (INSERM). He is currently in charge of the Department of Cardiovascular Imaging at the INSERM Unit 66, Hôpital Pitié, Paris, France. He is interested in signal and image processing for extracting morphological and functional information from image sequences, mainly in the fields of ultrasound investigations, X-ray computed tomography, and digital angiography.

J. Idier et **J.-F. Giovannelli**, « Structural stability of least squares prediction methods », *IEEE Trans. Signal Processing*, vol. 46, n°11, pp. 3109–3111, novembre 1998.

ε_{1s}, ε_{2s} being $N(0, 2)$, the l_1-periodogram does not perform much worse than the standard l_2-periodogram.

V. Conclusions

A new type of the periodogram is developed for observations contaminated by impulse random errors having an unknown heavy-tailed error distribution. A nonquadratic residual loss function used for a fitting of observations is a key point that separates the new periodogram from the standard one. The Huber's minimax robust statistics are applied for a choice of this residual function. The formulas for the asymptotic bias and variance of the robust M-periodogram are obtained. The simulation given for the l_1-periodogram demonstrates a radical improvement in the quality of the periodogram.

Acknowledgment

The author would like to thank the two anonymous referees for their helpful comments.

References

[1] P. J. Huber, *Robust Statistics.* New York: Wiley, 1981.
[2] P. J. Rousseeuw and A. M. Leroy, *Robust Regression and Outliers Detection.* New York: Wiley, 1987.
[3] C. L. Nikias and M. Shao, *Signal Processing with Alpha-Stable Distributions and Applications.* New York: Wiley, 1995.
[4] P. J. Huber, "Robust regression: Asymptotics, conjectures and Monte Carlo," *Ann. Math. Statist.*, vol. 1, no. 5, pp. 799–821, 1973.
[5] B. T. Poljak and J. Z. Tsypkin, "Robust identification," *Automatika*, vol. 16, pp. 53–63, 1980.

Structural Stability of Least Squares Prediction Methods

Jérôme Idier and Jean-François Giovannelli

***Abstract*—A structural stability condition is sought for least squares linear prediction methods in the given data case. Save the Toeplitz case, the structure of the normal equation matrix yields no acknowledged guarantee of stability. Here, a new sufficient condition is provided, and several least squares prediction methods are shown to be structurally stable.**

I. Introduction

This correspondence addresses stability conditions of linear prediction filters in the *given data* case. A simple condition of strict stability of the prediction filter is proposed, which applies to least squares estimates. Whereas general stability tests [1], as well as simpler sufficient conditions [2], are known to apply to the estimated predictor itself, the proposed condition applies to the normal equation matrix (NEM). As a consequence, it shows that some least squares methods are *structurally stable*, i.e., that they ensure the predictor stability for any data sequence.

Manuscript received February 19, 1998; revised April 16, 1998. The associate editor coordinating the review of this paper and approving it for publication was Dr. Eric Moulines.

The authors are with Laboratoire des Signaux et Systèmes, Supélec, Plateau de Moulon, Gif-sur-Yvette, France (e-mail: idier@lss.supelec.fr).

Publisher Item Identifier S 1053-587X(98)07819-2.

Structural stability of the *autocorrelation method* is a well-known result. Because the NEM is positive definite and Toeplitz, the proof can be identified to that of the stability of the prediction error filter in the *given covariance* case [3]. The *post-windowed* approach is also known to be structurally stable [4], although the associated NEM is not Toeplitz. With regard to other methods, such as the *covariance method*, the *modified covariance method*, and the *prewindowed method* [5], the lack of structural stability is also acknowledged. On the other hand, the question of structural stability remains open for some other methods, such as the *smoothness priors long autoregressive method* of Kitagawa and Gersch [6]. In addition, in the case of *weighted least squares methods*, the effect of a forgetting factor on stability is unknown. In nearly all cases but the autocorrelation approach, the NEM is still positive (semi)definite, but it is not Toeplitz. The main contribution of the paper is to show that positive definite normal equation matrices still provide stable prediction filters, provided that the associated *displacement matrix* is positive semidefinite. Then, in the light of this property, structural stability of classical *least squares methods* is examined (or reexamined).

II. Conditions of Stability

A. Problem Formulation

Let M be a positive definite matrix of given size $(P+1)\times(P+1)$ defined as a function of the complex-valued data sequence $\mathbf{x} = [x_1, \ldots, x_n, \ldots, x_N]^{\mathbf{t}}$. Let $\boldsymbol{\alpha} = [1 \mid -\mathbf{a}^{\mathbf{t}}]^{\mathbf{t}}$ and

$$J(\mathbf{a}) = \boldsymbol{\alpha}^{\dagger} M \boldsymbol{\alpha} \tag{1}$$

be a quadratic criterion to be minimized with respect to the vector of prediction parameters $\mathbf{a} = [a_1, \ldots, a_P]^{\mathbf{t}}$. Let us introduce the following partition for M:

$$M = \begin{bmatrix} \rho & \mathbf{r}^{\dagger} \\ \mathbf{r} & R \end{bmatrix} \tag{2}$$

so that the minimum of $J(\mathbf{a})$ is reached by the prediction vector $\hat{\mathbf{a}} = R^{-1}\mathbf{r}$.

Our first contribution is to propose a simple condition on the structure of matrix M to ensure the stability of the allpole filter defined by $\hat{\mathbf{a}}$. Equivalently, the issue is to guarantee that the roots of the monic polynomial

$$A(z) \triangleq z^P - \sum_{k=1}^{P} a_k z^{P-k}. \tag{3}$$

lie within the unit circle.

A. Sufficient Condition

For any square matrix Q of size $n \times n$, let us denote, respectively, $\underline{Q}|$, $|\overline{Q}$, $|\underline{Q}$, and $\overline{Q}|$ as the northwest, southeast, northeast, and southwest matrices of size $(n-1)\times(n-1)$ extracted from Q. According to such a notation, the matrix R introduced in (2) is nothing but $|\overline{M}$, and

$$\Delta \triangleq |\overline{M} - \underline{M}| \tag{4}$$

is the displacement matrix of M, whose rank defines the distance from Tœplitz matrices [7]. The following result shows that the positivity of the displacement matrix plays a specific role with regard to the stability of the estimated prediction filter.

Theorem 1: Let M be a positive definite matrix. Then, with the notations of (2) and (4), $\hat{\mathbf{a}} = R^{-1}\mathbf{r}$ defines a stable prediction filter if $\Delta \geq 0$.

Proof: Let A be a monic polynomial of degree P, and let z_0 stand for one of its roots

$$A(z) = (z - z_0)B(z) \tag{5}$$

where B is a monic polynomial of degree $P-1$. In addition, let

$$\mathring{A}(z) = (z - z_0/|z_0|)B(z) \tag{6}$$

be the polynomial obtained by shifting z_0 onto the unit circle. Finally, let us denote $\boldsymbol{\alpha}$, $\boldsymbol{\beta}$, and $\mathring{\boldsymbol{\alpha}}$, and $\mathbf{a}$, $\mathbf{b}$ and $\mathring{\mathbf{a}}$ as the innovation and prediction vectors corresponding to A, B, and $\mathring{A}$, respectively, in conformity with the notation introduced in (3).

In terms of innovation vectors, (5) reads

$$\boldsymbol{\alpha} = \begin{bmatrix} \boldsymbol{\beta} \\ 0 \end{bmatrix} - z_0 \begin{bmatrix} 0 \\ \boldsymbol{\beta} \end{bmatrix}$$

which provides the following expression for (1):

$$J(\mathbf{a}) = \boldsymbol{\beta}^\dagger (\underline{M} + |z_0|^2 \overline{M} - z_0 \underline{M} - z_0^\star \overline{M})\boldsymbol{\beta}.$$

In the same way, (6) yields

$$J(\mathring{\mathbf{a}}) = \boldsymbol{\beta}^\dagger \left(\underline{M} + \overline{M} - \frac{z_0}{|z_0|}\underline{M} - \frac{z_0^\star}{|z_0|}\overline{M} \right)\boldsymbol{\beta}$$

and a combination of the latter two equations provides the following result:

$$J(\mathbf{a}) = \boldsymbol{\beta}^\dagger \overline{M}\boldsymbol{\beta}|z_0|^2 + (J(\mathring{\mathbf{a}}) - \boldsymbol{\beta}^\dagger(\overline{M} + \underline{M})\boldsymbol{\beta})|z_0| + \boldsymbol{\beta}^\dagger \underline{M}\boldsymbol{\beta}.$$

Since neither $J(\mathring{\mathbf{a}})$ nor $\boldsymbol{\beta}$ depend on $|z_0|$, $J(\mathbf{a})$ is a quadratic function of $|z_0|$. Moreover, since M is positive, $\overline{M}$ is also positive, and $J(\mathbf{a})$ passes through a unique minimum on $\mathbb{R}_+$. It is easy to check that

$$\left.\frac{\partial J(\mathbf{a})}{\partial |z_0|}\right|_{|z_0|=1} = J(\mathring{\mathbf{a}}) + \boldsymbol{\beta}^\dagger \Delta \boldsymbol{\beta} \tag{7}$$

which is strictly positive. As a function of $|z_0|$, we can conclude that $J(\mathbf{a})$ is strictly increasing for any $|z_0| \geq 1$. Hence, its unique minimum is necessarily reached *strictly inside* the unit circle. Then, as a function of $\mathbf{a}$, since M is positive, J passes through a unique minimum that is necessarily achieved for a polynomial $\hat{A}$ with all its roots within the unit circle. □

In the following, the matrix M will be said to be *canonical* when the conditions of Theorem 1 are fulfilled.

Remark 1: The conditions of Theorem 1 are $M > 0$ and $\Delta \geq 0$, but the slightly modified conditions $M \geq 0$ and $\Delta > 0$ are also sufficient, as is apparent from (7) (note that $\Delta > 0 \Rightarrow \overline{M} > 0$).

Remark 2: Let $\bar{A}(z) = (z - 1/z_0^\star)B(z)$ the polynomial obtained by "reflecting" z_0 with respect to the unit circle, and let $\bar{\mathbf{a}}$ be the corresponding prediction vector. Then, it is easy to show that

$$J(\mathbf{a}) - |z_0|^2 J(\bar{\mathbf{a}}) = (|z_0|^2 - 1)\boldsymbol{\beta}^\dagger \Delta \boldsymbol{\beta}. \tag{8}$$

This provides a simple alternative to (7) to conclude that $\hat{A}$ has no roots outside the unit circle, but it does not prove that the roots are *strictly* interior.

Remark 3: The condition $M > 0$ is clearly too restrictive: Positivity of $\boldsymbol{\alpha}^\dagger M \boldsymbol{\alpha}$ could be required for "innovation-type" vectors $\boldsymbol{\alpha} = [1 \mid -\mathbf{a}^\mathbf{t}]^\mathbf{t}$ only. On the other hand, $\Delta \geq 0$ depends on the value of the upperleft entry ρ, whereas the estimate $\hat{\mathbf{a}} = (\overline{M})^{-1}\mathbf{r}$ does not depend on it. Actually, it can be shown that the conditions of Theorem 1 can be relaxed under the following form: $\overline{M} > 0$ and $\widetilde{\Delta} \geq 0$, where $\widetilde{\Delta} = \Delta$, save that $\mathbf{r}^\dagger \hat{\mathbf{a}}$ is the upper-left entry of $\widetilde{\Delta}$. Yet, such broader conditions are not necessary, whereas they do not enjoy the same simplicity as the original conditions of Theorem 1.

Example 1—Toeplitz Case: If matrix M is Toeplitz, then $\Delta = 0$, and (8) boils down to the simpler form $J(\mathbf{a}) = |z_0|^2 J(\mathring{\mathbf{a}})$. It is interesting to notice that in the given covariance case, the latter relation has a direct counterpart in terms of mean-squared prediction error, which classically ensures the stability of the prediction error filter [3].

Example 2—Diagonal Case: If matrix M is diagonal, the conditions of Theorem 1 are fulfilled for any increasing series of positive diagonal coefficients. This is a trivial example of a non-Toeplitz canonical matrix.

Example 3—Mixed Case: It is easy to check that the set of canonical matrices forms a convex cone. As a consequence, a positive definite Toeplitz matrix whose diagonal entries are augmented by any increasing positive sequence remains canonical.

Viewed as new possibilities of testing stability, the conditions of Theorem 1 or the broader conditions of Remark 3 are only of moderate interest since testing the positivity of a matrix is not simpler than directly testing the stability of the estimated predictor with a standard stability test. Moreover, such conditions are only sufficient, and they are mainly restricted to normal equation approaches. Nonetheless, they provide a new tool for the study of *structural stability* for some prediction methods, as shown in the following section.

III. Application to Least Squares Prediction Estimation Methods

A. Basic Cases

The most classical least squares prediction estimation methods correspond to quadratic forms $J(\mathbf{a}) = \|X\boldsymbol{\alpha}\|^2$. By construction, the normal matrix $M = X^\dagger X$ is positive semidefinite, and the data matrix X differs according to the windowing assumption. The four classical cases correspond to the *autocorrelation method* (AC), the *post-windowed* method (POST), the *covariance method* (COV), and the *prewindowed method* (PRE) [5]. Simple calculations yield, respectively

$$\begin{cases} \Delta^{\mathrm{AC}} = \mathbf{0} \\ \Delta^{\mathrm{POST}} = \mathbf{x}_P^\star \mathbf{x}_P^\mathbf{t} \\ \Delta^{\mathrm{COV}} = \mathbf{x}_P^\star \mathbf{x}_P^\mathbf{t} - \mathbf{x}_N^\star \mathbf{x}_N^\mathbf{t} \\ \Delta^{\mathrm{PRE}} = -\mathbf{x}_N^\star \mathbf{x}_N^\mathbf{t} \end{cases}$$

where $\mathbf{x}_n \triangleq [x_n, \ldots, x_{n-P+1}]^\mathbf{t}$. Obviously, matrix M^{AC} is canonical; given Remark 1, M^{POST} is also canonical if $\mathbf{x}_P \neq \mathbf{0}$. On the other hand, neither M^{COV} nor M^{PRE} are canonical (unless $\mathbf{x}_N = \alpha \mathbf{x}_P$, with $|\alpha| \leq 1$, or $\mathbf{x}_P = \mathbf{0}$, respectively). In fact, the existence of counterexamples shows that the covariance and the prewindowed methods are not structurally stable [5].

B. Regularized Methods

Kitagawa and Gersch [6] have proposed a *smoothness priors long autoregressive method*, which is based on a penalized least squares

criterion based on the prewindowed approach

$$J_{\mathrm{KG}}^{\mathrm{PRE}}(\mathbf{a}) = \boldsymbol{\alpha}^{\dagger} M^{\mathrm{PRE}} \boldsymbol{\alpha} + \lambda \sum_{p=1}^{P} p^{2k} a_p^2 \tag{9}$$

where λ is a regularization parameter, and k is the so-called *smoothness order*. The justification stems from the Parseval's relation [6]

$$\int_{-1/2}^{1/2} \left| \frac{d^k A(e^{2i\pi f})}{df^k} \right|^2 df = (2\pi)^{2k} \sum_{p=1}^{P} p^{2k} a_p^2.$$

Criterion (9) can be put into the form of (1), which yields

$$M_{\mathrm{KG}}^{\mathrm{PRE}} = M^{\mathrm{PRE}} + \lambda \operatorname{diag}\{p^{2k}\}_{p=0,\ldots,P}.$$

The same regularization technique applies to the other windowing alternatives. In particular, the regularized form of the autocorrelation method has been studied in [8] in the context of Doppler spectral analysis. Since the associated NEM $M_{\mathrm{KG}}^{\mathrm{COV}}$ has the mixed structure of Example 3, we can conclude that the *regularized autocorrelation method* is structurally stable for any smoothness order $k \geq 0$ and any $\lambda \geq 0$. Furthermore, it remains stable if the penalizing term incorporates several terms corresponding to different smoothness orders. Finally, the smoothness order need not be restricted to entire values. For instance, the canonical matrix obtained for $k = 1/2$ has a null second-order displacement rank [7], which is a potentially interesting property with a view to fast inversion.

The following corollary shows that the original regularized prewindowed method of Kitagawa and Gersch becomes structurally stable beyond a certain level of regularization. Similar results can be derived for the regularized versions of the covariance and modified covariance methods.

Corollary 1: For any $k > 0$, $M_{\mathrm{KG}}^{\mathrm{PRE}}$ is canonical if $\lambda > \sum_{p=1}^{P} |x_{N+1-p}|^2/(p^{2k} - (p-1)^{2k})$.

Proof: Matrix $M_{\mathrm{KG}}^{\mathrm{PRE}}$ is positive definite. Its displacement matrix reads $\Delta_{\mathrm{KG}}^{\mathrm{PRE}} = \lambda D - \mathbf{x}_N^{\star}\mathbf{x}_N^{\mathbf{t}}$, with $D \triangleq \operatorname{diag}\{p^{2k} - (p-1)^{2k}\}_{p=1,\ldots,P}$. From [9, Th. 32, p. 45]

$$\det \Delta_{\mathrm{KG}}^{\mathrm{PRE}} = \lambda^p \left(1 - \lambda^{-1}\mathbf{x}_N^{\star} D^{-1} \mathbf{x}_N^{\mathbf{t}}\right) \prod_{1}^{P} (p^{2k} - (p-1)^{2k})$$

and it is apparent that the condition $\lambda \geq \mathbf{x}_N^{\star} D^{-1} \mathbf{x}_N^{\mathbf{t}}$ is necessary to the positive semidefiniteness of $\Delta_{\mathrm{KG}}^{\mathrm{PRE}}$. Actually, it is also sufficient since the $P-1$ other conditions that express the positivity of the minors are similar but less restrictive than $\det \Delta_{\mathrm{KG}}^{\mathrm{PRE}} \geq 0$. □

The particular case $k = 0$ provides a method that has been proposed *per se* in the context of *linear minimum free energy estimation* by Silverstein [10]. It basically reduces to adding a positive constant λ to the main diagonal of the NEM. Obviously, the autocorrelation version is still canonical since the NEM remains Toeplitz, positive definite. On the other hand, the case $k = 0$ is excluded from the canonicity condition of Corollary 1. Yet, it is intuitive that such a method becomes structurally stable for large values of λ. This is actually so, since, from the sufficient condition of stability $\|\hat{\mathbf{a}}\| < 1/P$ [2], it is possible to deduce that $\lambda > \|\mathbf{r}\|\sqrt{P}$ ensures that $\hat{\mathbf{a}}$ defines a stable prediction filter.

C. Adaptive Versions

In order to extend least squares prediction methods to adaptative contexts, the normal approach is to reweight the successive terms of the criterion according to a forgetting factor. The resulting NEM reads $M = X^{\dagger}\Gamma X$, where Γ is a diagonal matrix with geometrically increasing positive entries on its main diagonal. For instance, let us define $\Gamma_{\gamma}^{\mathrm{AC}} = \operatorname{diag}\{\gamma^{N-k}\}_{k=1,\ldots,N+P}$ in the autocorrelation case and $\Gamma_{\gamma}^{\mathrm{COV}} = \operatorname{diag}\{\gamma^{N-k}\}_{k=P,\ldots,N-1}$ in the covariance case, with $0 < \gamma \leq 1$. Then, we can deduce

$$\Delta_{\gamma}^{\mathrm{AC}} = (1-\gamma)\underline{M}]^{\mathrm{AC}} \tag{10a}$$

$$\Delta_{\gamma}^{\mathrm{COV}} = (1-\gamma)\underline{M}]^{\mathrm{COV}} + \gamma^{N-P}\mathbf{x}_P^{\star}\mathbf{x}_P^{\mathbf{t}} - \mathbf{x}_N^{\star}\mathbf{x}_N^{\mathbf{t}}. \tag{10b}$$

As a consequence, structural stability is preserved by the adaptative version of the autocorrelation method. In the same way, this could be shown for the adaptative postwindowed method. On the other hand, the adaptative version of the covariance method is not guaranteed to be structurally stable. However, from (10b), it becomes stable if γ is chosen such as

$$(1-\gamma)\mathbf{x}_N^{\dagger}\underline{M}]^{\mathrm{COV}}\mathbf{x}_N + \gamma^{N-P}\left|\mathbf{x}_N^{\mathbf{t}}\mathbf{x}_P\right|^2 > \left|\mathbf{x}_N^{\mathbf{t}}\mathbf{x}_N\right|^2.$$

IV. Conclusion

In the framework of least squares prediction in the given data case, the estimated prediction vector $\hat{\mathbf{a}}$ is the solution of a normal equation. In order to compute $\hat{\mathbf{a}}$, it is a classical result that the complexity of the appropriate generalized Levinson algorithm linearly increases with respect to the distance of the normal equation matrix to Toeplitz, i.e., the rank of the displacement matrix [7]. In this paper, we have shown that the positive definiteness of the displacement matrix ensures that the estimated prediction filter is stable (provided that the normal equation matrix is also positive definite). This result provides a unifying sufficient condition that proves that some classical least squares prediction methods are structurally stable: the autocorrelation method, the postwindowed method, and the autocorrelation version of the regularized method proposed by [6]. It also provides a simple lower bound on the regularization parameter for the original (prewindowed) version to be structurally stable.

References

[1] Y. Bistritz, "Zero location with respect to the unit circle of discrete-time linear system polynomials," *Proc. IEEE*, vol. 72, pp. 1131–1142, Sept. 1984.

[2] B. Picinbono and M. Benidir, "Some properties of lattice autoregressive filters," *IEEE Trans. Acoust., Speech, Signal Processing*, vol. ASSP-34, pp. 342–349, Apr. 1986.

[3] S. Lang and J. McClellan, "A simple proof of stability for all-pole linear prediction model," *Proc. IEEE*, vol. 67, pp. 860–861, May 1979.

[4] B. Friedlander, "Lattice filters for adaptative processing," *Proc. IEEE*, vol. 70, pp. 829–867, Aug. 1982.

[5] S. M. Kay and S. L. Marple, "Spectrum analysis—A modern perpective," *Proc. IEEE*, vol. 69, pp. 1380–1419, Nov. 1981.

[6] G. Kitagawa and W. Gersch, "A smoothness priors long AR model method for spectral estimation," *IEEE Trans. Automat. Contr.*, vol. AC-30, pp. 57–65, Jan. 1985.

[7] B. Friedlander, M. Morf, T. Kailath, and L. Ljung, "New inversion formulas for matrices classified in terms of their distances from Toeplitz matrices," *Linear Algebra Appl.*, vol. 27, pp. 31–60, 1979.

[8] J.-F. Giovannelli, A. Herment, and G. Demoment, "A Bayesian method for long AR spectral estimation: A comparative study," *IEEE Trans. Ultrason. Ferroelect., Freq. Contr.*, vol. 43, pp. 220–233, Mar. 1996.

[9] P. Lascaux and R. Theodor, *Analyse Numérique Matricielle Appliquée à l'Art de l'Ingénieur*. Paris, France: Masson, 1986, vol. 1.

[10] S. D. Silverstein, "Linear minimum free energy estimation: A computationally efficient noise suppression spectral estimation algorithm," *IEEE Trans. Signal Processing*, vol. 39, pp. 1348–1359, June 1991.

J.-F. Giovannelli et J. Idier, « Bayesian interpretation of periodograms », *IEEE Trans. Signal Processing*, vol. 49, n°7, pp. 1988–1996, juillet 2001.

1388 IEEE TRANSACTIONS ON SIGNAL PROCESSING, VOL. 49, NO. 7, JULY 2001

Bayesian Interpretation of Periodograms

Jean-François Giovannelli and Jérôme Idier

***Abstract*—The usual nonparametric approach to spectral analysis is revisited within the regularization framework. Both usual and windowed periodograms are obtained as the squared modulus of the minimizer of regularized least squares criteria. Then, particular attention is paid to their interpretation within the Bayesian statistical framework. Finally, the question of unsupervised hyperparameter and window selection is addressed. It is shown that maximum likelihood solution is both formally achievable and practically useful.**

***Index Terms*—Hyperparameters, penalized criterion, periodograms, quadratic regularization, spectral analysis, windowing, window selection, zero-padding.**

NOMENCLATURE

FT	Fourier transform.
IFT	Inverse Fourier transform.
CFT	Continuous frequency.
DF	Discrete frequency.
UP	Usual periodogram.
WP	Windowed periodogram.
L^2	$L^2_{\mathbb{C}}([0,1])$.
H^Q	$H^Q_{\mathbb{C}}([0,1])$.
ℓ^2	$\ell^2_{\mathbb{C}}(\mathbb{Z})$
$\mathcal{F}$	Discrete time FT ($\ell^2 \to L^2$).
$\mathcal{W}_N$	Truncated IFT ($L^2 \to \mathbb{C}^N$).
$\mathcal{W}_N^\dagger$	Adjoint operator of $\mathcal{W}_N$.
F_P	Square Fourier matrix ($\mathbb{C}^P \to \mathbb{C}^P$).
W_{NP}	Truncated IFT matrix ($\mathbb{C}^P \to \mathbb{C}^N, N \leq P$).
$W_{NP}^\dagger$	Hermitian matrix of W_{NP}.
$\mathbb{N}_N$	$\{0,1,\ldots,N-1\}$.

I. INTRODUCTION

SPECTRAL analysis is a fundamental problem in signal processing. Historical papers such as [1], tutorials such as [2] and books such as [3] and [4] are evidence of the basic role of spectral analysis, whether it is parametric or not.

The nonparametric approach has recently prompted renewed interest [5] (see also [6]) within the regularization framework, and the present contribution brings a new look at these methods. It provides statistical principles rather than empirical ones in order to derive periodogram estimators. From this standpoint, the major contribution of the paper is twofold. First, it proposes new coherent interpretations of existing periodograms and modern justification for windowing techniques. Second, it introduces a maximum likelihood method for automatic selection of the window shape.

Moreover, [5] suffers from a twofold limitation. On the one hand, the proposed model relies on the discrete frequency, whereas the frequency is a continuous variable. On the other hand, restriction to separable regularization functions does not allow spectral smoothness to be accounted for. The present contribution overcomes such limitations.

It takes advantage of a natural model in spectral analysis of complex discrete-time series: the sum of side-by-side pure frequencies. Two cases are investigated.

1) the continuous frequency (CF) case, which relies on an infinite number of pure frequencies $\nu \in [0,1[$ with amplitudes $a(\nu), a \in L^2$;
2) the discrete frequency (DF) one, which relies on a finite number, say P (usually large), of equally spaced pure frequencies $\nu = p/P$, with amplitudes a_p. Let us note that $\boldsymbol{a} = [a_0,\ldots,a_{P-1}] \in \mathbb{C}^P$, and $\boldsymbol{\nu} = [\nu_0,\ldots,\nu_{P-1}] \in [0,1[^P$.

For N complex observed samples $\boldsymbol{y} = [y_0,\ldots,y_{N-1}] \in \mathbb{C}^N$, such models read

$$\begin{aligned} \text{CF: } y_n &= \int_0^1 a(\nu) e^{2i\pi\nu n} d\nu + b_n \\ \text{DF: } y_n &= P^{-1/2} \sum_{p=0}^{P-1} a_p e^{2i\pi pn/P} + b_n \end{aligned} \tag{1}$$

where $\boldsymbol{b} = [b_0,\ldots,b_{N-1}] \in \mathbb{C}^N$ accounts for model and observation uncertainties. Let us introduce $\mathcal{W}_N$ and W_{NP}:

$$\begin{aligned} &\text{CF: } \mathcal{W}_N : L^2 \longrightarrow \mathbb{C}^N \\ &\text{DF: } W_{NP} : \mathbb{C}^P \longrightarrow \mathbb{C}^N \end{aligned} \tag{2}$$

the CF and DF truncated IFT so that

$$\begin{aligned} &\text{CF: } \boldsymbol{y} = \mathcal{W}_N a + \boldsymbol{b} \\ &\text{DF: } \boldsymbol{y} = W_{NP}\boldsymbol{a} + \boldsymbol{b}. \end{aligned} \tag{3}$$

The current problem consists in estimating the amplitudes a and/or $\boldsymbol{a}$. Thanks to the linearity of these models w.r.t. the amplitudes, the problem clearly falls in the class of linear estimation problems [7]–[9]. However, in practice, estimation relies on a finite, maybe small, number of data N. As a consequence, in the CF case, a continuous frequency function a lying in L^2 must be selected from only N data. Such a problem is known to be ill-posed in the sense of Hadamard [8]. In the same way, under the DF formulation, since the amplitudes outnumber the available data, the problem is underdeterminate.

This kind of problem is nowadays well identified [8], [10] and can be fruitfully tackled by means of the regularization

Manuscript received October 24, 2000; revised March 7, 2001. The associate editor coordinating the review of this paper and approving it for publication was Prof. Jian Li.

The authors are with the Laboratoire des Signaux et Systèmes SUPÉLEC, Gif-sur-Yvette, France (emaux: giova@lss.supelec.fr; idier@lss.supelec.fr).

Publisher Item Identifier S 1053-587X(01)05353-3.

approach. This approach rests on a compromise between fidelity to the data and fidelity to some prior information about the solution. As mentioned above, such an idea has already been introduced in several papers [5], [11]–[14]. In the autoregressive spectral estimation problem, [11] proposes to account for spectral smoothness as a function of autoregressive coefficients. Otherwise, high-resolution spectral estimation has been addressed within the regularization framework, founded on the Poisson-Gaussian model [14]. The present paper deepens Gaussian models and is organized as follows.

Section II focuses on the interpretation of usual periodograms (UPs), and Section III deals with the interpretation of windowed periodograms (WPs), both using penalized approaches with quadratic regularization. Results are exposed in four propositions, and the corresponding proofs are given in Appendix A. A Bayesian interpretation is presented in Section IV, whereas the problem of parameter estimation and window selection are addressed in Section V. Finally, conclusions and perspectives for future works are presented in Section VI.

II. Usual Periodogram

A. Continuous Frequency

The problem at stake consists of estimating $a \in L^2$ given data $\boldsymbol{y}$ such that (3). A first possible approach is founded on the least squares (LS) criterion

$$(\boldsymbol{y} - \mathcal{W}_N a)^\dagger (\boldsymbol{y} - \mathcal{W}_N a) = \sum_{n=0}^{N-1} \left| y_n - \int_0^1 a(\nu) e^{2i\pi\nu n} d\nu \right|^2$$

but since $\mathcal{W}_N$ is one-to-many and not many-to-one, there exists an infinity of solutions in L^2. Here, the preferred solution for raising the indetermination relies on regularized least squares (RLS). The simplest RLS criterion is founded on quadratic "separable regularization"

$$\mathcal{Q}_u(a) = (\boldsymbol{y} - \mathcal{W}_N a)^\dagger (\boldsymbol{y} - \mathcal{W}_N a) + \lambda \int_0^1 |a(\nu)|^2 d\nu \quad (4)$$

where "u" stands for usual. The regularization parameter $\lambda \geq 0$ balances the tradeoff between confidence in the data and confidence in the penalization term. For any $\lambda > 0$, the proposition below gives the minimizer $\hat{a}^\lambda$ of (4).

Proposition 1 (CF/UP): For any $\lambda > 0$, the unique minimizer of (4) reads

$$\hat{a}^\lambda(\nu) = (1+\lambda)^{-1} \sum_{n=0}^{N-1} y_n e^{-2i\pi\nu n}. \quad (5)$$

■

Proof: See Appendix A.

B. Discrete Frequency

This subsection investigates the DF counterpart of the previous result. In the DF approach, the LS criterion reads

$$(\boldsymbol{y} - W_{NP}\boldsymbol{a})^\dagger (\boldsymbol{y} - W_{NP}\boldsymbol{a}) \quad (6)$$

but since W_{NP} is one-to-many and not many-to-one, there also exists an infinity of solutions in $\mathbb{C}^P$. According to the quadratic "separable regularization," the corresponding RLS criterion is

$$Q_u(\boldsymbol{a}) = (\boldsymbol{y} - W_{NP}\boldsymbol{a})^\dagger (\boldsymbol{y} - W_{NP}\boldsymbol{a}) + \lambda \boldsymbol{a}^\dagger \boldsymbol{a} \quad (7)$$

with optimum given in the next proposition.

Proposition 2—(DF/UP): For any $\lambda > 0$, the unique minimizer of (7) reads

$$\hat{\boldsymbol{a}}^\lambda = (1+\lambda)^{-1} F_P \tilde{\boldsymbol{y}}_P \quad (8)$$

where $\tilde{\boldsymbol{y}}p$ denotes the vector $\boldsymbol{y}$ zero-padded up to size P. ■

Proof: See Appendix A.

C. Usual Periodogram: Concluding Remarks

In the CF cases, the squared modulus of the penalized solutions $|\hat{a}^\lambda(\nu)|^2$ is proportional to the usual zero-padded periodogram. Moreover, $|\hat{a}^\lambda|^2$ is[1] a discretized version of $|\hat{a}^\lambda(\nu)|^2$ over the frequency grid $\boldsymbol{\nu}$. Therefore, within the proposed framework, *separable quadratic regularization* leads to the *usual zero-padding* technique associated with the practical computation of periodograms. Moreover, when λ tends to zero, the proportionality factor tends to one. It is noticeable that in this case, the criteria (4) and (7) degenerate, but their minimizer does not. They are the solution of the constraint problems

$$\text{CF: } \min_{a \in L^2} \int_0^1 |a(\nu)|^2 d\nu \text{ s.t. } \boldsymbol{y} = \mathcal{W}_N a$$
$$\text{DF: } \min_{\boldsymbol{a} \in \mathbb{C}^P} \boldsymbol{a}^\dagger \boldsymbol{a} \qquad \text{s.t. } \boldsymbol{y} = W_{NP}\boldsymbol{a}$$

i.e., solution of the noiseless problems adressed in [5] and [6].

III. Windowed Periodogram

The previous section investigates the relationships between the separable regularizers and the usual (nonwindowed) periodograms. The present section focuses on smoothing regularizers and windowed periodograms (see [15], which analyzes dozens of windows to compute smoothed periodograms).

A. Continuous Spectra

This subsection generalizes the usual norm in L^2 to the Sobolev [16] regularizer

$$\mathcal{R}_Q(a) = \int_0^1 \sum_{q=0}^{Q} \alpha_q \left| \frac{d^q a}{d\nu^q}(\nu) \right|^2 d\nu$$

which can be interpreted as a measure of spectral smoothness. The α_q are positive real coefficients and can be generalized to positive real functions [8]. $\mathcal{R}_Q$ is defined onto the Sobolev space [16] $H^Q \subset L^2$. Note that $H^0 = L^2$ and that the usual norm invoked in Section II-A is the regularizer $\mathcal{R}_0$ with $\alpha_0 = 1$.

Remark 1: Strictly speaking, $\mathcal{R}_Q(a)$ is not a spectral smoothness measure since it is not a function of $|a(\nu)|$ but a function of $a(\nu)$, including phase. A true spectral smoothness measure does not depend on the phase of $a(\nu)$ and does not yield a quadratic criterion. The same remark holds for the definition of spectral smoothness proposed by Kitagawa and Gersh [11].

[1] If $u \in \mathbb{C}^P$, $|u|^2$ denotes the vector of the squared moduli of the component of u.

Accounting for spectral smoothness by means of $\mathcal{R}_Q(a)$ yields a new penalized criterion

$$\mathcal{Q}_s(a) = (\boldsymbol{y} - \mathcal{W}_N a)^\dagger (\boldsymbol{y} - \mathcal{W}_N a) + \lambda \mathcal{R}_Q(a) \tag{9}$$

where the index "s" stands for smoothness.

Proposition 3—(CF/WP): With the previous notations and definitions, the minimizer of (9) reads

$$\hat{a}^\omega(\nu) = \sum_{n=0}^{N-1} \omega_n y_n e^{-2i\pi\nu n} \tag{10}$$

i.e., a windowed FT. The window shape is

$$\omega_n = (1 + \lambda \varepsilon_n)^{-1} \tag{11}$$

$$\text{with } \varepsilon_p = \sum_{q=0}^{Q} \alpha_q (2\pi p)^{2q} \text{ for } p \in \mathbb{Z}. \tag{12}$$

Proof: See Appendix A. ■

B. Discretized Spectra

This subsection is devoted to the generalization of criterion (7) to nonseparable penalization

$$Q_s(\boldsymbol{a}) = (\boldsymbol{y} - W_{NP}\boldsymbol{a})^\dagger (\boldsymbol{y} - W_{NP}\boldsymbol{a}) + \lambda \boldsymbol{a}^\dagger \Pi_a \boldsymbol{a}. \tag{13}$$

Given that the sought spectrum is circular periodic, the penalization term has to be designed under circularity constraint. As a consequence, Π_a is a circular matrix, and its eigenvalues, denoted $e_p, p \in \mathbb{N}_p$, can be calculated as the FT of the first row of Π_a. Moreover, without loss of generality, we assume that the diagonal elements of Π_a^{-1} are equal to one, and any scaling factor is integrated in the parameter λ.

Proposition 4—(DF/WP): The minimizer of (13) reads

$$\hat{\boldsymbol{a}}^w = F_P \breve{\boldsymbol{y}} \tag{14}$$

where the $\breve{\boldsymbol{y}}_p = w_p \tilde{y}_p$ for $p \in \mathbb{N}_P$ and

$$w_p = (1 + \lambda e_p)^{-1}.$$

Proof: See Appendix A ■

C. Windowed Periodograms: Concluding Remarks

Hence, in the CF case, the squared modulus of the penalized solution $\hat{a}^\omega$ is the windowed periodogram associated with window ω_n. Moreover, the DF solution $\hat{a}^\omega$ is a discretized version of $\hat{a}^\omega$ as soon as the e_n are identified with the ε_n. As a conclusion, *quadratic smoothing regularizers* interpret *windowed periodograms*. Moreover, it is noteworthy that $\hat{a}^\omega(\nu)$ and $\hat{a}^\omega$ only depend on e_n and ε_n for $n \in \mathbb{N}_N$.

Remark 2—Empirical Power: One can easily show that

$$\begin{aligned} \text{CF: } \int_0^1 |a(\nu)|^2 d\nu &= \sum_{n=0}^{N-1} \omega_n^2 |y_n|^2 \\ \text{DF: } \boldsymbol{a}^\dagger \boldsymbol{a} &= \sum_{n=0}^{N-1} w_n^2 |y_n|^2. \end{aligned} \tag{15}$$

Hence, the empirical power of the estimated spectra is smaller than the empirical power of the observed data, and equality holds if and only if $\lambda = 0$.

Example 1—Zero-Order Penalization: The most simple example consists in retrieving the nonwindowed case of Section II-A and B. Let us apply the previous Propositions 3 and 4 with regularizers

$$\begin{aligned} &\text{CF: } \int_0^1 |a(\nu)|^2 d\nu && \text{i.e., } Q = 0 \text{ and } \alpha_0 = 1 \\ &\text{DF: } \boldsymbol{a}^\dagger \boldsymbol{a} && \text{i.e., } \Pi_a = I_P. \end{aligned} \tag{16}$$

Then, we have $\varepsilon_n = e_n = 1$; the criteria (9) and (13), respectively, become (4) and (7), and the solutions (10) and (14), respectively, become (5) and (8). As expected, the nonwindowed solutions are retrieved. A more interesting example is the one given below.

Example 2—First-Order Penalization: Let the penalization term be

$$\begin{aligned} &\text{CF: } \int_0^1 |a'(\nu)|^2 d\nu \\ &\text{DF: } \frac{1}{2} P^2 \sum_{k=0}^{P} |a_k - a_{k-1}|^2 \end{aligned} \tag{17}$$

with $a_P = a_0$ for notational convenience of the circularity assumption. Application of Propositions 3 and 4, respectively, yields $\varepsilon_n = 4\pi^2 n^2$ (CF case) and $e_n = (1 - \cos 2\pi n/P)$ (DF case). The corresponding windows read

$$\begin{aligned} &\text{CF: } \omega_n = (1 + 4\pi^2 n^2 \lambda)^{-1} \\ &\text{DF: } w_n = (1 + \lambda - \lambda \cos 2\pi n/P)^{-1}. \end{aligned} \tag{18}$$

In the following, we refer to them as the Cauchy and the inverse cosine windows. Moreover, for a finer discretization of the spectral domain, $\lim_{P\to\infty} e_n = \varepsilon_n$, and one can retrieve the Cauchy window as the limit of the inverse cosine window (see Figs. 1 and 2).

IV. Bayesian Interpretation

This section is devoted to Bayesian interpretations of the penalized solutions presented in Propositions 1, 2, 3, and 4. Moreover, since usual nonwindowed forms are particular cases of windowed forms, we focus on the latter.

Since the considered criteria are quadratic, their Bayesian interpretations rely on Gaussian laws. Therefore, the Bayesian interpretations only require the characterization of means and correlation structures for the stochastic models at work.

A. Discrete Frequency Approach

In the DF case, i.e., in the finite dimension vector space, the Bayesian interpretation of the criteria (7) and (13) as a *posterior* co-log-likelihood is a classical result [10]. Within this probabilistic framework, the likelihood of the parameters $\boldsymbol{a}$ attached to the data $\boldsymbol{y}$ is

$$f(\boldsymbol{y}|\boldsymbol{a}) = (\pi r_b)^{-N} \exp \frac{-1}{r_b} (\boldsymbol{y} - W_{NP}\boldsymbol{a})^\dagger (\boldsymbol{y} - W_{NP}\boldsymbol{a}).$$

From a statistical viewpoint, it essentially results from the linearity of the model (3) and from the hypothesis of a zero-mean, circular (in the statistical sense), stationary, white, and Gaussian noise vector $\boldsymbol{b}$, with variance r_b.

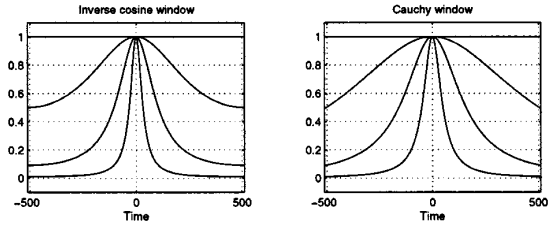

Fig. 1. Inverse cosine (lhs) and Cauchy windows (rhs) as a function of λ. In both cases, $\lambda = 0$ yields a constant shape. Furthermore, for any $\lambda\omega_0 = \omega_0 = 1$. Otherwise, as λ increases, the window shape decreases faster to zero, and the corresponding spectrum is smoothed.

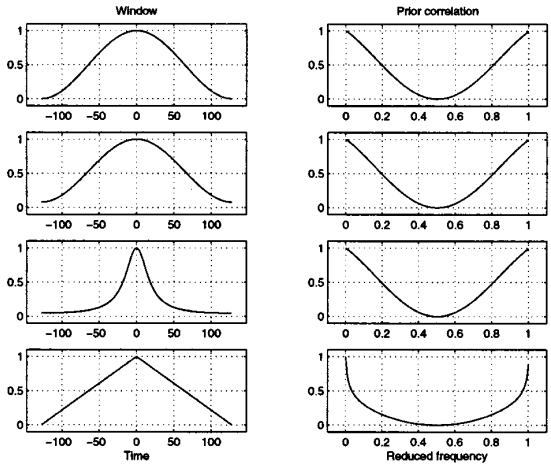

Fig. 2. Usual windows and the corresponding correlations. The lhs column shows the time window, and the rhs column shows the associated correlations. From top to bottom: the Hamming, the Hanning, the inverse cosine, and the triangular.

Moreover, in order to interpret the regularization term of (13), a zero-mean, circular, correlated Gaussian prior with covariance $R_a = r_a \Pi_a^{-1}$ is introduced.[2] Matrix Π_a^{-1} is the normalized covariance structure, i.e., all its diagonal elements are equal to 1, whereas r_a stands for the prior power. Therefore, the prior density reads

$$f(\boldsymbol{a}) = (\pi r_a)^{-N} \det \Pi_a \exp \frac{-1}{r_a} \boldsymbol{a}^\dagger \Pi_a \boldsymbol{a}.$$

The Bayes rule ensures the fusion of the likelihood and the prior into the *posterior* density

$$f(\boldsymbol{a}|\boldsymbol{y}) \propto \exp \frac{-1}{r_b} Q_s(\boldsymbol{a})$$

where Q_s is given by (13). The regularization parameter λ is clearly $\lambda = r_b/r_a$.

Thus, we have a Bayesian interpretation of the criterion (13) related to windowed periodograms. Interpretation of the criterion (7) related to usual ones results from a white prior: $\Pi_a = I_P$. Finally, interpretations of the RLS solutions (8) and (14) themselves result from the choice of the maximum *a posterior* (MAP) as a punctual estimate. Moreover, thanks to the Gaussian character of *posterior* law, other basic Bayesian estimators such as *posterior* mean (PM) and marginal MAP (MMAP), are equal to the MAP solution itself.

[2]Rigorously speaking, this is possible only if Π_a is invertible.

B. Continuous Frequency Case

1) General Theory: In the CF case, the Bayesian interpretation is more subtle since it relies on continuous index stochastic processes. Indeed, no *posterior* likelihood for the parameter a is available. Therefore, there is no direct *posterior* interpretation of the criteria (4) and (9), nor is there MAP interpretation of the estimates (5) and (10). Roughly speaking, the *posterior* law vanishes everywhere. Nevertheless, there is a proper Bayesian interpretation of the estimates (5) and (10) as PM or MMAP, as shown below.

Let us introduce a zero-mean, circular (in the statistical sense) and Gaussian prior law [17] for a. This law is fully characterized by its correlation structure $\gamma_a(\nu), \nu \in [-1, 1]$, which is entirely described by its values for $\nu \in [0, 1]$ thanks to Hermitian symmetry. Furthermore, the usual circular-periodicity assumption for $a(\nu)$ results in another symmetry property: $\gamma_a(1/2 + \nu) = \gamma_a(1/2 - \nu)$ any $\nu \in [0, 1/2]$.

By assuming $\gamma_a \in L_2$, the latter can be expanded into a Fourier series

$$\gamma_a(\nu) = \sum_{p \in \mathbb{Z}} \overset{\circ}{\gamma}_a(p) e^{-2i\pi\nu p}, \quad \nu \in [0, 1]$$

with Fourier coefficients $\overset{\circ}{\gamma}_a \in \ell_2$ given by

$$\overset{\circ}{\gamma}_a(p) = \int_{[0,1]} \gamma_a(\nu) e^{-2i\pi\nu p}, \quad p \in \mathbb{Z}.$$

Let us note that $c_a(\nu) = \gamma_a(\nu)/r_a$ is the normalized correlation and that $\overset{\circ}{c}_a \in \ell_2$ is the corresponding Fourier sequence.

Proposition 5: With the previous notations and prior choice, the *posterior* mean of $a(\nu)$ is

$$E[a(\nu)|\boldsymbol{y}] = \hat{a}^\omega(\nu) = \sum_{n=0}^{N-1} \omega_n y_n e^{-2i\pi\nu n} \tag{19}$$

$$\text{with } \omega_n = [1 + \lambda \overset{\circ}{c}_a(n)^{-1}]^{-1}. \tag{20}$$

■

Proof: See Appendix A

Comparison of (19)–(20) and (10)–(11) immediately gives the Bayesian interpretation of windowed FT as PM[3] :$\overset{\circ}{c}_a(n) = \varepsilon_n^{-1}$, i.e., identification of the Fourier coefficients of the prior correlation $c_a(\nu)$ and the FT of the discrete correlation Π_a.

2) Example 3: The present subsection is devoted to a precise Bayesian interpretation of deterministic Examples 1 and 2. As we will see, there is a new obstacle in the Bayesian interpretation of these examples because the underlying correlations do not lie in L_2. In order to overcome this difficulty, we first interpret the penalization of both zero-order and first-order derivatives

$$\mathcal{R}_2(a) = \alpha_0 \int_0^1 |a(\nu)|^2 d\nu + \alpha_1 \int_0^1 |a'(\nu)|^2(\nu) d\nu. \tag{21}$$

The case of pure zero order and pure first order are obtained in Section IV-B.II.b and c as limit processes.

[3]Since $a(\nu) \mid y$ is a scalar Gaussian random variable, $E[a(\nu) \mid y]$ is also the MMAP.

As seen in Proposition 3, the associated coefficients are $\varepsilon_p = a_0 + 4\pi^2\alpha_1 p^2,\ p \in \mathbb{Z}$. According to Proposition 5, the Fourier series coefficients for $\gamma_a(\nu)$ are $\overset{\circ}{\gamma}_a(p) = \varepsilon_p^{-1}$. It is clear that $\overset{\circ}{\gamma} \in \ell_2$; hence, $\gamma_a \in L_2$ and

$$\gamma_a(\nu) = \sum_{p\in\mathbb{Z}} \frac{1}{\alpha_0 + 4\pi^2\alpha_1 p^2} e^{-2i\pi\nu p}, \quad \nu \in [0,1]. \tag{22}$$

It is shown in Appendix B that, with $\alpha = \sqrt{\alpha_0/\alpha_1}$ and $\alpha' = \sqrt{\alpha_0\alpha_1}$, $\gamma_a(\nu)$ reads

$$\gamma_a(\nu) = \frac{\cosh\alpha\,(|\nu| - 1/2)}{2\alpha'\sinh\alpha/2}, \quad \nu \in [-1,1] \tag{23}$$

and several analytic properties are straightforwardly deduced. In particular, γ_a has a continuous derivative over [-1,1]-{0}, and the slopes at $\nu = 0^-$ and $\nu = 0^+$ are, respectively, $1/\alpha_1$ and $-1/\alpha_1$. γ_a is minimum at $\nu = 1/2$ and maximum at $\nu = -1, \nu = 0$, and $\nu = 1$. Moreover, its integral from 0 to 1 remains constant and equals $1/\alpha_0$.

a) Markov Property: The present paragraph addresses the Markov property of the underlying prior process $a(\nu)$ [18], [19]. This process cannot be seen as a Markov chain since it is circular-periodic: "Future" frequency and "past" frequency cannot be independent. However, we show the Markov property for the conditional process $\bar{a}(\nu) = [a(\nu)|a(1)]_{\nu\in[0,1]}$. It is shown in Appendix B that its correlation structure reads

$$\gamma_{\bar{a}}(\nu,\nu') = \gamma_a(\nu-\nu') - \frac{\gamma_a(\nu)\gamma_a(\nu')}{\gamma_a(0)} \tag{24}$$

$$= \frac{\sinh\alpha\nu'\sinh\alpha(1-\nu)}{\alpha'\sinh\alpha} \tag{25}$$

for any $\nu,\nu' \in [0,1], \nu \geq \nu'$. According to the sufficient factorization of the correlation function proposed in [[20], p. 64], it turns out that $\bar{a}(\nu)$ is a Markov chain.

b) Limit Case as $\alpha_1 \to 0$: As α_1 tends to zero, it is easy to show that for each $\nu \in]0,1[$, the correlation $\gamma_a(\nu)$ tends to zero, i.e., there is no more correlation between $a(\nu_1)$ and $a(\nu_2)$ as soon as $\nu_1 \neq \nu_2$ and $(\nu_1,\nu_2) \neq (0,1)$. Moreover, $\gamma_a(0)$ and $\gamma_a(1)$ tend to infinity, whereas the integral of γ_a over [0,1] remains $1/\alpha_0$. Roughly speaking, the limit correlation is a Dirac distribution at $\nu = 0$ and $\nu = 1$ with weight $1/2\alpha_0$ i.e., the limit process is a circular white Gaussian noise with "pseudo-power" $1/\alpha_0$.

c) Limit Case as $\alpha_0 \to 0$: This case is more complex than the previous one since $\forall\nu \in [0,1], \gamma_a(\nu)$ tends to infinity as α_0 tends to zero. Therefore, we propose a characterization of the limit process *via* its increments. Let $\nu_1,\nu_2,\nu_1',\nu_2' \in [0,1], \nu_1 < \nu_2 < \nu_1' < \nu_2'$. Let us also note the frequency increments $\tau_\nu = \nu_2 - \nu_1$ and $\tau_\nu' = \nu_2' - \nu_1'$, and the vector of the increments themselves $i = [a(\nu_2) - a(\nu_1), a(\nu_4) - a(\nu_3)] \in \mathbb{C}^2$. This vector is clearly Gaussian and zero mean. Furthermore, it is shown in Appendix B that its covariance matrix reads

$$R_i = \frac{1}{2\alpha_1}\begin{bmatrix} \tau_\nu(1-\tau_\nu) & 2\tau_\nu\tau_\nu' \\ 2\tau_\nu\tau_\nu' & \tau_\nu'(1-\tau_\nu') \end{bmatrix}. \tag{26}$$

It turns out that the process $\tilde{a}(\nu) = a(\nu) - a(0)$ is a Brownian bridge [21, p. 36].

V. Hyperparameter and Window Slection

The problem of hyperparameter estimation within the regularization framework is a delicate one. It has been extensively studied, and numerous techniques have been proposed and compared [22]–[27]. The maximum likelihood (ML) approach is often chosen associated with the Bayesian interpretation. In the following subsections, we address regularization parameter estimation and automatic window selection using ML estimation.

A. Hyperparameters Estimation

In our context, the ML technique consists of integrating the amplitudes out of the problem and maximizing the resulting marginal likelihood w.r.t. the hyperparameters. Thanks to the linear and Gaussian assumptions, the marginal law for the data, namely, the likelihood function, is also Gaussian

$$f(\boldsymbol{y}; r_a, r_b) \propto (\det R_y)^{-1} \exp -\boldsymbol{y}^\dagger R_y^{-1}\boldsymbol{y}. \tag{27}$$

Moreover, the covariance structure R_y can be easily derived, as shown in the two following sections.

1) Discrete Frequency Marginal Covariance: In the present case, since all random quantities are in a finite dimensional linear space, the covariance is clearly

$$R_y = r_a(W_{NP}\Pi_a^{-1}W_{NP}^\dagger + \lambda I_N) = r_a\Sigma_y.$$

Accounting for the circular structure of the matrix Π_a, we have $\Pi_a = F_P\Lambda_\Pi F_P^\dagger$, where Λ_Π is the diagonal matrix of eigenvalues: $e_p, p \in \mathbb{N}_P$. Given the property (33) in Appendix B, Σ_y is shown to be diagonal

$$\Sigma_y = \mathrm{diag}[\lambda + e_n^{-1}], \quad n \in \mathbb{N}_N. \tag{28}$$

2) Continuous Frequency Marginal Covariance: In the present case, the marginal covariance matrix R_y has already been derived in (32) in Appendix A. Hence, R_y and Σ_y are diagonal:

$$\Sigma_y = \frac{1}{r_a}R_y = \mathrm{diag}[\lambda + \varepsilon_n^{-1}], \quad n \in \mathbb{N}_N. \tag{29}$$

Remark 3: In both cases, Σ_y only depends on e_n/ε_n for $n \in \mathbb{N}_N$. Consequently, the likelihood function and the ML parameter only depend on the N first coefficients.

3) Maximization: The opposite of the logarithm of the likelihood, namely, the co-log-likelihood (CLL)

$$\mathrm{CLL}(r_a,\lambda) = N\log r_a + \log\det\Sigma_y + \frac{1}{r_a}\boldsymbol{y}^\dagger\Sigma_y^{-1}\boldsymbol{y} \tag{30}$$

must be minimized w.r.t. r_a and λ. Partial minimization is tractable w.r.t. r_a and yields $\hat{r}_a = \boldsymbol{y}^\dagger\Sigma_y^{-1}\boldsymbol{y}/N$. Substitution of $\hat{r}_a$ in (30) gives

$$\mathrm{CLL}(\lambda) = \log\det\Sigma_y + N\log\boldsymbol{y}^\dagger\Sigma_y^{-1}\boldsymbol{y}. \tag{31}$$

Furthermore, since Σ_y is a diagonal matrix

$$\mathrm{CLL}(\lambda) = \sum_{n=1}^N \log(\lambda + e_n^{-1}) + N\log\sum_{n=1}^N \frac{|y_n|^2}{\lambda + e_n^{-1}}$$
$$= \log\left\{\prod_{n=1}^N(\lambda + e_n^{-1})\left[\sum_{n=1}^N \frac{|y_n|^2}{\lambda + e_n^{-1}}\right]^N\right\}$$

in the DF case. Substitution of e_n by ε_n yields the CF case. In both cases, CLL (λ) is the logarithm of the ratio of two degree $N-1$ polynomials of the variable λ with a strictly positive denominator. Minimization w.r.t. λ is not explicit, but it can be numerically performed.

4) Simulation Results: ML hyperparameter selection is illustrated for the problem of Section IV-B2. Computations have been performed on the basis of of 512 sample signals simulated by filtering standard Gaussian noises with the filter of impulse response $h = [1, -2, 3, -2, 1]$. Let us note that a^* as the true spectrum.

CLL has been computed on a (α_0, α_1)-grid of 100×100 logarithmically spaced values from 10^{-10} to 10^{10}. The first observation is that CLL is fairly regular and usually shows a unique minimum located between 10^{-1} and 10^{1} for α_0 and between 10^{-2} and 1 for α_1. However, a few "degenerated" cases have been observed for which $\hat{\alpha}_0^{ML}$ or $\hat{\alpha}_1^{ML}$ seem to be null or infinite. Let us note $\hat{\alpha}_0^{ML}$, $\hat{\alpha}_1^{ML}$ as the CLL minimizer[4] and $\hat{a}_{RLS}^{ML}$ as the corresponding RLS periodogram.

Since a^* is known in the proposed simulation study, various spectral distances [30] can be computed as functions of α_0 and α_1. L_1 distance, L_2 distance, the Itakura–Saito divergence (ISD) as well as the Itakura–Saito symmetric distance (SIS) have been considered. Each one provides an optimal couple $(\hat{\alpha}_0^{L_1}, \hat{\alpha}_1^{L_2}), (\hat{\alpha}_0^{L_2}, \hat{\alpha}_1^{L_2}), (\hat{\alpha}_0^{ISD}, \hat{\alpha}_1^{ISD})$, and $(\hat{\alpha}_0^{SIS}, \hat{\alpha}_1^{SIS})$, respectively. The corresponding spectra are, respectively, denoted $\hat{a}_{RLS}^{L_1}, \hat{a}_{RLS}^{ISD}$, and $\hat{a}_{RLS}^{SIS}$.

According to our experiments, as shown in Fig. 3, $\hat{a}_{RLS}^{L_2}, \hat{a}_{RLS}^{ISD}$, and the a^* can be graded by smoothness and estimation accuracy. From the smoothest to the roughest, the following gradation has always been observed: $\hat{a}_{RLS}^{L_2}, a^*$ and $\hat{a}_{RLS}^{ISD}$. Furthermore, $\hat{a}_{RLS}^{L_2}$ is systematically oversmoothed, whereas $\hat{a}_{RLS}^{ISD}$ is systematically undersmoothed. Moreover, the first one qualitatively approximates more precisely α^* in linear scale, whereas the second one reproduces more accurately α^* in a logarithmic scale and especially the two notches. This is due to the presence of the spectra ratio in the Itakura-Saito distance that emphasizes the small values of the spectra.

Finally, from our experience and as shown in Fig. 3, the maximum likelihood solution $\hat{a}_{RLS}^{ML}$ establishes a relevant compromise between $\hat{a}_{RLS}^{L_2}$ and $\hat{a}_{RLS}^{ISD}$ since it is smooth enough, whereas the two notches remain accurately described.

Quantitative comparisons have been conducted between the two practicable methods (when a^* is not known): the usual periodogram and the proposed method, i.e., the RLS solution with automatic ML hyperparameters. The obtained results are reported in Table I. They clearly show an improvement of about 40–50% for all the considered distances.

B. Window Selection

It has been shown that the ML technique allows the estimation of the regularization parameter. The problem of window selection is now addressed. Let us consider a set of K windows, i.e., K matrices Π_a^k for $k \in \mathbb{N}_K$. Index k becomes a new hyperparameter as well as λ and can be jointly estimated. The likelihood function (31) is now

$$\mathrm{CLL}(\lambda, k) = \log\det(\Sigma_y^k) + \log N \boldsymbol{y}^\dagger (\Sigma_y^k)^{-1} \boldsymbol{y}.$$

Maximization w.r.t. hyperparameters can be achieved in the same way as above for each value of $k \in \mathbb{N}_K$. The maximum maximorum can then be easily selected.

Numerous simulations have been performed. They are not reported here since they show similar results as the previous ones. However, it has been observed that the triangular window is the most often selected among Cauchy, inverse cosine, Hanning, Hamming, and triangle.

[4]Efficient algorithms are available in order to maximize the likelihood, such as gradient-based [28] or EM type [29]. They have not been implemented here as far as a mere feasibility study is concerned.

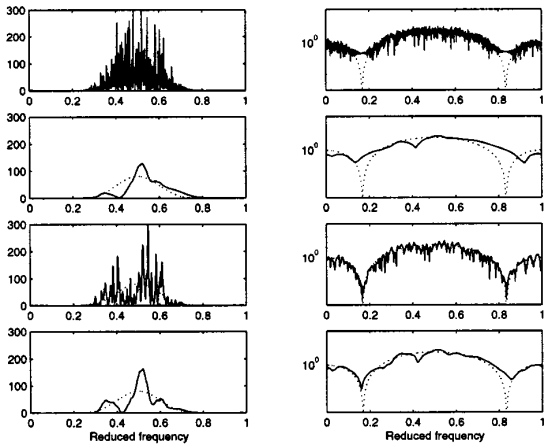

Fig. 3. Qualitative comparison. True spectra (dotted lines) and estimated ones (solid lines). The lhs column gives linear plots and the rhs column gives logarithmic plots. From top to bottom: Usual periodograms, $\hat{a}_{RLS}^{L_2}$, $\hat{a}_{RLS}^{ISD}$, and $\hat{a}_{RLS}^{ML}$.

TABLE I
QUANTITATIVE COMPARISON. THE FIRST LINE REFERS TO THE USUAL PERIODOGRAM, WHEREAS THE SECOND ONE REFERS TO THE RLS SOLUTION WITH ML HYPERPARAMETERS. THE THIRD LINE GIVES THE QUANTITATIVE IMPROVEMENT

	L_1	L_2	AIS	SIS
UP	0.766	1.14	751	750
RLS + ML	0.471	0.567	420	422
Gain	38.5%	50.3%	44.1%	43.8%

VI. CONCLUSION

In this paper, the usual nonparametric approach to spectral analysis has been revisited within the regularization framework. We have shown that usual and windowed periodograms could be obtained *via* the minimizer of regularized least squares criteria. In turn, penalized quadratic criteria are interpreted within the Bayesian framework so that periodograms are interpreted *via* Bayesian estimators. The corresponding prior is a zero-mean Gaussian process, fully specified by its correlation function. Particular attention is paid to the connection between correlation structure and window shape. With regard to *quadratic* regularization, the present study significantly deepens a recent contribution by Sacchi *et al.* [5], given that the latter addresses neither windowed periodograms, nor the continuous frequencial

setting. Extension to the *nonquadratic*[31] and two-dimensional (time–frequency) case would be of particular interest, and we are presently working on this issue.

Whereas the first part of our contribution provides interpretations of pre-existing tools for spectral analysis, new estimation schemes are derived in the second part: unsupervised hyperparameter and window selection. It is shown that maximum likelihood solutions are both formally achievable and practically useful.

Appendix A
Proof of Propositions

A. Proof of Proposition 1

Several proofs are available, and the proposed one relies on variational principles [32]. Application of these principles to quadratic regularization of linear problem yields the functional (8)

$$-2\mathcal{W}_N^\dagger(\boldsymbol{y}-\mathcal{W}_N a)+2\lambda I_{L^2}a=0$$

where I_{L^2} stands for the identity application from L^2 onto itself, and $\mathcal{W}_N^\dagger$ stands for the adjoint application of $\mathcal{W}_N$ (see Appendix B). After elementary algebra, we find

$$(\mathcal{W}_N^\dagger\mathcal{W}_N+\lambda I_{L^2})a=\mathcal{W}_N^\dagger\boldsymbol{y}.$$

As shown in Appendix B, $\mathcal{W}_N\mathcal{W}_N^\dagger=I_N$; then, taking the FT and, next, the IFT gives

$$\hat{a}^\lambda(\nu)=(1+\lambda)^{-1}\mathcal{W}_N^\dagger\boldsymbol{y}=(1+\lambda)^{-1}\sum_{n=0}^{N-1}y_n e^{-2i\pi\nu n}.$$

B. Proof of Proposition 2

The minimizer of the RLS criterion (7) obviously is

$$\hat{\boldsymbol{a}}^\lambda=\left(W_{NP}^\dagger W_{NP}+\lambda I_P\right)^{-1}W_{NP}^\dagger\boldsymbol{y}.$$

Refer to Appendix B for a detailed calculus required to analyze the normal matrix $(W_{NP}^\dagger W_{NP}+\lambda I_P)$. $W_{NP}^\dagger W_{NP}$ and I_P are circulant matrices, and this property also holds for their sum, which hence is diagonal in the Fourier basis. Elementary algebra leads to

$$\begin{aligned}\hat{\boldsymbol{a}}^\lambda=&F_P\begin{bmatrix}(1+\lambda)^{-1}I_N & O_{N,P-N}\\ O_{P-N,N} & \lambda^{-1}I_{P-N}\end{bmatrix}\begin{bmatrix}I_N\\ O_{P-N,N}\end{bmatrix}\boldsymbol{y}\\ =&(1+\lambda)^{-1}F_P\tilde{\boldsymbol{y}}_P.\end{aligned}$$

C. Proof of Proposition 3

The proof is founded on a time domain version of the criterion (9), resulting from application of the Plancherel–Parseval theorem to the successive derivatives of a

$$\int_0^1\left|\frac{d^q a}{d\nu^q}(\nu)\right|^2 d\nu=\sum_{n\in\mathbb{Z}}(2\pi n)^{2q}|z_n|^2$$

where $z_n=\int_0^1 a(\nu)e^{2i\pi\nu n}d\nu$. Summation w.r.t. q and inversion of summation w.r.t. q and w.r.t. n gives

$$R_Q(a)=\sum_{n\in\mathbb{Z}}e_n|z_n|^2$$

where the weighting coefficients e_p fulfill (12). Hence, the time domain counterpart of criterion (4) reads

$$\mathcal{Q}_s(a)=(\boldsymbol{y}-\boldsymbol{z})^\dagger(\boldsymbol{y}-\boldsymbol{z})+\lambda\sum_{n\in\mathbb{Z}}e_n|z_n|^2.$$

Thanks to separability, the solution is easily derived: $\hat{z}_n^\omega=(1+\lambda e_n)^{-1}y_n$ if $n\in\mathbb{N}_N$ and $\hat{z}_n^\omega=0$ elsewhere. a^ω is the Fourier transform of the sequence $\{\hat{z}_n^\omega\}_{n\in\mathbb{Z}}$

$$\hat{a}^\omega(\nu)=\sum_{n=0}^{N-1}\hat{z}_n^\omega e^{-2i\pi\nu n}.$$

D. Proof of Proposition 4

Elementary linear algebra provides the minimizer of (13)

$$\hat{\boldsymbol{a}}^\omega=\left(W_{NP}^\dagger W_{NP}+\lambda\Pi_a\right)^{-1}W_{NP}^\dagger\boldsymbol{y}.$$

Accounting for its circular structure, the Fourier basis diagonalizes Π_a

$$\Pi_a=F_P\Lambda_\Pi F_P^\dagger$$

where Λ_Π is the diagonal matrix of the eigenvalues $e_0,\ldots,e_{P-1}$ of Π_a. Hence

$$\hat{\boldsymbol{a}}^\omega=F_P(I_P+\lambda\Lambda_\Pi)\tilde{\boldsymbol{y}}_P$$

and we easily find

$$\hat{\boldsymbol{a}}^\omega=F_P\breve{\boldsymbol{y}}$$

with $\breve{y}_p=\omega_p\tilde{y}_p$ for $p\in\mathbb{N}_P$, i.e., the data vector windowed by

$$\omega_n=(1+\lambda e_n)^{-1}.$$

E. Proof of Proposition 5

Let $\nu_0\in[0,1]$ and $a_0=a(\nu_0)$. Thanks to the linearity of the model (3) and thanks to the Gaussian assumption for a and $\boldsymbol{b}$, the joint law of $(a_0,\boldsymbol{y})$ is also Gaussian. Hence, the random variable $(a_0|\boldsymbol{y})$ is clearly Gaussian, and it is well known that its mean reads

$$\mathrm{E}[a_0|\boldsymbol{y}]=R_{a_0y}R_y^{-1}\boldsymbol{y}$$

where $R_{a_0}y=\mathrm{E}a_0y^\dagger$, and $R_{\boldsymbol{y}}=\mathrm{E}[\boldsymbol{y}\boldsymbol{y}^\dagger]$. Elementary algebra and independence of a and $\boldsymbol{b}$ yield

$$\begin{aligned}R_{a_0y_n}=&\int_0^1\mathrm{E}[a(\nu_0)a(\nu)^*]e^{-2i\pi\nu n}d\nu+\mathrm{E}[a(\nu_0)b_n]\\ =&\overset{\circ}{\gamma}_a(\nu)e^{-2i\pi\nu_0 n}.\end{aligned}$$

Moreover, under the previously mentioned assumptions, the generic entry R_{mn} for R_y is

$$\begin{aligned}R_{mn}=\mathrm{E}[y_m y_n^*]=&\int\int_0^1\mathrm{E}[a(\nu)a(\nu')^*]\\ &\times\exp[2i\pi(\nu n-\nu' m)]d\nu' d\nu+r_b\delta_{n-m}\\ =&(\overset{\circ}{\gamma}_a(\nu)+r_b)\delta_{n-m}\end{aligned}\tag{32}$$

where δ_n stands for the Kronecker sequence. Therefore, R_y is a diagonal matrix with elements $\overset{\circ}{\gamma}_a(\nu) + r_b$. Hence

$$\hat{a}_0 = \sum_{n=0}^{N-1} \left[1 + \lambda\, \overset{\circ}{c}_a(n)^{-1}\right]^{-1} y_n e^{-2i\pi\nu_0 n}$$

with $\lambda = r_b/r_a$.

Appendix B
Technical Results

This appendix collects several useful properties of Fourier operators. In particular, special attention is paid to W_{NP} and $\mathcal{W}_N$. Some of the stated properties are classical. We have reported them in order to make our notations and normalization conventions explicit. The other properties are less usual, but all of them have straightforward proofs.

A. Discrete Case

Structure of F_P: In the case of $N = P$, the matrix W_{NP} identifies with the square matrix $F_P^\dagger$, where F_P performs the discrete FT for vectors of size P. We have the well-known orthogonality relations $F_P^\dagger F_P = F_P F_P^\dagger = I_P$ and $F_P^t = F_P$.

Structure of W_{NP}: The matrix W_{NP} evaluates the FT on a discrete grid of P points for sequences of N points ($P \geq N$). Straightforward expansion of the product provides

$$W_{NP} F_P = [I_N \quad O_{N,P-N}]. \tag{33}$$

As a consequence, we obtain

$$W_{NP}^\dagger \boldsymbol{y} = F_P \begin{bmatrix} I_N \\ O_{P-N,N} \end{bmatrix} \boldsymbol{y} = F_P \tilde{\boldsymbol{y}}_P \tag{34}$$

where $\tilde{\boldsymbol{y}}_P$ is the zero-padded version of $\boldsymbol{y}$ up to length P.

Structure of $W_{NP}^\dagger W_{NP}$: The matrix $W_{NP} W_{NP}^\dagger$ has a very simple structure since, for $P \geq N$: $W_{NP} W_{NP}^\dagger = I_N$. Otherwise, $W_{NP}^\dagger W_{NP}$ is a non-negative, Hermitian, $P \times P$ circulant matrix. Circularity results from digonalization in the Fourier basis F_P

$$W_{NP}^\dagger W_{NP} = F_P \Lambda F_P^\dagger$$

and from (33)

$$\Lambda = \begin{bmatrix} I_N & O_{N,P-N} \\ O_{P-N,N} & O_{P-N,P-N} \end{bmatrix}.$$

As a consequence, $W_{NP}^\dagger W_{NP}$ has only two eigenvalues (1 and 0) of respective order N and $P - N$. Such a structure is useful in the proof of Propositions 2 and 4 in Appendix A.

B. Continuous Case

1) The $\mathcal{W}_N$ Operator: The linear application $\mathcal{W}_N : a \in L^2 \longrightarrow \boldsymbol{z} \in \mathbb{C}^N$ is defined by $z_n = \int_0^1 a(\nu) e^{2i\pi\nu n} d\nu$ for $n \in \mathbb{N}_N$. The adjoint operator $\mathcal{W}_N^\dagger : \boldsymbol{z} \in \mathbb{C}^N \longrightarrow a = \mathcal{W}_N^\dagger \boldsymbol{z}$ is the linear operator such that

$$\forall\, a \in L^2, \forall\, \boldsymbol{z} \in \mathbb{C}^N \quad \langle \mathcal{W}_N a, \boldsymbol{z} \rangle_{\mathbb{C}^N} = \langle a, \mathcal{W}_N^\dagger \boldsymbol{z} \rangle_{L^2}$$

where $\langle \cdot, \cdot \rangle_{\mathbb{C}^N}$ and $\langle \cdot, \cdot \rangle_{L^2}$ stand for the standard inner product in $\mathbb{C}^N$ and L^2, respectively. It is given by

$$a(\nu) = \mathcal{W}^\dagger \boldsymbol{z} = \sum_{n=0}^{N-1} z_n e^{-2i\pi\nu n}.$$

This can be justified as follows: By inverting the order of the finite sum $\sum_0^{N-1}$ and the definite integral $\int_0^1$, we get

$$\langle W_N a, \boldsymbol{z} \rangle_{\mathbb{C}^N} = \int_0^1 a(\nu) \sum_{n=0}^{N-1} z_n^* e^{2i\pi\nu n} = \langle a, \mathcal{W}_N^\dagger \boldsymbol{z} \rangle_{L^2}.$$

Finally, elementary algebra shows that the composed application $\mathcal{W}_N \mathcal{W}_N^\dagger$ is the identity application from $\mathbb{C}^N$ onto itself.

2) Technical Results for the Example in Section IV-B2:

a) Fourier Series (22): The proof of (22) consists of three steps. The first one relies on the Fourier relationship between Cauchy and Laplace functions

$$\frac{2\beta}{\beta^2 + 4\pi^2 t^2} = \int_{\mathbb{R}} e^{-\beta|f|} e^{-2j\pi t f} df, \quad t \in \mathbb{R}.$$

The second step is founded on discrete time $t = n \in Z$ and expansion in a series of integrals

$$\begin{aligned} \frac{2\beta}{\beta^2 + 4\pi^2 n^2} &= \int_{\mathbb{R}} e^{-\beta|f|} e^{-2j\pi n f} df \\ &= \sum_{p \in \mathbb{Z}} \int_0^1 e^{-\beta|\nu - p|} e^{-2j\pi n \nu} d\nu \\ &= \int_0^1 \sum_{p \in \mathbb{Z}} e^{-\beta|\nu - p|} e^{-2j\pi n \nu} d\nu \end{aligned}$$

since the invoked series are convergent. The last step is a simple geometric series calculus

$$\sum_{p \in \mathbb{Z}} e^{-\beta|\nu - p|} = \frac{\cosh \beta\,(\nu - 1/2)}{\sinh \beta/2}, \quad \nu \in [0, 1]$$

which is easily obtained by rewriting the series as the sum of a series for $p \in \mathbb{Z}_-$ (i.e., $p \leq \nu$) and a series for $p \in \mathbb{Z}_+^*$ (i.e., $p \geq \nu$).

b) Conditional Process: Let us note $\nu, \nu' \in [0, 1], \nu > \nu'$. The partitioned vector $\bar{\boldsymbol{a}} = [a(\nu), a(\nu'), a(1)]^t = [\tilde{\boldsymbol{a}} | a_1]^t$ is clearly a zero-mean Gaussian vector with covariance

$$R_{\bar{\boldsymbol{a}}} = \begin{bmatrix} \gamma_a(0) & \gamma_a(\nu - \nu') & \gamma_a(\nu) \\ \gamma_a(\nu - \nu') & \gamma_a(0) & \gamma_a(\nu') \\ \gamma_a(\nu) & \gamma_a(\nu') & \gamma_a(0) \end{bmatrix}.$$

According to the conditional covariance matrix formula $R_{\tilde{\boldsymbol{a}}|a_1} = R_{\tilde{\boldsymbol{a}}} - R_{\tilde{\boldsymbol{a}} a_1}^t R_{a_1}^{-1} R_{\tilde{\boldsymbol{a}} a_1}$, we immediately get (24). Accounting for the explicit expression for $\gamma_a(\nu)$ given by (23), simple expansion of hyperbolic functions yields (25).

c) Law of Increments: We have $\nu_1, \nu_2, \nu_1', \nu_2' \in [0, 1]$, $\nu_1 < \nu_2 < \nu_1' < \nu_2'$. Let us introduce the collection of the four values $\underline{\boldsymbol{a}} = [a(\nu_1), a(\nu_2), a(\nu_1'), a(\nu_2')]$, which is clearly a zero-mean and Gaussian vector with covariance $R_{\underline{\boldsymbol{a}}}$. The increment vector $\boldsymbol{i} = [a(\nu_2) - a(\nu_1), a(\nu_2') - a(\nu_1')] \in \mathbb{C}^2$ is a linear transform of the vector $\underline{\boldsymbol{a}}$: $\boldsymbol{i} = H\underline{\boldsymbol{a}}$ with increment covariance $R_{\boldsymbol{i}}$

$$H = \begin{bmatrix} -1 & 1 & 0 & 0 \\ 0 & 0 & -1 & 1 \end{bmatrix}, \quad R_{\boldsymbol{i}} = H R_{\underline{\boldsymbol{a}}} H^t = \begin{bmatrix} r_i & \rho \\ \rho & r_i' \end{bmatrix}$$

with $r_i = 2(\gamma_a(0) - \gamma_a(\nu_2 - \nu_1))$, $r_i' = 2(\gamma_a(0) - \gamma_a(\nu_2' - \nu_1'))$, and $\rho = \gamma_a(\nu_2 - \nu_2') + \gamma_a(\nu_1 - \nu_1') - \gamma_a(\nu_1 - \nu_2') - \gamma_a(\nu_2 - \nu_1')$. Finally, Taylor development at $\alpha_0 = 0$ yields $r_i = (\nu_2 - \nu_1)(1 - (\nu_2 - \nu_1))/2\alpha_1$, $r_i' = (\nu_2' - \nu_1')(1 - (\nu_2' - \nu_1'))/2\alpha_1$, and $\rho = (\nu_2 - \nu_1)(\nu_2' - \nu_1')/\alpha_1$ and proves(26).

ACKNOWLEDGMENT

The first author is particularly thankful to Alain, Naomi, Philippe, and Denise for committed support and coaching.

REFERENCES

[1] E. R. Robinson, "A historical perspective of spectrum estimation," *Proc. IEEE*, vol. 9, pp. 885–907, Sept. 1982.

[2] S. M. Kay and S. L. Marple, "Spectrum analysis—a modern perpective," *Proc. IEEE*, vol. 69, pp. 1380–1419, Nov. 1981.

[3] S. L. Marple, *Digital Spectral Analysis with Applications*. Englewood Cliffs, NJ: Prentice-Hall, 1987.

[4] S. M. Kay, *Modern Spectral Estimation*. Englewood Cliffs, NJ: Prentice-Hall, 1988.

[5] M. D. Sacchi, T. J. Ulrych, and C. J. Walker, "Interpolation and extrapolation using a high-resolution discrete Fourier transforms," *IEEE Trans. Signal Processing*, vol. 46, pp. 31–38, January 1998.

[6] M. D. Sacchi and T. J. Ulrych, "Estimation of the discrete Fourier transform, a linear inversion approach," *Geophysics*, vol. 61, no. 4, pp. 1128–1136, 1996.

[7] H. W. Sorenson, *Parameter Estimation*. New York: Marcel Dekker, 1980, vol. 9.

[8] A. Tikhonov and V. Arsenin, *Solutions of Ill-Posed Problems*. Washington, DC: Winston, 1977.

[9] M. Z. Nashed and G. Wahba, "Generalized inverses in reproducing kernel spaces: An approach toregularization of linear operators equations," *SIAM J. Math. Anal.*, vol. 5, pp. 974–987, 1974.

[10] G. Demoment, "Image reconstruction and restoration: Overview of common estimationstructure and problems," *IEEE Trans. Acoust., Speech, Signal Processing*, vol. 37, pp. 2024–2036, Dec. 1989.

[11] G. Kitagawa and W. Gersch, "A smoothness priors long AR model method for spectral estimation," *IEEE Trans. Automat. Contr.*, vol. AC-30, pp. 57–65, Jan. 1985.

[12] G. Wahba, "Automatic smoothing of the log periodogram," *J. Amer. Statist. Assoc., Theory Methods Section*, vol. 75, no. 369, pp. 122–132, Mar. 1980.

[13] G. L. Bretthorst, *Bayesian Spectrum Analysis and Parameter Estimation*, J. Berger, S. Fienberg, J. Gani, K. Krickeberg, and B. Singer, Eds. New York: Springer-Verlag, 1988, vol. 48.

[14] F. Dublanchet, J. Idier, and P. Duvaut, "Direction-of-arrival and frequency estimation using Poisson-Gaussian modeling," in *Proc. IEEE ICASSP*, Munich, Germany, 1997, pp. 3501–3504.

[15] F. J. Harris, "On the use of windows for harmonic analysis with the discrete Fourier transform," *Proc. IEEE*, vol. 66, pp. 51–83, Jan. 1978.

[16] A. Bertin, *Espaces de Hilbert*. Paris, France: l'ENSTA, 1993.

[17] H. Cramér and M. R. Leadbetter, *Stationary and Related Stochastic Processes*. New York: Wiley, 1967.

[18] P. Brémaud, "Markov Chains. Gibbs fields, Monte Carlo Simulation, and Queues," in *Texts in Applied Mathematics 31*. New York: Spinger, 1999.

[19] J. M. F. Moura and G. Sauraj, "Gauss-Markov random fields (GMrf) with continuous indices," *IEEE Trans. Inform. Theory*, vol. 43, pp. 1560–1573, Sept. 1997.

[20] E. Wong, "Stochastic processes in information and dynamical systems," in *Series in Systems Science*. New York: McGraw-Hil, 1971.

[21] R. N. Bhattacharya and E. C. Waymire, *Stochastic Processes with Applications*. New York: Wiley, 1990.

[22] G. H. Golub, M. Heath, and G. Wahba, "Generalized cross-validation as a method for choosing a good ridge parameter," *Technometrics*, vol. 21, no. 2, pp. 215–223, May 1979.

[23] D. M. Titterington, "Common structure of smoothing techniques in statistics," *Int. Statist. Rev.*, vol. 53, no. 2, pp. 141–170, 1985.

[24] P. Hall and D. M. Titterington, "Common structure of techniques for choosing smoothing parameter in regression problems," *J. R. Statist. Soc. B*, vol. 49, no. 2, pp. 184–198, 1987.

[25] A. Thompson, J. C. Brown, J. W. Kay, and D. M. Titterington, "A study of methods of choosing the smoothing parameter in image restoration by regularization," *IEEE Trans. Pattern Anal. Machine Intell.*, vol. 13, pp. 326–339, Apr. 1991.

[26] N. Fortier, G. Demoment, and Y. Goussard, "Comparison of GCV and ML methods of determining parameters in image restoration by regularization," *J. Vis. Commun. Image Repres.*, vol. 4, pp. 157–170, 1993.

[27] J.-F. Giovannelli, G. Demoment, and A. Herment, "A Bayesian method for long AR spectral estimation: a comparative study," *IEEE Trans. Ultrason. Ferroelectr. Freq. Contr.*, vol. 43, pp. 220–223, Mar. 1996.

[28] D. P. Bertsekas, *Nonlinear Programming*. Belmont, MA: Athena Scientific, 1995.

[29] R. Shumway and D. Stoffer, "An approach to time series smoothing and forecasting using the EM algorithm," *J. Time Series Anal.*, pp. 253–264, 1982.

[30] M. Basseville, "Distance measures for signal processing and pattern recognition," *Signal Process.*, vol. 18, no. 4, pp. 349–369, Dec. 1989.

[31] P. Ciuciu, J. Idier, and J.-F. Giovannelli, "Markovian high resolution spectral analysis," in *Proc. IEEE ICASSP*, Phoenix, AZ, 1999, pp. 1601–1604.

[32] D. G. Luenberger, *Optimization by Vector Space Methods*, 1 ed. New York: John Wiley, 1969.

Jean-François Giovannelli was born in Béziers, France, in 1966. He graduated from the École Nationale Supérieure de l'Électronique et de ses Applications, Paris, France, in 1990. He received the Doctoral degree in physics from Université de Paris-Sud, Orsay, France, in 1995.

He is presently an assistant professor with the Département de Physique, the Laboratoire des Signaux et Systémes, Université de Paris-Sud. He is interested in regularization methods for inverse problems in signal and image processing, mainly in spectral characterization. His application fields essentially concern medical imaging.

Jérôme Idier was born in France in 1966. He received the diploma degree in electrical engineering from the École Supérieure d'Électricité, Gif-sur-Yvette, France, in 1988 and the Ph.D. degree in physics from the Université de Paris-Sud, Orsay, France, in 1991.

Since 1991, he has been with the Laboratoire des Signaux et Systèmes, Centre National de la Recherche Scientifique, Gif-sur-Yvette. His major scientific interest is in probabilistic approaches to inverse problems for signal and image processing.

J.-F. Giovannelli, J. Idier, G. Desodt et D. Muller, « Regularized adaptive long autoregressive spectral analysis », *IEEE Trans. Geosci. Remote Sensing*, vol. 39, n°10, pp. 2194–2202, octobre 2001.

2194 IEEE TRANSACTIONS ON GEOSCIENCE AND REMOTE SENSING, VOL. 39, NO. 10, OCTOBER 2001

Regularized Adaptive Long Autoregressive Spectral Analysis

Jean-François Giovannelli, Jérôme Idier, Daniel Muller, and Guy Desodt

***Abstract*—This paper is devoted to adaptive long autoregressive spectral analysis when i) very few data are available and ii) information does exist beforehand concerning the spectral smoothness and time continuity of the analyzed signals. The contribution is founded on two papers by Kitagawa and Gersch [1], [2]. The first one deals with spectral smoothness in the regularization framework, while the second one is devoted to time continuity in the Kalman formalism. The present paper proposes an original synthesis of the two contributions. A new regularized criterion is introduced that takes both pieces of information into account. The criterion is efficiently optimized by a Kalman smoother. One of the major features of the method is that it is entirely unsupervised. The problem of automatically adjusting the hyperparameters that balance data-based versus prior-based information is solved by maximum likelihood (ML). The improvement is quantified in the field of meteorological radar.**

***Index Terms*—Adaptive spectral analysis, hyperparameter estimation, long autoregressive model, maximum likelihood (ML), meteorological Doppler radar, regularization, spectral smoothness, time continuity.**

I. Introduction

ADAPTIVE spectral analysis and time-frequency analysis are of major importance in fields as widely varied as speech processing [3], acoustical attenuation measurements [4], [5], ultrasonic Doppler velocimetry [6], or Doppler radars [7]–[11]. [12] gives a synthesis of the various methods for these problems, and provides a number of bibliographical introductions.

The present paper focuses on short-time analysis. Typically, for analysis of pulsed Doppler signals, only eight or 16 samples are available to estimate one spectrum, with possibly various shapes (multimodal or not, of large spectral width or not, mixed clutter, etc.). Under such circumstances, the construction of the sought spectra becomes extremely tricky on the sole basis of the samples. As a point of reference, let us recall that several hundred samples are usually needed to compute an averaged periodogram with a fair bias-variance compromise [13], [14]. Therefore, parametric methods have generally been preferred, among which autoregressive (AR) methods play a central role. The AR coefficients estimation is usually tackled in the least squares (LS) framework [15], [16]. These methods often provide a solution at points where nonparametric methods are useless. But when the number of data is very low, these techniques become, in their turn, useless, especially if various spectral shapes are expected due to model order limitations.

In order to construct a reliable image, structural information about the sought spectrum sequence must be accounted for. Our investigation is therefore restricted to the cases in which two kinds of information are foreknown: *spectral smoothness* and *time continuity*. This *a priori* information is the foundation of the proposed construction.

In the framework of stationary AR analysis, Kitagawa and Gersch proposed a method integrating the idea of spectral smoothness [1] by which a *high-order AR model* can be robustly estimated, thereby getting around the difficult problem of order selection and providing the ability to estimate various spectral shapes. For the nonstationary case, and aside from [1], the same authors introduced in [2] a Markovian model for the regressor sequence in the Kalman formalism in order to reflect time continuity. The present paper reviews [1] and [2] and makes an original synthesis suited to the special configuration of Doppler signals. A new Regularized LS (RegLS) criterion simultaneously includes the spectral and time information and is optimized by a Kalman smoother (KS).

One of the major features of the method is that it is entirely unsupervised: the adjustment of parameters that weight the relative contributions of the observation *versus* the *a priori* knowledge is automatically set by maximum likelihood (ML).

A comparative study is proposed in the context of pulsed Doppler radars. Special attention is payed to atmospheric and/or meteorological context imaging or identification: ground clutter, rain clutter, sea echos, etc. Adaptive spectral estimation of mixed clutter is achieved by means of several usual AR methods and the proposed one. The latter achieves qualitative and quantitative improvements w.r.t. usual methods.

The paper is organized as follows. Section II mainly introduces notations and problem statement. Section III focuses on usual LS methods and usual adaptive extensions. The proposed method is presented in Section IV, and Section V deals with the KS. The problem of automatic parameter estimation is addressed in Section VI. Simulation results are presented in Section VII. Finally, conclusions and perspectives for future works are presented in Section VIII.

II. Problem Statement

The problem is that of processing pulsed Doppler signals from electronic scanning radars or ultrasound velocimeter. The reader may consult [6], [7] for a technological review. The pulsed Doppler systems are such that the observed signals do

Manuscript received May 31, 20; revised January 19, 2001.

J.-F. Giovannelli and J. Idier are with the Laboratoire des Signaux et Systèmes (CNRS–SIPÉLEC–UPS) SUPÉLEC, 91192 Gif-sur-Yvette Cedex, France (e-mail: giova@lss.supelec.fr; idier@lss.supelec.fr).

D. Muller and G. Desodt are with the Société Thomson, 92220 Bagneux, France.

Publisher Item Identifier S 0196-2892(01)09291-9.

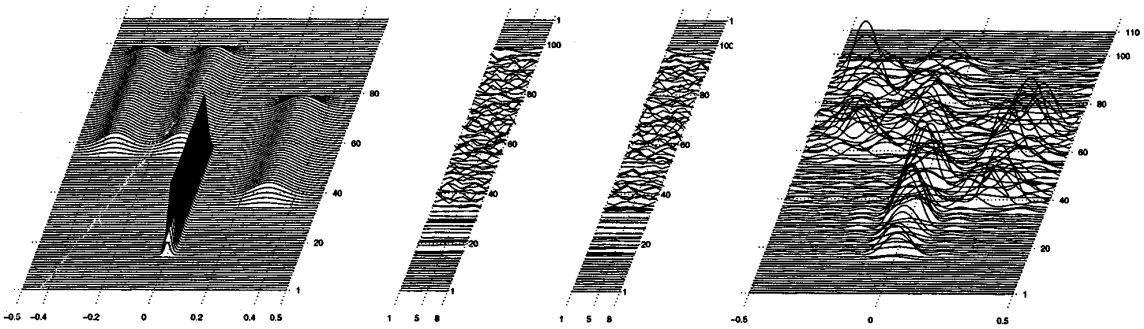

Fig. 1. Simulated observations over 110 range bins with eight samples per bin (corresponding to eight Doppler pulses). The left-hand side (LHS) figure shows the true spectra sequence. The narrow zero-mean spectra characterizes ground clutter (bin 15 to 57). Rain clutter induces more or less broad, single-mode spectra (bin 35 to 75). Lastly, sea echos resulting from wave phenomena exhibit two maxima (bin 56 to 95). The middle figure shows the real part and imaginary part of the data and the rhs one shows the associated periodograms.

not occur in the usual form of time-frequency problems. So, neither the usual time-frequency methods nor the one proposed by Kitagawa and Gersch can be directly applied, and part of the presented work consists in constructing an appropriate method for the encountered configuration.

The measurements are available as a set of complex signals $\mathcal{Y} = [\boldsymbol{y}_1, \ldots, \boldsymbol{y}_M]$, depth-wise juxtaposed in M range bins. It is assumed that each $\boldsymbol{y}_m = [y_{m1}, \ldots, y_{mN}]^t$ is a N sample vector extracted from a zero-mean stationary process. Fig. 1 gives a Gaussian simulated example over $M = 110$ bins for which $N = 8$ samples are observed per bin. The successive regressors are denoted $\boldsymbol{a}_m = [a_{mp}]$, where m indicates the considered bin ($m \in \mathbb{N}_M^* = \{1, 2, \ldots, M\}$) and p the order of the autoregression coefficient ($p \in \mathbb{N}_P^*$). Let us note $\boldsymbol{A} = [\boldsymbol{a}_1, \ldots, \boldsymbol{a}_M] \in \mathbb{C}^{N \times P}$ the collection of the whole set of coefficients. Let us also introduce r_m and r_m^e for signal and prediction error powers. The remainder of the paper is devoted to estimation of these quantities. The next section deals with the usual LS methods and their adaptive extension, and shows their inadequacy for the problem at stake.

III. Review of Classical Methods

A. Stationary Spectral Analysis

This subsection is devoted to spectral analysis applied to a single bin m. Assuming a Gaussian distribution for the observed signal, the likelihood of the AR coefficients $f(\boldsymbol{y}_m | \boldsymbol{a}_m)$ shows a special form [17, p. 82], but its maximization raises a difficult problem. A few authors [18], [19] have undertaken to solve it, but firstly, the available algorithms cannot guarantee global maximization, and secondly, they are not computationally efficient for the applications under the scope of the paper. To remedy these disadvantages, the following approximation of the likelihood function is usually accepted [16, p. 185]:

$$f(\boldsymbol{y}_m | \boldsymbol{a}_m) = (\pi r_m^e)^{-N} \exp\left(\frac{-Q_m^{\mathrm{LS}}(\boldsymbol{a}_m)}{r_m^e}\right) \tag{1}$$

involving the norm of the prediction error vector

$$Q_m^{\mathrm{LS}}(\boldsymbol{a}_m) = \boldsymbol{e}_m^\dagger \boldsymbol{e}_m = (\boldsymbol{y}_m - Y_m a_m)^\dagger (\boldsymbol{y}_m - Y_m \boldsymbol{a}_m) \tag{2}$$

i.e., a quadratic form with regard to the $\boldsymbol{a}_m$, namely, the LS criterion. The $\boldsymbol{y}_m$ and Y_m are the vector and matrix designed according to some chosen windowing assumption [15, p. 217], [20, (2)]. There are four possible forms: nonwindowed (covariance method), prewindowed, postwindowed, double-windowed, i.e., pre- and postwindowed (autocorrelation method). Let us note L, the size of $\boldsymbol{y}_m$: $L = N - P$, $L = N$, or $L = N + P$, according to the chosen form. This choice is of importance since it strongly influences spectral resolution for short time analysis [15].

Whatever the chosen form, the maximization of (1) comes down to the minimization of (2) and yields

$$\hat{\boldsymbol{a}}_m^{\mathrm{LS}} = \arg\min_{\boldsymbol{a}_m} Q_m^{\mathrm{LS}}(\boldsymbol{a}_m) = (Y_m^\dagger Y_m)^{-1} Y_m^\dagger \boldsymbol{y}_m. \tag{3}$$

As a prerequisite, the problem of choosing the model order P must be tackled. P must be high enough to describe various PSD and low enough to avoid spurious peaks, i.e., to ensure spectral smoothness. This compromise can usually be set by means of criteria such as FPE [21], AIC [22], CAT [23], or MDL [24], but, in the situation of prime interest here, they fail because the available amount of data is too small [25]. Actually, there exists no satisfying compromise in term of model order, since too few data are available to estimate DSPs with possibly complex structures.

B. Adaptive Spectral Analysis

For the "multirange bin" analysis, the first idea consists in processing each bin independently. According to the LS approach, it amounts to minimizing a global LS criterion

$$Q^{\mathrm{LS}}(\boldsymbol{A}) = \sum_{m=1}^{M} Q_m^{\mathrm{LS}}(\boldsymbol{a}_m). \tag{4}$$

However, the resulting spectra hold unrealistic variations in the spatial direction (see Fig. 4). In order to remedy this problem, the adaptive least squares (ALS) approach accounts for spatial continuity by processing the data from several bins, possibly in weighted form, to estimate each $\boldsymbol{a}_m$. A first approach uses a series of LS criteria including the data in a spatial window of length W. A widely used alternative is the exponential decay

memory which uses geometrically weighted LS criteria, with parameter $\lambda \in [0,1]$. The latter is more popular because it is simpler: λ is merely incorporated into a standard recursive LS algorithm [15, p. 266]. In both cases, the degree of adaptivity, i.e., the spatial continuity is modulated by W or λ.

C. Conclusion

Whatever the variant, the main disadvantage of these approaches has to do with the parameter settings.

1) From the spectral standpoint, smoothness is introduced in a roundabout fashion, *via* the model order (adjusted by P) and the compromise no longer exists when the amount of data is reduced.
2) From the spatial standpoint, continuity is also indirectly introduced (and tuned by W or λ) and no automatic method for adjusting this parameters is available.

These limitations are unavoidable in the simple LS formalism, and to alleviate this problem, we resort to the regularization theory. In this framework, the proposed approach:

- includes the spectral smoothness and spatial continuity in the estimation criterion itself;
- allows long-AR model to be robustly estimated, and then various spectra to be identified;
- provides automatic parameter setting, i.e., an entirely unsupervised method.

IV. Long AR (Spatial Continuity) Spectral Smoothness

A. Spatial Continuity Model

The first idea consists in building a spectral distance. Following [2], starting with the PSD in bin m

$$S_m(\nu) = \frac{r_m^e}{|1 - A_m(\nu)|^2}, \quad A_m(\nu) = \sum_{p=1}^{P} a_{mp} e^{-2j\pi\nu p} \tag{5}$$

the proposed spectral distance between S_m and $S_{m'}$ is founded on the kth Sobolev distance between A_m and $A_{m'}$

$$D_k(m,m') \propto \int_0^1 \left| \frac{\mathrm{d}^k}{\mathrm{d}\nu^k} [A_m(\nu) - A_{m'}(\nu)] \right|^2 d\nu.$$

Calculations similar to those of [2] yield a quadratic form

$$D_k(m,m') = (\boldsymbol{a}_m - \boldsymbol{a}_{m'})^\dagger \Delta_k (\boldsymbol{a}_m - \boldsymbol{a}_{m'}) \tag{6}$$

where $\Delta_k = \mathrm{diag}\left[1^{2k}, \ldots, P^{2k}\right]$ is the kth spectral matrix.

B. Spectral Smoothness Model

The spectral smoothness measure proposed by Kitagawa and Gersch in [2] (see also [26]) is easily deduced from (6) as the distance to a constant DSP

$$D_k(m) \propto \boldsymbol{a}_m^\dagger \Delta_k \boldsymbol{a}_m. \tag{7}$$

According to [1], [2], $k \in \mathbb{Z}_+$, but Δ_k as well as (6) and (7) can be extended to $k \in \mathbb{R}_+$.

Remark 1: Strictly speaking, $D_k(m,m')$ and $D_k(m)$ are not spectral distances nor spectral smoothness measures since they are not functions of the PSD itself. However, they are quadratic and this has two advantages: it considerably simplifies regressor calculations (see Section V) as well as regularization parameter estimation (see Section VI).

C. Double Smoothness

Starting with the spectral smoothness (7) and the spatial distance (6), a new quadratic penalization is introduced

$$Q^\infty(\boldsymbol{A}) = \frac{1}{r_\mathrm{s}} \sum_{m=1}^{M} D_k(m) + \frac{1}{r_\mathrm{d}} \sum_{m=1}^{M-1} D_k(m, m+1). \tag{8}$$

It integrates both spectral smoothness and spatial continuity, respectively, tuned by $\lambda_\mathrm{s} = 1/r_\mathrm{s}$ and $\lambda_\mathrm{d} = 1/r_\mathrm{d}$.

Remark 2: The penalization (8) has a Bayesian interpretation [27] as a Gaussian prior for the sought regressors

$$f(\boldsymbol{A}) \propto \exp\left[-Q^\infty(\boldsymbol{A})\right] \tag{9}$$

useful for hyperparameter estimation in Section VI.

D. Regularized Least Squares

From the LS criteria (4) and the penalization term (8), the proposed RegLS criterion reads

$$\begin{aligned} Q^{\mathrm{Reg}}(\boldsymbol{A}) =& Q^{\mathrm{LS}}(\boldsymbol{A}) + Q^\infty(\boldsymbol{A}) \\ =& \sum_{m=1}^{M} \frac{1}{r_m^e} (\boldsymbol{y}_m - Y_m \boldsymbol{a}_m)^\dagger (\boldsymbol{y}_m - Y_m \boldsymbol{a}_m) \\ &+ \frac{1}{r_\mathrm{s}} \sum_{m=1}^{M} \boldsymbol{a}_m^\dagger \Delta_k \boldsymbol{a}_m \\ &+ \frac{1}{r_\mathrm{d}} \sum_{m=1}^{M-1} (\boldsymbol{a}_m - \boldsymbol{a}_{m+1})^\dagger \Delta_k (\boldsymbol{a}_m - \boldsymbol{a}_{m+1}) \end{aligned} \tag{10}$$

involving three terms which respectively measure fidelity to the data, spectral smoothness and spatial regularity. The regularized solution is defined as the minimizer of (10)

$$\hat{\boldsymbol{A}}_{\mathrm{Reg}} = \arg\min_{\boldsymbol{A}} Q^{\mathrm{Reg}}(\boldsymbol{A}). \tag{11}$$

Remark 3: The regularized criterion (10) has a clear Bayesian interpretation [27]. Likelihood (1) and prior (9) can be fused thanks to the Bayes rule, into a Gaussian posterior law for the sought regressors

$$f(\boldsymbol{A}|\mathcal{Y}) \propto \exp\left[-Q^{\mathrm{Reg}}(\boldsymbol{A})\right]. \tag{12}$$

Solution (11) is also the MAP estimate.

E. Optimization Stage

Several options are available to compute (11). Since $Q^{\mathrm{Reg}}(\boldsymbol{A})$ is quadratic, $\hat{\boldsymbol{A}}_{\mathrm{Reg}}$ is the solution of an $MP \times MP$ linear system. Moreover, since the involved matrix is sparse, direct inversion should be tractable but not recommendable here ($M = 110$, $P = 7$). Another approach may be found in gradient or relaxation methods [28] since $Q^{\mathrm{Reg}}(\boldsymbol{A})$ is differentiable and convex. But, given the depth-wise structure, another algorithm is preferred: KS. Here we resort to the initial viewpoint of Kitagawa and Gersch in [2]. However, it is

noticeable that [2] does not mention the minimized criterion, whereas our KS is designed to minimize (10).

V. Kalman Smoothing

A. State-Space Form

1) The successive prediction vectors $\boldsymbol{a}_m$ are related by a first-order state equation

$$\boldsymbol{a}_{m+1} = \alpha_m \boldsymbol{a}_m + \varepsilon_m \tag{13}$$

in which each $\boldsymbol{\varepsilon}_m$ is a complex, zero-mean, circular, vector with covariance matrix $P_m^{\varepsilon} = r_m^{\varepsilon}\Delta_k^{-1}$ and the $\boldsymbol{\varepsilon}_m$-sequence, is depth-wise white.

2) The full state model also brings in the initial mean and covariance: the null vector and $P^a = r^a \Delta_k^{-1}$, respectively.

3) The observation equation is the recurrence equation for the AR model in each bin, written in compact form as

$$\boldsymbol{y}_m = Y_m \boldsymbol{a}_m + \boldsymbol{e}_m \tag{14}$$

i.e., a generalized version of the one proposed in [2], adapted to depthwise vectorial data. Each $\boldsymbol{e}_m$ is a complex, zero-mean, circular vector with covariance $r_m^e I_L$. The $\boldsymbol{e}_m$ sequence is also depthwise white.

Remark 4: [2] accounts for spatial continuity by means of a special case of (13): $\boldsymbol{a}_{m+1} = \boldsymbol{a}_m + \boldsymbol{\varepsilon}_m$. The latter has two drawbacks, though. Firstly, it is introduced apart from the idea of spectral smoothness. Secondly, from a Bayesian point of view, this equation is interpreted as a Brownian process with an increasing variance, which may cause drifts to appear in the estimated spectra. On the contrary, the new coefficients α_m can be chosen in order to ensure stationarity of the model (13) or to minimize the homogeneous criterion (10).

B. Equivalence Between Parameter Settings

1) Homogeneous Criterion: This section establishes the formal link between the parameters of the KS (r^a and $\alpha_m, r_m^{\varepsilon}$) and those of the regularized criterion (10) (r_{d} and r_{s}). [29] states that the KS associated to (13) and (14) minimizes $Q^{\mathrm{KS}}(\boldsymbol{A})$

$$\begin{aligned} &= \sum_{m=1}^{M} \frac{1}{r_m^e}(\boldsymbol{y}_m - Y_m\boldsymbol{a}_m)^{\dagger}(\boldsymbol{y}_m - Y_m\boldsymbol{a}_m) \\ &\quad + \sum_{m=1}^{M-1} \frac{1}{r_m^{\varepsilon}}(\boldsymbol{a}_{m+1} - \alpha_m\boldsymbol{a}_m)^{\dagger}\Delta_k^{-1}(\boldsymbol{a}_{m+1} - \alpha_m\boldsymbol{a}_m) \\ &\quad + \frac{1}{r^a}\boldsymbol{a}_1^{\dagger}\Delta_k^{-1}\boldsymbol{a}_1. \end{aligned} \tag{15}$$

Partial expansions yield identification of (10) and (15) through the following count-down recursion.

1) Initialization $(m = M-1)$

$$\alpha_{M-1} = (1+\rho)^{-1}, \text{ and } r_{M-1}^{\varepsilon} = r_{\mathrm{d}}\alpha_{M-1}.$$

2) Count-down recursion $(m = M-2, \ldots, 1)$

$$\alpha_m = (2+\rho-\alpha_{m+1})^{-1}, \text{ and } r_m^{\varepsilon} = r_{\mathrm{d}}\alpha_m.$$

3) The last step yields the initial power

$$r^a = r_{\mathrm{d}}(1+\rho-\alpha_1)^{-1}$$

with $\rho = r_{\mathrm{d}}/r_{\mathrm{s}} \in \mathbb{R}_+^*$. These equations allow us to precompute the coefficients of the KS in order to minimize (10).

2) Limit Model: This section is devoted to the asymptotic behavior of the α_m-sequence. For the sake of notational simplicity, the sequence is rewritten in a count-up form

$$\begin{aligned} m &= 1 : \overline{\alpha}_1 = (1+\rho)^{-1} \\ m &\in \mathbb{N}^* : \tilde{\alpha}_{m+1} = (2+\rho-\overline{\alpha}_m)^{-1}. \end{aligned} \tag{16}$$

It is clear that $\tilde{\alpha}_1 \in]0,1[$ since $\rho \in \mathbb{R}_+^*$. Let us introduce $f(u) = (2+\rho-u)^{-1}$. It is straightforward that $f(]0,1[) \subset]0,1[$, so the entire $\tilde{\alpha}_m$-sequence remains in $]0,1[$. Moreover, if it exists, the limit $\alpha_\infty \in [0,1]$ necessarily fulfills $f(\alpha_\infty) = \alpha_\infty$. Elementary algebra yields

$$\alpha_\infty = \frac{\theta - \sqrt{\theta^2 - 4}}{2} \tag{17}$$

with $\theta = 2+\rho = 2+r_{\mathrm{d}}/r_{\mathrm{s}}$. Finally, one can effortlessly see that $\forall\, u, v \in]0,1[$, we have $|f(u)-f(v)| \leqslant (1+\rho)^{-2}|u-v|$, i.e., f is a Lipschitz function with ratio in $]0,1[$. Hence, the sequence effectively converges toward α_∞. It is also easy to see that the sequence is monotonous: increasing if $\alpha_1 < \alpha_\infty$ and decreasing otherwise. In the present case, comparison of α_1 in (16) and α_∞ in (17) shows that the $\tilde{\alpha}_m$-sequence is decreasing (in the count-up form), hence, α_m is increasing.

Finally, since $r_m^{\varepsilon} = r_{\mathrm{d}}\alpha_m$, the corresponding limit state power is given by

$$r_\infty^{\varepsilon} = r_{\mathrm{d}}\alpha_\infty. \tag{18}$$

3) Associated Stationary Criterion: This section is devoted to the stationary limit model: the special case of (13), with $\alpha_m = \alpha_\infty$ and $r_m^{\varepsilon} = r_\infty^{\varepsilon}$, i.e., a stationary first-order AR model for the $\boldsymbol{a}_m$-sequence. The initial power is denoted r_∞^a for notational coherence, even if it is not defined as a limit. It is actually defined according to r_∞^{ε} and α_∞ in order to ensure stationarity for the first-order AR model: $r_\infty^a = r_\infty^{\varepsilon}/(1-\alpha_\infty^2)$.

Replacement of α_m, r_m^{ε}, r^a by α_∞, r_∞^{ε}, r_∞^a in (15) yields the criterion minimized by the stationary KS

$$\begin{aligned} Q^{\mathrm{S}}(\boldsymbol{A}) &= \sum_{m=1}^{M} \frac{1}{r_m^e}(\boldsymbol{y}_m - Y_m\boldsymbol{a}_m)^{\dagger}(\boldsymbol{y}_m - Y_m\boldsymbol{a}_m) \\ &\quad + \frac{(1-\alpha_\infty)^2}{r_\infty^{\varepsilon}} \sum_{m=1}^{M} \boldsymbol{a}_m^{\dagger}\Delta_k\boldsymbol{a}_m \\ &\quad + \frac{\alpha_\infty}{r_\infty^{\varepsilon}} \sum_{m=1}^{M-1} (\boldsymbol{a}_m - \boldsymbol{a}_{m+1})^{\dagger}\Delta_k(\boldsymbol{a}_m - \boldsymbol{a}_{m+1}) \\ &\quad + \frac{\alpha_\infty(1-\alpha_\infty)}{r_\infty^{\varepsilon}} \left(\boldsymbol{a}_1^{\dagger}\Delta_k\boldsymbol{a}_1 + \boldsymbol{a}_M^{\dagger}\Delta_k\boldsymbol{a}_M\right) \end{aligned}$$

where superscript "S" stands for stationary. Since we have $r_{\mathrm{d}} = r_{\infty}^{\varepsilon}/\alpha_{\infty}$ from (18) and $r_{\mathrm{s}} = r_{\infty}^{\varepsilon}/(1-\alpha_{\infty})^2$ from (17), one can effortlessly see that

$$Q^{\mathrm{S}}(\boldsymbol{A}) = Q^{\mathrm{Reg}}(\boldsymbol{A}) + \frac{\alpha_{\infty}(1-\alpha_{\infty})}{r_{\infty}^{\varepsilon}}\left(\boldsymbol{a}_1^{\dagger}\Delta_k\boldsymbol{a}_1 + \boldsymbol{a}_M^{\dagger}\Delta_k\boldsymbol{a}_M\right).$$

So the stationary criterion $Q^{\mathrm{S}}(\boldsymbol{A})$ and the initial homogeneous one $Q^{\mathrm{Reg}}(\boldsymbol{A})$ are equal apart from the edge effects, i.e., two terms regarding the first and last regressors. As a consequence, the minimizer of $Q^{\mathrm{Reg}}(\boldsymbol{A})$ and $Q^{\mathrm{S}}(\boldsymbol{A})$ are practically equivalent and the latter is preferred since it does not require precomputation of the α_m and r_m^{ε}.

C. Kalman Smoother Equations

- Initialization $(m = 1)$

$$\boldsymbol{a}_{1|1} = 0 \tag{19}$$
$$P_{1|1} = r_{\infty}^{a}\Delta_k^{-1}. \tag{20}$$

- Filtering phase (for $m = 2, \ldots, M$)
  — Prediction step

$$\boldsymbol{a}_{m|m-1} = \alpha_{\infty}\boldsymbol{a}_{m-1|m-1} \tag{21}$$
$$P_{m|m-1} = \alpha_{\infty}^2 P_{m-1|m-1} + r_{\infty}^{\varepsilon}\Delta_k^{-1}. \tag{22}$$

  — Correction step

$$K_m = P_{m|m-1}Y_m^{\dagger} \tag{23}$$
$$R_m = r_m^e I_L + K_m^{\dagger}Y_m \tag{24}$$
$$\boldsymbol{e}_m = \boldsymbol{y}_m - Y_m\boldsymbol{a}_{m|m-1} \tag{25}$$
$$\boldsymbol{a}_{m|m} = \boldsymbol{a}_{m|m-1} + K_m R_m^{-1}\boldsymbol{e}_m. \tag{26}$$
$$P_{m|m} = P_{m|m-1} - K_m R_m^{-1} K_m^{\dagger}. \tag{27}$$

- Smoothing count-down phase (for $m = M-1, \ldots, 1$)

$$Q_m = \alpha_{\infty}P_{m|m}P_{m+1|m}^{-1} \tag{28}$$
$$\boldsymbol{a}_{m|M} = \boldsymbol{a}_{m|m} + Q_m\left(\boldsymbol{a}_{m+1|M} - \boldsymbol{a}_{m+1|m}\right) \tag{29}$$
$$P_{m|M} = P_{m|m} + Q_m\left(P_{m+1|M} - P_{m+1|m}\right)Q_m^{\dagger}. \tag{30}$$

D. Fast Algorithm

Fast algorithms used to take a primordial position in past decades, especially for real-time computations. More specifically, for adaptive spectral analysis of the ultrasound Doppler signal, the MARASCA algorithm [27] has been used in a real-time high-resolution velocimeter prototype. But it has two drawbacks, resulting in a rigid spectral and spatial continuity tuning. On the one hand, it proceeds by blocks and incorporates spatial continuity by using the regressor of the current block as a prior mean for the next one; on the other hand, the fast version is developed only for the zero-order smoothness $(k = 0)$.

To our knowledge, no fast algorithm exists for the KF in the configuration of interest, mainly because of the structures of the state equation and the smoothness matrix. However, a fast algorithm may be developed on the basis of high-order displacement matrices [30]. More precisely, it is easy to see that the displacement matrix of order $2k+1$ (if integer) is null for Δ_k. Taking advantage of this property may result in a fast version of the proposed algorithm.

However, calculation time problems are now less crucial than they used. The standard KS algorithm only takes 0.36 s[1] to process the entire data set of Fig. 1, so real time computations can probably be achieved.

VI. Hyperparameters Estimation

The estimated $\boldsymbol{a}_m$-sequence and spectra sequence depends on $M+4$ hyperparameters: smoothness and AR orders k and P, power sequence r_m^e, and two regularization parameters λ_{s} and λ_{d}.

A. Power Parameters

The M parameters r_m^e are needed by the proposed RegLS method as well as the LS and ALS procedures, and the same empirical estimates will be used for all of them. In the criterion (10), parameters r_m^e only act as weighting coefficients, so that the successive terms are of equivalent weight. The proposed empirical technique replaces the prediction error powers r_m^e by the signal powers r_m themselves. A simple empirical estimate $\hat{r}_m = \boldsymbol{y}_m^{\dagger}\boldsymbol{y}_m/N$ could be used. However, since the estimation variance is high for $N = 8$, in practice, a more efficient technique consists in smoothing the sequence $\hat{r}_m$. Let us note that [2] proposes a scheme, which is equivalent in principle.

B. Order Parameters

The proposed framework allows us to estimate long AR models to describe various spectral shapes. Moreover, by choosing the maximal order $P = N-1$, we get rid of the difficult problem of model-order selection. In fact, as expected and confirmed in Section VII-C, as long as P is large enough, it does not significantly affect the spectral shape.

On the other hand, to our experience, the smoothness order k does not affect the spectrum sequence provided that $k \neq 0$. So the smoothness order is *a priori* tuned to $k = 1$, i.e., a first-order derivative spectra penalization. Moreover, Section VII-C also provides a quantitative sensitivity study of the spectra sequence with regard to this parameter.

C. Regularization Parameters

The problem of regularization parameter estimation within the proposed framework is a delicate one. It has been extensively studied and several techniques have been proposed and compared [26], [31]–[35]. The ML approach is often chosen within the Bayesian framework mentioned in Remarks 2 and 3. The Gaussian likelihood function (1) and the Gaussian prior (9) together yield a Gaussian marginal law for the observed samples $f(\mathcal{Y}; \lambda_{\mathrm{s}}, \lambda_{\mathrm{d}})$, i.e., the regularization parameter likelihood. The hyperparameter-co-log-likelihood (HCLL) is easily computed

[1]The proposed algorithm has been implemented using the computing environment Matlab on a personal computer, Pentium III, with a 450 MHz CPU and 128 Mo of RAM.

for a given hyperparameter set, as a function of innovation vectors $\boldsymbol{e}_m$ and covariances R_m, i.e., two of the KF subproducts

$$\mathrm{HCLL}(\lambda_\mathrm{s}, \lambda_\mathrm{d}) = \sum_{m=1}^{M} \ln\det R_m + \boldsymbol{e}_m^\dagger R_m^{-1} \boldsymbol{e}_m$$

ignoring constant coefficients. This expression is the generalization of a more conventional identity, available for scalar observations [2]. The error covariance matrix R_m is an $L \times L$ matrix, L possibly ranging from $L = 1$ to $L = N + P$ according to the windowing form and model order. Since $L = 1$ is selected in the presented computations, no specific algorithm has been developed for inversion nor determinant calculations.

The ML estimate

$$\left(\hat{\lambda}_\mathrm{s}^{\mathrm{ML}}, \hat{\lambda}_\mathrm{d}^{\mathrm{ML}}\right) = \underset{\lambda_\mathrm{s},\lambda_\mathrm{d}}{\arg\min}\, \mathrm{HCLL}(\lambda_\mathrm{s}, \lambda_\mathrm{d}) \tag{31}$$

can be computed by means of several algorithms: coordinate/gradient descent algorithm [28] or EM algorithms [36], [37], but none of them can ensure global optimization. Here, the optimization stage is tackled by means of a coordinate descent algorithm with a golden section line search [28]. Since HCLL is a function of two variables only, the optimization stage only requires about 10 s.

VII. Simulation Results and Comparisons

The present section assesses the effectiveness of the proposed method, compared to the usual ones by processing the example shown in Fig. 1.

A. Quantitative Comparison Criterion

Since the true spectrum sequence is known in the presented simulations, quantitative criteria are computable on the basis of distances between estimated spectra $\hat{S}_m(\nu)$ and true ones $S_m(\nu)$, accumulated over the M bins. Normalized distances

$$\mathrm{L}^r = \frac{\sum_{m=1}^{M} \int_0^1 |\hat{S}_m(\nu) - S_m(\nu)|^r \mathrm{d}\nu}{\sum_{m=1}^{M} \int_0^1 |S_m(\nu)|^r \mathrm{d}\nu}$$

with $r = 1$ and $r = 2$ have been computed. The normalization is chosen so that a null estimated spectrum results in a 100% error. Practically, the integrals are approximated by discrete summation over the frequency domain $\nu = q/Q$, $q \in \mathbb{N}_{Q-1}$, with $Q = 1024$.

B. Tuning Parameters

1) Usual Methods: Since no automatic parameter tuning is available for usual methods, these parameters have been chosen in order to produce the best L^2 distance. Moreover, we have checked that such a quantitative procedure finds itself in good agreement with the visual appreciation.

1) First of all, it is noticeable that, even for a short model, the nonwindowed and prewindowed methods systematically yield numerous spurious peaks. The best results have been obtained with the postwindowed form[2] (double-windowed behaves similarly) so, the estimated spectra are of poor resolution [15].
2) As expected, since the true spectra show up to three modes, the best results have been obtained with $P = 3$ for both LS and ALS.
3) Finally, as far as the ALS method is concerned, $W = 20$ has been selected.

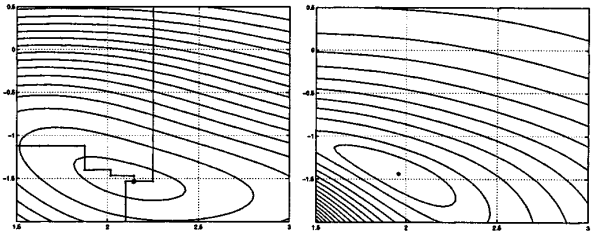

Fig. 2. The left and right figure, respectively, show HCLL and L^2 distance (L^1 behaves similarly) as a function of regularization parameters $(\lambda_\mathrm{s}, \lambda_\mathrm{d})$, respectively [read on the vertical and the horizontal axis ($\log_{10}$ scaled)]. In both cases, a star $(*)$ locates the minimum.

2) Regularized Method: The HCLL function has been computed on a fine discrete $\log_{10}$ grid of 100×100 values between -2 and 1 for λ_s and between 1 and 3 for λ_d. The result is the HCLL sheet shown in Fig. 2 (LHS). It is fairly regular and exhibits a single minimum at $\hat{\lambda}_\mathrm{s}^{\mathrm{ML}} = -1.53$ and $\hat{\lambda}_\mathrm{d}^{\mathrm{ML}} = 2.16$. Moreover, Fig. 2 right-hand side (RHS) shows the corresponding L^2 distances, and the strikingly similar behavior of $\mathrm{HCLL}(\lambda_\mathrm{s}, \lambda_\mathrm{d})$ and $\mathrm{L}^2(\lambda_\mathrm{s}, \lambda_\mathrm{d})$ is a strong argument in favor of the likelihood as a criterion for parameters tuning.

However, it must be mentioned that a variation of on-decade on λ_s or λ_d entails a nearly imperceptible variation in the estimated spectra and a fraction of percent error. This point is especially important for qualifying the robustness of the proposed method. Contrary to the choice of model order in the usual AR analysis, which is critical, the choice of $(\lambda_\mathrm{s}, \lambda_\mathrm{d})$ offers broad leeway and can be made reliably.

Practically, the adjustment is set using the coordinate descent algorithm, and Fig. 2 (LHS) illustrates its convergence from three different starting points.

C. Order Sensitivity

This section assesses the sensitivity of the method with regard to the order parameters k and P. For $P = 1$ to $P = 7$ and for $k = 0$ to $k = 2$ (step .25), we have computed the ML estimate (31)

$$\left(\hat{\lambda}_\mathrm{s}^{\mathrm{ML}}(P,k), \hat{\lambda}_\mathrm{d}^{\mathrm{ML}}(P,k)\right) = \underset{\lambda_\mathrm{s},\lambda_\mathrm{d}}{\arg\min}\, \mathrm{HCLL}(\lambda_\mathrm{s}, \lambda_\mathrm{d}, P, k)$$

and the corresponding optimal likelihood and distance

$$\mathrm{HCLL}_{\mathrm{opt}}(P,k) = \mathrm{HCLL}\left(\hat{\lambda}_\mathrm{s}^{\mathrm{ML}}(P,k), \hat{\lambda}_\mathrm{d}^{\mathrm{ML}}(P,k), P, k\right)$$

[2]A possible explanation for this rather counterintuitive fact, is that the postwindowed form is somewhat "self penalizing," i.e., the corresponding criterion incorporates quadratic penalization terms: $\boldsymbol{a}_m^\dagger M \boldsymbol{a}_m$, where M only depends upon the data.

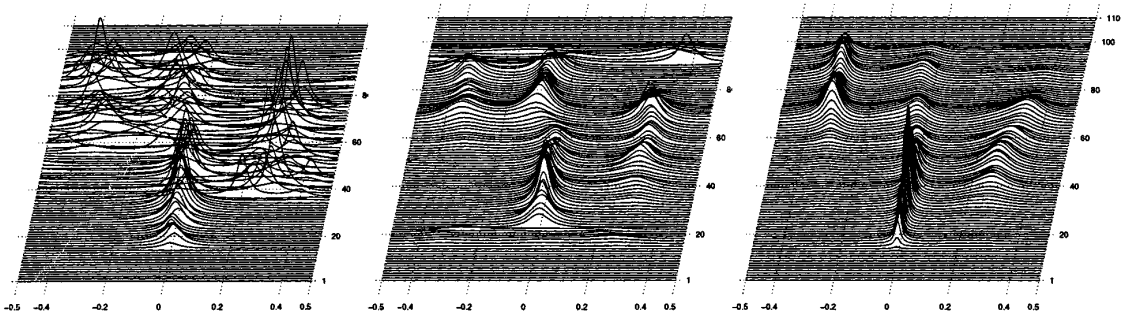

Fig. 3. (Top) Optimal likelihood $\mathrm{HCLL}_{\mathrm{opt}}(P,k)$ and (bottom) distances $\mathrm{L}^2_{\mathrm{opt}}(P,k)$ as a function of order P for several smoothness order $k = 0.5$, 1, 1.5, and 2.

$$\mathrm{L}^r_{\mathrm{opt}}(P,k) = \mathrm{L}^r\left(\hat{\lambda}^{\mathrm{ML}}_{\mathrm{s}}(P,k), \hat{\lambda}^{\mathrm{ML}}_{\mathrm{d}}(P,k), P, k\right).$$

They are plotted in Fig. 3 as a function of P for the several values of k.

As far as the likelihood is concerned, the following applies.

- $\mathrm{HCLL}_{\mathrm{opt}}$ is a decreasing (almost linear) function of model order P: the ML selected order is the maximal one $P = N - 1 = 7$.
- $\mathrm{HCLL}_{\mathrm{opt}}$ does not depend on k (the four curves are over plotted) so that, given P, the triplet $(\lambda_{\mathrm{s}}, \lambda_{\mathrm{d}}, k)$ "over-parameterizes" the likelihood and k is indifferent.

As far as the L^2 is concerned, it still behaves similarly to the likelihood. It is roughly decreasing with P and not depending upon k. As a conclusion, the maximization of the likelihood with regard to k and P does not provide any improvement and the recommended scheme described in Section VI-B is an efficient one.

D. Qualitative Evaluation

We have then compared the usual methods at their best (optimally adjusted parameters knowing the true spectra) with the proposed method (automatic selection of regularization parameters without knowledge of the true spectra). The results obtained by LS, ALS, and RegLS are presented in Fig. 4. A simple qualitative comparison with the reference Fig. 1 already leads to four conclusions.

1) The ML strategy provides a good value for the regularization parameters, and the L^2 (and L^1) distance is in accordance with the qualitative assessment.
2) The effect of the regularization is obvious. Estimated spectra are in much greater conformity with the true ones. The spectrum shapes are reproduced more precisely in one, two, or three modes. Their positions and their amplitudes are correctly estimated.
3) Moreover, the spectral resolution for the ground clutter is strongly enhanced. It is essentially due to the coherent accounting for spectral and spatial continuity resulting in a robust nonwindowed form.
4) However, it can be seen that the sudden transitions at the beginning of the ground clutter is slightly oversmoothed. This can be expected from quadratic regularization and may be at least partially avoided by introducing nonquadratic regularization [38]–[40].

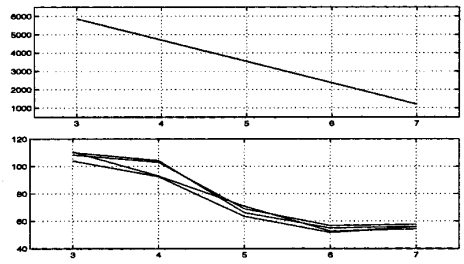

Fig. 4. Estimated spectra from left to right: usual LS estimate, adaptive LS estimate, and regularized LS estimate (proposed method). Corresponding true spectra and data are shown in Fig. 1. Quantitative results are given in Table I.

TABLE I
QUANTITATIVE COMPARISON OF THE PERIODOGRAM, LSMS, AND THE REGULARIZED ONE. L^1 AND L^2 INDICATES THE DISTANCES BETWEEN ESTIMATED AND TRUE SPECTRA

Method	L^2	L^1
Periodogram	87.1%	92.9%
Best LS	76.6%	85.4%
Best ALS	66.4%	75.5%
ML & RegLS	57.9%	69.2%

E. Quantitative Evaluation

In the nonadaptive context, quantitative comparisons have previously been performed in [1], [26]. The adaptive extension originally proposed by Kitagawa and Gersch has also been quantitatively assessed in [2].

For the proposed method, quantitative comparison have been achieved by evaluating L^1 and L^2 distances between true and estimated spectra. The results are listed in Table I and show an L^2 improvement of about 10% form periodogram to best LS, 10% from best LS to best ALS and 10% from best ALS to the entirely automatic proposed method.

VIII. CONCLUSION AND PERSPECTIVES

This paper tackles short-time adaptive AR spectral estimation within the regularization framework. It proposes a new regular-

ized LS criterion accounting for spectral smoothness and spatial continuity. The criterion is efficiently optimized by a special Kalman smoother. In this sense, the present study significantly deepens the contributions of [1], [2], given that the latter separately address spectral smoothness and spatial continuity. Moreover, the proposed method is entirely unsupervised, and it is shown that ML regularization parameters are both formally achievable and practically useful. Finally, a simulated comparison study is proposed in the field of Doppler radars. It shows an improvement of about 10%, comparing some usual methods at their best versus the entirely automatic proposed one.

Future works will be devoted to compensate for the oversmoothing character of quadratic regularization in the presence of spatial breaks. [41] accounts for spatial continuity while preserving breaks by way of a non-Gaussian state model and extended KF algorithms. In our mind, a preferable approach could be to introduce nonquadratic convex penalty terms and to minimize the resulting criterion using descent algorithms [38], [39], [42].

Acknowledgment

The authors wish to thank Mr. Grün and Mrs. Groen for their expert editorial assistance.

References

[1] G. Kitagawa and W. Gersch, "A smoothness priors long AR model method for spectral estimation," *IEEE Trans. Automat. Contr.*, vol. AC-30, pp. 57–65, Jan. 1985.

[2] ——, "A smoothness priors time-varying AR coefficient modeling of nonstationary covariance time series," *IEEE Trans. Automat. Contr.*, vol. AC-30, pp. 48–56, Jan. 1985.

[3] Y. Grenier, "Modèles ARMA à coefficients dépendant du temps," *Trait. Signal*, vol. 3, no. 4, pp. 219–233, 1986.

[4] R. Kuc, "Employing spectral estimation procedures for characterizing diffuse liver disease," in *Tissue Characterization with Ultrasound*, 1986, ch. 6, pp. 147–166.

[5] J. Idier, J.-F. Giovannelli, and B. Querleux, "Bayesian time-varying AR spectral estimation for ultrasound attenuation measurement in biological tissues," in *Proc. Section Bayesian Statistical Science*, Alicante, Spain, 1994, pp. 256–261.

[6] P. Péronneau, *Vélocimétrie Doppler. Application en Pharmacologie Cardiovasculaire Animale et Clinique*. Paris, France: INSERM, 1991.

[7] D. K. Barton and S. Leonov, *Radar Technology Encyclopedia*. London, U.K.: Artech House, 1997.

[8] G. Le Foll, P. Larzabal, and H. Clergeot, "A new parametric approach for wind profiling with Doppler radar," *Radio Sci.*, vol. 32, pp. 1391–1408, July–Aug. 1997.

[9] J. M. B. Dias and J. M. N. Leitão, "Nonparametric estimation of mean Doppler and spectral width," *IEEE Trans. Geosci. Remote Sensing*, vol. 38, pp. 271–282, Jan. 2000.

[10] N. Allan, C. L. Trump, D. B. Trizna, and D. J. McLaughlin, "Dual-polarized Doppler radar measurements of oceanic fronts," *IEEE Trans. Geosci. Remote Sensing*, vol. 37, pp. 395–417, Jan. 1999.

[11] F. Barbaresco, "Turbulences estimation with new regularized super-resolution Doppler spectrum parameters," in *RADME* Rome, Italy, 1998.

[12] M. Basseville, N. Martin, and P. Flandrin, "Méthodes temps-fréquence et segmentation de signaux," in *Numéro Spécial de Traitement du Signal*. Paris, France: JOUVE, 1992, vol. 9.

[13] J. B. Allen, "Short term spectral analysis, synthesis, and modification by discrete Fourier transform," *IEEE Trans. Acoust., Speech, Signal Processing*, vol. ASSP-25, pp. 235–238, June 1977.

[14] J. B. Allen and L. R. Rabiner, "A unified approach to short-time Fourier analysis and synthesis," *Proc. IEEE*, vol. 65, pp. 1558–1564, Nov. 1977.

[15] S. L. Marple, *Digital Spectral Analysis With Applications*. Englewood Cliffs, NJ: Prentice-Hall, 1987.

[16] S. M. Kay, *Modern Spectral Estimation*. Englewood Cliffs, NJ: Prentice-Hall, 1988.

[17] B. Picinbono, *Éléments de Probabilité*. Gif-sur-Yvette, France: Cours de SUPÉLEC, 1991, vol. 1127.

[18] S. M. Kay, "Recursive maximum likelihood estimation of autoregressive processes," *IEEE Trans. Acoust., Speech, Signal Processing*, vol. ASSP-21, pp. 56–65, 1983.

[19] D. T. Pham, "Maximum likelihood estimation of the autoregressive model by relaxation on the reflection coefficients," *IEEE Trans. Signal Processing*, vol. 36, pp. 1363–1367, Aug. 1988.

[20] S. M. Kay and S. L. Marple, "Spectrum analysis—A modern perpective," *Proc. IEEE*, vol. 69, pp. 1380–1419, Nov. 1981.

[21] H. Akaike, "Statistical predictor identification," *Ann. Inst. Statist. Math.*, vol. 22, pp. 207–217, 1970.

[22] ——, "A new look at the statistical model identification," *IEEE Trans. Automat. Contr.*, vol. AC-19, pp. 716–723, Dec. 1974.

[23] E. Parzen, "Some recent advances in time series modeling," *IEEE Trans. Automat. Contr.*, vol. AC-19, pp. 723–730, Dec. 1974.

[24] J. Rissanen, "Modeling by shortest data description," *Automatica*, vol. 14, pp. 465–471, 1978.

[25] T. J. Ulrych and R. W. Clayton, "Time series modeling and maximum entropy," *Phys. Earth Planetary Interiors*, vol. 12, pp. 188–200, 1976.

[26] J.-F. Giovannelli, G. Demoment, and A. Herment, "A Bayesian method for long AR spectral estimation: A comparative study," *IEEE Trans. Ultrason. Ferroelect. Freq. Contr.*, vol. 43, pp. 220–233, Mar. 1996.

[27] A. Houacine and G. Demoment, "A Bayesian method for adaptive spectrum estimation using high order autoregressive models," in *Mathematics in Signal Processing II*, J. G. McWhirter, Ed. Oxford, U.K.: Clavendon, 1990, pp. 311–323.

[28] D. P. Bertsekas, *Nonlinear Programming*. Belmont, MA: Athena Scientific, 1995.

[29] A. H. Jazwinski, *Stochastic Process and Filtering Theory*. New York: Academic, 1970.

[30] A. H. Sayed and T. Kailath, "A state-space approach to adaptive RLS filtering," *IEEE Trans. Signal Processing Mag.*, pp. 18–60, July 1994.

[31] G. H. Golub, M. Heath, and G. Wahba, "Generalized cross-validation as a method for choosing a good ridge parameter," *Technometrics*, vol. 21, pp. 215–223, May 1979.

[32] D. M. Titterington, "Common structure of smoothing techniques in statistics," *Int. Statist. Rev.*, vol. 53, no. 2, pp. 141–170, 1985.

[33] P. Hall and D. M. Titterington, "Common structure of techniques for choosing smoothing parameter in regression problems," *J. R. Statist. Soc. B*, vol. 49, no. 2, pp. 184–198, 1987.

[34] A. Thompson, J. C. Brown, J. W. Kay, and D. M. Titterington, "A study of methods of choosing the smoothing parameter in image restoration by regularization," *IEEE Trans. Pattern Anal. Machine Intell.*, vol. 13, pp. 326–339, Apr. 1991.

[35] N. Fortier, G. Demoment, and Y. Goussard, "GCV and ML methods of determining parameters in image restoration by regularization: Fast computation in the spatial domain and experimental comparison," *J. Visual Comm. Image Repres.*, vol. 4, pp. 157–170, June 1993.

[36] R. Shumway and D. Stoffer, "An approach to time series smoothing and forecasting using the EM algorithm," *J. Time Series Anal.*, pp. 253–264, 1982.

[37] S. E. Levinson, L. R. Rabiner, and M. M. Sondhi, "An introduction to the application of the theory of probabilistic function of a Markov process to automatic speech processing," *Bell Syst. Tech. J.*, vol. 62, pp. 1035–1074, Apr. 1982.

[38] C. A. Bouman and K. D. Sauer, "A generalized Gaussian image model for edge-preserving MAP estimation," *IEEE Trans. Image Processing*, vol. 2, pp. 296–310, July 1993.

[39] P. J. Green, "Bayesian reconstructions from emission tomography data using a modified EM algorithm," *IEEE Trans. Med. Imag.*, vol. 9, pp. 84–93, Mar. 1990.

[40] L. Rudin, S. Osher, and C. Fatemi, "Nonlinear total variation based noise removal algorithm," *Phys. D*, vol. 60, pp. 259–268, 1992.

[41] G. Kitagawa, "Non-Gaussian state-space modeling of nonstationary time series," *J. Amer. Statist. Assoc.*, vol. 82, pp. 1032–1041, Dec. 1987.

[42] J. Idier, "Convex half-quadratic criteria and interacting auxiliary variables for image restoration," *IEEE Trans. Image Processing*, vol. 10, July 2001.

Jean-François Giovannelli was born in Béziers, France, in 1966. He received the degree from the École Nationale Supérieure de l'Électronique et de ses Applications, Paris, France, and the Ph.D. degree in physics from the Laboratoire des Signaux et Systèmes, Université de Paris-Sud, Orsay, France, in 1990 and 1995, respectively.

He is currently an Assistant Professor with the Département de Physique, Université de Paris-Sud, Paris, France. He is interested in regularization methods for inverse problems in signal and image processing, mainly in spectral characterization. Application fields essentially concern radar and medical imaging.

Jérôme Idier was born in France in 1966. He received the diploma degree in electrical engineering from the École Supérieure d'Électricité, Paris, France, and the Ph.D. degree in physics from the Université de Paris-sud, Orsay, in 1988 and 1991, respectively.

Since 1991, he has been with the Centre National de la Recherche Scientifique, Paris, France, assigned to the Laboratoire des Signaux et Systèmes. His major scientific interests are in probabilistic approaches to inverse problems for signal and image processing.

Daniel Muller was born in Saint-Cloud, France, on August 12, 1961. He received the degree from "Ecole Polytechnique," Palaiseau, France, in 1983, and the Ph.D. degree in electrical engineering from "Ecole Supérieure d'Electricité," Gif-sur-Yvette, France, in 1985.

In 1985, he joined Thales, formerly Thomson-CSF, France, where he was involved in the functional design and performance assessment of several new Radar products and demonstrators. He is now in charge of the Algorithms and Functional Architecture Department, in the Technical Direction of the "Radar Development" Business Unit, Thales Air Defence.

Guy Desodt was born in Bailleul, France, on May 8, 1952.

He has been with the Thales Group, formerly Thomson-CSF, France, for 22 years, working in the area of ground-based and naval radars. His main areas of interest are innovative radar architectures, including new signal and data processing chains, like adaptive Doppler processing, multibeam adaptive digital beam forming, and noncooperative target recognition.

P. Ciuciu, J. Idier et **J.-F. Giovannelli**, « Regularized estimation of mixed spectra using a circular Gibbs-Markov model », *IEEE Trans. Signal Processing*, vol. 49, n°10, pp. 2201–2213, octobre 2001.

2202 IEEE TRANSACTIONS ON SIGNAL PROCESSING, VOL. 49, NO. 10, OCTOBER 2001

Regularized Estimation of Mixed Spectra Using a Circular Gibbs–Markov Model

Philippe Ciuciu, Jérôme Idier, and Jean-François Giovannelli

***Abstract*—Formulated as a linear inverse problem, spectral estimation is particularly underdetermined when only short data sets are available. Regularization by penalization is an appealing nonparametric approach to solve such ill-posed problems. Following Sacchi *et al.*, we first address line spectra recovering in this framework. Then, we extend the methodology to situations of increasing difficulty: the case of smooth spectra and the case of *mixed* spectra, i.e., peaks embedded in smooth spectral contributions. The practical stake of the latter case is very high since it encompasses many problems of target detection and localization from remote sensing.**

The stress is put on adequate choices of penalty functions: Following Sacchi *et al.*, *separable* functions are retained to retrieve peaks, whereas Gibbs–Markov potential functions are introduced to encode spectral smoothness. Finally, mixed spectra are obtained from the conjunction of contributions, each one bringing its own penalty function.

Spectral estimates are defined as minimizers of strictly convex criteria. In the cases of smooth and mixed spectra, we obtain nondifferentiable criteria. We adopt a *graduated nondifferentiability* approach to compute an estimate. The performance of the proposed techniques is tested on the well-known Kay and Marple example.

***Index Terms*—High-resolution, mixed spectra, regularization, spectral estimation, spectral smoothness.**

I. Introduction

THE PROBLEM of spectral estimation has been receiving considerable attention in the signal processing community since it arises in various fields of engineering and applied physics, such as spectrometry, geophysics [1], biomedical Doppler echography [3], radar, etc. In particular, our primary field of interest is short-time estimation of atmospheric sounding or wind profiling, possibly superimposed on a small set of targets, from radar Doppler data [4].

A survey of classical methods for spectral estimation can be found in [2]. When the problem at hand is the restoration of *smooth spectra* (SS), basic nonparametric methods based on the discrete Fourier transform (DFT) such as periodograms are often taken up. Such techniques usually involve a windowing or an averaging step, which requires a sufficiently large data set. By contrast, estimation of *line spectra* (LS) is more often dealt with in parametric methods, such as Pisarenko's harmonic decomposition [5], Prony's approaches [6], [7], or autoregressive (AR) methods [2], [8], [9]. These techniques are known for their ability to separate close harmonics. Consequently, they are usually considered under the heading of *high-resolution* methods [2].

In the more difficult case of *mixed spectra* (MS), i.e., small sets of harmonics embedded in smooth spectral components, no satisfying techniques exist according to [2], [9], and [10]. The main aim of the present paper is to contribute to filling the gap within a nonparametric framework related to a recent contribution due to Sacchi *et al.* [1]. One important conclusion drawn in the latter was that enhanced nonparametric methods can reach high resolution, which somewhat contradicts the state of the art sketched in [2].

Following [1], Section II starts with modeling the unknown spectral amplitudes as the DFT of the available observations. In particular, the number of Fourier coefficients to be estimated is larger than the length of the data sequence. The current problem is therefore underdetermined. Then, we resort to regularization by penalization to balance the lack of information provided by data with an available prior knowledge, such as spikyness or spectral regularity. Since the main part of our construction is made in a deterministic framework, Section II is also devoted to a natural question: Is it theoretically justified to resort to our approach to estimate power spectral densities (PSDs).

Three penalty functions are designed for solving the LS, SS, and MS issues, respectively (see Section III). Following [1], a *separable* function is retained for line spectra (Section III-B). To deal with smooth spectra estimation, our construction is inspired by Gibbs–Markov edge-preserving models for image restoration [11]–[13] (see Section III-C). Finally, mixed spectra are obtained from the conjunction of contributions, each one bringing its own penalty function (Section III-D).

In all cases, the spectral estimate is defined as the minimizer of a strictly convex criterion, which is chosen nonquadratic to avoid oversmoothing effects [1], [14]. Practical computation of spectral estimates is tackled in Section IV. In the cases of smooth and mixed spectra, we obtain a nondifferentiable criterion, and we adopt a *graduated nondifferentiability* approach to compute an estimate. The performances of our spectral estimates are tested in Section V on the well-known Kay and Marple example [2]. Finally, concluding remarks and perspectives are drawn in Section VI.

Manuscript received May 1, 2000; revised June 21, 2001. The associate editor coordinating the review of this paper and approving it for publication was Prof. Philippe Loubaton.

P. Ciuciu is with the Commissariat à l'Énergie Atomique DSV/DRM/SHFJ, Orsay, France (e-mail: ciuciu@shfj.cea.fr).

J. Idier and J.-F. Giovannelli are with the Laboratoire des Signaux et Systèmes, CNRS-SUPÉLEC-UPS, Gif-sur-Yvette, France (e-mail: name@lss.supelec.fr).

Publisher Item Identifier S 1053-587X(01)07765-0.

II. Problem Statement

A. Deterministic Framework

Following contributions such as [1] and [15], we formulate spectral estimation as a linear underdetermined inverse problem in a deterministic framework. Given discrete time observations $\boldsymbol{y} = [y_0, y_1, \ldots, y_{N-1}]^t$, the goal is to recover the energy distribution of data between frequencies 0 and 1. In the general setting of the paper, complex discrete data are processed to estimate spectral coefficients for normalized frequencies between 0 and 1 (the real data case is specifically examined in Appendix D).

The harmonic frequency model is usually considered for this task. In such a model, the distribution of spectral amplitudes $X(\nu)$ is continuous with respect to (w.r.t.) frequencies ν. Then, the inverse discrete-time Fourier transform links the unknown spectral function $X(\nu) \in L^2_{\mathbb{C}}[0, 1]$ to a complex time series $(x_n)_{n\in\mathbb{Z}}$ (of finite energy) according to

$$x_n = \int_0^1 X(\nu)\, e^{2j\pi\nu n}\, d\nu, \qquad n \in \mathbb{Z}. \tag{1}$$

The signal $(x_n)_{n\in\mathbb{Z}}$ is partially observed through the data

$$x_n = y_n, \qquad n \in \mathbb{N}_N \triangleq \{0, 1, \ldots, N-1\}.$$

Within this setting, our approach consists in extracting a deterministic extension $(x_n)_{n\in\mathbb{Z}}$ of the data $\boldsymbol{y}$. Since this extension is of finite energy, it cannot be interpreted in general as a sample path of a stationary random process (see Section II-B for details).

Estimating $X(\nu)$ from $\boldsymbol{y}$ is a discrete-time continuous-frequency problem. Akin to [1], we propose to solve a discrete frequency approximation. It corresponds to the juxtaposition of a large number of sinusoids, say $P \gg N$, at equally sampled frequencies $\nu_p = p/P$, $p \in \mathbb{N}_P$. The accuracy of the approximation depends strongly on P since the discrete counterpart of (1) reads

$$y_n = \sum_{p=0}^{P-1} X_p\, e^{2j\pi\nu_p n}, \qquad n \in \mathbb{N}_N \tag{2}$$

where $X_p \in \mathbb{C}$ are unknown spectral amplitudes. In the case of line spectrum estimation, choosing a large P seems clear since the harmonic components do not necessarily coincide with any sample of the grid. In the case of a continuous background, P is selected for suitably balancing the tradeoff between an efficient computation of the estimate and a more accurate result. If $P = N$ could be satisfactory for smooth spectra (e.g., Gaussian spectra with variance $\sigma > 0.1$), it could be preferable to consider higher values for piecewise smooth spectra with sharp transitions, such as ARMA PSDs with zeros of the MA part close to the poles of the AR part [16].

Let $w_0 = \exp(2j\pi/P)$ so that $W_{NP} = [w_0^{np}]_{n\in\mathbb{N}_N}^{p\in\mathbb{N}_P}$ is an $N \times P$ Fourier matrix, and an equivalent formulation of (2) is

$$\boldsymbol{y} = W_{NP}\boldsymbol{X} \tag{3}$$

where $\boldsymbol{X} = [X_0, X_1, \ldots, X_{P-1}]^t$. Since $N \ll P$, (3) is underdetermined, and there exists an infinite number of solutions. The problem is to incorporate structural information to raise the underdeterminacy in an appropriate manner.

B. Random Processes

Following [1], our spectral estimation approach is based on the ground of deterministic Fourier analysis. Hence, a natural question arises: Is it theoretically justified to resort to our construction to estimate PSDs. In this subsection, we put forward that our approach is not a natural tool as far as PSD estimation is concerned.

Let $(S_n)_{n\in\mathbb{Z}}$ be a complex-valued random time series defined by

$$S_n = \int_0^1 e^{2j\pi\nu n}\, dS(\nu) \tag{4}$$

where $dS(\nu)$ stands for the random spectral measure of S. In a discrete-frequency framework, (4) can be approximated by

$$S_n^P = \sum_{p=0}^{P-1} S([p/P, (p+1)/P[)\, e^{2j\pi np/P}.$$

Our approach consists in estimating the variables $S([p/P, (p+1)/P[)$ and then in evaluating a spectrum of S through the vector of squared modulus $|S([p/P, (p+1)/P[)|^2$ (see Section III). In the case of a regular random process, such quantities are random. Thus, they do not identify with a discretized version of the PSD.

Nonetheless, as shown in [17], it is possible to exhibit a family of singular random processes for which our approach allows us to characterize the power spectral measure of such processes.

III. Methodology

A. General Setting

Sacchi *et al.* [1] have proposed a penalized approach, where an estimator of spectral amplitudes is defined as

$$\widehat{\boldsymbol{X}} \text{ minimizes } \mathcal{J}(\boldsymbol{X}) \text{ in } \mathbb{C}^P \tag{5}$$

with

$$\mathcal{J} = \mathcal{Q} + \lambda\mathcal{R} \tag{6}$$

$$\mathcal{Q}(\boldsymbol{X}) = \|\boldsymbol{y} - W_{NP}\boldsymbol{X}\|^2 \tag{7}$$

and the power spectrum estimator easily deduces as the squared modulus of the components of $\hat{\boldsymbol{X}}$.

The hyperparameter $\lambda > 0$ controls the tradeoff between the closeness to data and the confidence in a structural prior embodied in $\mathcal{R}$. In particular, in the case of *accurate data* ($\lambda \to 0$; see [1, Sec. 4.A]), Sacchi *et al.*resort to Lagrange multipliers to prove that $\hat{\boldsymbol{X}}$ identifies with the constrained minimizer of $\mathcal{R}(\boldsymbol{X})$ subject to (3).

In [1], the chosen penalty function reads

$$\mathcal{R}(\boldsymbol{X}) = \sum_{p=0}^{P-1} \log(1 + |X_p|^2/2\tau^2) \tag{8}$$

where $\tau > 0$ is a tunable scaling parameter that controls the amount of sparseness in the solution. In [18] and [19], the abso-

lute norm $\mathcal{R}(\boldsymbol{X}) = \sum_{p=0}^{P-1} |X_p|$ is used instead because of its convexity, even if it is nonsmooth at zero. In both cases, let us remark that $\mathcal{R}$ is

- separable, i.e., it is a sum of scalar functions (9a)
- shift-invariant:
$$\mathcal{R}(X_0, X_1, \ldots, X_{P-1}) = \mathcal{R}(X_1, \ldots, X_{P-1}, X_0) \tag{9b}$$
- symmetry-invariant:
$$\mathcal{R}(X_0, X_1, \ldots, X_{P-1}) = \mathcal{R}(X_{P-1}, \ldots, X_1, X_0) \tag{9c}$$
- circular:
$$\mathcal{R}(X_0, \ldots, X_{P-1}) = \mathcal{R}(|X_0|, \ldots, |X_{P-1}|). \tag{9d}$$

Reference [1] adopts the classical Bayesian interpretation of $\hat{\boldsymbol{X}}$ as a maximum *a posteriori* estimate. As a random vector, $\boldsymbol{X}$ is given a prior neg-log-density proportional to $\mathcal{R}(\boldsymbol{X})$, which amounts to choosing a product of circular Cauchy density functions as the *a priori* model. In such a probabilistic framework, properties of $\mathcal{R}$ can be restated as properties of the complex random vector $\boldsymbol{X}$; it is white according to (9a), stationary according to (9b), reversible according to (9c), and phases are uniformly distributed according to (9d).

Considering a circular model is rather natural since no phase information is available. Stationarity and reversibility are also fair assumptions, unless some specific frequency domain shape information is known *a priori* (see [15] and references therein). Finally, choosing an independent prior seems justified as far as line spectra estimation is concerned. In the present paper, this framework is generalized to other kinds of spectra. More specifically, a stationary Gibbs–Markov model in the frequency domain will be introduced to incorporate spectral smoothness (see Section III-C).

From the computational viewpoint, (8) may not be the better choice since $\log(1 + x^2)$ is not a convex function on $\mathbb{R}_+$: $\hat{\boldsymbol{X}}$ is not necessarily unique, and minimizing (6) using a local method such as the *iterative reweighted least squares* (IRLS) algorithm used in [1] may provide a local minimizer instead of a global solution. The absolute norm is also a possible choice [18], [19]. However, because it is nondifferentiable at zero, its optimization requires more sophisticated numerical tools, such as quadratic programming methods. In the present paper, we restrict the choice to *strictly convex* penalty functions $\mathcal{R}$ in order to ensure that $\mathcal{J}$ is also strictly convex. As a consequence, $\mathcal{J}$ admits no local minima. Moreover, the minimizer $\hat{\boldsymbol{X}}$ is unique and continuous w.r.t. the data [21]; this guarantees the well-posedness of the regularized problem [22]. Finally, many deterministic descent methods (such as gradient-based methods and the IRLS algorithm [23], [24]) will be ensured to converge toward $\hat{\boldsymbol{X}}$ if $\mathcal{R}$ is

- continuously differentiable (C^1) (10a)
- strictly convex (10b)
- "infinite at infinity": $\lim_{\|\boldsymbol{X}\| \to \infty} \mathcal{R}(\boldsymbol{X}) = \infty.$ (10c)

The construction of penalty functions that fulfill (10) forms the guideline of the next three subsections in the LS, SS, and MS cases, respectively.

B. Line Spectra

We are naturally led to penalty functions $\mathcal{R}_L$ that satisfy (9) and (10) (the subscript "L" stands for *line*). It is not difficult to see that (9) imposes the following form for $\mathcal{R}_L$:

$$\mathcal{R}_L(\boldsymbol{X}) = \sum_{p=0}^{P-1} R_0(\rho_p) \tag{11}$$

where $\rho_p = |X_p|$ and R_0: $\mathbb{R}_+ \mapsto \mathbb{R}$. Then, the following proposition characterizes those functions R_0 that ensure the convexity of $\mathcal{R}_{\mathrm{L}}$.

Proposition 1: Let f: $\mathbb{C} \mapsto \mathbb{R}$ be a circular function. Then, f is (resp. strictly) convex *if and only if* its restriction on $\mathbb{R}_+$ is a (resp. strictly) convex, nondecreasing (resp. increasing) function.

Proof: This property corresponds to the scalar case ($m = 1$) of Theorem 2 (Section III-C), which is proved in Appendix B. ■

From Proposition 1, it is apparent that $\mathcal{R}_{\mathrm{L}}(\boldsymbol{X})$ is not convex if $R_0(\rho) = \log(1 + \rho^2/2\tau^2)$. Moreover, it can be then proved that $\mathcal{J}$ is not convex either. Thus, we prefer an alternate *convex* function R_0 that would enhance spectral peaks like the Cauchy prior does. We have borrowed such penalty functions from the field of *edge-preserving* image restoration [11]–[13], [25]–[27]. More precisely, we propose to resort to the following set of functions:

$$\mathcal{S} = \Big\{ f\colon \mathbb{R}_+ \mapsto \mathbb{R} \text{ convex, increasing, } C^1, \quad f'(0^+) = 0$$
$$0 < \lim_{x \to 0^+} f'(x)/x < \infty, \quad \lim_{x \to \infty} f'(x) < \infty \Big\}.$$

If $R_0 \in \mathcal{S}$, the global criterion $\mathcal{J}$ clearly fulfills (10). On the other hand, functions in $\mathcal{S}$ behave quadratically around zero and linearly at infinite

$$0 < \lim_{x \to 0^+} f(x)/x^2 < \infty, \qquad 0 < \lim_{x \to \infty} f(x)/x < \infty.$$

This is a relevant behavior for erasing small variations, as well as for preserving large peaks and discontinuities that would be oversmoothed by quadratic penalization.

Some functions of $\mathcal{S}$, such as the *fair* function $R_0(\rho) = \rho/\tau_0 - \ln(1 + \rho/\tau_0)$ [12], [28] or Huber's function $R_0(\rho) = \rho^2/2\tau_0 + \tau_0/2$ if $\rho < \tau_0$, ρ otherwise [29], have also been known for a long time in the field of robust statistics [28], [29]. They behave quadratically under the threshold τ_0 and linearly above. In practical simulations (see Section V-B-2), we have selected the *hyperbolic* potential $R_0(\rho) = \sqrt{\tau_0^2 + \rho^2}$ in $\mathcal{S}$.

C. Smooth Spectra

1) Complex Gibbs–Markov Regularization: In the field of signal and image restoration, Gibbs–Markov potential functions are often used as roughness penalty functions [11]–[13], [21], [26], [27], [30]. Adopting this approach in the case of spectral

regularity, one might think of simply penalizing differences between complex coefficients, using

$$\mathcal{R}_S^1(\boldsymbol{X}) = \sum_{p=0}^{P-1} R_1(|X_{p+1} - X_p|) \tag{12}$$

where $X_P = X_0$ because of the circularity constraint. In (12), the subscript "S" stands for *smooth*. Then, provided that R_1 is convex and nondecreasing on $\mathbb{R}_+$, it is not difficult to deduce that $\mathcal{R}_\mathrm{S}^1$ is convex from Proposition 1. When R_1 is quadratic, the estimated spectrum is a windowed periodogram, i.e., a low-resolution solution [14]. In Section V-B3, we have performed simulations using the hyperbolic function $R_1(\rho) = \sqrt{\tau_1^2 + \rho^2}$ in order to obtain solutions of higher resolution. The corresponding results are actually disappointing (e.g., Fig. 3). Empirically, we observe that the penalty term (12) corresponds to spectral smoothness only roughly, whereas it produces hardly controllable artifacts. In fact, (12) is not a circular function of $\boldsymbol{X}$: $\mathcal{R}_\mathrm{S}^1$ does not satisfy (9d). The regularization function $R_1(|X_{p+1} - X_p|)$ also introduces a smoothness constraint on the phases of the sinusoids, which does not coincide with some available prior knowledge. For this reason, let us examine the consequences of restricting to circular penalty terms.

2) Circular Gibbs–Markov Regularization: The simplest circular energy coding spectral continuity is clearly

$$\mathcal{R}_S^2(\boldsymbol{X}) = \sum_{p=0}^{P-1} R_1(\rho_{p+1} - \rho_p) \tag{13}$$

since only two magnitudes ρ_p and ρ_{p+1} are involved. As an extension, one could consider higher order smoothness terms such as $R_1(\rho_{p+1} - 2\rho_p + \rho_{p-1})$, which would be better adapted to restore piecewise linear unknown functions.

It is readily seen that (13) satisfies all conditions (9), save separability. Unfortunately, $\mathcal{R}_\mathrm{S}^2$ is not convex if R_1 is an even, convex function. This negative result is a solidforward consequence of Corollary 1, which is stated below. Therefore, we propose to retain a slightly more general circular expression

$$\mathcal{R}_\mathrm{S}(\boldsymbol{X}) = \sum_{p=0}^{P-1} \mu R_1(\rho_{p+1} - \rho_p) + R_2(\rho_p) \tag{14}$$

where parameter $\mu \geqslant 0$ tunes the amount of spectral smoothness, and R_2: $\mathbb{R}_+ \mapsto \mathbb{R}$. Expression (14) still satisfies conditions (9b)–(9d).

In the following, a necessary and sufficient condition for the convexity of $\mathcal{R}_\mathrm{S}$ is given. For this purpose, the definition of a *coordinatewise nondecreasing* function is a prerequisite. We also provide a useful theorem regarding the composition of convex functions.

Definition 1: A function f: $\mathbb{R}_+^m \mapsto \mathbb{R}$ is said to be *coordinatewise nondecreasing if and only if* $\forall i \in \{1, \ldots, m\}$

$$\forall \boldsymbol{x} \in \mathbb{R}_+^m,\ \forall t \geqslant 0, \qquad f(\boldsymbol{x}) \leqslant f(\boldsymbol{x} + t\mathbf{1}_i)$$

where $\mathbf{1}_i$ is the ith canonical vector. The function f is said to be *coordinatewise increasing* if the latter inequalities are strict.

Theorem 1: Let f: $\mathbb{R}_+^m \mapsto \mathbb{R}$ be a convex, coordinatewise nondecreasing (resp. increasing) function, and let $\boldsymbol{g} : \mathbb{R}^n \mapsto \mathbb{R}_+^m$ be a function such that each component $g_k : \mathbb{R}^n \mapsto \mathbb{R}_+$ is (resp. strictly) convex. Then, $f \circ \boldsymbol{g}$ is (resp. strictly) convex on $\mathbb{R}^n$.

Proof: See Appendix A. ■

Theorem 2: Let f: $\mathbb{C}^m \mapsto \mathbb{R}$ be a circular function. Then, f is (resp. strictly) convex *if and only if* its restriction on $\mathbb{R}_+^m$ is a (resp. strictly) convex coordinatewise nondecreasing (resp. increasing) function.

Proof: See Appendix B. ■

Because $R_1(\rho_{p+1} - \rho_p)$ is not a coordinatewise nondecreasing function of $\boldsymbol{\rho} = [\rho_0\ \ldots, \rho_{P-1}]^t$, (13) is not convex, according to Theorem 2. In the case of (14), application of Theorem 2 yields the following result.

Corollary 1: Let R_1: $\mathbb{R} \mapsto \mathbb{R}$ and R_2: $\mathbb{R}_+ \mapsto \mathbb{R}$ be C^1 functions that satisfy the following assumptions:

- R_1 is even and convex (15a)
- R_2 is (resp. strictly) convex and nondecreasing (resp. increasing) (15b)
- $\mu \leqslant \mu_\mathrm{sup} = R_2'(0^+)/2R_1'(\infty)$. (15c)

Then, function $\mathcal{R}_\mathrm{S}$ defined by (14) is (resp. strictly) convex.

Proof: See Appendix C. ■

Inequality (15c) gives an upper bound on the smoothness level that can be introduced while maintaining convexity of $\mathcal{R}_\mathrm{S}$. It is important to notice that $\mu_\mathrm{sup} > 0$ imposes $R_2'(0^+) > 0$. In the rest of the paper, we have selected the simplest potential R_2 that satisfies $R_2'(0^+) > 0$, i.e., $R_2(\rho) = \rho$. Combined with the hyperbolic function $R_1(\rho) = \sqrt{\tau_1^2 + \rho^2}$, such a choice yields that $\mathcal{R}_\mathrm{S}$ is convex if $\mu \leqslant 1/2$.

The condition $R_2'(0^+) > 0$ means that $R_2(|\cdot|)$ is not differentiable on $\mathbb{C}$ at zero, and therefore, $\mathcal{R}_\mathrm{S}$ is nondifferentiable. Although conditions (15) are only sufficient, we have the intuition that convexity and differentiability are actually incompatible properties of $\mathcal{R}_\mathrm{S}$, as defined by (14). In Section IV, we propose to minimize a close approximation of $\mathcal{R}_\mathrm{S}$ that conciliates convexity and differentiability so that a converging approximation of $\hat{\boldsymbol{X}}$ can be easily computed.

D. Mixed Spectra

A *mixed* spectrum consists of both frequency peaks and smooth spectral components; therefore, we propose to split vector $\boldsymbol{X}$ into two sets of unknown variables: $\boldsymbol{X}_L$ for the frequency peaks and $\boldsymbol{X}_S$ for the smoother components. The resulting fidelity to data term $\mathcal{Q}_\mathrm{M}$ reads

$$\mathcal{Q}_\mathrm{M}(\boldsymbol{X}) = \|\boldsymbol{y} - W_{NP}(\boldsymbol{X}_\mathrm{L} + \boldsymbol{X}_\mathrm{S})\|^2 = \|\boldsymbol{y} - W_{NP}\boldsymbol{X}[1,\ 1]^t\|^2$$

where $\boldsymbol{X} = [\boldsymbol{X}_\mathrm{L}|\boldsymbol{X}_\mathrm{S}]$ is a $P \times 2$ complex matrix. The subscript "M" stands for *mixed*.

Then, it is only natural to introduce $\mathcal{R}_\mathrm{L}$ [which is defined by (11)] and $\mathcal{R}_\mathrm{S}$ [which is defined by (14)] as specific penalty terms for $\boldsymbol{X}_\mathrm{L}$ and $\boldsymbol{X}_\mathrm{S}$, respectively. The resulting criterion $\mathcal{J}_\mathrm{M}$ reads

$$\mathcal{J}_\mathrm{M}(\boldsymbol{X}) = \mathcal{Q}_\mathrm{M}(\boldsymbol{X}) + \lambda_\mathrm{L}\mathcal{R}_\mathrm{L}(\boldsymbol{X}_\mathrm{L}) + \lambda_\mathrm{S}\mathcal{R}_\mathrm{S}(\boldsymbol{X}_\mathrm{S}) \tag{16}$$

which is a nondifferentiable function w.r.t. vanishing components of $\boldsymbol{X}_\mathrm{S}$, if $R_2'(0^+) > 0$. On the other hand, $\mathcal{J}_\mathrm{M}$ is (resp.

strictly) convex w.r.t. $\boldsymbol{X}$ if $\mathcal{R}_{\mathrm{L}}$, and $\mathcal{R}_{\mathrm{S}}$ are (resp. strictly) convex. Then, the global minimizer is uniquely defined by

$$\widehat{\boldsymbol{X}} = \left[\widehat{\boldsymbol{X}}_{\mathrm{L}} \middle| \widehat{\boldsymbol{X}}_{\mathrm{S}}\right] = \arg\min_{\boldsymbol{X}} \mathcal{J}_{\mathrm{M}}(\boldsymbol{X}).$$

In the Bayesian framework adopted in [1], it is not difficult to see that $(\hat{\boldsymbol{X}}_{\mathrm{L}}, \hat{\boldsymbol{X}}_{\mathrm{S}})$ corresponds to the joint MAP solution obtained from a prior neg-log-density proportional to $\lambda_{\mathrm{L}}\mathcal{R}_{\mathrm{L}}(\boldsymbol{X}_{\mathrm{L}}) + \lambda_{\mathrm{S}}\mathcal{R}_{\mathrm{S}}(\boldsymbol{X}_{\mathrm{S}})$. Finally, the estimated frequency distribution is taken as the squared modulus of the components of $\hat{\boldsymbol{X}}_{\mathrm{L}} + \hat{\boldsymbol{X}}_{\mathrm{S}}$.

Among possible refinements, a shorter vector $\boldsymbol{X}_{\mathrm{S}}$ could be introduced to encode the smooth components of the spectrum, as long as they require less accuracy. Then, the fidelity to data term would become

$$\mathcal{Q}_{\mathrm{M}}(\boldsymbol{X}) = \|\boldsymbol{y} - W_{NP}\boldsymbol{X}_{\mathrm{L}} - W_{QP}\boldsymbol{X}_{\mathrm{S}}\|^2$$

where $Q < P$. Such a modification could provide a (probably slight) increase of overall convergence speed at roughly constant quality of estimation.

IV. Optimization Stage

A. Graduated Nondifferentiability

Nondifferentiable (i.e., *nonsmooth*) convex criteria can neither be straightforwardly minimized by gradient-based algorithms since the gradient is not defined everywhere nor by coordinate descent methods [31, p. 61]. Nonetheless, there exist several ways to efficiently minimize such criteria [31]–[34]. Here, we resort to the so-called *regularization method* [31], [32], [35], [36]. In the following, it is instead referred to as a *graduated nondifferentiability* (GND) approach, in order to avoid the possible confusion with the notion of regularization for ill-posed problems. The principle is to successively minimize a discrete sequence of convex differentiable approximations that converge toward the original nonsmooth criterion.

We have adopted the GND approach because it is flexible, easy to implement, and mathematically convergent. Under suitable conditions, the series of minimizers converges to the solution of the initial nonsmooth programming problem [31], [32], [35], [36]. More specifically, we have the following result, based on [31, pp. 21–22].

Proposition 2: Let $\mathcal{J}\colon \mathbb{C}^P \mapsto \mathbb{R}$ fulfill (10b) and (10c) but not (10a), and let $\mathcal{J}_\varepsilon$ $(\varepsilon > 0)$ be a series of approximations of $\mathcal{J}$ that fulfills the three conditions (10). If $\mathcal{J}_\varepsilon$ converges toward $\mathcal{J}$ in the following sense:

$$\begin{cases} \forall \boldsymbol{X},\ \lim_{\varepsilon\to 0}\mathcal{J}_\varepsilon(\boldsymbol{X}) = \mathcal{J}(\boldsymbol{X}) \\ \lim_{\varepsilon\to 0}\mathcal{J}_\varepsilon\left(\hat{\boldsymbol{X}}_\varepsilon\right) \geqslant \mathcal{J}\left(\hat{\boldsymbol{X}}\right) \end{cases} \tag{17}$$

where

$$\widehat{\boldsymbol{X}} = \arg\min_{\boldsymbol{X}\in\mathbb{C}^P} \mathcal{J}(\boldsymbol{X}), \qquad \widehat{\boldsymbol{X}}_\varepsilon = \arg\min_{\boldsymbol{X}\in\mathbb{C}^P} \mathcal{J}_\varepsilon(\boldsymbol{X})$$

then

$$\lim_{\varepsilon\to 0}\hat{\boldsymbol{X}}_\varepsilon = \hat{\boldsymbol{X}}.$$

Remark 1: In more general settings, convergence results akin to Proposition 2 can be obtained using the theory of Γ convergence, which is a powerful mathematical tool in the study of the limiting behavior of the minimizer of a series of functions [37].

The remaining part of the section is devoted to the case of smooth spectra, i.e., to the minimization of $\mathcal{J}_S$ defined by (6), (7), and (14). Extension to the minimization of $\mathcal{J}_M$ is straightforward.

B. Differentiable Approximation of Convex Gibbs–Markov Penalty Function

Practically, it is a prerequisite to build a differentiable convex approximation $\mathcal{R}_{\mathrm{S},\varepsilon}$ of the penalty term $\mathcal{R}_{\mathrm{S}}$ such that the series

$$\mathcal{J}_\varepsilon = \mathcal{Q} + \lambda\mathcal{R}_{S,\varepsilon} \tag{18}$$

satisfies the conditions of Proposition 2. Our construction of $\mathcal{R}_{\mathrm{S},\varepsilon}$ is based on the hyperbolic differentiable approximation of the magnitude function $|\cdot|$:

$$\varphi_\varepsilon\colon \mathbb{C} \mapsto \mathbb{R}_+, \qquad \varphi_\varepsilon(x) = \sqrt{\varepsilon^2 + |x|^2} \tag{19}$$

where $\varepsilon > 0$. Such an approximation is known to satisfy conditions (17) [31, pp. 21–22] and has been already used in the field of image restoration [26], [27]. It is also called the *standard mollifier procedure* [26].

Let $q_p = \varphi_\varepsilon(X_p) = \varphi_\varepsilon(\rho_p)$ denote the above differentiable approximation of ρ_p and $\boldsymbol{q} = [q_0, q_1, \ldots, q_{P-1}]^t$. Then, the resulting modified smoothness penalty term $\mathcal{R}_{\mathrm{S},\varepsilon}$ satisfies (10), whereas $\mathcal{R}_{\mathrm{S}}$ only satisfies (10b) and (10c), according to the following consequence of Theorem 1 and of Corollary 1.

Corollary 2: Let R_1 meet the weak form of conditions (15) in Corollary 1, along with $R_2(\rho) = \rho$. Then, the modified penalty term

$$\mathcal{R}_{\mathrm{S},\varepsilon}(\boldsymbol{X}) = \sum_{p=0}^{P-1} \mu R_1(q_{p+1} - q_p) + q_p \tag{20}$$

is a strictly convex function of $\boldsymbol{X}$.

Proof: Let us remark that $\mathcal{R}_{\mathrm{S},\varepsilon} = \mathcal{R}_{\mathrm{S}} \circ \boldsymbol{\varphi}$, where $\boldsymbol{\varphi} = (\varphi_\varepsilon, \ldots, \varphi_\varepsilon)$ and $\mathcal{R}_{\mathrm{S}}$ is defined by (14) with $R_2(\rho) = \rho$. Then, the proof is an application of Theorem 1, with $\boldsymbol{g} = \boldsymbol{\varphi}$ and $f = \mathcal{R}_{\mathrm{S}}$, given that i) each φ_k is strictly convex, and ii) according to Corollary 1, the restriction of $\mathcal{R}_{\mathrm{S}}$ on $\mathbb{R}_+^m$ is convex and coordinatewise increasing.[1] ■

C. Minimization of $\mathcal{J}_\varepsilon$

According to the principle of GND, for a finite sequence $\varepsilon_1 > \varepsilon_2 > \cdots > \varepsilon_K > 0$, the minimizers $\hat{\boldsymbol{X}}_{\varepsilon_k}$ are recursively computed. At the kth iteration, a standard iterative descent algorithm is used to compute $\hat{\boldsymbol{X}}_{\varepsilon_k}$. At iteration $k+1$, $\hat{\boldsymbol{X}}_{\varepsilon_k}$ is used as the initial solution, and the process is repeated until $k = K$. Practical considerations regarding the stopping criterion, the updating rule of ε_k, and the number K of iterations are reported in Section V.

For any $\varepsilon > 0$, the computation of $\hat{\boldsymbol{X}}_\varepsilon$ can be obtained with many mathematically converging descent algorithms since $\mathcal{J}_\varepsilon$ fulfills (10). Practically, several numerical strategies are studied and compared in [38].

[1] Rigorous application of Corollary 1 only provides that the restriction of $\mathcal{R}_{\mathrm{S}}$ on $\mathbb{R}_+^m$ is nondecreasing. A careful inspection of Appendix C is needed to check that the strict result actually holds.

- The Polak–Ribiere version of conjugate gradient (CG) algorithm is implemented with a 1-D search [39].
- It is shown that the IRLS method proposed in [38] does not extend beyond the case of separable penalty functions.
- An original *residual steepest descent* (RSD) [23] method is developed. It can also be seen as a deterministic *half-quadratic* algorithm based on Geman and Yang's construction [24], [30].

For a small value of ε_K, GND coupled with CG is more efficient than a single run of CG at $\varepsilon = \varepsilon_K$. This point is illustrated in Section V. In [38], the same conclusion is drawn concerning GND coupled with RSD.

V. Experiments

We illustrate the performances of the proposed spectral estimators in the context of short-time estimation by processing the well-known Kay and Marple example [2]. Such data have been extracted from a realization of a second-order stationary random process. Since our approach is not theoretically well-suited for dealing with such processes, the spectral estimates will not be consistent with the true spectrum. Nonetheless, the results presented in the following prove that consistency is not a crucial issue as short-time estimation is addressed. As a preliminary question, the next subsection addresses the problem of hyperparameter selection.

A. Hyperparameter Selection

In the first set of simulation results (Section V-B), hyperparameter values have been empirically selected after several trials as those that visually work "the best." An alternative way for solving this step could be automatic hyperparameter selection. More specifically, when the sample size of the observations is large enough (several hundreds of data), the maximum likelihood estimate (MLE) can provide a valuable solution. In the last ten years, efficient Monte Carlo Markov chain methods have been proposed to compute the MLE, for instance, in the context of unsupervised line spectrum estimation [40].

In the case of small data sets, the MLE would probably lack of reliability, and more realistic solutions must be found, depending on the application. Automatic or assisted calibration of hyperparameters based on a training data set is sometimes possible. For instance, in the context of Doppler radar imaging as addressed in [41, Ch. V], an initial data set is recorded as the radar points at a reference direction that corresponds to an identified scenario, such as atmospheric sounding and wind profiling. This step allows us to calibrate the radar sensor, but it could also be used to choose the hyperparameters for the whole recording.

B. Kay and Marple Example

1) Practical Considerations: Following [1], the performances of the proposed methods are tested using the Kay and Marple reference data set [2], which allows easy comparison with pre-existent approaches. The data sequence is real, of length $N = 64$, and consists of three sinusoids at fractional frequencies 0.1, 0.2, and 0.21 superimposed on an additive colored noise sequence. The SNR of each harmonic is 10, 30, and 30 dB, respectively, where the SNR is defined as the ratio of the sinusoid power to the total power in the passband of the colored noise process. The passband of the noise is centered at 0.35. The true spectrum appears in Fig. 1.

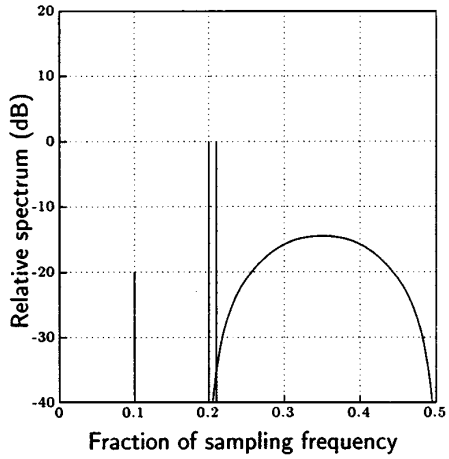

Fig. 1. True spectrum.

Given the real nature of data and the symmetry properties studied in Appendix D, the spectra are only plotted on a half period $[0, 0.5]$. The different estimates have been computed using $P = 512$. In practice, taking $P > 512$ does not markedly improve the resolution.

With regard to the numerical implementation of CG, the following conjunction has been selected as stopping criterion:

$$|\mathcal{J}(\boldsymbol{X}^i) - \mathcal{J}(\boldsymbol{X}^{i-1})|/\mathcal{J}(\boldsymbol{X}^i) < \alpha_1$$
$$\|\boldsymbol{X}^i - \boldsymbol{X}^{i-1}\|_*/\|\boldsymbol{X}^i\|_* < \alpha_2$$
$$\|\nabla \boldsymbol{X}^i\|_* < \alpha_3$$

where $\boldsymbol{X}^i$ denotes the solution at the ith iteration of the minimization stage, and $*$ is 1 or 2. Following Vogel and Oman [26], we have chosen the l_1 norm instead, and the thresholds have been set to $(\alpha_1, \alpha_2, \alpha_3) = (10^{-7}, 10^{-5}, 10^{-6})$.

The same stopping criterion has been adopted for RSD, except that the third condition has not been tested.

2) Estimation of LS: The spectrum estimates depicted in Fig. 2 minimize penalized criteria with a separable penalty function: Fig. 2(a) corresponds to the quadratic potential $R_0(\rho) = \rho^2$, and Fig. 2(b) corresponds to the hyperbolic potential $R_0(\rho) = \sqrt{\tau_0^2 + \rho^2}$ for $(\lambda, \tau_0) = (0.06, 0.002)$.

As shown in [1] and [14], quadratic regularization yields the zero-padded periodogram of the data sequence up to a multiplicative constant. Since the nominal resolution of a 64-point sequence is 0.015, close sinusoids at 0.2 and 0.21 are not resolved. Moreover, this estimate is dominated by sidelobes that mask important features of the signal. In the following, the DFT of the zero-padded data sequence has been used to initialize all iterative minimization procedures.

The line spectra estimate depicted in Fig. 2(b) is very similar to the spectral estimate computed with the Cauchy–Gauss model [1 , Fig. 6], as well as to the result given by the Hildebrand–Prony method [2, Fig. 6(b)]; the sinusoids are retrieved

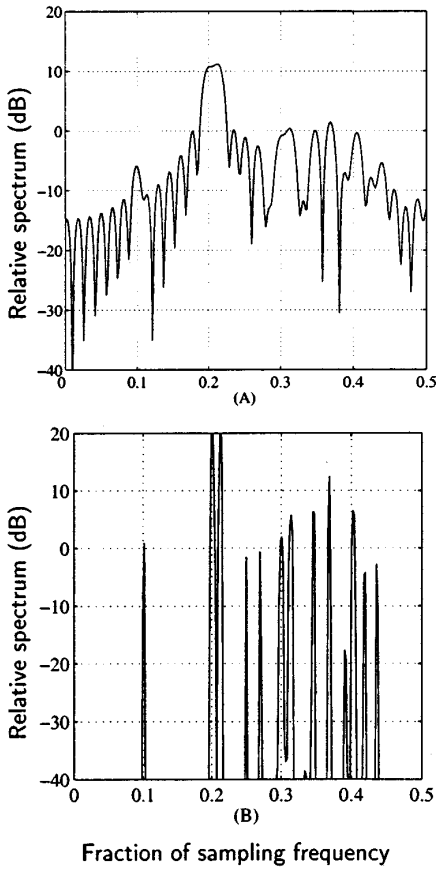

Fig. 2. Spectra reconstructed with separable regularization. (a) Zero-padded periodogram. (b) Line spectra reconstructed with the hyperbolic potential $(\lambda, \tau_0) = (0.06, 0.002)$.

at the exact frequencies but with powers different from the original ones. Nonetheless, the power ratio (20 dB) is preserved between the three harmonics. On the other hand, the broadband part of the spectrum is not recovered. It is replaced by several spectral lines. This problem is also encountered in [1] and [15] and in high-resolution parametric methods discussed by Kay and Marple [2].

From a computational standpoint, the IRLS method of [1] has been used as minimization tool. It is known to be convergent in the present situation [23], [24]. The solution is reached in about 5–10 s on a standard Pentium II PC.

3) Estimation of SS:

a) Complex Regularization: Fig. 3 shows the spectrum estimate computed from a convex penalized criterion with the noncircular penalty function $\mathcal{R}_{\mathrm{S}}^{1}$ defined by (12). It has been obtained with $\tau_1 = 0.1$ and $\lambda = 0.6$. Although the latter value corresponds to a high level of regularization, there remain some artifacts, where the reversal of the lowest sinusoid is the main defect. In our opinion, such results definitely disqualify noncircular penalty functions.

b) Regularization of the Power Spectrum: The three spectrum estimates depicted in Fig. 4 are obtained with a penalty function $\mathcal{R}_{\mathrm{S},\varepsilon}$ defined by (20). Three hyperparameters $(\lambda, \mu, \tau_1) \in \mathbb{R}_+^3$ need to be adjusted, let alone the target value

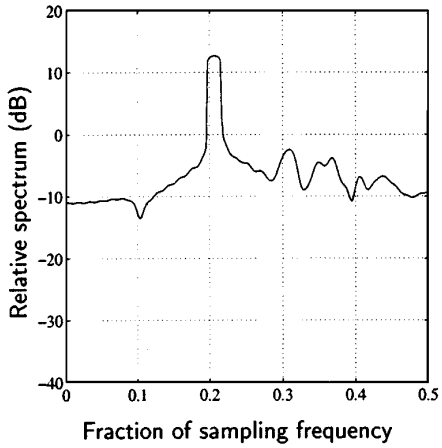

Fig. 3. Smooth spectrum reconstructed with a complex Gibbs–Markov penalty function. Parameters have been fixed to $(\lambda, \tau_1) = (0.6, 0.1)$.

ε_K for the closest approximation $\mathcal{J}_{\varepsilon_K}$ of $\mathcal{J}$. The results of Fig. 4 have been computed with $(\lambda, \tau_1) = (0.05, 0.001)$.

First, let us begin with general comments on Fig. 4. Akin to Fig. 2(b), the three results produce nearly no sidelobes, compared with the periodogram. None of the three results allow us to separate the two close harmonics, although a narrowband component around frequency 0.2 is clearly distinguished. Similarly, the lowest sinusoid at frequency 0.1 is recovered under a broaden format. This is not surprising since smoothness has been incorporated through the penalty function.

In Fig. 4(a) and (b), the value of μ has been chosen to correspond to the bound of convexity of $\mathcal{R}_{\mathrm{S},\varepsilon}$: $\mu = \mu_{\mathrm{sup}} = 0.5$, according to Section III-C2, and different values of ε_K have been compared. A small parameter value $\varepsilon_K = 0.001$ yields a rather inadequate blocky result, as shown in Fig. 4(b). The discontinuities are due to the quasinondifferentiability of $\mathcal{R}_{\mathrm{S},\varepsilon}$. The rougher approximation depicted in Fig. 4(a) ($\varepsilon_K = 0.9$) provides a smoother estimate. However, it is not smooth enough compared with the broadband part of the true spectrum. Increasing μ beyond the bound of convexity is necessary to get smoother results. The spectrum of Fig. 4(c) has been computed with $\mu = 5$ and $\varepsilon_K = 0.9$. It provides a more regular broadband response that is quite close to the smooth part of the true spectrum. Among the estimators tested in [2], the MLE (Capon method) shown in [2, Fig. 16(l)] provides a somewhat similar result. We retain such a tuning as a good candidate for the smooth part of the mixed model.

With regard to practical aspects of minimization, the three results correspond to contrasted situations.

- In the case of Fig. 4(a), $\varepsilon_K = 0.9$ yields a criterion that is sufficiently far from nondifferentiability to be efficiently minimized in a single run of CG (i.e., $K = 1$), spending about 25 s of CPU time.
- Fig. 4(b) has been obtained after three iterations of GND based on CG: $(\varepsilon_1, \varepsilon_2, \varepsilon_3) = (0.1, 0.01, 0.001)$, which globally took about 35 s of CPU time. In comparison, a single run at ε_3 takes about 60 s, as depicted in Fig. 5.
- The value $\mu = 5$ corresponding to Fig. 4(c) does not ensure that the criterion is convex. Hence, it is possibly mul-

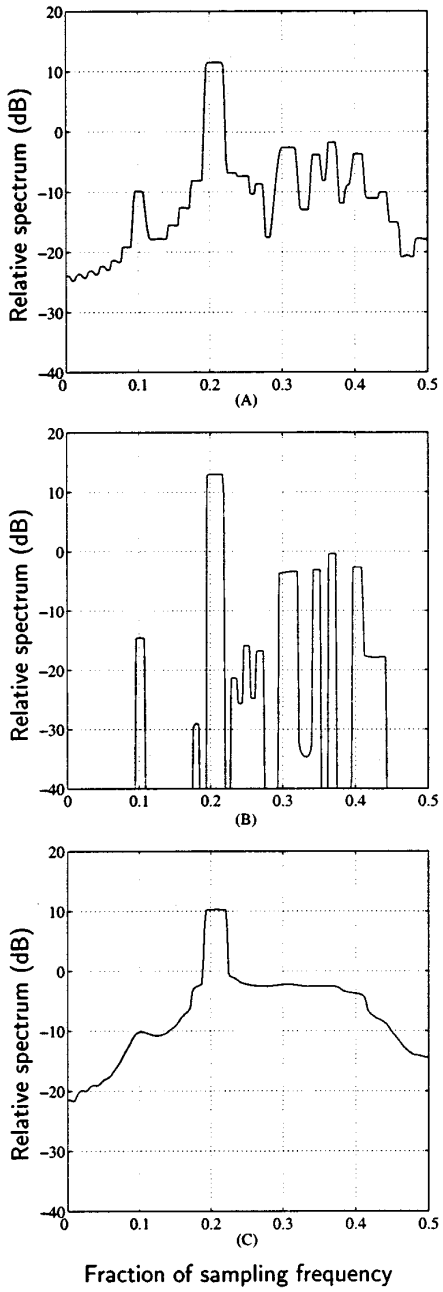

Fig. 4. Smooth spectra reconstructed with a circular Gibbs–Markov penalty function $(\lambda, \tau_1) = (0.05, 0.001)$. (a) Convex case where $\mu = \mu_{\sup} = 0.5$, $\varepsilon_K = 0.9$. (b) Convex case where $\mu = \mu_{\sup} = 0.5$, $\varepsilon_K = 0.001$. (c) Nonconvex case where $\mu = 5$, $\varepsilon_K = 0.9$.

timodal. For this reason, we gradually increase the value of μ, following the *graduated nonconvexity* (GNC) approach [42], [43]. The principle is very similar to the GND technique described in Section IV. The empirically chosen law of evolution for μ is simply $\mu_k = k \times \mu_{\sup}$, and therefore, the initial criterion $\mathcal{J}_{\mu_1}$ is convex, as prescribed by the GNC approach.

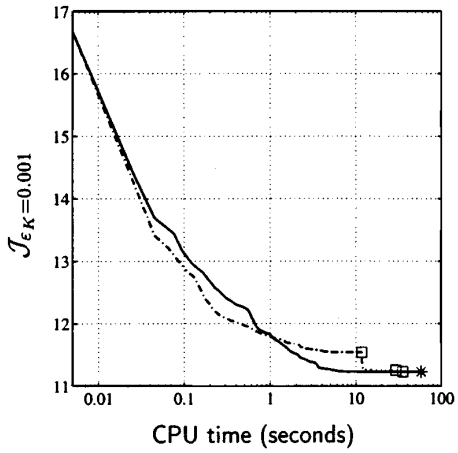

Fig. 5. Performance of the GND algorithm coupled with CG in the SS case. The solid line corresponds to the minimization of $\mathcal{J}_{0.001}$ in a single run, and dashed-dotted lines correspond to the GND process coupled with CG.

4) Estimation of MS: The spectrum estimates depicted in Fig. 6(a) and (b) are obtained from the minimization of a differentiable approximation of the penalized criterion $\mathcal{J}_{\mathrm{M}}$ defined by (16):

$$\mathcal{J}_{M,\varepsilon}(\boldsymbol{X}) = \mathcal{Q}_{\mathrm{M}}(\boldsymbol{X}) + \lambda_L \mathcal{R}_L(\boldsymbol{X}_{\mathrm{L}}) + \lambda_{\mathrm{S}} \mathcal{R}_{S,\varepsilon}(\boldsymbol{X}_{\mathrm{S}}). \quad (21)$$

The regularizing terms $\mathcal{R}_{\mathrm{L}}$ (11) and $\mathcal{R}_{\mathrm{S},\varepsilon}$ (20) depend on τ_0 and on $(\mu, \tau_1, \varepsilon_K)$, respectively. Given the results presented in the two previous subsections, we have retained $\tau_0 = 0.002$, $\tau_1 = 0.001$, $\varepsilon_K = 0.9$, and we have tested the two settings $\mu = \mu_{\sup} = 0.5$ and $\mu = 5$.

Two additional hyperparameters $(\lambda_{\mathrm{L}}, \lambda_{\mathrm{S}})$ appear in (21). It is *a priori* suited to choose the same order of magnitude for the values of λ_{L} and λ_{S}; otherwise, the overpenalized term would yield a vanishing component. The values $\lambda_{\mathrm{L}} = 0.005$, $\lambda_{\mathrm{S}} = 0.0033$ have been retained.

Fig. 6(a) corresponds to $\mu = \mu_{\sup}$; therefore, the minimized criterion is strictly convex. The result has been computed with CG. It clearly shows that the mixed model is able to resolve close sinusoids, whereas the broadband response is much closer from the SS estimate of Fig. 4(a) than from the LS estimate of Fig. 2(b). However, the broadband response is not smooth enough, and the small sinusoidal component is not as sharp as expected.

Fig. 6(b) corresponds to $\mu = 5$; therefore, the minimized criterion is not convex and possibly multimodal. The result has been computed with GNC based on CG. The three spectral lines have sharp responses at the sinusoid frequencies, and the power ratio between the different harmonics is preserved. Moreover, its smooth part is very close to the broadband component of the true spectrum. It is clearly the most satisfactory result among all estimates proposed in this paper. It also outperforms classical solutions computed on the same data set in [2].

Fig. 6(c) and (d) separately show $|\hat{\boldsymbol{X}}_{\mathrm{L}}|^2$ and $|\hat{\boldsymbol{X}}_{\mathrm{S}}|^2$, which are the components of the solution depicted in Fig. 6(b). As expected, the former is rather spiky, whereas the latter is rather smooth. However, perfect separation was not the goal since it

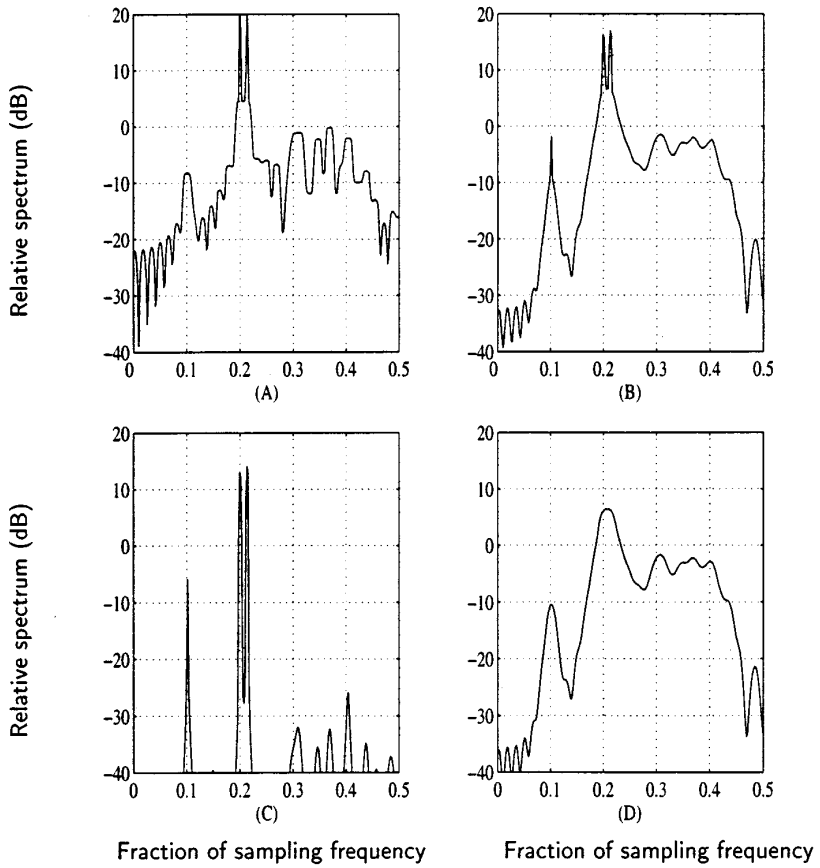

Fig. 6. Mixed spectra. (a) Convex case $\mu = 0.5$. (b) Nonconvex extension $\mu = 5$. (c) and (d) correspond respectively to the line ($|\hat{\boldsymbol{X}}_{\mathrm{L}}|^2$) and smooth ($|\hat{\boldsymbol{X}}_{\mathrm{S}}|^2$ parts of $|\hat{\boldsymbol{X}}|^2$ depicted in (b).

would require that true decisions be taken regarding the presence of a line at each frequency sample, whereas our motivation was only to accurately estimate the whole spectrum. There is a somewhat similar difference between *image segmentation* and *edge-preserving restoration*.

VI. Concluding Remarks

In the context of short-time estimation, we have proposed a new class of nonlinear spectral estimators, defined as minimizers of strictly convex energies. First, we have addressed separable penalization introduced in [1] and [18] for enhancing spectral lines.

Then, a substantial part of the paper has been devoted to smooth spectra restoration. We have introduced circular Gibbs–Markov penalty functions inspired from common models for signal and image restoration. However, the fact that penalization applies to moduli of complex quantities introduces specific difficulties. A rigorous mathematical study has been conducted in order to build criteria gathering the expected properties such as differentiability, strict convexity, and the ability to discriminate spectra in favor of the smoothest.

Finally, since many practical spectral analysis problems involve both spectral lines and smooth components, we have proposed an original form of mixed criterion to superimpose the two kinds of components. We argue that this approach provides a very sharp tool for the detection of isolated objects embedded in broadband events. One possible application is the tracking of planes using a Doppler radar instrument since the informative data is often embedded on meteorological clutter at low SNR. The proposed spectral estimators have then been extended to this framework to additionally take spatial or temporal continuity into account [41, ch. V].

After the present study, some issues remain open. On the one hand, we observed in Section V that minimizing a convex criterion did not always yield a sufficiently smooth estimate. In practice, we resorted to graduated nonconvexity to overcome the limitation found in the convex analysis framework. By now, it is hard to tell whether the latter takes root in fundamental reasons or if we simply failed in finding the "good" convex penalty function.

On the other hand, the proposed penalty functions are quite sophisticated. In practice, several hyperparameters have to be tuned, which is not always a simple task. In some situations, hyperparameter values can be selected using training data. Otherwise, depending on the size of the data set, automatic selection using an MLE approach may provide an alternative solution.

Finally, the question of asymptotic properties remains open. For instance, given the well-known properties of the averaged periodogram, it could be interesting to study the properties of averaged versions of our smooth spectra estimator.

APPENDIX A
PROOF OF THEOREM 1

The stated sufficient condition is acknowledged in the scalar case [44, Th. 5.1].

First, let us prove the implication in the large sense. For any $\boldsymbol{x}, \boldsymbol{y} \in \mathbb{C}^m$, $\boldsymbol{x} \neq \boldsymbol{y}$ and any $\alpha \in (0, 1)$, let $\boldsymbol{t} = \alpha\boldsymbol{x} + \overline{\alpha}\boldsymbol{y}$ and $\overline{\alpha} = 1 - \alpha$. Each g_k is convex:

$$g_k(\boldsymbol{t}) \leqslant \alpha g_k(\boldsymbol{x}) + \overline{\alpha} g_k(\boldsymbol{y}). \tag{22}$$

Then, using repeatedly the fact that f is a coordinatewise nondecreasing function, we deduce

$$\begin{aligned} f(\boldsymbol{g}(\boldsymbol{t})) &\leqslant f(\alpha\boldsymbol{g}(\boldsymbol{x}) + \overline{\alpha}\boldsymbol{g}(\boldsymbol{y})), && (23)\\ &\leqslant \alpha f(\boldsymbol{g}(\boldsymbol{x})) + \overline{\alpha} f(\boldsymbol{g}(\boldsymbol{y})) && (24) \end{aligned}$$

where the latter inequality holds because f is convex.

In order to prove the strict formulation, we remark that there is at least one k such that $x_k \neq y_k$; therefore, the corresponding inequality (22) becomes strict because g_k is strictly convex. Then, the strict counterpart of inequalities (23) and (24) also holds since f is coordinatewise increasing (remark that the strict convexity of f is unnecessary here).

APPENDIX B
PROOF OF THEOREM 2

A. Sufficient Condition

Let $f\colon \mathbb{R}_+^m \mapsto \mathbb{R}$ be a (resp. strictly) convex and coordinatewise nondecreasing (resp. increasing) function, and let $\boldsymbol{g}\colon \mathbb{C}^m \mapsto \mathbb{R}_+^m$ be the mapping of the moduli: $\forall \boldsymbol{x} \in \mathbb{C}^m$, $\boldsymbol{g}(\boldsymbol{x}) = (|x_1|, |x_2|, \ldots, |x_m|)$. We have to prove that $f \circ \boldsymbol{g}$ is (resp. strictly) convex.

In the large sense, this result is an immediate consequence of Theorem 1 for $n = 2m$. However, the strict counterpart of Theorem 1 does not apply since $|\cdot|$ is not a *strictly* convex function. We need a more specific derivation, which is actually generalizable to any function $\boldsymbol{g}$ with *hemivariate* [45] convex components.

Let us consider the proof of Theorem 1. If f is strictly convex, (24) readily becomes strict, provided that $\boldsymbol{g}(\boldsymbol{x}) \neq \boldsymbol{g}(\boldsymbol{y})$. Otherwise, assume $\boldsymbol{g}(\boldsymbol{x}) = \boldsymbol{g}(\boldsymbol{y})$ so that (24) reads $f(\boldsymbol{g}(\boldsymbol{t})) \leqslant f(\boldsymbol{g}(\boldsymbol{x}))$. Since $\boldsymbol{x} \neq \boldsymbol{y}$, there exists at least one k such that $x_k \neq y_k$. Then, $|x_k| = |y_k|$ implies $|t_k| < |x_k|$ since t_k belongs to the cord (x_k, y_k) of the centered circle of radius $|x_k|$. Since f is coordinatewise increasing, it follows that $f(\boldsymbol{g}(\boldsymbol{t})) < f(\boldsymbol{g}(\boldsymbol{x}))$, which is the expected strict counterpart of inequality (24).

B. Necessary Condition

Let $f\colon \mathbb{C}^m \mapsto \mathbb{R}$ be a strictly convex, circular function. Its restriction on $\mathbb{R}_+^m$ is obviously strictly convex. We have to prove that it is also coordinatewise increasing.

Let $\mathbf{1}_k$ be the kth canonical vector in $\mathbb{R}^m$, and let $\tilde{f}_{\boldsymbol{x},k}(t) = f(\boldsymbol{x} + (t - x_k)\mathbf{1}_k)$ be the restriction of f to the line $\{\boldsymbol{u}, u_n = x_n, \forall n \neq k\}$ for any $t \in \mathbb{R}$, $\boldsymbol{x} \in \mathbb{R}^m$. First, let us prove that all such restrictions $\tilde{f}_{\boldsymbol{x},k}$ are even functions, i.e., that $\tilde{f}_{\boldsymbol{x},k}(-t) = \tilde{f}_{\boldsymbol{x},k}(t)$

$$\forall n \in \mathbb{N}_m,\ |x_n + (t - x_k)(\mathbf{1}_k)_n| = \begin{cases} |x_n|, & \text{if } n \neq k \\ |t|, & \text{if } n = k. \end{cases}$$

Consequently, $|x_n + (-t - x_k)(\mathbf{1}_k)_n| = |x_n + (t - x_k)(\mathbf{1}_k)_n|$, and hence, $f(\boldsymbol{x} - (t - x_k)\mathbf{1}_k) = f(\boldsymbol{x} + (t - x_k)\mathbf{1}_k)$ since f is circular. Therefore, $\tilde{f}_{\boldsymbol{x},k}$ is even.

Since $\tilde{f}_{\boldsymbol{x},k}$ is even and strictly convex on $\mathbb{R}$, it is increasing on $\mathbb{R}_+$, as shown below: $\forall s, t, 0 < s < t$, let $\alpha = (s+t)/2t$ so that $s = \alpha t + (1-\alpha)(-t)$. Since $\alpha \in (0, 1)$ and $\tilde{f}_{\boldsymbol{x},k}$ is strictly convex, $\tilde{f}_{\boldsymbol{x},k}(s) < \alpha\tilde{f}_{\boldsymbol{x},k}(t) + (1 - \alpha)\tilde{f}_{\boldsymbol{x},k}(-t) = \tilde{f}_{\boldsymbol{x},k}(t)$ because $\tilde{f}_{\boldsymbol{x},k}$ is even.

As a conclusion, all restrictions $\tilde{f}_{\boldsymbol{x},k}$ are increasing on $\mathbb{R}_+$, i.e., f is coordinatewise increasing on $\mathbb{R}_+^m$.

APPENDIX C
PROOF OF COROLLARY 1

First, let us decompose $\mathcal{R}_{\mathrm{S}}$ according to $\mathcal{R}_{\mathrm{S}}(\boldsymbol{X}) = (1/2)\sum_{p=0}^{P-1} S(X_p, X_{p+1})$, with

$$\begin{aligned} S(X_1, X_2) &= S(\rho_1, \rho_2) \\ &= R_2(\rho_1) + R_2(\rho_2) + 2\mu R_1(\rho_1 - \rho_2) \end{aligned} \tag{25}$$

and let us prove that conditions (15) imply the convexity of S on $\mathbb{C}^2$, which is a sufficient condition for the convexity of $\mathcal{R}_{\mathrm{S}}$ on $\mathbb{C}^P$. Apply Theorem 2 to S. On one hand, S is convex on $\mathbb{R}_+^2$ as a sum of convex functions of (ρ_1, ρ_2). It is even strictly convex if R_2 is strictly convex.

On the other hand, let us prove that S is coordinatewise nondecreasing or even increasing as a function of (ρ_1, ρ_2) if conditions (15) hold. Since R_1 is even, $S(\rho_1, \rho_2) = S(\rho_2, \rho_1)$; therefore, we need only to study the behavior of S as a function of, say, ρ_1. Since R_1 is even and convex on $\mathbb{R}$, it is nondecreasing on $\mathbb{R}_+$ (the strict counterpart of this result is shown at the end of Appendix B). As a sum of nondecreasing functions of ρ_1, it is obvious that S is nondecreasing if $\rho_1 \geqslant \rho_2$. If $\rho_1 < \rho_2$, the condition $\partial S/\partial_{\rho_1} \geqslant 0$ reads

$$\forall \rho_1, \rho_2 > 0, \qquad \rho_1 < \rho_2, \qquad R_2'(\rho_1) \geqslant 2\mu R_1'(\rho_2 - \rho_1)$$

which is equivalent to (15c) since R_1' and R_2' are nondecreasing. Finally, if R_2 is strictly convex, S is shown to be coordinatewise increasing along the same lines.

APPENDIX D
REAL DATA CASE

The purpose of this Appendix is to show that the proposed spectral estimation method (in either versions, LS, SS, and MS) automatically preserves the Hermitian structure of the spectrum when real data are processed so that the estimated power spectrum is symmetric.

Let us denote $\hat{\boldsymbol{X}} = \mathcal{H}(\hat{\boldsymbol{X}})$ as the expected Hermitian property of $\hat{\boldsymbol{X}}$, with

$$\mathcal{H}(X_0, X_1, \ldots, X_{P-1}) \triangleq (X_0^*, X_{P-1}^*, \ldots, X_1^*).$$

Equivalently, $\boldsymbol{X} = \mathcal{H}(\boldsymbol{X})$ means that the inverse DFT $\boldsymbol{x} = \text{IDFT}^{-1}(\boldsymbol{X})$ is a real vector. Convexity of the minimized criterion plays a basic role in the fulfillment of the Hermitian property of $\hat{\boldsymbol{X}}$, as stated in the following proposition.

Proposition 3: Consider a real data set $\boldsymbol{y} \in \mathbb{R}^N$ and a penalty function $\mathcal{R}$: $\mathbb{R}_+^P \mapsto \mathbb{R}$ that fulfills (9b)–(9d) and (10b)–(10c). First, the criterion $\mathcal{J}$ defined by (6) and (7) possesses the Hermitian symmetry $\mathcal{J}(\mathcal{H}(\boldsymbol{X})) = \mathcal{J}(\boldsymbol{X})$, $\forall \boldsymbol{X} \in \mathbb{C}^P$. Second, the unique minimizer of $\mathcal{J}$ satisfies $\hat{\boldsymbol{X}} = \mathcal{H}(\hat{\boldsymbol{X}})$.

Proof: Let us consider a non-Hermitian complex vector $\boldsymbol{X} \in \mathbb{C}^P$, i.e., $\boldsymbol{X} \neq \mathcal{H}(\boldsymbol{X})$. Introduce $\boldsymbol{x} = \text{IDFT}^{-1}(\boldsymbol{X})$ so that

$$\mathcal{Q}(\boldsymbol{X}) = \sum_{n=0}^{N-1} |y_n - x_n|^2$$

$$\mathcal{Q}(\mathcal{H}(\boldsymbol{X})) = \sum_{n=0}^{N-1} |y_n - x_n^*|^2.$$

Obviously, $\mathcal{Q}(\mathcal{H}(\boldsymbol{X})) = \mathcal{Q}(\boldsymbol{X})$ since $|y - x| = |y - x^*|$, $\forall y \in \mathbb{R}, x \in \mathbb{C}$. On the other hand, the modulus of the components of $\mathcal{H}(\boldsymbol{X})$ reads $(|X_0^*|, |X_{P-1}^*|, \ldots, |X_1^*|) = (|X_0|, |X_{P-1}|, \ldots, |X_1|)$, which proves that $\mathcal{R}(\mathcal{H}(\boldsymbol{X})) = \mathcal{R}(\boldsymbol{X})$ since $\mathcal{R}$ is shift-invariant (9b), symmetry-invariant (9c), and circular (9d). Finally, the identity $\mathcal{J}(\mathcal{H}(\boldsymbol{X})) = \mathcal{J}(\boldsymbol{X})$ gathers the two results. The first part of the proof is completed.

Now, consider the middle point

$$\boldsymbol{Z} = (\boldsymbol{X} + \mathcal{H}(\boldsymbol{X}))/2 \tag{26}$$

which obviously satisfies $\mathcal{H}(\boldsymbol{Z}) = \boldsymbol{Z}$. Since $\mathcal{J}$ is strictly convex

$$\mathcal{J}(\boldsymbol{Z}) < (\mathcal{J}(\boldsymbol{X}) + \mathcal{J}(\mathcal{H}(\boldsymbol{X})))/2 = \mathcal{J}(\boldsymbol{X}).$$

As a consequence, $\hat{\boldsymbol{X}} = \mathcal{H}(\hat{\boldsymbol{X}})$. ■

Proposition 3 directly applies to the LS and SS cases (including differentiable approximations considered in Section IV-B), whereas a straightforward generalization is needed in the MS case. Along the same lines, it can be proved that $\mathcal{J}_{\text{M}}(\boldsymbol{X}_{\text{L}}, \boldsymbol{X}_{\text{S}}) = \mathcal{J}_{\text{M}}(\mathcal{H}(\boldsymbol{X}_{\text{L}}), \mathcal{H}(\boldsymbol{X}_{\text{S}}))$ in $\mathbb{C}^P \times \mathbb{C}^P$ and that $(\mathcal{H}(\hat{\boldsymbol{X}}_{\text{L}}), \mathcal{H}(\hat{\boldsymbol{X}}_{\text{S}})) = (\hat{\boldsymbol{X}}_{\text{L}}, \hat{\boldsymbol{X}}_{\text{S}})$, if both penalty functions $\mathcal{R}_{\text{L}}$ and $\mathcal{R}_{\text{S}}$ fulfill (9b)–(9d) and (10b)–(10c).

The remaining question concerns the situation where the criterion is nonconvex, as encountered in [1], or in GNC experiments, which are reported in Section V. Then, it does not seem possible to show that all minimizers (global or local) are Hermitian. However, the Hermitian symmetry of the criterion itself still holds (the corresponding part of the proof of Proposition 3 remains valid). This property has two favorable consequences.

- If $\mathcal{J}$ is unimodal, i.e., it has one global minimizer $\hat{\boldsymbol{X}}$ and no local minimizer, then $\mathcal{H}(\hat{\boldsymbol{X}}) = \hat{\boldsymbol{X}}$. Since strict convexity implies unimodality, this is an alternate argument for the second part of the proof of Proposition 3.
- The gradient of $\mathcal{J}$ is Hermitian: $\mathcal{H}(\nabla\mathcal{J}(\boldsymbol{X})) = \nabla\mathcal{J}(\boldsymbol{X})$; therefore, gradient-based algorithms can be expected to propagate Hermitian symmetry along iterations from a Hermitian initialization point. We have also checked the same property for the IRLS algorithm used in [1].

References

[1] M. D. Sacchi, T. J. Ulrych, and C. J. Walker, "Interpolation and extrapolation using a high-resolution discrete Fourier transform," *IEEE Trans. Signal Processing*, vol. 46, pp. 31–38, Jan. 1998.

[2] S. M. Kay and S. L. Marple, "Spectrum analysis—A modern perspective," *Proc. IEEE*, vol. 69, pp. 1380–1419, Nov. 1981.

[3] J.-F. Giovannelli, G. Demoment, and A. Herment, "A Bayesian method for long AR spectral estimation: A comparative study," *IEEE Trans. Ultrason. Ferroelect. Freq. Contr.*, vol. 43, pp. 220–233, Mar. 1996.

[4] H. Sauvageot, "Radar météorologie. télédetection active de l'atmosphere," Eyrolles, Paris, France, 1982.

[5] V. Pisarenko, "The retrieval of harmonics from a covariance function," *J. R. Astron. Soc.*, vol. 33, pp. 347–360, 1973.

[6] B. P. Hildebrand, *Introduction to Numerical Analysis*. New York: McGraw-Hill, 1956.

[7] R. N. McDonough and W. H. Huggins, "Best least-squares representation of signals by exponentials," *IEEE Trans. Automat. Contr.*, vol. AC-13, pp. 408–412, Aug. 1968.

[8] T. J. Ulrych and R. W. Clayton, "Time series modeling and maximum entropy,", vol. 12, pp. 188–200, 1976.

[9] S. M. Kay, *Modern Spectral Estimation*. Englewood Cliffs, NJ: Prentice-Hall, 1988.

[10] S. L. Marple, *Digital Spectral Analysis with Applications*. Englewood Cliffs, NJ: Prentice-Hall, 1987.

[11] H. R. Künsch, "Robust priors for smoothing and image restoration," *Ann. Inst. Stat. Math.*, vol. 46, pp. 1–19, 1994.

[12] S. Brette and J. Idier, "Optimized single site update algorithms for image deblurring," in *Proc. IEEE ICIP*, Lausanne, Switzerland, Sept. 1996, pp. 65–68.

[13] P. Charbonnier, L. Blanc-Féraud, G. Aubert, and M. Barlaud, "Deterministic edge-preserving regularization in computed imaging," *IEEE Trans. Image Processing*, vol. 6, pp. 298–311, Feb. 1997.

[14] J.-F. Giovannelli and J. Idier, "Bayesian interpretation of periodograms," *IEEE Trans. Signal Processing*, vol. 49, pp. 1988–1996, Sept. 2001.

[15] S. D. Cabrera and T. W. Parks, "Extrapolation and spectral estimation with iterative weighted norm modification," *IEEE Trans. Signal Processing*, vol. 39, pp. 842–851, Apr. 1991.

[16] C. I. Byrnes, T. T. Georgiou, and L. Anders, "A new approach to spectral estimation: A tunable high-resolution spectral estimator," *IEEE Trans. Signal Processing*, vol. 48, pp. 3189–3205, Nov. 2000.

[17] P. Ciuciu and J. Idier, "Statistical interpretation of short-time spectral estimators: Valid case and fundamental limit!," Lab. Signaux Syst., Gif-sur-Yvette, France, Tech. Rep. GPI-L2S, 2001.

[18] N. Moal and J.-J. Fuchs, "Sinusoids in white noise: A quadratic programming approach," in *Proc. IEEE ICASSP*, Seattle, WA, May 1998, pp. 2221–2224.

[19] J.-J. Fuchs, "Multipath time-delay estimation," *IEEE Trans. Signal Processing*, vol. 47, pp. 237–243, June 1999.

[20] D. P. Bertsekas, *Nonlinear Programming*. Belmont, MA: Athena Scientific, 1995.

[21] C. A. Bouman and K. D. Sauer, "A generalized Gaussian image model for edge-preserving MAP estimation," *IEEE Trans. Image Processing*, vol. 2, pp. 296–310, July 1993.

[22] A. Tikhonov and V. Arsenin, *Solutions of Ill-Posed Problems*. Washington, DC: Winston, 1977.

[23] R. Yarlagadda, J. B. Bednar, and T. L. Watt, "Fast algorithms for l_p deconvolution," *IEEE Trans. Acoust. Speech, Signal Processing*, vol. ASSP-33, pp. 174–182, Feb. 1985.

[24] J. Idier, "Convex half-quadratic criteria and interacting auxiliary variables for image restoration," *IEEE Trans. Image Processing*, vol. 10, pp. 1001–1009, July 2001.

[25] P. J. Green, "Bayesian reconstructions from emission tomography data using a modified EM algorithm," *IEEE Trans. Med. Imag.*, vol. 9, pp. 84–93, Mar. 1990.

[26] R. V. Vogel and M. E. Oman, "Iterative methods for total variation denoising," *SIAM J. Sci. Comput.*, vol. 17, pp. 227–238, Jan. 1996.

[27] Y. Li and F. Santosa, "A computational algorithm for minimizing total variation in image restoration," *IEEE Trans. Image Processing*, vol. 5, pp. 987–995, May 1996.

[28] W. J. Rey, *Introduction to Robust and Quasi-Robust Statistical Methods*. Berlin, Germany: Springer-Verlag, 1983.

[29] P. J. Huber, *Robust Statistics*. New York: Wiley, 1981.

[30] D. Geman and C. Yang, "Nonlinear image recovery with half-quadratic regularization," *IEEE Trans. Image Processing*, vol. 4, pp. 932–946, July 1995.

[31] R. Glowinski, J. L. Lions, and R. Trémolières, "Analyze numérique des inéquations variationnelles, tome 1: Théorie générale, méthodes mathématiques pour l'informatique," Dunod, Paris, France, 1976.

[32] D. Bertsekas, "Nondifferentiable optimization approximation," in *Mathematical Programming Studies*, M. L. Balinski and P. Wolfe, Eds. Amsterdam, The Netherlands, 1975, vol. 3, pp. 1–25.

[33] C. Lemaréchal, *Non Differentiable Optimization*, Nonlinear Optimization ed., L. C. W. Dixon, E. Spedicato, and G. P Szego, Eds. Boston, MA, 1980, pp. 149–199.

[34] K. C. Kiwiel, *Methods of Descent for Nondifferentiable Optimization*, ser. Lecture Notes in Mathematics. New York: Springer-Verlag, 1986.

[35] R. Acar and C. R. Vogel, "Analysis of bounded variation penalty methods for ill-posed problems," *Inv. Prob.*, vol. 10, pp. 1217–1229, 1994.

[36] M. Z. Nashed and O. Scherzer, "Stable approximation of nondifferentiable optimization problems with variational inequalities," *J. Amer. Math. Soc.*, vol. 204, pp. 155–170, 1997.

[37] G. Alberti, "Variational models for phase transitions, an approach via Gamma-convergence," in *Differential Equations and Calculus of Variations*, G. Buttazzo *et al.*, Eds. New York: Springer-Verlag, 1999.

[38] P. Ciuciu and J. Idier, "A half-quadratic block-coordinate descent method for spectral estimation," Lab. Signaux Syst., Gif-sur-Yvette, France, Tech. Rep. GPI-L2S, 2000.

[39] W. H. Press, B. P. Flannery, S. A. Teukolsky, and W. T. Vetterling, *Numerical Recipes, the Art of Scientific Computing*. Cambridge, MA: Cambridge Univ. Press, 1986.

[40] C. Andrieu and A. Doucet, "Joint Bayesian model selection and estimation of noisy sinusoids via reversible jump MCMC," *IEEE Trans. Signal Processing*, vol. 47, pp. 2667–2676, Oct. 1999.

[41] P. Ciuciu, "Méthodes markoviennes en estimation spectrale non paramétrique. Applications en imagerie radar Doppler," Ph.D. dissertation, Univ. Paris-Sud, Orsay, France, Oct. 2000.

[42] A. Blake and A. Zisserman, *Visual Reconstruction*. Cambridge, MA: MIT Press, 1987.

[43] M. Nikolova, J. Idier, and A. Mohammad-Djafari, "Inversion of large-support ill-posed linear operators using a piecewise Gaussian MRF," *IEEE Trans. Image Processing*, vol. 7, pp. 571–585, Apr. 1998.

[44] R. T. Rockafellar, *Convex Analysis*: Princeton Univ. Press, 1970.

[45] J. Ortega and W. Rheinboldt, *Iterative Solution of Nonlinear Equations in Several Variables*. New York: Academic, 1970.

Philippe Ciuciu was born in France in 1973. He graduated from the École Supérieure d'Informatique Électronique Automatique, Paris, France, in 1996. He also received the D.E.A. and Ph.D. degrees in signal processing from the Université de Paris-Sud, Orsay, France, in 1996 and 2000, respectively.

Since November 2000, he has held a postdoctoral position with the Service Hospitalier Frédéric Joliot, Commissariat à l'Énergie Atomique, Orsay. His research interests include spectral analysis and optimization, and presently, he focuses on statistical methods and regularized approaches in signal and image processing for functional brain imaging.

Jérôme Idier was born in France in 1966. He received the diploma degree in electrical engineering from the École Supérieure d'Électricité, Gif-sur-Yvette, France, in 1988 and the Ph.D. degree in physics from the Université de Paris-Sud, Orsay, France, in 1991.

Since 1991, he has been with the Laboratoire des Signaux et Systèmes, Centre National de la Recherche Scientifique, Gif-sur-Yvette. His major scientific interest is in probabilistic approaches to inverse problems for signal and image processing.

Jean-François Giovannelli was born in Béziers, France, in 1966. He graduated from the École Nationale Supérieure de l'Électronique et de ses Applications, Cergy, France, in 1990. He received the Ph.D. degree in physics at the Laboratoire des Signaux et Systèmes, Université de Paris-Sud, Orsay, France, in 1995.

He is presently an Assistant Professor with the Département de Physique, Université de Paris-Sud. He is interested in regularization methods for inverse problems in signal and image processing, mainly in spectral characterization. Applications fields essentially concern radars and medical imaging.

J.-F. Giovannelli, J. Idier, R. Boubertakh et A. Herment, « Unsupervised frequency tracking beyond the Nyquist limit using Markov chains », *IEEE Trans. Signal Processing*, vol. 50, n°12, pp. 1–10, décembre 2002.

IEEE TRANSACTIONS ON SIGNAL PROCESSING, VOL. 50, NO. 12, DECEMBER 2002 2905

Unsupervised Frequency Tracking Beyond the Nyquist Frequency Using Markov Chains

Jean-François Giovannelli, Jérôme Idier, Rédha Boubertakh, and Alain Herment

***Abstract*—This paper deals with the estimation of a sequence of frequencies from a corresponding sequence of signals. This problem arises in fields such as Doppler imaging, where its specificity is twofold. First, only short noisy data records are available (typically four sample long), and experimental constraints may cause spectral aliasing so that measurements provide unreliable, ambiguous information. Second, the frequency sequence is smooth. Here, this information is accounted for by a Markov model, and application of the Bayes rule yields the *a posteriori* density. The maximum *a posteriori* is computed by a combination of Viterbi and descent procedures. One of the major features of the method is that it is entirely unsupervised. Adjusting the hyperparameters that balance data-based and *prior*-based information is done automatically by maximum likelihood (ML) using an expectation-maximization (EM)-based gradient algorithm. We compared the proposed estimate to a reference one and found that it performed better: Variance was greatly reduced, and tracking was correct, even beyond the Nyquist frequency.**

***Index Terms*—Aliasing inversion, Bayesian statistic, EM algorithm, forward-backward procedure, frequency tracking, hyperparameter estimation, maximum a posteriori, maximum likelihood, meteorological Doppler radar, regularization, ultrasonic Doppler velocimetry, Viterbi algorithm.**

I. Introduction

FREQUENCY tracking (or mean frequency tracking) is currently of interest [1]–[6], especially in fields such as the ultrasonic characterization of biological tissues, synthetic aperture radar, and speech processing. Our main interest is its use in Doppler imaging (radars [7], ultrasound blood flow mapping [8]–[10]). There are two main features in this area.

1) One is that only short noisy data records are available (typically four sample long), and they are in a vectorial form. Moreover, the constraints on the sampling frequency may cause spectral aliasing so that measurements provide small amounts of ambiguous information.
2) The second is that there is information on the smoothness of the sought frequency sequence. This *a priori* information is the foundation of the proposed construction. It allows robust tracking, even beyond the Nyquist limit.

Manuscript received September 29, 2000; revised July 11, 2002. The associate editor coordinating the review of this paper and approving it for publication was Prof. Bjorn Ottersten.

J.-F. Giovannelli and J. Idier are with the Laboratoire des Signaux et Systèmes, Centre National de la Recherche Scientifique, Supélec, Université de Paris-Sud, Orsay, France (giova@lss.supelec.fr).

R. Boubertakh and A. Herment are with the Unité Institut National pour la Santé et la Recherche Médicale 494, Imagerie Médicale Quantitative, Hôpital de la Pitié Salpétrière, Paris, France.

Digital Object Identifier 10.1109/TSP.2002.805501

The most popular methods used for spectral characterization rely on periodogram and empirical correlations. The mean frequency is usually estimated by computing the mean frequency of the periodogram [8] over the standardized frequency range $\nu \in (-0.5, +0.5]$. Another popular estimate is proportional to the phase of the first empirical correlation lag [11], [12]. It is also provided by a first-order autoregression in a least squares framework [13], but better accuracy is obtained by using all the available estimated correlation lags in a Taylor series expansion of the correlation function [12], [14]. The resulting estimate is also the mean frequency of the periodogram. However, the estimated parameters vary greatly, particularly when short data records are used. Moreover, the estimated frequency approaches zero when the true frequency becomes near the Nyquist frequency $\nu \simeq \pm 0.5$ (due to the periodogram 1-periodicity) [8]. To reduce this bias, [15] uses the maximum of the periodogram instead of its mean (and yields a maximum likelihood (ML) estimate; see Section III-A and [16, p. 410]), and [8] iteratively shifts the frequency of the data. This results in greater variance so that no frequency tracking remains possible beyond $\nu = \pm 0.5$.

Thus, all the current methods have two drawbacks. First, the tracking problem is tackled by a (necessary suboptimal) two-step procedure:

1) Estimate frequencies in the aliased band $(-0.5, +0.5]$.
2) Detect and inverse aliasing.

Second, they are clearly based on empirical second-order statistics that perform poorly with short data records independently processed. Unfortunately, the inverse aliasing in step 2 often fails due to the great variations in the estimated aliased frequencies of step 1. This is usually compensated for by post-smoothing the aliased frequency sequence. This provides spatial continuity but affects the aliased frequency discontinuities, therefore limiting the capacity to detect aliasing. The proposed method copes with the great variation and aliasing in a single step; it models the whole data set (by noisy cisoids) and the smoothness of the frequency sequence (by a Markov random walk) in the regularization/Bayesian framework. It then becomes possible to smooth frequency sequence and invert aliasing at the same time, avoiding the pitfalls of chaining these operations.

We have found several papers [3], [17], [18] that adopt such a framework, and this study provides four additional features.

1) First, it deals with vectorial data records as they occur in Doppler imaging (see Section II).
2) Second, it enables tracking beyond the Nyquist frequency, whereas others have not investigated this problem.

3) Third, exact frequency likelihood functions are computed, whereas [17] uses a detection step, and [3] uses an approximation.
4) Last, the tracking method is entirely unsupervised with a maximum likelihood hyperparameter estimation. This is not a straightforward task in the context of frequency tracking since the nonlinear character of the data as functions of frequencies prevents the explicit handling of the likelihood function of the hyperparameter. We have developed an EM-like gradient procedure, inspired by [19]–[21]. It can be derived only after discretizing the frequencies on a finite grid.

The paper is organized as follows. The notation, signal model, and assumptions are defined in Section II. Section III contains the proposed regularized method, and Section IV gives a discrete approximation. Section V is devoted to the estimation of hyperparameters. The performance of the proposed method is demonstrated by the computer simulations in Section VI, whereas Section VII gives our conclusion and describes possible extensions.

II. Statement, Notations and Assumptions

In Doppler imaging, the signals to be analyzed occur as a set of complex signals $\mathcal{Y} = [\boldsymbol{y}_1, \ldots, \boldsymbol{y}_T]$ juxtaposed spatially in T range bins [22], [23]. The data record $\boldsymbol{y}_t = [y_t(1), \ldots, y_t(N)]^t$ ("t" denotes the matrix transpose) is extracted from a cisoid in additive complex noise. The amplitude and the frequency of the cisoid are $a_t \in \mathbb{C}$ and $\nu_t \in \mathbb{R}$:

$$\boldsymbol{y}_t = a_t\, \boldsymbol{z}(\nu_t) + \boldsymbol{b}_t = a_t\, [1, \ldots, e^{j2\pi\nu_t(N-1)}]^t + \boldsymbol{b}_t. \qquad (1)$$

The vectors $\boldsymbol{\nu} = [\nu_1, \ldots, \nu_T]^t$ and $\boldsymbol{a} = [a_1, \ldots, a_T]^t$ collect the frequencies and corresponding amplitudes. Finally, the true parameters are denoted with a star. This paper builds a robust estimate $\widehat{\boldsymbol{\nu}}$ for $\boldsymbol{\nu}^\star$ on the basis of data set $\mathcal{Y}$ (see Fig. 1 for a simulated example).

Remark 1: Model (1) is frequently used for spectral problems; it has three main features. First, while it is linear w.r.t. a_t, it is not so w.r.t. ν_t; the problem to be solved is nonlinear. Second, $\boldsymbol{z}(\nu_t)$ is a 1-periodic function w.r.t. ν_t, and this causes the difficulties of aliasing, frequency ambiguity, likelihood periodicity, etc. Last, this periodicity is also the keystone of the paper; aliasing is inverted, using a coherent statistical approach that takes periodicity into consideration.

The following definition of periodicity is used throughout the paper.

Definition 1: Let $A \subset \mathbb{R}^T$ and $\varphi : A \to \mathbb{R}$. Let us note $\mathbf{1} = [1, \ldots, 1]^t \in \mathbb{R}^T$. φ is said to be

- separately-1-periodic (S1P) if $\forall \boldsymbol{u} \in A$, $\forall \boldsymbol{k} \in \mathbb{Z}^T$ (such that $\boldsymbol{u} + \boldsymbol{k} \in A$): $\varphi(\boldsymbol{u}) = \varphi(\boldsymbol{u} + \boldsymbol{k})$;
- globally-1-periodic (G1P) if $\forall \boldsymbol{u} \in \mathbb{R}^T$, $\forall k_0 \in \mathbb{Z}$ (such that $\boldsymbol{u} + k_0\mathbf{1} \in A$): $\varphi(\boldsymbol{u}) = \varphi(\boldsymbol{u} + k_0\mathbf{1})$.

The proposed estimation method deals with periodicity and aliasing inversion thanks to the following assumptions. They are stated for the sake of simplicity and calculation tractability as well as coherence with the applications under the scope of this paper.

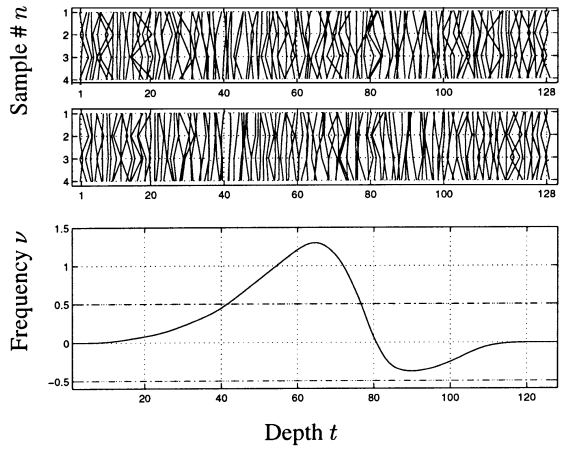

Fig. 1. Simulated observations over $T = 128$ range bins with $N = 4$ samples per bin. From top to bottom: real parts, imaginary parts of the data $\boldsymbol{y}_t$, and the true frequency sequence $\nu_t^\star$.

- Parameter dependence.
  - H_1: $\boldsymbol{a}$, $\boldsymbol{\nu}$ and the $\boldsymbol{b}_t$ are independent.
- Law for measurement and modeling noise $\boldsymbol{b}_t$.
  - H_2^a: Each $\boldsymbol{b}_t$ is $\mathcal{N}(r_b I_N)$.
  - H_2^b: The sequence of $\boldsymbol{b}_t$ is itself white.
- Law for parameters $\boldsymbol{a}$ and $\boldsymbol{\nu}$.
  - H_3^a: $\boldsymbol{a}$ is $\mathcal{N}(r_a I_T)$, i.e., white.
  - H_3^b: $\boldsymbol{\nu}$ is, on the contrary, correlated: $\mathcal{N}(R_\nu)$

where $\mathcal{N}(R)$ stands for a complex zero-mean Gaussian vector with covariance R, and $I_P, P \in \mathbb{N}^*$ denotes the $P \times P$ identity matrix.

The first assumption H_1 is quite natural since no information is available about the relative fluctuations of noise and objects. The assumptions H_2^a, and H_2^b are also natural since no correlation structure is expected in noise. Similarly, we have no information about the variation of the amplitude sequence; therefore, an independent law is used. A Gaussian law is preferred (H_3^a) to make the calculations tractable. Contrarily, the smoothness of the frequency sequence is modeled as a positive correlation. A Markovian structure (specified below) is a simple, useful way to account for it. Several choices are available, but the Gaussian one is also stated for the sake of simplicity (H_3^b).

III. Proposed Method

A. Likelihood

Assumption H_2^a yields a parametric structure for each likelihood function $f(\boldsymbol{y}_t \,|\, \nu_t, a_t)$:

$$f(\boldsymbol{y}_t \,|\, \nu_t, a_t) = (\pi r_b)^{-N} \exp\left[-\frac{1}{r_b} CLL(\nu_t, a_t)\right]$$

involving the opposite of the logarithm of the likelihood function (up to constant terms) i.e., the Co-Log-Likelihood (CLL):

$$\mathrm{CLL}(\nu_t, a_t) = [\boldsymbol{y}_t - a_t \boldsymbol{z}(\nu_t)]^\dagger\, [\boldsymbol{y}_t - a_t \boldsymbol{z}(\nu_t)]\,.$$

From a deterministic standpoint, $\mathrm{CLL}(\nu_t, a_t)$ is clearly the least squares (LS) estimation criterion.

Considering the whole frequency vector $\boldsymbol{\nu}$ and the whole data set $\mathcal{Y}$, assumption H_2^b yields

$$f(\mathcal{Y}\,|\,\boldsymbol{\nu},\boldsymbol{a}) = (\pi r_b)^{-NT}\exp\left[-\frac{1}{r_b}CLL(\boldsymbol{\nu},\boldsymbol{a})\right] \qquad (2)$$

where the global CLL is a global LS criterion

$$CLL(\boldsymbol{\nu},\boldsymbol{a}) = \sum_{t=1}^{T} CLL(\nu_t, a_t).$$

Remark 2: According to Definition 1, the likelihood function CLL$(\cdot,\boldsymbol{a})$ is S1P for all $\boldsymbol{a}\in\mathbb{C}^T$. Therefore, two configurations $\boldsymbol{\nu}$ and $\boldsymbol{\nu}+\boldsymbol{k}$ ($\boldsymbol{k}\in\mathbb{Z}^T$) for the frequency sequence are equilikelihood. As a consequence, an ML approach suffers from T independent frequency ambiguities.

B. Amplitude Law and Marginalization

The parameters of interest are the frequencies, whereas the amplitudes are nuisance parameters. These are integrated out of the problem in the usual Bayesian approach.

Given separability assumption H_1, one has $f(\boldsymbol{\nu},\boldsymbol{a}) = f(\boldsymbol{\nu})f(\boldsymbol{a})$, and the marginal law can easily be deduced:

$$f(\mathcal{Y},\boldsymbol{\nu}) = f(\boldsymbol{\nu})\int_{\boldsymbol{a}} f(\mathcal{Y}\,|\,\boldsymbol{a},\boldsymbol{\nu})f(\boldsymbol{a})d\boldsymbol{a} = f(\boldsymbol{\nu})f(\mathcal{Y}\,|\,\boldsymbol{\nu}).$$

The joint law for the amplitudes is separable according to assumption H_3^a. Since likelihood (2) is also separable, marginalization can be performed independently.

$$f(\mathcal{Y}\,|\,\boldsymbol{\nu}) = \prod_{t=1}^{T}\int_{a_t} f(\boldsymbol{y}_t\,|\,\nu_t,a_t)f(a_t)da_t. = \prod_{t=1}^{T} f(\boldsymbol{y}_t\,|\,\nu_t). \qquad (3)$$

The Gaussian amplitude assumption H_3^a results in analytic derivations and yield the marginal likelihood for the data $\boldsymbol{y}_t$, given ν_t, which is zero mean Gaussian vector. Its covariance R_t is given in Appendix A-B as well as its determinant (23) and its inverse (24). $f(\boldsymbol{y}_t\,|\,\nu_t)$ then reads

$$f(\boldsymbol{y}_t\,|\,\nu_t) = \beta\exp\left[-\gamma_t\right]\exp\left[\alpha P_t(\nu_t)\right] \qquad (4)$$

with $\alpha = Nr_a/(r_b(Nr_a+r_b))$, $\beta = \pi^{-N}r_b^{1-N}/(Nr_a+r_b)$, $\gamma_t = \boldsymbol{y}_t^{\dagger}\boldsymbol{y}_t/r_b$, and P_t is the periodogram of vector $\boldsymbol{y}_t$

$$P_t(\nu_t) = \frac{1}{N}\left|\sum_{n=1}^{N} y_t(n)e^{-2j\pi\nu_t n}\right|^2.$$

The joint law for the whole data set given the frequency sequence is obtained by the product (3)

$$f(\mathcal{Y}\,|\,\boldsymbol{\nu}) = \beta^T\exp\left[-\gamma\right]\exp\left[-\alpha\mathrm{CLML}(\boldsymbol{\nu})\right] \qquad (5)$$

where γ is the sum of the γ_t for $t\in\mathbb{N}_T^* = \{1,\ldots,T\}$, and where CLML is the co-log-marginal-likelihood

$$CLML(\boldsymbol{\nu}) = -\sum_{t=1}^{T} P_t(\nu_t) \qquad (6)$$

which is the opposite of the sum of the periodograms of data $\boldsymbol{y}_t$ at frequency ν_t in gate t.

Remark 3: This remark is the marginal counterpart of Remark 2. As well as CLL$(\cdot,\boldsymbol{a})$, CLML$(\cdot)$ is S1P. There are still many ambiguities as in the nonmarginal case. This was expected since no information about the frequency sequence has been accounted for in CLML$(\boldsymbol{\nu})$ w.r.t. CLL$(\boldsymbol{\nu},\boldsymbol{a})$. In contrast, periodicity will be eliminated in the next subsection by accounting for the frequency sequence smoothness.

C. Prior Law for Frequency Sequence

Unlike amplitudes, the frequency sequence is smooth. A Markovian structure accurately accounts for this information, and there are many algorithms suited to computing this structure. The choice of the family law is not crucial for using these algorithms, but we have used the Gaussian family

$$f(\nu_{t+1}\,|\,\nu_t) = (2\pi r_\nu)^{-1/2}\exp\left[-\frac{1}{2r_\nu}(\nu_{t+1}-\nu_t)^2\right].$$

The complete law for the chain also involves the initial state. It is assumed to be uniformly distributed over a symmetric set $\mathbb{K}$ defined by $K\in\mathbb{N}^*$: $\mathbb{K} = [-K/2;+K/2]$. Therefore, $f(\nu_1) = (1/K)\mathbb{1}_K^0(\nu_1)$, where $\mathbb{1}_K^0$ is 1 in $\mathbb{K}$ and 0 outside.

The recursive conditioning rule immediately yields

$$f(\boldsymbol{\nu}) = (2\pi r_\nu)^{-(T-1)/2}\exp\left[-\frac{1}{2r_\nu}\mathrm{CLP}(\boldsymbol{\nu})\right] \qquad (7)$$

where CLP$(\boldsymbol{\nu})$ is the co-log-prior

$$\mathrm{CLP}(\boldsymbol{\nu}) = \widetilde{K}\mathbb{1}_K^\infty(\nu_1) + \sum_{t=1}^{T-1}(\nu_{t+1}-\nu_t)^2. \qquad (8)$$

$\widetilde{K} = 2r_\nu\log K$ and $\mathbb{1}_K^\infty$ is 1 in $\mathbb{K}$ and $+\infty$ outside. In the deterministic framework, CLP$(\boldsymbol{\nu})$ is a quadratic norm for the first-order differences, namely, a regularization term [24]–[26].

D. Posterior Law

Fusion of *prior* -based and data-based information is achieved by the Bayes rule, which provides the *a posteriori* density for $\boldsymbol{\nu}$

$$f(\boldsymbol{\nu}\,|\,\mathcal{Y}) = \frac{f(\mathcal{Y}\,|\,\boldsymbol{\nu})f(\boldsymbol{\nu})}{f(\mathcal{Y})}.$$

The marginal law $f(\mathcal{Y})$ for the whole data set $\mathcal{Y}$ is not analytically tractable, essentially due to the nonlinearity of the periodogram w.r.t. ν_t and the correlated structure of $\boldsymbol{\nu}$. Fortunately, this p.d.f. does not depend on $\boldsymbol{\nu}$; therefore, the *a posteriori* density remains explicit up to a positive constant. *Prior* structure of (7) and (8) and likelihood structure of (5) and (6) immediately yield the *posterior* law

$$f(\boldsymbol{\nu}\,|\,\mathcal{Y}) \propto \exp\left[-\alpha CLPL(\boldsymbol{\nu})\right] \qquad (9)$$

where the co-log-posterior-likelihood function (CLPL) reads

$$\mathrm{CLPL}(\boldsymbol{\nu}) = -\sum_{t=1}^{T} P_t(\nu_t) + \lambda\sum_{t=1}^{T-1}(\nu_{t+1}-\nu_t)^2 + \mathbb{1}_K^\infty(\nu_1) \qquad (10)$$

where $\lambda = 1/2\alpha r_\nu$, up to irrelevant constants. In the deterministic framework, CLPL is a regularized least squares (RLS) criterion. It has three terms: one measures fidelity to the data, the

second measures fidelity to the *prior* smoothness, and the third enforces the first frequency $\nu_1 \in \mathbb{K}$. The regularization parameter λ (depending on hyperparameters $\boldsymbol{r} = [r_a, r_b, r_\nu]$) balances the compromise between *prior* -based and data-based information.

E. Point Estimate

As a point estimate, a popular choice is the maximum *a posteriori* (MAP) i.e., the maximizer of the *posterior* law of (9) or the minimizer of the RLS criterion (10):

$$\widehat{\boldsymbol{\nu}}^{\mathrm{MAP}} = \arg\max_{\boldsymbol{\nu}\in\mathbb{R}} f(\boldsymbol{\nu}\,|\,\mathcal{Y}) = \arg\min_{\boldsymbol{\nu}\in\mathbb{R}} \mathrm{CLPL}(\boldsymbol{\nu}). \tag{11}$$

Remark 4: This remark is the posterior counterpart of Remarks 2 and 3. Whereas CLL and CLML are S1P, CLPL is not; regularization breaks periodicities, favors solutions according to prior probabilities, and enables some ambiguities to be removed. Nevertheless, a global indetermination remains: CLPL is a G1P function. This is essentially due to the facts that i) the marginal likelihood CLML is a S1P function, and ii) the regularization term CLP is a G1P function (since it only involves frequency differences). As a consequence, two frequency profiles, which are different from a constant integer level, remain equi-likelihood. Finally, the latter indeterminacy can be removed by choosing an appropriate K: $K = 1$ enforces the first frequency ν_1 to remain in $(-0.5, +0.5]$, and the corresponding CLPL is no longer G1P.

Proposition 1: With the previous notations and definitions, the MAP estimate is such that

$$|\widehat{\nu}_{t+1}^{\mathrm{MAP}} - \widehat{\nu}_t^{\mathrm{MAP}}| \leqslant \frac{1}{2} \quad \text{for } t \in \mathbb{N}_{T-1}^*. \tag{12}$$

Proof: See Appendix B. ■

F. Optimization Stage

The proposed approach allows ambiguous periodicity to be removed at the expense of accepting local minima in the built energy (10). A gradient procedure [27] can achieve *local* minimization of (10) and CLPL gradient involves the periodograms derivatives

$$P_t'(\nu_t) = 2j\pi \sum_{n=1-N}^{N-1} n\widehat{c}_t(n)e^{2j\pi\nu_t n}$$

when rewriting $P_t(\nu_t)$ as a function of empirical correlation lags $\widehat{c}_t(n)$ of the signal $\boldsymbol{y}_t$. It is also possible to calculate the second-order derivative

$$P_t''(\nu_t) = -4\pi^2 \sum_{n=1-N}^{N-1} n^2\widehat{c}_t(n)e^{2j\pi\nu_t n}$$

and to implement second-order descent algorithms.

There are several ways of coping with *global* optimization, e.g., graduated nonconvexity [28], [29] and stochastic algorithms such as simulated annealing [30], [31]. We have used a dynamic programming procedure for computational simplicity. It is based on a discrete approximation of the *prior* law for the frequencies. This approximation allows global optimization (on an arbitrary fine discrete frequency grid) and provides a convenient framework for estimating hyperparameters.

IV. Discrete State Markov Chain

This section is devoted to a discrete approximation for

1) maximizing *posterior* law for the frequency sequence $\boldsymbol{\nu}$;
2) building an ML procedure for estimating hyperparameters.

We have therefore introduced an equally spaced discretization of the frequency range $[\nu_m; \nu_M]$ in P states $\nu^1, \ldots, \nu^P$ ($\nu_M = -\nu_m = 2.5$ and $P = 128$ in our simulations).

A. Probabilities

Discretization and normalization of the *a priori* law (7) yields the state transition probabilities:

$$\begin{aligned}\mathbb{P}_t(p,q) &= \Pr\left[\nu_{t+1} = \nu^p \,|\, \nu_t = \nu^q\right] \\ &= \frac{\exp\left(\frac{-(\nu^p-\nu^q)^2}{2r_\nu}\right)}{\sum_{p=1}^{P}\exp\left(\frac{-(\nu^p-\nu^q)^2}{2r_\nu}\right)}.\end{aligned} \tag{13}$$

Note that $\mathbb{P}_t$ does not depend on t, i.e., the proposed chain is homogeneous $\mathbb{P}_t = \mathbb{P}$. The full state model also includes the initial probabilities $_{\mathbf{P}}(p)$ chosen constant over $(-0.5, +0.5]$ (see Remark 4).

The marginal (w.r.t. amplitudes) likelihood function for the observation sequence given by (4) yields the observation probability distribution $\mathbb{O}_t(p) = f(\boldsymbol{y}_t\,|\,\nu_t = \nu^p)$.

B. Available Algorithms

The Markov chain is now convenient for using algorithms given in [32] and [33]: the Viterbi and the Forward-Backward algorithms. They enable us to compute

- the MAP;
- the hyperparameters likelihood as well as its gradient.

1) Viterbi Algorithm: The Viterbi algorithm, which is shown in Appendix C-A, has been implemented to cope with global optimization (on a discrete grid) and performs a step-by-step optimization of the *posterior* law. The required observation probabilities are also readily precomputable by the FFT.

2) Forward–Backward Algorithm: We have used a normalized version of the procedure, as recommended in [34] and [35], to avoid computational problems. It is founded on forward and backward probabilities

$$\begin{aligned}\mathcal{F}_t(p) &= \frac{\Pr\left[\mathcal{Y}_1^t, \nu_t = \nu^p\right]}{\Pr\left[\mathcal{Y}_1^t\right]} \\ \text{and} \quad \mathcal{B}_t(p) &= \frac{\Pr\left[\mathcal{Y}_{t+1}^T \,|\, \nu_t = \nu^p\right]}{\Pr\left[\mathcal{Y}_{t+1}^T \,|\, \mathcal{Y}_1^t\right]}\end{aligned}$$

where $\mathcal{Y}_t^{t'} = [\boldsymbol{y}_t, \ldots, \boldsymbol{y}_{t'}]$ denotes the partial observation matrix from time t to t'.

The (count-up) Forward algorithm, which is given in Appendix C-B, computes non-normalized probabilities $\overline{\mathcal{F}}_t(p)$, normalization coefficients $\mathcal{N}_t$, and the $\mathcal{F}_t(p)$ themselves. As a result, the observation likelihood can be deduced

$$\Pr\left[\mathcal{Y}\right] = \prod_{t=1}^{P} \mathcal{N}_t. \tag{14}$$

It is useful for estimating ML hyperparameters in Section V. The (count-down) Backward step, which is described in Appendix C-C, yields marginal *a posteriori* probabilities (see [32, p. 10])

$$p_t(p) = \Pr\left[\nu_t = \nu^p \,|\, \mathcal{Y}\right] = \mathcal{F}_t(p)\mathcal{B}_t(p) \tag{15}$$

and double marginal *a posteriori* probabilities (see [32, p. 11])

$$\begin{aligned} p_t(p,q) =& \Pr\left[\nu_{t-1} = \nu^q, \nu_t = \nu^p \,|\, \mathcal{Y}\right] \\ =& \mathcal{N}_t\, \mathcal{F}_{t-1}(p)\, \mathcal{B}_t(q)\, \mathbb{P}(p,q)\, \mathbb{O}_t(q) \end{aligned} \tag{16}$$

which are both needed to calculate the likelihood gradient.

V. Estimating Hyperparameters

The MAP estimate of (11) depends on a unique regularization parameter λ function of three hyperparameters $\boldsymbol{r} = [r_a, r_b, r_\nu]$. This section is devoted to their estimation using the available data set $\mathcal{Y}$.

Estimating hyperparameters within the regularization framework is generally a delicate problem. It has been extensively studied, several techniques have been proposed and compared [36]–[41] and the preferred strategy is founded on ML.

The ML estimation consists of i) expressing the hyperparameter likelihood (HL) as $HL_{\mathcal{Y}}(\boldsymbol{r}) = f(\mathcal{Y})$ and ii) maximizing the resulting function. Although we have chosen a simple Gaussian law, $\boldsymbol{\nu}$ cannot be marginalized in closed form because $\boldsymbol{\nu}$ enters $f(\mathcal{Y}|\boldsymbol{\nu})$ in a complex manner. Fortunately, the discrete state approximation of Section IV provides a satisfactory solution to this problem. It also allows us to devise several kinds of algorithms for local maximization of the likelihood. One such scheme is the acknowledged expectation-maximization (EM) algorithm, although its application reveals uneasy in the present context of a parametric model of hidden Markov chain ([19] provides a meaningful discussion of such situations; see also [20] and [21]). Section V-B is devoted to the EM framework, within which a gradient procedure is proposed. Section V-A deals with the computation of the likelihood and proposes a simple coordinatewise descent procedure.

A. Hyperparameter Likelihood

The hyperparameter likelihood $\mathrm{HL}_{\mathcal{Y}}$ can be deduced from the joint law for $(\boldsymbol{\nu}, \mathcal{Y})$ by frequency marginalization:

$$\mathrm{HL}_{\mathcal{Y}}(\boldsymbol{r}) = \sum_{p_1,\ldots,p_T=1}^{P} \Pr\left[\mathcal{Y}, \nu_1 = \nu^{p_1}, \ldots, \nu_T = \nu^{p_T}\right]$$

but the indices run over P^T states; therefore, the above summation is not directly tractable. However, the Forward procedure efficiently achieves a recursive marginalization; it yields $\mathrm{HL}_{\mathcal{Y}}(\boldsymbol{r})$ according to (14) and requires about TP^2 calculations.

Let us introduce the co-log-HL (CLHL) to be minimized w.r.t. hyperparameters vector $\boldsymbol{r}$:

$$\widehat{\boldsymbol{r}}^{\mathrm{ML}} = \arg\min_{\boldsymbol{r}} \mathrm{CLHL}_{\mathcal{Y}}(\boldsymbol{r}).$$

One possible optimization scheme is a coordinatewise descent algorithm with a golden section line search [27], but a more efficient scheme may be a gradient algorithm [27].

B. Likelihood Gradient

The EM algorithm relies on an auxiliary function, which is usually denoted Q [42], [43] built on two hyperparameter vectors $\boldsymbol{r}$ and $\boldsymbol{r}'$ by completing the observed data set $\mathcal{Y}$ with parameters to be marginalized $\boldsymbol{\nu}$:

$$\begin{aligned} Q(\boldsymbol{r}, \boldsymbol{r}') =& E_{\boldsymbol{\nu}}\Big[\log(\Pr\left[\boldsymbol{\nu}, \mathcal{Y}; \boldsymbol{r}'\right]) \Big| \mathcal{Y}; \boldsymbol{r}\Big] \\ =& \sum_{\boldsymbol{\nu}} \log \Pr\left[\boldsymbol{\nu}, \mathcal{Y}; \boldsymbol{r}'\right] \Pr\left[(\boldsymbol{\nu} \,|\, \mathcal{Y}; \boldsymbol{r})\right]. \end{aligned}$$

With the proposed notations, usual hidden Markov chains calculations yield

$$\begin{aligned} Q(\boldsymbol{r}, \boldsymbol{r}') =& \sum_{t=2}^{T} \sum_{p,q=1}^{P} p_t(p,q)\, \log \mathbb{P}'(p,q) \\ &+ \sum_{p=1}^{P} \mathbb{P}(p)\, \log\, \mathbb{P}'(p) + \sum_{t=1}^{T} \sum_{p=1}^{P} p_t(p)\, \log \mathbb{O}'_t(p) \end{aligned} \tag{17}$$

where we have the following.

- $(\mathbb{P}', \mathbb{P}', \mathbb{O}')$ and $(\mathbb{P}, \mathbb{P}, \mathbb{O})$ are parameters of the model under hyperparameters $\boldsymbol{r}'$ and $\boldsymbol{r}$, respectively.
- $p_t(p)$ and $p_t(p,q)$ denote the *a posteriori* marginal laws defined by (15) and (16), under hyperparameters $\boldsymbol{r}$.

The kth iteration of the EM scheme maximizes $Q(\boldsymbol{r}^{(k-1)}, \boldsymbol{r}')$ as a function of $\boldsymbol{r}'$ to yield $\boldsymbol{r}^{(k)}$ as the maximizer. Unfortunately, it seems impossible to derive an explicit expression for such a maximizer. However, an alternate route can be followed, given the key property

$$\frac{\partial Q(\boldsymbol{r}, \boldsymbol{r}')}{\partial \boldsymbol{r}'}\Big|_{\boldsymbol{r}'=\boldsymbol{r}} = -\frac{\partial \mathrm{CLHL}_{\mathcal{Y}}(\boldsymbol{r})}{\partial \boldsymbol{r}}.$$

As suggested by [19], this property enables us to calculate the gradient of $\mathrm{CLHL}_{\mathcal{Y}}(\boldsymbol{r})$ as the derivative of (17):

$$\frac{\partial Q}{\partial r'_a} = \sum_{t=1}^{T} \sum_{p=1}^{P} p_t(p) \frac{\partial \log \mathbb{O}'_t(p)}{\partial r'_a} \tag{18}$$

$$\frac{\partial Q}{\partial r'_b} = \sum_{t=1}^{T} \sum_{p=1}^{P} p_t(p) \frac{\partial \log \mathbb{O}'_t(p)}{\partial r'_b} \tag{19}$$

$$\frac{\partial Q}{\partial r'_\nu} = \sum_{t=2}^{T} \sum_{p,q=1}^{P} p_t(p,q) \frac{\partial \log \mathbb{P}'(p,q)}{\partial r'_\nu}. \tag{20}$$

The encountered derivatives $\partial \log \mathbb{O}'(p)/\partial r'_a$, $\partial \log \mathbb{O}'(p)/\partial r'_b$ and $\partial \log \mathbb{P}'(p,q)/\partial r'_\nu$, respectively, read

$$\frac{-N}{Nr'_a + r'_b} + \frac{N}{(Nr'_a + r'_b)^2} P_t(\nu^p)$$

$$\frac{1-N}{r'_b} - \frac{1}{Nr'_a + r'_b} + \frac{\boldsymbol{y}_t^\dagger \boldsymbol{y}_t}{r'^2_b} - \frac{Nr'_a(Nr'_a + 2r'_b)}{r'^2_b (Nr'_a + r'_b)^2} P_t(\nu^p)$$

$$\frac{1}{2r'^2_\nu}\Big((\nu^q - \nu^p)^2 - \sum_{r=1}^{P} (\nu^r - \nu^p)^2 \mathbb{P}'(p,r)\Big)$$

by derivation of (4) and (13). Finally, the likelihood gradient is readily calculated, and a gradient procedure can be applied.

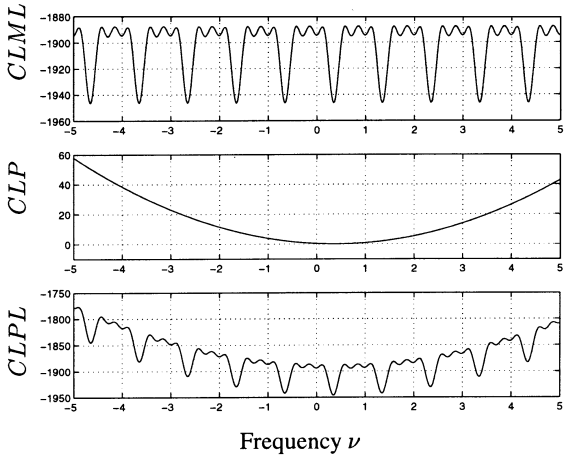

Fig. 2. Typical form of criteria. From top to bottom: CLML($\boldsymbol{\nu}$) (periodic), CLP($\boldsymbol{\nu}$) (quadratic), and CLPL($\boldsymbol{\nu}$) as a function of ν_t ($t = 50$). Regularization breaks periodicity.

VI. Simulation Results and Comparisons

The previous sections introduced a regularized method for frequency tracking and estimating hyperparameters. This section demonstrates the practical effectiveness of the proposed approach by processing[1] simulated signals shown in Fig. 1.

A. Hyperparameter Estimation

The hyperparameter likelihood function CLHL was first computed on a fine discrete grid of $25 \times 25 \times 25$ values, resulting in the level sets shown in Figs. 2 and 3. The function is fairly regular and has a single minimum.

The hyperparameters are tuned using two classes of descent algorithms:

- a coordinate-wise descent algorithm;
- a gradient descent algorithm.

The latter employs several descent directions: usual gradient, bisector correction, Vignes correction, and Polak-Ribière pseudo-conjugate direction. Two line search methods have also been implemented: usual dichotomy and quadratic interpolation. The starting point remains the empirical hyperparameter vector described in Appendix D.

All the strategies provide the correct minimizer, and they are compared in Table I and Fig. 3. The usual gradient generated zig-zagging trajectories and was slower than the other strategies. The three corrected direction strategies were 25 to 40% faster than the uncorrected ones with the Polak–Ribière pseudo-conjugate direction having a slight advantage. In contrast, interpolation did not result in any improvement within the corrected direction class.

The coordinate-wise descent algorithm performed well since it does not require any gradient calculation. Gradient calculus needs a lot more computation than the likelihood itself, due to summations in (18)–(20). Likelihood calculus took 0.05 s, whereas gradient calculus required 0.2 s., i.e., about four times more.

[1]Algorithms have been implemented using the computing environment *Matlab* on a Pentium III PC with a 450-MHz CPU and 128 MB of RAM.

We have therefore adopted the two fastest methods: coordinate-wise and Polak-Ribière pseudo-conjugate gradient, which took less than 3.5 s. Fig. 3 also illustrates the convergence.

B. Frequency Tracking

The optimization procedure used to compute the MAP (given ML hyperparameters) consisted of applying the Viterbi algorithm (described in Section IV-B1). The solution was used as the starting point for the gradient or the Hessian procedure (described in Section III-F). The Viterbi algorithm explored the whole set of possible frequencies (on a discrete grid) and found the correct interval for each frequency, whereas the gradient or Hessian procedure locally refined the optimum. Table II shows the computation times. We adopted the Hessian procedure since it performed almost ten times faster.

Fig. 4 illustrates typical results. The ML strategy

- lacked robustness for two reasons: Estimation was performed independently at each depth, and N was small;
- could not be corrected by an unwrap-like post-processing since the ML solution was too rough (as already mentioned).

For the regularized solution (also given in Fig. 4), a simple qualitative comparison with the reference led to three conclusions.

- The estimated frequency sequence conformed much better to the true one. The frequency sequence was more regular since smoothness was introduced as a *prior* feature.
- The estimated frequency sequence remained close to the true one even beyond the usual Nyquist frequency. This was essentially due to the coherent accounting for the whole set of data and smoothness of the frequency sequence.
- The proposed strategy for estimating hyperparameters is adequate. A variation of 0.1 of the hyperparameters resulted in an almost imperceptible variation in the estimated frequency sequence. This is especially important for qualifying the robustness of the proposed method; the choice of $\boldsymbol{r}$ offers relatively broad leeway and can be reliably made.

VII. Conclusion and Perspectives

This paper examines the problem of frequency tracking beyond the Nyquist frequency as it occurs in Doppler imaging when only short noisy data records are available. A solution is proposed in the Bayesian framework based on hidden Gauss–Markov models accounting for *prior* smoothness of the frequency sequence. We have developed a computationally efficient combination of dynamic programming and a Hessian procedure to calculate the maximum *a posteriori*. The method is entirely unsupervised and uses an ML procedure based on an original EM-based gradient procedure. The estimation of the ML hyperparameter is both formally achievable and practically useful.

This new Bayesian method allows tracking beyond the usual Nyquist frequency due to a coherent statistical framework that includes the whole set of data plus smoothness *prior*. To our

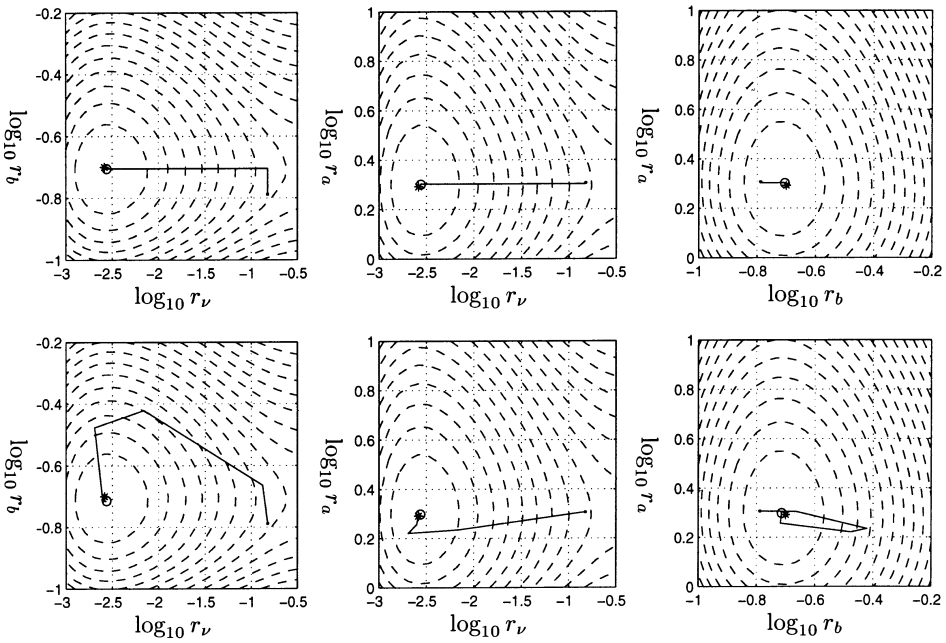

Fig. 3. Hyperparameter likelihood: typical behavior. Level sets of CLHL are plotted as dashed lines (—). The minima are located by a star ($*$), starting points (empirical estimates) by a dot, (.) and final estimate by a circle (o). The first row gives coordinate-wise algorithm, and the second row gives a gradient algorithm. First column: CLHL($\widehat{r}_a^{\mathrm{ML}}, r_b, r_\nu$); second column: CLHL($r_a, \widehat{r}_b^{\mathrm{ML}}, r_\nu$); third column: CLHL($r_a, r_b, \widehat{r}_\nu^{\mathrm{ML}}$). Each figure is $\log_{10}$ scaled.

TABLE I
DESCENT ALGORITHM COMPARISON. THE FIRST COLUMN GIVES THE METHOD AT WORK: (1) USUAL GRADIENT, (2) VIGNES CORRECTION, (3) BISECTOR CORRECTION, AND (4) POLAK-RIBIÉRE PSEUDO-CONJUGATE DIRECTION. (A) NO INTERPOLATION AND (B) QUADRATIC INTERPOLATION. (5) COORDINATE-WISE DESCENT METHOD. FOLLOWING COLUMNS SHOW THE REACHED MINIMUM AND THE MINIMIZER. SIXTH COLUMN GIVES THE NUMBER OF GRADIENTS AND FUNCTION CALCULUS, WHEREAS THE LAST GIVES COMPUTATION TIMES IN SECONDS (s)

Method	Reached minimum	$\log_{10} \widehat{r}_a^{\mathrm{ML}}$	$\log_{10} \widehat{r}_b^{\mathrm{ML}}$	$\log_{10} \widehat{r}_\nu^{\mathrm{ML}}$	Grad./Fun.	Time (s)
(1a)	4.513 10^2	0.297	-0.685	-2.424	17/59	5.55
(1b)	4.495 10^2	0.297	-0.679	-2.519	13/87	5.92
(2a)	4.494 10^2	0.292	-0.678	-2.537	9 /49	3.77
(2b)	4.494 10^2	0.299	-0.681	-2.554	13/92	6.14
(3a)	4.498 10^2	0.297	-0.695	-2.589	9 /53	4.07
(3b)	4.494 10^2	0.298	-0.679	-2.547	13/92	6.21
(4a)	4.497 10^2	0.283	-0.674	-2.507	7 /40	3.12
(4b)	4.500 10^2	0.297	-0.685	-2.618	9 /75	4.84
(5)	4.495 10^2	0.300	-0.671	-2.559	0 /81	3.41

TABLE II
COMPUTATION TIMES COMPARISON FOR FREQUENCY ESTIMATE

Method	Time (s)
MAP Viterbi	0.13
MAP Gradient	4.82
MAP Hessian	0.51

knowledge, this capability is an original contribution to the field of frequency tracking.

Future work may include the extension to Gaussian DSP [9], to multiple frequencies tracking [3], [17], and to the two-dimensional (2-D) problem. The latter and its connection to 2-D phase unwrapping [44]–[46] is presently being investigated.

APPENDIX A
AMPLITUDE MARGINALIZATION

A. Preliminary Results

This Section includes two useful results: For $\boldsymbol{u} \in \mathbb{C}^N$

$$\det\left[I_N + \boldsymbol{u}\boldsymbol{u}^\dagger\right] = 1 + \boldsymbol{u}^\dagger \boldsymbol{u} \tag{21}$$

$$\left(I_N + \boldsymbol{u}^\dagger \boldsymbol{u}\right)^{-1} = I_N - \frac{\boldsymbol{u}\boldsymbol{u}^\dagger}{1 + \boldsymbol{u}^\dagger \boldsymbol{u}} \tag{22}$$

where I_N stands for the $N \times N$ identity matrix.

B. Law for $(\boldsymbol{y}_t|\nu_t)$

Linearity of model (1) w.r.t. amplitudes and assumptions for a_t and $\boldsymbol{b}_t$ allow easy marginalization of $(\boldsymbol{y}_t, a_t|\nu_t)$: $\boldsymbol{y}_t|\nu_t$

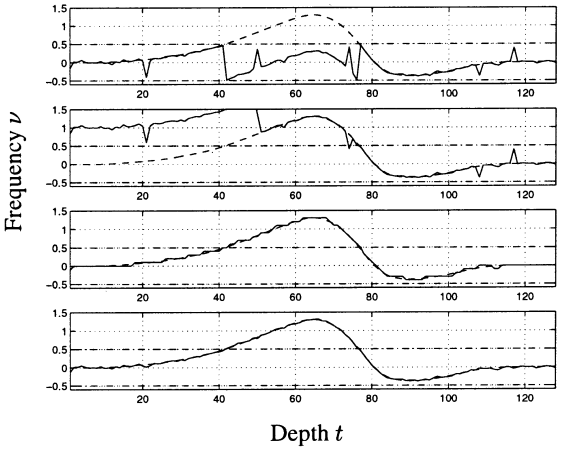

Fig. 4. Comparison of frequency profile estimates. From top to bottom: ML estimate (i.e., periodogram maximizer), unwrapped ML estimate, Viterbi-MAP estimate, and Hessian-MAP estimate.

is clearly a zero-mean and Gaussian vector with covariance $R_t = r_a \boldsymbol{z}(\nu_t)\boldsymbol{z}(\nu_t)^\dagger + r_b I_N$. From (21) and (22), its determinant and inverse reads

$$R_t^{-1} = \frac{1}{r_b} I_N - \frac{\alpha}{N} \boldsymbol{z}(\nu_t)\boldsymbol{z}(\nu_t)^\dagger \tag{23}$$

$$\det R_t = r_b^{N-1}(r_b + N r_a). \tag{24}$$

Appendix B
Proof of Proposition 1

A. Preliminary Result

The proposed proof is based on the decimal part function $D : \mathbb{R} \longrightarrow [-0.5; +0.5[$ defined by

$$\begin{cases} D(x) = x, & \text{if } x \in [-0.5; +0.5) \\ D \text{ is } 1 & \text{-periodic} \end{cases} \tag{25}$$

and the following straightforward properties:

$$D(x+k) = D(x), k \in \mathbb{Z} \tag{26}$$

$$|D(x)| \leqslant |x| \tag{27}$$

$$|D(x)| \leqslant \frac{1}{2} \tag{28}$$

$$y = D(x) \Rightarrow \exists k \in \mathbb{Z} \text{ such that } y = x + k. \tag{29}$$

B. Proof of Proposition

Let us define a frequency sequence $\boldsymbol{\nu}$ (with CLPL$(\boldsymbol{\nu}) < \infty$), which does not verify (12) of Proposition 1, i.e.,

$$\exists t_0 \in \mathbb{N}^*_{T-1} \text{ with } |\nu_{t_0+1} - \nu_{t_0}| > \frac{1}{2}. \tag{30}$$

Let us recursively build a new frequency sequence $\widetilde{\boldsymbol{\nu}}$:

$$\widetilde{\nu}_1 = \nu_1 \tag{31}$$

$$\widetilde{\nu}_{t+1} = \widetilde{\nu}_t + D(\nu_{t+1} - \widetilde{\nu}_t) \text{ for } t = 1, \ldots, T-1 \tag{32}$$

and prove that (12) of Proposition 1 holds for $\widetilde{\boldsymbol{\nu}}$ and that the criterion CLPL reduces from $\boldsymbol{\nu}$ to $\widetilde{\boldsymbol{\nu}}$:

$$|\widetilde{\nu}_{t+1} - \widetilde{\nu}_t| \leqslant \frac{1}{2} \text{ for } t \in \mathbb{N}^*_{T-1} \tag{33}$$

$$\text{CLPL}(\widetilde{\boldsymbol{\nu}}) < \text{CLPL}(\boldsymbol{\nu}). \tag{34}$$

- Relation (33) is straightforward; by (32), one can see

$$\widetilde{\nu}_{t+1} - \widetilde{\nu}_t = D(\nu_{t+1} - \widetilde{\nu}_t) \text{ for } t \in \mathbb{N}^*_{T-1}$$

and hence, by Property (28)

$$|\widetilde{\nu}_{t+1} - \widetilde{\nu}_t| \leqslant \frac{1}{2} \text{ for } t \in \mathbb{N}^*_{T-1}.$$

- Proof of (34) takes three steps, corresponding to each term of CLPL (10). By (31) and (32) and Property (29), one can see

$$\exists k_t \in \mathbb{Z} \text{ such that } \widetilde{\nu}_t = \nu_t + k_t \text{ for } t \in \mathbb{N}^*_T \tag{35}$$

(with $k_1 = 0$); therefore

$$P_t(\nu_t) = P_t(\widetilde{\nu}_t) \text{ for } t \in \mathbb{N}^*_T. \tag{36}$$

By (32) and (35) and invoking Property (26), we have

$$\widetilde{\nu}_{t+1} - \widetilde{\nu}_t = D(\nu_{t+1} - \widetilde{\nu}_t) = D(\nu_{t+1} - \nu_t)$$

hence, accounting for Property (27)

$$|\widetilde{\nu}_{t+1} - \widetilde{\nu}_t| \leqslant |\nu_{t+1} - \nu_t|. \tag{37}$$

Moreover, for $t = t_0$, we clearly have

$$|\widetilde{\nu}_{t_0+1} - \widetilde{\nu}_{t_0}| < |\nu_{t_0+1} - \nu_{t_0}| \tag{38}$$

thanks to hypothesis (30). Finally, we have

$$\mathbb{1}^\infty_K(\nu_1) = \mathbb{1}^\infty_K(\widetilde{\nu}_1). \tag{39}$$

Collecting (36)–(39) proves (34).

Appendix C
HMC Algorithms

A. Viterbi Algorithm

- `Precomputations`

$$\mathcal{D}(p,q) = \lambda(\nu^p - \nu^q)^2 \qquad (p, q \in \mathbb{N}^*_P)$$

$$\mathcal{L}(p,t) = -P_t(\nu^p) \qquad (p \in \mathbb{N}^*_P, t \in \mathbb{N}^*_T).$$

- `Initialization` $(t = 1)$

$$\mathcal{C}_1(p) = \mathcal{L}(p,1)\,\mathbb{1}^\infty_1(\nu^p) \qquad (p \in \mathbb{N}^*_P).$$

- `Iterations` $(t = 2, \ldots, T)$

$$\widetilde{\mathcal{C}}_t(p,q) = \mathcal{C}_{t-1}(q) + \mathcal{D}(p,q) + \mathcal{L}(p,t) \qquad (p, q \in \mathbb{N}^*_P)$$

$$\mathcal{C}_t(p) = \min_q \widetilde{\mathcal{C}}_t(p,q) \qquad (p \in \mathbb{N}^*_P)$$

$$\mathcal{P}_t(p) = \arg\min_q \widetilde{\mathcal{C}}_t(p,q) \qquad (p \in \mathbb{N}^*_P).$$

- `Termination` $(t = T)$

$$\widehat{p}_T = \arg\min_p \mathcal{C}_T(p).$$

- `Back tracking` $(t = T-1, \ldots, 1)$

$$\widehat{p}_t = \mathcal{P}_t(\widehat{p}_{t+1}).$$

B. Forward Algorithm

- `Initialization` $(t = 1)$

$$\begin{aligned}\overline{\mathcal{F}}_1(p) =& \mathbb{O}_1(p)\ \mathbf{P}(p) \qquad (p \in \mathbb{N}_P^*)\\ \mathcal{N}_1 =& \sum_{q=1}^{P} \overline{\mathcal{F}}_1(q)\\ \mathcal{F}_1(p) =& \frac{\overline{\mathcal{F}}_1(p)}{\mathcal{N}_1} \qquad (p \in \mathbb{N}_P^*).\end{aligned}$$

- `Iterations` $(t = 2, \ldots, T)$

$$\begin{aligned}\overline{\mathcal{F}}_t(p) =& \mathbb{O}_t(p) \sum_{q=1}^{P} \mathcal{F}_{t-1}(p)\mathbb{P}(q,p) \qquad (p \in \mathbb{N}_P^*)\\ \mathcal{N}_t =& \sum_{q=1}^{P} \overline{\mathcal{F}}_t(q)\\ \mathcal{F}_t(p) =& \frac{\overline{\mathcal{F}}_t(p)}{\mathcal{N}_t} \qquad (p \in \mathbb{N}_P^*).\end{aligned}$$

C. The Backward Algorithm

- `Initialization` $(t = T)$

$$\begin{aligned}\overline{\mathcal{B}}_T(p) =& 1 \qquad (p \in \mathbb{N}_P^*)\\ \mathcal{B}_T(p) =& 1 \qquad (p \in \mathbb{N}_P^*).\end{aligned}$$

- `Iterations` $(t = T-1, \ldots, 1)$

$$\begin{aligned}\overline{\mathcal{B}}_t(p) =& \sum_{q=1}^{P} \mathbb{O}_{t+1}(q)\mathcal{B}_{t+1}(p)\mathbb{P}(p,q) \qquad (p \in \mathbb{N}_P^*)\\ \mathcal{B}_t(p) =& \frac{\overline{\mathcal{B}}_t(p)}{\mathcal{N}_{t+1}} \qquad (p \in \mathbb{N}_P^*).\end{aligned}$$

Appendix D
Empirical Estimation of Hyperparameters

This section is devoted to the *empirical* estimation of hyperparameters used as a starting point in the maximization procedures of Section VI-A. These estimates are based on the correlation $r(n)$ of $\boldsymbol{y}_t|\nu_t$ and easily shown to verify $r(0) = r_a + r_b$, and $|r(1)| = r_a$, for all $t \in \mathbb{N}_T^*$. Empirical estimates $\widehat{r}(0)$ and $\widehat{r}(1)$ are computed from the whole data set $\mathcal{Y}$ and remain robust since T is large (even if N is small). Finally, one can compute $\widehat{r}_a = |\widehat{r}(1)|$, and $\widehat{r}_b = \widehat{r}(0) - |\widehat{r}(1)|$.

For r_ν, the estimation is based on the ML estimate of the frequency sequence in each range bin $t \in \mathbb{N}_T^*$. The proposed empirical estimate of r_ν is naturally the empirical variance of the differences between the ML frequencies. This procedure yields an overestimated value for r_ν. This result is expected since the sequence of ML frequencies varies greatly and has discontinuities, as mentioned above. Nevertheless, this estimate is a suitable starting point for the maximization procedures of Section VI-A.

References

[1] B. Boashash, "Estimating and interpreting the instantaneous frequency of a signal – Part 1: Fundamentals," *Proc. IEEE*, vol. 80, pp. 519–538, Apr. 1992.

[2] ——, "Estimating and interpreting the instantaneous frequency of a signal – Part 2: Algorithms and applications," *Proc. IEEE*, vol. 80, pp. 539–568, Apr. 1992.

[3] R. F. Barret and D. A. Holdsworth, "Frequency tracking using hidden Markov models with amplitude and phase information," *IEEE Trans. Signal Processing*, vol. 41, pp. 2965–2975, Oct. 1993.

[4] P. Tichavský and A. Nehorai, "Comparative study of four adaptive frequency trackers," *IEEE Trans. Signal Processing*, vol. 45, pp. 1473–1484, June 1997.

[5] P. J. Kootsookos and J. M. Spanjaard, "An extended Kalman filter for demodulation of polynomial phase signals," *IEEE Signal Processing Lett.*, vol. 5, pp. 69–70, Mar. 1998.

[6] H. C. So, "Adaptive algorithm for discret estimation of sinusoidal frequency," *Electron. Lett.*, vol. 36, no. 8, pp. 759–760, Apr. 2000.

[7] J. M. B. Dias and J. M. N. Leitão, "Nonparametric estimation of mean Doppler and spectral width," *IEEE Trans. Geosci. Remote Sensing*, vol. 38, pp. 271–282, Jan. 2000.

[8] A. Herment, G. Demoment, P. Dumée, J.-P. Guglielmi, and A. Delouche, "A new adaptive mean frequency estimator: Application to constant variance color flow mapping," *IEEE Trans. Ultrason. Ferroelectr. Freq. Contr.*, vol. 40, pp. 796–804, 1993.

[9] J.-F. Giovannelli, J. Idier, B. Querleux, A. Herment, and G. Demoment, "Maximum likelihood and maximum a posteriori estimation of Gaussian spectra. Application to attenuation measurement and color Doppler velocimetry," in *Proc. Int. Ultrason. Symp.*, vol. 3, Cannes, France, Nov. 1994, pp. 1721–1724.

[10] D. Hann and C. Greated, "The measurement of sound fileds using laser Doppler anemometry," *Acustica*, vol. 85, pp. 401–411, 1999.

[11] C. Kasai, K. Namekawa, A. Koyano, and R. Omoto, "Real-time two-dimensional blood flow imaging using an autocorrelation technique," *IEEE Trans. Sonics Ultrason.*, vol. SU-32, pp. 458–464, May 1985.

[12] R. F. Woodman, "Spectral moment estimation in MST radars," *Radio Sci.*, vol. 20, no. 6, pp. 1185–1195, Nov. 1985.

[13] T. Loupas and W. N. McDicken, "Low-order complex AR models for mean and maximum frequency estimation in the context of Doppler color flow mapping," *IEEE Trans. Ultrason. Ferroelectr. Freq. Contr.*, vol. 37, pp. 590–601, Nov. 1990.

[14] B. A. J. Angelsen and K. Kristoffersen, "Discrete time estimation of the mean Doppler frequency in ultrasonic blood velocity measurement," *IEEE Trans. Biomed. Eng.*, vol. BME-30, pp. 207–214, 1983.

[15] F.-K Li, D. N. Held, H. C. Curlander, and C. Wu, "Doppler parameter estimation for spaceborne synthetic-aperture radars," *IEEE Trans. Geosci. Remote Sensing*, vol. GE-23, pp. 47–56, Jan. 1985.

[16] S. M. Kay, *Modern Spectral Estimation*. Englewood Cliffs, NJ: Prentice-Hall, 1988.

[17] R. L. Streit and R. F. Barret, "Frequency line tracking using hidden Markov models," *IEEE Trans. Signal Processing*, vol. 38, pp. 586–598, Apr. 1990.

[18] E. S. Chornoboy, "Optimal mean velocity estimation for Doppler weather radars," *IEEE Trans. Geosci. Remote Sensing*, vol. 31, pp. 575–586, May 1993.

[19] S. E. Levinson, L. R. Rabiner, and M. M. Sondhi, "An introduction to the application of the theory of probabilistic function of a Markov process to automatic speech processing," *Bell Syst. Tech. J.*, vol. 62, no. 4, pp. 1035–1074, Apr. 1982.

[20] K. Lange, "A gradient algorithm locally equivalent to the EM algorithm," *J. R. Statist. Soc. B*, vol. 57, no. 2, pp. 425–437, 1995.

[21] G. J. McLachlan and T. Krishnan, *The EM Algorithm and Extensions*. New York: Wiley, 1997.

[22] H. E. Talhami and R. I. Kitney, "Maximum likelihood frequency tracking of the audio pulsed Doppler ultrasound signal using a Kalman filter," *Ultrasound Med. Biol.*, vol. 14, no. 7, pp. 599–609, 1988.

[23] D. K. Barton and S. Leonov, *Radar Technology Encyclopedia*. Norwell, MA: Artech House, 1997.

[24] G. Demoment, "Image reconstruction and restoration: Overview of common estimation structure and problems," *IEEE Trans. Acoust. Speech, Signal Processing*, vol. 37, pp. 2024–2036, Dec. 1989.

[25] A. Tikhonov and V. Arsenin, *Solutions of Ill-Posed Problems*. Washington, DC: Winston, 1977.

[26] B. R. Hunt, "Bayesian methods in nonlinear digital image restoration," *IEEE Trans. Commun.*, vol. C-26, pp. 219–229, Mar. 1977.

[27] D. P. Bertsekas, *Nonlinear Programming*. Belmont, MA: Athena Scientific, 1995.

[28] A. Blake and A. Zisserman, *Visual Reconstruction*. Cambridge, MA: MIT Press, 1987.

[29] M. Nikolova, J. Idier, and A. Mohammad-Djafari, "Inversion of large-support ill-posed linear operators using a piecewise Gaussian MRF," *IEEE Trans. Image Processing*, vol. 7, pp. 571–585, Apr. 1998.

[30] S. Geman and D. Geman, "Stochastic relaxation, Gibbs distributions, and the Bayesian restoration of images," *IEEE Trans. Pattern Anal. Mach. Intell.*, vol. PAMI-6, pp. 721–741, Nov. 1984.

[31] C. Robert, *Méthodes de Monte-Carlo par Chaînes de Markov*. Paris, France: Economica, 1996.

[32] L. R. Rabiner and B. H. Juang, "An introduction to hidden Markov models," *IEEE Acoust., Speech, Signal Processing Mag.*, pp. 4–16, 1986.

[33] G. D. Forney, "The Viterbi algorithm," *Proc. IEEE*, vol. 61, pp. 268–278, Mar. 1973.

[34] P. A. Devijver and M. Dekessel, "Champs aléatoires de Pickard et modélization d'images digitales," *Traitement du Signal*, vol. 5, no. 5, pp. 131–150, 1988.

[35] P. A. Devijver, "Baum's forward-backward algorithm revisited," *Pattern Recognit. Lett.*, vol. 3, pp. 369–373, Dec. 1985.

[36] G. H. Golub, M. Heath, and G. Wahba, "Generalized cross-validation as a method for choosing a good ridge parameter," *Technometr.*, vol. 21, no. 2, pp. 215–223, May 1979.

[37] D. M. Titterington, "Common structure of smoothing techniques in statistics," *Int. Statist. Rev.*, vol. 53, no. 2, pp. 141–170, 1985.

[38] P. Hall and D. M. Titterington, "Common structure of techniques for choosing smoothing parameter in regression problems," *J. R. Statist. Soc. B*, vol. 49, no. 2, pp. 184–198, 1987.

[39] A. Thompson, J. C. Brown, J. W. Kay, and D. M. Titterington, "A study of methods of choosing the smoothing parameter in image restoration by regularization," *IEEE Trans. Pattern Anal. Machine Intell.*, vol. 13, pp. 326–339, Apr. 1991.

[40] N. Fortier, G. Demoment, and Y. Goussard, "Comparison of GCV and ML methods of determining parameters in image restoration by regularization," *J. Visual Commun. Image Repres.*, vol. 4, pp. 157–170, 1993.

[41] J.-F. Giovannelli, G. Demoment, and A. Herment, "A Bayesian method for long AR spectral estimation: A comparative study," *IEEE Trans. Ultrason. Ferroelectr. Freq. Contr.*, vol. 43, pp. 220–233, Mar. 1996.

[42] L. E. Baum, T. Petrie, G. Soules, and N. Weiss, "A maximization technique occuring in the statistical analysis of probabilistic functions of Markov chains," *Ann. Math. Stat.*, vol. 41, no. 1, pp. 164–171, 1970.

[43] L. A. Liporace, "Maximum likelihood estimation for multivariate observations of Markov sources," *IEEE Trans. Inform. Theory*, vol. IT-28, pp. 729–734, Sept. 1982.

[44] D. C. Ghiglia and M. D. Pritt, *Two-Dimensional Phase Unwrapping*. New York: Wiley Interscience, 1998.

[45] M. Servin, J. L. Marroquin, D. Malacara, and F. J. Cueva, "Phase unwrapping with a regularized phase-tracking system," *Appl. Opt.*, vol. 37, no. 10, pp. 1917–1923, Apr. 1998.

[46] G. Nico, G. Palubinskas, and M. Datcu, "Bayesian approaches to phase unwrapping: Theoretical study," *IEEE Trans. Signal Processing*, vol. 48, pp. 2545–2556, Sept. 2000.

Jean-François Giovannelli was born in Béziers, France, in 1966. He graduated from the École Nationale Supérieure de l'Électronique et de ses Applications, Paris, France, in 1990 and received the Doctorat degree in physics from the Laboratoire des Signaux et Systèmes, Université de Paris-Sud, Orsay, France, in 1995.

He is presently Assistant Professor with the Département de Physique, Université de Paris-Sud. He is interested in regularization methods for inverse problems in signal and image processing, mainly in spectral characterization. Application fields essentially concern radar and medical imaging.

Jérôme Idier was born in France in 1966. He received the diploma degree in electrical engineering from the École Supérieure d'Électricité, Paris, France, in 1988 and the Ph.D. degree in physics from the Université de Paris-Sud, Orsay, France, in 1991.

Since 1991, he has been with the Centre National de la Recherche Scientifique, assigned to the Laboratoire des Signaux et Systèmes, Université de Paris-Sud. His major scientific interests are in probabilistic approaches to inverse problems for signal and image processing.

Rédha Boubertakh was born in Algiers, Algeria, in 1975. He received the diploma degree in electrical engineering from the École Nationale Polytechnique d'Alger, Algiers, in 1996. He is currently pursuing the Ph.D. degree at the INSERM Unit 494, Hôpital Pitié-Salpétrière, Paris, France.

He is interested in signal and image processing, mainly in the fields of magnetic resonance imaging.

Alain Herment was born in Paris, France, in 1948. He graduated from ISEP Engineering School, Paris, in 1971. He received the Doctorat d'État degree in physics from ISEP Engineering School in 1984.

Initially, he worked as an engineer at the Centre National de la Recherche Scientifique. In 1977, was a researcher at the Institut National pour la Santé et la Recherche Médicale (INSERM), Paris. He is currently in charge of the department of cardiovascular imaging at the INSERM Unit 66, Hôpital Pitié, Paris. He is interested in signal and image processing for extracting morphological and functional information from images sequences, mainly in the fields of ultrasound investigations, X-ray CT, and digital angiography.

V. Samson, F. Champagnat et **J.-F. Giovannelli**, « Point target detection and subpixel position estimation in optical imagery », *Applied Optics*, vol. 43, n°2, pp. 257–263, janvier 2004.

Point target detection and subpixel position estimation in optical imagery

Vincent Samson, Frédéric Champagnat, and Jean-François Giovannelli

We address the issue of distinguishing point objects from a cluttered background and estimating their position by image processing. We are interested in the specific context in which the object's signature varies significantly relative to its random subpixel location because of aliasing. The conventional matched filter neglects this phenomenon and causes a consistent degradation of detection performance. Thus alternative detectors are proposed, and numerical results show the improvement brought by approximate and generalized likelihood-ratio tests compared with pixel-matched filtering. We also study the performance of two types of subpixel position estimator. Finally, we put forward the major influence of sensor design on both estimation and point object detection. © 2004 Optical Society of America

OCIS codes: 040.1880, 100.5010, 100.0100.

1. Introduction

We tackle the problem of subpixel object detection in image sequences that arises, for instance, in infrared search-and-track applications. In this context the target signature is proportional to

$$\mathbf{s}_{\boldsymbol{\epsilon}}[i, j] = \int_{i-0.5}^{i+0.5} \int_{j-0.5}^{j+0.5} h_o(u - \epsilon_1, v - \epsilon_2) \mathrm{d}u \mathrm{d}v, \quad (1)$$

where $\mathbf{s}_{\boldsymbol{\epsilon}}[i, j]$ represents the percentage of light intensity at pixel (i, j), $\boldsymbol{\epsilon} = (\epsilon_1, \epsilon_2)$ refers to the object's random subpixel position, and h_o is the optical point-spread function (PSF). According to common sensor design, the energy of the signal component, $\mathbf{s} = \alpha \mathbf{s}_{\boldsymbol{\epsilon}}$, is almost entirely concentrated on a single pixel. However, unlike for amplitude α, which is unknown too, its dependence on location parameter $\boldsymbol{\epsilon}$ is highly nonlinear. Its influence in our application is rather significant because of aliasing and, unless a velocity model is available, an object's subpixel position is hardly predictable from frame to frame. Common sensor design leads to an image spot that is downsampled by almost a factor of 5. We can see from Fig. 1 the energy loss at the central pixel relative to subpixel location and the random change in spatial pattern that is due to aliasing. This phenomenon has a major effect on detection performance, as we show below. To our knowledge, this pitfall has not been addressed yet in the literature. The prevailing opinion is that there is no signature information on subpixel objects. Indeed, the various authors who dealt with small-object detection concentrated on clutter removal,[1–3] multispectral or hyperspectral fusion,[4,5] and multiframe tracking methods.[6–8] We focus here on the processing of a single frame. In Section 2 we formulate the detection problem in the classic model of a signal in additive Gaussian noise.[9] When the signal is deterministic, Neyman–Pearson strategy yields the conventional matched filter. In the present case, the signal from the target depends on unknown parameters, and we have to deal with a composite hypothesis test. A common procedure is given by the generalized likelihood-ratio test. But so-called nuisance parameters α and $\boldsymbol{\epsilon}$ can also be considered random variables with known distributions (some *a priori* density functions in the Bayesian terminology); then the straightforward extension of the likelihood-ratio test is to integrate the conditional distribution over α and $\boldsymbol{\epsilon}$. When we were modeling the signal component as a sample function we could also think of the class of random signal in noise-detection problems, which have been studied primarily in the Gaussian case. Unfortunately, when $\mathbf{s}_{\boldsymbol{\epsilon}}$ is

V. Samson (vsamson@irisa.fr) and F. Champagnat are with the Office National d'Études et de Recherches Aérospatiales, 29, Avenue de la Division Leclerc, 92322 Châtillon Cedex, France. J.-F. Giovannelli is with the Laboratoire des Signaux et Systèmes, Supélec, Plateau de Moulon, 91192 Gif-sur-Yvette Cedex, France.

Received 16 May 2003; revised manuscript received 6 August 2003; accepted 11 August 2003.
0003-6935/04/020257-07$15.00/0

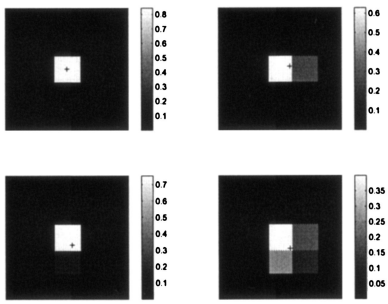

Fig. 1. Examples of image spots for several cross-marked subpixel positions (windows of size 5 × 5 pixels). Sensor design parameter r_c is set to its common value of 2.44 (see Section 3).

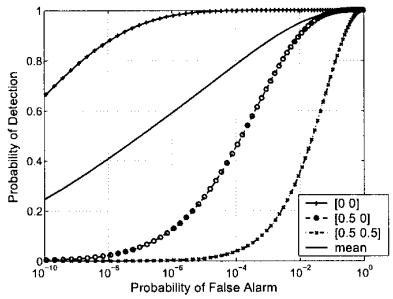

Fig. 3. Examples of PMF theoretical ROC curves for several true subpixel positions (SNR, 15 dB): the ideal case, where $\boldsymbol{\epsilon}^* = \boldsymbol{\epsilon}_0 = (0, 0)$; $\boldsymbol{\epsilon}^* = (0.5, 0)$; and the worst case, where $\boldsymbol{\epsilon}^* = (0.5, 0.5)$. The mean curve was drawn for uniformly sampled $\boldsymbol{\epsilon}^*$.

considered a random vector, its empirical distribution proves to be highly non-Gaussian when $\boldsymbol{\epsilon}$ is uniformly sampled.

For instance, the histogram of the central pixel depicted in Fig. 2 shows that a Gaussian fit is not satisfactory at all. In Section 3 we define more precisely the optical system model used in our numerical experiments. We consider both Gaussian white noise and fractal noise of unknown correlations generated by a standard technique of spectral synthesis. Section 4 is devoted to the position-estimation problem, i.e., estimation of parameter $\boldsymbol{\epsilon}$. We propose two estimators that take into account the fact that signal amplitude α is also unknown. We demonstrate the performance of these estimators in terms of mean-square errors (MSEs). As for the detection problem, we finally illustrate the expected improvement in quality brought by correctly sampled optics compared with common sensor design.

2. Detection Problem

We consider a local detection window sliding across the image. The problem is to decide whether an object is present at the window's central pixel. Its solution involves a binary test that typically reads as follows:

$$\begin{aligned} H_0 &: \quad \mathbf{z} = \mathbf{n}, \\ H_1 &: \quad \mathbf{z} = \alpha \mathbf{s}_{\boldsymbol{\epsilon}} + \mathbf{n}, \end{aligned} \tag{2}$$

where $\mathbf{z}$ is the vector that collects the window data, $\mathbf{s} = \alpha \mathbf{s}_{\boldsymbol{\epsilon}}$ is the object response (signal vector), and $\mathbf{n}$ is

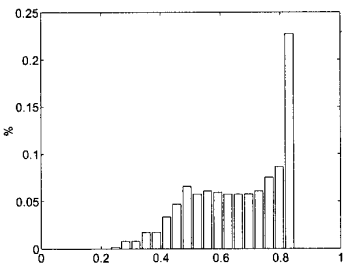

Fig. 2. Empirical distribution of the image-spot central pixel $\mathbf{s}_{\boldsymbol{\epsilon}}[0, 0]$ for a uniformly random position $\boldsymbol{\epsilon} \sim \square_{[-0.5,0.5)^2}$.

the additive Gaussian noise. The signature shape is known and deterministic, so $\mathbf{s}$ depends only on the two unknown parameters, $\alpha \in \square$ and $\boldsymbol{\epsilon} \in \varepsilon = [-0.5, 0.5)^2$. Noise vector $\mathbf{n}$ is assumed to be centered (in practice we first remove the empirical mean from the data) with a known or previously estimated covariance matrix $\mathbf{R}$. Thus, if we assume that $\mathbf{n}$ is independent of $\mathbf{s}$, the following conditional distributions are Gaussian:

$$\begin{aligned} p(\mathbf{z}|H_0) &\sim \square(0, \mathbf{R}), \\ p(\mathbf{z}|H_1, \alpha, \boldsymbol{\epsilon}) &\sim \square(\alpha \mathbf{s}_{\boldsymbol{\epsilon}}, \mathbf{R}). \end{aligned} \tag{3}$$

Let us first assume that parameters α and $\boldsymbol{\epsilon}$ are given. The problem amounts to a simple hypothesis test, which is to detect a deterministic signal in Gaussian noise. The Neyman–Pearson strategy, or likelihood-ratio test, is given by

$$\frac{p(\mathbf{z}|H_1, \alpha, \boldsymbol{\epsilon})}{p(\mathbf{z}|H_0)} \underset{H_0}{\overset{H_1}{\gtrless}} \text{threshold}. \tag{4}$$

It is equivalent to classical matched filtering, which simply compares the statistic $\alpha \square_{\boldsymbol{\epsilon}}(\mathbf{z}) = \alpha \mathbf{s}_{\boldsymbol{\epsilon}}{}^t \mathbf{R}^{-1} \mathbf{z}$ with some threshold.

A. Pixel-Matched Filtering

As the exact object location is unknown in practice, we could assume by default that $\boldsymbol{\epsilon} = \boldsymbol{\epsilon}_0 = (0, 0)$, i.e., that the object is at the center of the pixel, whereas the true location would correspond to $\epsilon = \epsilon^*$. Thus the detector, which consists in thresholding the pixel-matched filter (PMF) $\alpha \square_{\boldsymbol{\epsilon}_0}(\mathbf{z})$, is optimum, provided that $\boldsymbol{\epsilon}^* = \boldsymbol{\epsilon}_0$. Otherwise it is mismatched and therefore suboptimum. Because the conditional distributions of $\square_{\boldsymbol{\epsilon}_0}(\mathbf{z})$ under each assumption are Gaussian, we easily get the expression for the probability of detection P_d and of false alarm P_{fa}. The corresponding receiver operating characteristic (ROC) curves for critical values of $\boldsymbol{\epsilon}^*$ are depicted in Fig. 3. They clearly show that the PMF performance worsens significantly as $\boldsymbol{\epsilon}_0$ differs from $\boldsymbol{\epsilon}^*$. But, beyond extreme situations (related to a true target location between two or four pixels instead of the center), the mean curve represents the average statistics over uniformly random positions. We can see that the price

paid for deviation from the ideal curve, if one neglects the random location, is rather high even at a favorable signal-to-noise (SNR) ratio. For a SNR of 15 dB and at a P_{fa} of 10^{-4}, the probability of detection decreases from nearly 1 to 0.8.

The object response also depends (linearly this time) on amplitude α, which is generally unknown. Yet, assuming strictly positive amplitude, we can see that, whenever $\alpha > 0$, thresholding $\alpha\square_{\boldsymbol{\epsilon}_0}(\mathbf{z})$ gives the same ROC curve as thresholding $\square_{\boldsymbol{\epsilon}_0}(\mathbf{z})$. Without any assumption about α, a classical solution is to estimate it by maximum-likelihood (ML) theory. Indeed under the assumption of Gaussian noise, the optimum value of α for a given $\boldsymbol{\epsilon}$ is explicit:

$$\begin{aligned}\hat{\alpha}(\boldsymbol{\epsilon}) &= \arg\max_{\alpha\in\square} p(\mathbf{z}|H_1, \alpha, \boldsymbol{\epsilon}) \\ &= \arg\min_{\alpha\in\square} (\mathbf{z} - \alpha\mathbf{s}_{\boldsymbol{\epsilon}})^t\mathbf{R}^{-1}(\mathbf{z} - \alpha\mathbf{s}_{\boldsymbol{\epsilon}}) \\ &= \frac{\mathbf{s}_{\boldsymbol{\epsilon}}^t\mathbf{R}^{-1}\mathbf{z}}{\mathbf{s}_{\boldsymbol{\epsilon}}^t\mathbf{R}^{-1}\mathbf{s}_{\boldsymbol{\epsilon}}};\end{aligned} \tag{5}$$

then the generalized PMF (GPMF) is equal to

$$\hat{\alpha}(\boldsymbol{\epsilon}_0)\square_{\boldsymbol{\epsilon}_0}(\mathbf{z}) = \frac{|\mathbf{s}_{\boldsymbol{\epsilon}_0}^t\mathbf{R}^{-1}\mathbf{z}|^2}{\mathbf{s}_{\boldsymbol{\epsilon}_0}^t\mathbf{R}^{-1}\mathbf{s}_{\boldsymbol{\epsilon}_0}}. \tag{6}$$

B. Subpixel Detectors

Our aim is to build refined detectors that improve the performance of the GPMF by taking into account the variability of the object's signature owing to its random subpixel location. Several solutions may be used. We recall the most popular one first.

1. *Generalized-Likelihood-Ratio Test*

A ML estimation of the two unknown parameters leads to the generalized-likelihood-ratio test (GLRT):

$$\begin{aligned}\square_g(\mathbf{z}) &= \frac{\max_{(\alpha,\boldsymbol{\epsilon})} p(\mathbf{z}|H_1, \alpha, \boldsymbol{\epsilon})}{p(\mathbf{z}|H_0)} \\ &= \frac{p(\mathbf{z}|H_1, \hat{\alpha}_{\mathrm{ML}}, \hat{\boldsymbol{\epsilon}}_{\mathrm{ML}})}{p(\mathbf{z}|H_0)} \gtrless \text{threshold}.\end{aligned} \tag{7}$$

It consists in estimating amplitude α and possible object location $\boldsymbol{\epsilon}$ by computing

$$\begin{aligned}\hat{\boldsymbol{\epsilon}}_{\mathrm{ML}} &= \arg\max_{\boldsymbol{\epsilon}\in\varepsilon} p[\mathbf{z}|H_1, \hat{\alpha}(\boldsymbol{\epsilon}), \boldsymbol{\epsilon}] \\ &= \arg\max_{\boldsymbol{\epsilon}\in\varepsilon} \frac{|\mathbf{s}_{\boldsymbol{\epsilon}}^t\mathbf{R}^{-1}\mathbf{z}|^2}{\mathbf{s}_{\boldsymbol{\epsilon}}^t\mathbf{R}^{-1}\mathbf{s}_{\boldsymbol{\epsilon}}}.\end{aligned} \tag{8}$$

Then thresholding the estimated filter $\hat{\alpha}_{\mathrm{ML}}\square_{\hat{\boldsymbol{\epsilon}}_{\mathrm{ML}}}(\mathbf{z})$, where $\hat{\alpha}_{\mathrm{ML}} = \hat{\alpha}(\hat{\boldsymbol{\epsilon}}_{\mathrm{ML}})$ is given by Eq. (5), yields

$$\hat{\alpha}_{\mathrm{ML}}\square_{\hat{\boldsymbol{\epsilon}}_{\mathrm{ML}}}(\mathbf{z}) = \frac{|\mathbf{s}_{\hat{\boldsymbol{\epsilon}}_{\mathrm{ML}}}^t\mathbf{R}^{-1}\mathbf{z}|^2}{\mathbf{s}_{\hat{\boldsymbol{\epsilon}}_{\mathrm{ML}}}^t\mathbf{R}^{-1}\mathbf{s}_{\hat{\boldsymbol{\epsilon}}_{\mathrm{ML}}}}. \tag{9}$$

2. *Exact-Likelihood-Ratio Test*

In a Bayesian approach, we propose to consider the two unknown parameters α and $\boldsymbol{\epsilon}$ as manifestations of independent random variables with given probability-density functions $p(\alpha)$ and $p(\boldsymbol{\epsilon})$. Then the optimal procedure is the exact-likelihood-ratio test (ELRT).

To compute the density function of data under H_1 and to get the likelihood ratio, we have to integrate the conditional density $p(\mathbf{z}|H_1, \alpha, \boldsymbol{\epsilon})$ over prior distributions of nuisance random parameters α and $\boldsymbol{\epsilon}$. The likelihood ratio can be expressed as

$$\square(\mathbf{z}) = \frac{p(\mathbf{z}|H_1)}{p(\mathbf{z}|H_0)} = \frac{\int_\varepsilon\int_\square p(\mathbf{z}|H_1, \alpha, \boldsymbol{\epsilon})p(\alpha)p(\boldsymbol{\epsilon})\mathrm{d}\alpha\mathrm{d}\boldsymbol{\epsilon}}{p(\mathbf{z}|H_0)}. \tag{10}$$

Given prior distributions $p(\alpha)$ and $p(\boldsymbol{\epsilon})$, $\square(\mathbf{z})$ is the optimal Neyman–Pearson test whenever α and $\boldsymbol{\epsilon}$ really satisfy the models $p(\alpha)$ and $p(\boldsymbol{\epsilon})$. By default we choose a noninformative prior distribution for α and adopt a uniform distribution inside the pixel for $\boldsymbol{\epsilon}$, which seems to be quite a reasonable assumption for the subpixel target position. So we get

$$\square(\mathbf{z}) \propto \int_\varepsilon \frac{1}{(\mathbf{s}_{\boldsymbol{\epsilon}}{}^t\mathbf{R}^{-1}\mathbf{s}_{\boldsymbol{\epsilon}})^{1/2}} \exp\left(\frac{|\mathbf{s}_{\boldsymbol{\epsilon}}^t\mathbf{R}^{-1}\mathbf{z}|^2}{2\mathbf{s}_{\boldsymbol{\epsilon}}^t\mathbf{R}^{-1}\mathbf{s}_{\boldsymbol{\epsilon}}}\right)\mathrm{d}\boldsymbol{\epsilon}. \tag{11}$$

Unfortunately, because of the intricate nonlinear dependence of $\mathbf{s}_{\boldsymbol{\epsilon}}$ on $\boldsymbol{\epsilon}$, explicit integration over $\boldsymbol{\epsilon}$ appears not to be tractable, and the probability distribution of $\square(\mathbf{z})$ is not as simple as that of $\square_{\boldsymbol{\epsilon}_0}(\mathbf{z})$. A quadrature approximation is required for computing $\square(\mathbf{z})$, whereas derivation of its density requires Monte Carlo simulations.

3. *Approximate Likelihood-Ratio Test*

In relation (11), we can approximate the double integral over $\boldsymbol{\epsilon}$ to any desired accuracy by using some quadrature rule and evaluating integrand $f(\boldsymbol{\epsilon}|\mathbf{z})$ at discrete samples $\boldsymbol{\epsilon}_k \in \boldsymbol{\varepsilon} = [-0.5, 0.5)^2$. But, for the sake of computational efficiency, we propose to use a coarse approximation of likelihood ratio $\square_a(\mathbf{z})$ based on a bidimensional trapezoidal rule that involves only nine positions: the center of the pixel $\boldsymbol{\epsilon}_0 = (0, 0)$; the four half-pixel positions $(0, \pm 0.5)$ and $(\pm 0.5, 0)$, denoted $\boldsymbol{\epsilon}_k$, $k = 1, \ldots, 4$; and the four corners $(\pm 0.5, \pm 0.5)$, denoted $\boldsymbol{\epsilon}_k$, $k = 5, \ldots, 8$:

$$\square_a(\mathbf{z}) = \tfrac{1}{4}\left[f(\boldsymbol{\epsilon}_0|\mathbf{z}) + \tfrac{1}{2}\sum_{k=1}^{4} f(\boldsymbol{\epsilon}_k|\mathbf{z}) + \tfrac{1}{4}\sum_{k=5}^{8} f(\boldsymbol{\epsilon}_k|\mathbf{z})\right]. \tag{12}$$

4. *Subspace Model*

An alternative to this probabilistic viewpoint can be built on a geometric approach that restricts signal vector $\mathbf{s} = \alpha\mathbf{s}_{\boldsymbol{\epsilon}}$ to vary in some P-dimensional subspace, with P less than the vector size.[10] The observed data under H_1 are rewritten as

$$\mathbf{z} \simeq \mathbf{S}\mathbf{a} + \mathbf{n} = \sum_{p=1}^{P} a_p\mathbf{s}_p + \mathbf{n}, \tag{13}$$

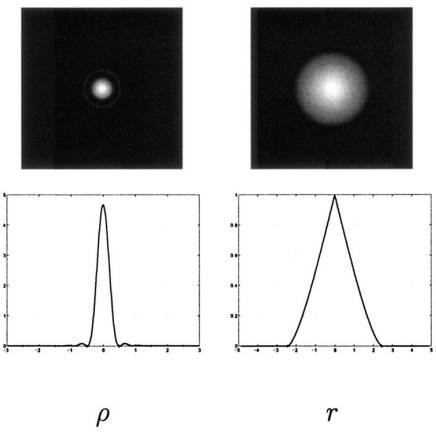

Fig. 4. Left, radial PSF $h_o(u, v)$ (top) and slice along a diameter (bottom). Right, corresponding optical transfer function $\tilde{h}_o(\nu_u, \nu_v)$ and slice along a diameter ($r_c = 2.44$).

where structural matrix $\mathbf{S}$ is formed by P independent vectors $\mathbf{s}_p$. Coefficients a_p of the linear combination are the new parameters that describe the signal's variability. As a result of linearity, the ML estimation of vector $\mathbf{a}$ has an explicit solution (which is identical to the least-squares estimator):

$$\hat{\mathbf{a}}_{\mathrm{ML}} = (\mathbf{S}^t\mathbf{R}^{-1}\mathbf{S})^{-1}\mathbf{S}^t\mathbf{R}^{-1}\mathbf{z}, \tag{14}$$

and the GLRT amounts to threshold the following statistic:

$$\square(\mathbf{z}) = \mathbf{z}^t\mathbf{R}^{-1}\mathbf{S}(\mathbf{S}^t\mathbf{R}^{-1}\mathbf{S})^{-1}\mathbf{S}^t\mathbf{R}^{-1}\mathbf{z}. \tag{15}$$

Matrix $\mathbf{S}$ depends only on ϵ. α is a scale parameter; in practice, one identifies it by discretizing ε, making a singular value decomposition, and retaining singular vectors $\mathbf{s}_p$ that correspond to the P greatest singular values. We chose $P = 1$, which gives better results than higher orders. Therefore, under hypothesis H_1, $\mathbf{z} \simeq a_1\mathbf{s}_1 + \mathbf{n}$, and $\square(\mathbf{z})$ is identical to the GPMF with $\mathbf{s}_{\epsilon_0}$ replaced by $\mathbf{s}_1$.

3. Application to Optical Imagery

A. Optical System

In our application we can model the imaging system by a diffraction-limited, unaberrated optics with circular aperture and incoherent illumination.[11,12] Object signal pattern $\mathbf{s}_\epsilon$ is then given by the integration of h_o on each pixel [see Eq. (1)], where h_o is the radial point-spread function (PSF) defined by the Airy disk:

$$h_o(u, v) = \frac{1}{\pi}\left[\frac{J_1(\pi\rho r_c)}{\rho}\right]^2, \qquad \rho = \sqrt{u^2 + v^2}. \tag{16}$$

J_1 is a Bessel function of the first kind, and $r_c = v_c/v_s$ designates the normalized cutoff frequency (v_s is the sampling frequency and $v_c = D/\lambda$ is the radial cutoff frequency defined by the ratio of the lens's aperture diameter D to wavelength λ). Figure 4 depicts the two-dimensional PSF and a slice along one diameter as well as their Fourier transform. Common sensor design uses $r_c = 2.44$, so the pixel size is equal to the width of the main lobe of the PSF. However, this implies a downsampling factor $v_n/v_s = 2r_c = 4.88$ (where $v_n = 2v_c$ is the Nyquist frequency). In Subsection 3.B below, we present some numerical results of detection performance that resulted from using this classical sensor design. Examples of image spots $\mathbf{s}_\epsilon$ are shown in Fig. 1 for various values of ϵ.

Remark 1. We have the following property:

$$\sum_{(i,j)\in\square^2} \mathbf{s}_\epsilon[i, j] = \int_{\square^2} h_o(u, v)\mathrm{d}u\mathrm{d}v = 1.$$

B. Numerical Results

The performance of the five classes of detector, the GPMF and the GLRT of α and ϵ, the ELRT, the approximate-likelihood ratio test (ALRT), and finally the GLRT with the subspace model (denoted the SM-GLRT), were compared in terms of ROC curves. We deduced the probabilities of detection and false alarm from the empirical distributions of these statistics under each hypothesis by generating samples of Gaussian noise $\mathbf{n}$ and uniformly distributed ϵ in $\varepsilon = [-0.5, 0.5)^2$. The amplitude was assumed to be unknown but set to a constant value α in the simulations because we had no information about a reliable prior distribution $p(\alpha)$.

We considered first the Gaussian white noise $\mathbf{n} \sim \square(0, \sigma^2)$. The SNR was then defined by

$$\mathrm{SNR} = 10\ \log_{10}\left(\frac{\alpha^2 E}{\sigma^2}\right), \qquad E = \int_\varepsilon \sum_{(i,j)\in\square^2} (\mathbf{s}_\epsilon[i, j])^2 \mathrm{d}\epsilon. \tag{17}$$

For common sensor design ($r_c = 2.44$), the average energy of the image spot was $E \simeq 0.52$. The ROC curves are depicted in Fig. 5 for two SNRs. The figure shows that the GLRT, the ELRT (actually, a refined approximation of it), and the coarse approximation ALRT exhibit significantly better performance than the SM-GLRT and the GPMF. We can also see that the performance gain is greater for high SNR, whereas it tends to be rather small for low SNR and low probability of false alarm. Conversely, if provision of the GPMF, the SM-GLRT, and the ALRT is computationally cheap, provision of the GLRT and the ELRT is much more intensive.

As complementary tests, we tested the five detectors on a fractal background image generated by a variant of the ppmforge software.[13]

The synthesis algorithm depends on autosimilarity parameter H, called the Hurst parameter, which was set to 0.7 in this experiment. The resultant image depicted in Fig. 6 is a realistic simulation of a cloud

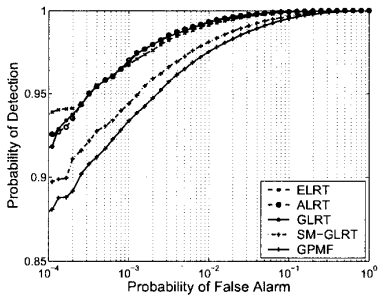

$$\mathrm{SNR} = 16.2\ \mathrm{dB}\ (\alpha/\sigma = 9)$$

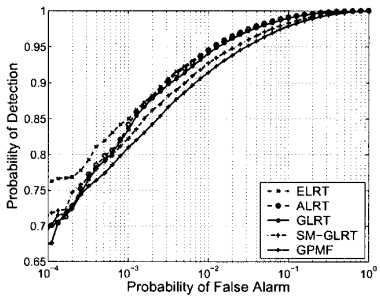

$$\mathrm{SNR} = 14.1\ \mathrm{dB}\ (\alpha/\sigma = 7)$$

Fig. 5. Empirical ROC curves in the Gaussian white-noise case with common sensor design ($r_c = 2.44$) for two different SNRs. These curves were obtained for 9×10^4 instances of noise.

scene. Covariance matrix $\mathbf{R}$ of this stationary background was estimated by empirical correlations of the whole image. We then computed the performance of the various detectors for a given target amplitude as illustrated in Fig. 7. The ROC curves look quite different from those for the white-noise case, but we can see again that the GLRT, the ELRT, and the ALRT exhibit similar performance and provide a significant gain in detection compared with the GPMF and the SM-GLRT.

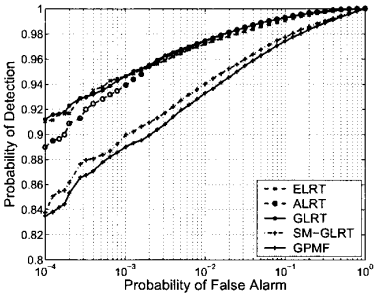

Fig. 7. Empirical ROC curves obtained for the fractal image of Fig. 6 for a true (but assumed unknown) target amplitude $\alpha = 60$ gray levels. The standard deviation of the correlated noise on the whole image is ~104 gray levels, and the estimated innovation standard deviation is ~4.6. The following generalized definition of the SNR, $10 \log_{10}(\alpha^2 \int_\varepsilon \mathbf{s}_\epsilon{}^t \mathbf{R}^{-1} \mathbf{s}_\epsilon d\epsilon)$, leads to an estimated SNR value of 18.1 dB.

C. Influence of the Optics

Besides a desire to perfect and evaluate subpixel detectors, one additional motivation for this research was a wish to analyze the influence of aliasing on detection performance. This is why we also tested the detectors on correctly sampled optics to compare their performance with that obtained by use of a common sensor design. In the correctly sampled design, the focal plane is sampled at the Nyquist frequency (implying a denser sensor array or a smaller lens diameter) such that aliasing is suppressed. Parameter r_c of the PSF is equal to 0.5, and the signal energy is now spread over several pixels. By comparison, Fig. 8 presents examples of image spots that correspond to such a design. Detection performance is depicted in Fig. 9 for a SNR of 15 dB. We can see that the choice of detection algorithm is just a moderate factor in this situation. The five detectors exhibit quite similar behavior, but at the same SNR they perform much better than in the aliased case. The gain in P_{fa} amounts at least to a factor of 10 for all the detectors. Such a result speaks in favor of using a denser focal plane for point target detection.

Remark 2. In the presence of aliasing, term $\mathbf{s}_\epsilon{}^t \mathbf{R}^{-1} \mathbf{s}_\epsilon$ depend on $\boldsymbol{\epsilon}$, even when the noise is white.

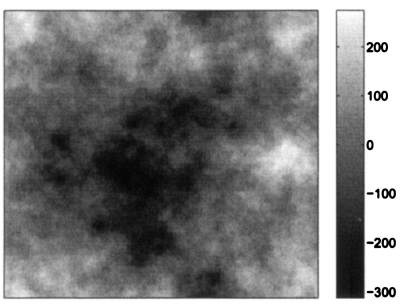

Fig. 6. Simulation of a cloud fractal image of 200×200 pixels (Hurst parameter, $H = 0.7$).

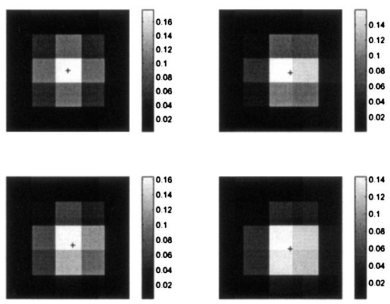

Fig. 8. Examples of image spots corresponding to a correctly sampled optics ($r_c = 0.5$) to be compared with those of Fig. 1.

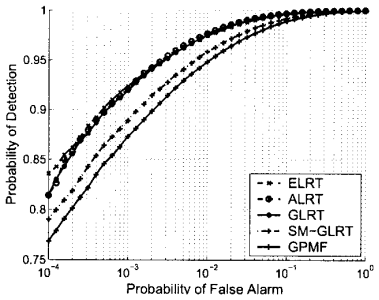

$r_c = 2.44$

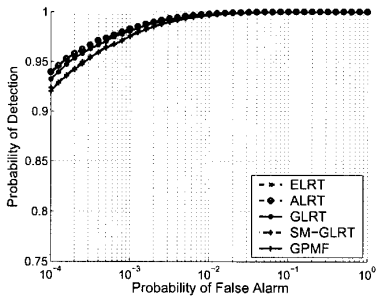

$r_c = 0.5$

Fig. 9. Empirical ROC curves in the Gaussian white-noise case with common sensor design (top, $r_c = 2.44$) compared with correctly sampled optics (bottom, $r_c = 0.5$) for the same SNR of 15 dB. These curves were obtained for 4×10^5 instances of noise.

For example, in a common sensor design, signal energy $E_\epsilon = \mathbf{s}_\epsilon{}^t\mathbf{s}_\epsilon$ varies from 0.21 to 0.72. Such is not the case for the correctly sampled optics where E_ϵ is constant and equal to $E \simeq 0.08$.

4. Performance of Subpixel Position Estimators

So far we have focused on the detection strategy. In a second step, once a potential target is detected on a given pixel we are interested also in accurate estimation of its subpixel position. Such a problem has already been addressed, in particular for estimation of positions of stars in astronomical applications.[14] Several types of estimator are possible. We consider here the maximum likelihood (ML) estimator and, following the Bayesian approach introduced previously, the posterior mean. It is important to note that signal amplitude α is also unknown and that therefore we have to estimate it or integrate over it. Indeed, it is not valid to suppose that the amplitude is known in the context of the infrared search-and-track algorithm.

The ML estimator of $\boldsymbol{\epsilon}$ is given in Eq. (8) by replacement of α with its estimate $\hat{\boldsymbol{\alpha}}$. In fact, $\hat{\boldsymbol{\epsilon}}_{\mathrm{ML}}$ and $\hat{\alpha}_{\mathrm{ML}} = \hat{\alpha}(\hat{\boldsymbol{\epsilon}}_{\mathrm{ML}})$ are identical to joint maximum *a posteriori* (MAP) estimators with noninformative prior distributions on the two parameters.

The PM estimator is defined as

$$\hat{\boldsymbol{\epsilon}}_{\mathrm{PM}} = \int_{\varepsilon} \boldsymbol{\epsilon} p(\boldsymbol{\epsilon}|H_1, \mathbf{z}) \mathrm{d}\boldsymbol{\epsilon}, \tag{18}$$

where the posterior law is deduced from Bayes's rule:

$$p(\boldsymbol{\epsilon}|H_1, \mathbf{z}) = \frac{p(\mathbf{z}|H_1, \boldsymbol{\epsilon})p(\boldsymbol{\epsilon})}{p(\mathbf{z}|H_1)} = \frac{p(\boldsymbol{\epsilon})}{p(\mathbf{z}|H_1)} \int_{\square} p(\mathbf{z}|H_1, \alpha, \boldsymbol{\epsilon}) p(\alpha) \mathrm{d}\alpha. \tag{19}$$

So we have to integrate over α and then over $\boldsymbol{\epsilon}$. As above, we consider a diffuse prior law on $\square$ for α and a uniform law on ε for $\boldsymbol{\epsilon}$. We get the following expression in the same way as for the likelihood ratio in relation (11):

$$p(\boldsymbol{\epsilon}|H_1, \mathbf{z}) \propto \frac{1}{(\mathbf{s}_\epsilon{}^t\mathbf{R}^{-1}\mathbf{s}_\epsilon)^{1/2}} \exp\left(\frac{|\mathbf{s}_\epsilon{}^t\mathbf{R}^{-1}\mathbf{z}|^2}{2\mathbf{s}_\epsilon{}^t\mathbf{R}^{-1}\mathbf{s}_\epsilon}\right). \tag{20}$$

We studied the performance of these two estimators in terms of average MSE. In practice, optimization or integration over $\boldsymbol{\epsilon}$ is approximated numerically for a finite discrete grid of 20×20 values $\boldsymbol{\epsilon}_k \in \varepsilon$. Given a true position $\boldsymbol{\epsilon}^*$, we can estimate

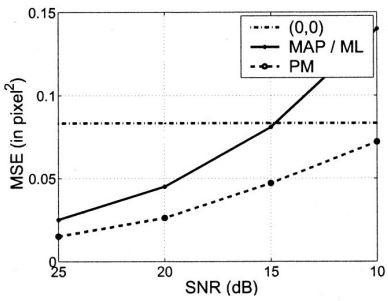

$r_c = 2.44$

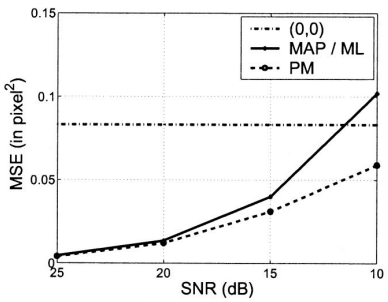

$r_c = 0.5$

Fig. 10. Average MSEs of position estimators in the Gaussian white-noise case with common sensor design (top, $r_c = 2.44$) compared with correctly sampled optics (bottom, $r_c = 0.5$). MAP, maximum *a posteriori*.

bias and variance of an estimator $\hat{\boldsymbol{\epsilon}}$ by using Monte Carlo simulations. We consider Gaussian white noise, and we vary the SNR. Figure 10, left, compares ML and PM estimators to the pixel estimator; it is assumed by default that the target location is at the center of the pixel [$\hat{\boldsymbol{\epsilon}} = (0, 0)$], whose MSE is 1/12. At a favorable SNR the two subpixel estimators are far better than the default estimator, but the gain decreases when noise becomes important. For a SNR of 15 dB, the ML yields an error similar to that of the default estimator, whereas the PM notably has a twice smaller error. By comparison, Fig. 10, right, shows the estimation performances obtained in the unaliased case ($r_c = 0.5$) for equivalent SNRs. ML and PM logically perform better because the signal is correctly sampled.

5. Conclusions and Directions for Future Research

We have presented the problem of detection of subpixel objects embedded in additive Gaussian noise. Subpixel location and signal amplitude were assumed to be unknown. Unknown subpixel location was shown to have a great influence on detection performance in the aliased case, whereas the conventional matched filter neglects it. Thus we derived four types of improved detector, the GLRT, the ELRT, the ALRT, and the SM-GLRT, from the likelihood ratio. We illustrated their performance in comparison with the classic GPMF. Numerical results for both white and correlated noise show that the ELRT, the ALRT, and the GLRT are competitive, whereas the SM-GLRT does not reach the same quality but slightly improves the performance of the GPMF. Use of the ALRT seems to be a good trade-off because it is not so computationally demanding as the ELRT and the GLRT; moreover, the performance gain proves to be only moderate for unaliased optics. This conclusion has important consequences for sensor design. It suggests that the popular design of a pixel that covers the main lobe of the Airy disk exactly is not optimum for point object detection. Future research will consist in studying the robustness of these detectors to real data and ways in which we can take into account non-Gaussian distributions of background noise. As far as the position-estimation problem is concerned, we have demonstrated prospective gains that must also be confirmed with more-realistic data.

References and Notes

1. C. D. Wang, "Adaptive spatial/temporal/spectral filters for background clutter suppression and target detection," Opt. Eng. **21,** 1033–1038 (1982).
2. A. Margalit, I. S. Reed, and R. M. Gagliardi, "Adaptive optical target detection using correlated images," IEEE Trans. Aerosp. Electron. Syst. **21,** 394–405 (1985).
3. T. Soni, J. R. Zeidler, and W. H. Ku, "Performance evaluation of 2-D adaptive prediction filters for detection of small objects in image data," IEEE Trans. Image Process. **2,** 327–340 (1993).
4. X. Yu, L. E. Hoff, I. S. Reed, A. M. Chen, and L. B. Stotts, "Automatic target detection and recognition in multiband imagery: a unified ML detection and estimation approach," IEEE Trans. Image Process. **6,** 143–156 (1997).
5. E. A. Ashton, "Detection of subpixel anomalies in multispectral infrared imagery using an adaptive Bayesian classifier," IEEE Trans. Geosci. Remote Sens. **36,** 506–517 (1998).
6. I. S. Reed, R. M. Gagliardi, and H. M. Shao, "Application of three-dimensional filtering to moving target detection," IEEE Trans. Aerosp. Electron. Syst. **19,** 898–905 (1983).
7. S. D. Blostein and T. S. Huang, "Detecting small, moving objects in image sequences using sequential hypothesis testing," IEEE Trans. Signal Process. **39,** 1611–1629 (1991).
8. J. M. Mooney, J. Silverman, and C. E. Caefer, "Point target detection in consecutive frame staring infrared imagery with evolving cloud clutter," Opt. Eng. **34,** 2772–2784 (1995).
9. H. L. Van Trees, *Detection, Estimation and Modulation Theory* (Wiley, New York, 1968), Part 1.
10. D. Manolakis and G. Shaw, "Detection algorithms for hyperspectral imaging applications," Signal Process. Mag. **19,** 29–43 (2002).
11. J. W. Goodman, *Introduction à l'Optique de Fourier et à l'Holographie* (Masson, Paris, 1972).
12. R. C. Hardie, K. J. Barnard, J. G. Bognar, E. E. Armstrong, and E. A. Watson, "High-resolution image reconstruction from a sequence of rotated and translated frames and its application to an infrared imaging system," Opt. Eng. **37,** 247–260 (1998).
13. The ppmforge software is an open-source program originally designed by John Walker and included with the PBMPLUS and NetPBM raster image utilities; ppmforge generates random fractal forgeries of clouds, planets, and starry skies. A manual page can be found at http://netpbm.sourceforge.net/doc/ppmforge.html, and the source code is available, for example, at the following web address: http://www.ehynan.com/java_applet/fractal_applet/FractApplet/ppmfcprt/.
14. K. A. Winick, "Cramer–Rao lower bounds on the performance of charge-coupled-device optical position estimators," J. Opt. Soc. Am. A **3,** 1809–1815 (1986).

J.-F. Giovannelli et A. Coulais, « Positive deconvolution for superimposed extended source and point sources. », *Astronomy and Astrophysics*, vol. 439, pp. 401–412, 2005.

A&A 439, 401–412 (2005)
DOI: 10.1051/0004-6361:20047011

Astronomy & Astrophysics

Positive deconvolution for superimposed extended source and point sources

J.-F. Giovannelli[1] and A. Coulais[2]

[1] Groupe Problèmes Inverses, Laboratoire des Signaux et Systèmes (CNRS – Supélec – UPS), Plateau de Moulon, 91192 Gif-sur-Yvette, France
e-mail: giova@lss.supelec.fr
[2] Laboratoire d'Étude du Rayonnement de la Matière en Astrophysique (LERMA), Observatoire de Paris, 61 Avenue de l'Observatoire, 75014 Paris, France
e-mail: alain.coulais@obspm.fr

Received 5 January 2004 / Accepted 2 May 2005

Abstract. The paper deals with the construction of images from visibilities acquired using aperture synthesis instruments: Fourier synthesis, deconvolution, and spectral interpolation/extrapolation. Its intended application is to specific situations in which the imaged object possesses two superimposed components: (*i*) an extended component together with (*ii*) a set of point sources. It is also specifically designed to the case of positive maps, and accounts for a known support. Its originality lies within joint estimation of the two components, coherently with data, properties of each component, positivity and possible support. We approach the subject as an inverse problem within a regularization framework: a regularized least-squares criterion is specifically proposed and the estimated maps are defined as its minimizer. We have investigated several options for the numerical minimization and we propose a new efficient algorithm based on augmented Lagrangian. Evaluation is carried out using simulated and real data (from radio interferometry) demonstrating the capability to accurately separate the two components.

Key words. techniques: image processing – techniques: interferometric

1. Introduction

Radio interferometers can be seen as instruments measuring a set of 2D-Fourier coefficients (visibilities) of the brightness distribution of a region in the sky. Visibilities are measured in the Fourier domain (the (u, v)-plane) by means of different baselines (projected distance between cross-correlated antennas). Practically, there are two principal deficiencies (Thompson et al. 2001) in the visibilities

1. the limited coverage of the (u, v)-plane;
2. measurements errors (especially in millimeter range).

Regarding point 1, three limitations are encountered.

- Usually the central part of the aperture (up to the antenna diameter) is not observed. From this stand point, interferometers behave as high pass filters.
- Information above the longest baseline is unavailable. In this sense the instruments behave as low pass filters.
- The (u, v)-plane coverage is irregular, especially when there is a small number of antennas. This results in dirty beam (Fourier transform of visibility weights) with intricate structure and strong sidelobes.

Thus, such instruments can be seen as band pass filters with an intricate impulse response (dirty beam), and noisy output. As a consequence, the available data is relatively poor for imaging objects with various spatial structures extended over the whole frequency domain. In order to compensate for these deficiencies, a large number of methods (from model fitting to non parametric deconvolution) has been continuously proposed (see review in Starck et al. 2002) and specialized for different types of maps. The present paper deals with a particular type of map consisting of the superimposition of two components.

- *Point Source* (PS), or nearly black objects: essentially null-component, with a few strong point sources.
- *Extended Sources* (ES): spatially extended, smooth components.

The problem at hand is to build reliable and accurate estimates of two distinct maps (one for PS, one for ES) from a unique given set of visibilities. The question arises e.g. for radio imaging of the solar corona at meter wavelength where very strong storms are superimposed over a more stable and large quiet Sun radio-emission (see Sect. 4.1).

Remark 1. From a statistical standpoint, PS/ES can be modelized as set of uncorrelated/correlated pixels, respectively.

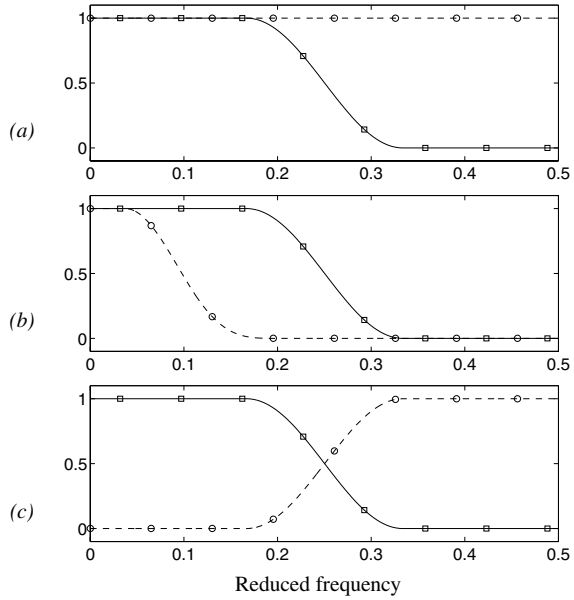

Fig. 1. a) The solid line with squares (resp. dashed line with circles) shows spectral content for ES (resp. PS). Both of them have low frequencies components. **b)** The two lines show spectral contents of correlated components (ES), with different level of correlation. **c)** Elementary decomposition for wavelet transform. The solid line with squares (resp. dashed line with circles) shows low (resp. high) frequency content.

In the Fourier plane they are respectively characterized by an extension over the whole frequency domain (PS) and an extension reduced to the low frequencies domain (ES). In particular, both of them have significant components in the low frequencies domain (see Fig. 1a).

1.1. General bibliographical analysis

In order to compensate for the deficiencies in the available data, additional information is (implicitly or explicitly) accounted for. Practically, most existing methods are founded on specific expected properties of observed and reconstructed sources. The proposed analysis relies on underlying decompositions of unknown image.

PS based methods – A first part of existing methods relies on PS properties. Into this category fall original versions of CLEAN (Hogbom 1974; Fomalont 1973), which iteratively withdraw the PS contribution to the dirty map. Early Maximum Entropy Methods (MEM) (Ables 1974) are also founded on the properties of PS: in a regularized context, they introduce separable penalization terms (without pixel interaction) and favor high-amplitude PS.

ES based methods – Two main classes of methods have been proposed to account for the correlation of ES.

- The correlation structure is introduced by a *convolution kernel*. This is the case in MEM with an Intrinsic Correlation Function (ICF) (Gull 1989) and Pixon methods (Dixon et al. 1996; Puetter & Yahil 1999).
- The other class of method relies on *pixel interactive* penalty. The early versions involve quadratic penalties (Tikhonov & Arsenin 1977). Extensions to other penalties have also been widely developed (O'Sullivan 1995; Snyder et al. 1992; Mugnier et al. 2004).

Mixed ES+SP model – The case of an *explicit model mixing ES and PS* has also been addressed; however, literature in this case is poor. To our knowledge, two papers have been published: (Magain et al. 1998) and (Pirzkal et al. 2000). They introduced the decomposition of the search map as the sum of a PS map and an ES map. From a spectral standpoint, PS / ES are respectively characterized as shown in Fig. 1a (see also Rem. 1). The present paper is founded on this approach (see Sect. 1.2).

Multi-resolution / subband methods – Another class of method received a large attention, namely the multi-resolution and subband approaches.

- The approach proposed by (Weir 1992; Bontekoe et al. 1994) introduces structure by means of different ICF. The unknown map is the sum of several ES, with different level of correlation, i.e. several low frequency components. The underlying decomposition is shown in Fig. 1b in the case of two components.
- We also have witnessed the development of multi-resolution extensions of CLEAN (Wakker & Schwarz 1988) as well as more subtle approaches based on wavelet decomposition and MEM (Starck et al. 1994; Pantin & Starck 1996; Starck et al. 2001). These methods are less specific and widely used for general deconvolution. They aim at reconstructing maps with different scales by splitting the Fourier plane into various zones. They basically rely on (recursive) decomposition in low and high frequencies as shown in Fig. 1c.

1.2. PS plus ES: proposed developments

As mentioned above, the present paper is devoted to the estimation of two distinct maps (one for ES and one for PS) from a unique set of visibilities. We then naturally resort to the work of Magain et al. (1998) and Pirzkal et al. (2000). In both cases the PS map is written in a parametric manner founded on positions and amplitudes of peaks. Smoothness of the ES is included by means of Gaussian ICF and MEM penalty (Pirzkal et al. 2000) and Tikhonov penalty (Magain et al. 1998). Nevertheless, they both have several limitations. On the one hand, (Pirzkal et al. 2000) relies on the knowledge of the position of the PS which is not available to us. On the other hand, the drawback of (Magain et al. 1998) is twofold.

1. It does not deconvolve with the total PSF.
2. The optimized criterion is intricate w.r.t. the PS positions so, it is not always possible to find the global minimum of the criterion (Magain et al. 1998, p. 474).

On the contrary, our approach achieves a complete deconvolution. Moreover, our work introduces properties so that an optimal solution is properly defined and practically attainable. In a unique coherent framework, the proposed method simultaneously accounts for intricate dirty beam, noise, the existence of point sources superimposed onto a smooth component, positivity, and the possible knowledge of a support. The estimated maps are defined as the constrained minimizer of a penalized least-squares criterion specifically adapted to this situation. So that, the method assigns a coherent value to unmeasured Fourier coefficients. The basic ideas developed here have already been partly presented within spectral analysis (Ciuciu et al. 2001), spectrometry (Mohammad-Djafari et al. 2002) and satellite imaging (Samson et al. 2003).

The paper is organized as follows. In Sect. 2, we define notations and state the problem in three classical forms: Fourier synthesis, spectral extrapolation/interpolation and deconvolution. All three cases concern rank-deficient linear inverse problems with additive noise. The proposed method is presented in Sect. 3. Section 3.1 introduces the regularization principles used in the subsequent sections; Sects. 3.2 and 3.3 respectively deal with PS and ES map; Sect. 3.4 is devoted to the main contribution: the reconstruction of two maps simultaneously, one consisting of PS, and the other of ES. Simulation and real data computations are presented throughout Sect. 4. From a numerical optimization viewpoint, the proposed method reduces to a constrained quadratic programming problem and various options have been studied and compared. The proposed algorithm founded on augmented Lagrangian principle is presented in Sect. 5. In Sect. 6 we set out conclusions and perspectives.

2. Problem statement and least squares solution

The usual model[1] for the instrument writes as a weighted truncated noisy Fourier transform (discrete and regular):

$$\boldsymbol{y} = \boldsymbol{W}\boldsymbol{T}\boldsymbol{F}\boldsymbol{x} + \boldsymbol{b}, \tag{1}$$

where $\boldsymbol{x} \in \mathbb{R}^N$ is the unknown map and $\boldsymbol{y}$ and $\boldsymbol{b} \in \mathbb{C}^M$ are the Fourier coefficient and noise (N unkown parameters for M measurements). $\boldsymbol{F}$ is the $N \times N$ normalized FFT matrix and $\boldsymbol{T}$ is a $0/1$-binary truncation (or sampling) $M \times N$ matrix ($\boldsymbol{T}$ discards frequencies outside the (u, v)-plane coverage). $\boldsymbol{W}$ is a $M \times M$ diagonal matrix accounting for visibility weights. For the sake of simplicity and in accordance with real data processed in Sect. 4.3, the subsequent developments are devoted to unitary weights $\boldsymbol{W} = \boldsymbol{I}_M$; they can easily be extended to include non unitary ones. Appendix B gives useful properties of these matrices. The reconstruction of $\boldsymbol{x}$ from $\boldsymbol{y}$, i.e. the inversion of (1), is a Fourier synthesis problem.

In formulation (1), the data $\boldsymbol{y}$ are in the (u, v)-plane while the map $\boldsymbol{x}$ is in the image plane. Two other statements are usually given: one regarding the (u, v)-plane only and the other the image plane exclusively.

[1] In terms of an usual approximation, after calibration, regridding, ... Moreover, for the sake of readability, equations are given in 1D and computation results are presented in 2D.

1. In the Fourier domain, (1) becomes a simple truncation by an invertible change of variable $\mathring{\boldsymbol{x}} = \boldsymbol{F}\boldsymbol{x}$:

$$\boldsymbol{y} = \boldsymbol{T}\,\mathring{\boldsymbol{x}} + \boldsymbol{b}\,. \tag{2}$$

   Its inversion becomes a problem of extrapolating / interpolating "missing" Fourier coefficients.
2. Furthermore, denoting $\bar{\boldsymbol{y}} = \boldsymbol{T}^{\mathrm{t}}\boldsymbol{y}$ the zero-padded data, and $\mathring{\bar{\boldsymbol{y}}} = \boldsymbol{F}^{\dagger}\bar{\boldsymbol{y}}$ the dirty map, (1) becomes a convolution

$$\mathring{\bar{\boldsymbol{y}}} = \boldsymbol{H}\boldsymbol{x} + \widetilde{\boldsymbol{b}} \tag{3}$$

   where $\boldsymbol{H} = \boldsymbol{F}^{\dagger}\boldsymbol{T}^{\mathrm{t}}\boldsymbol{T}\boldsymbol{F}$ is a (circulant) convolution matrix and $\widetilde{\boldsymbol{b}} = \boldsymbol{T}^{\mathrm{t}}\boldsymbol{b}$. (Superscripts "t" and "†" respectively denotes matrix transpose and conjugate-transpose). The instrument response (the dirty beam) is read in any one line of $\boldsymbol{H}$, up to a circular shift. The inversion becomes a deconvolution problem.

   Remark 2. It should be noted, however, that the correlations of $\boldsymbol{b}$ and $\widetilde{\boldsymbol{b}}$ differ from one another, and that in this sense, the two problems are not equivalent.

Whichever formulation is envisaged, the tackled problem is a rank-deficient linear inverse problem with additive noise. Indeed, the number of observed Fourier coefficient is far less than the number of pixels ($M \ll N$) and the operators $\boldsymbol{T}\boldsymbol{F}$ for (1), $\boldsymbol{T}$ for (2) or $\boldsymbol{H}$ for (3) have $N - M$ singular values equal to 0, and M singular values equal to 1. Consequently, the least-squares criterion

$$J^{\mathrm{LS}}(\boldsymbol{x}) = \|\boldsymbol{y} - \boldsymbol{T}\boldsymbol{F}\boldsymbol{x}\|^2 \tag{4}$$

possesses an infinite number of minimizers. The dirty map is one such solution since it cancels out J^{LS}, and the other ones are obtained by adding maps with frequency components outside the (u, v)-plane coverage only.

3. Regularization

So, the selection of a unique solution requires a priori information on the searched maps to be taken into account. In order to achieve this, we resort to regularization techniques (Idier 2001a; Demoment 1989; Tarantola 1987), allowing diverse types of information to be considered, in order to exclude or avoid non desirable solutions.

3.1. Criterion, penalization and constraints

- Positivity and support. This information is naturally encoded by hard constraints for the pixels. Let us note $\mathcal{M}$, the collection of pixels on the map, $\mathcal{S}$ the collection of pixels on a support, and $\bar{\mathcal{S}}$ its complement in $\mathcal{M}$.
  - ($\mathrm{C_s}$): support
    $\forall p \in \bar{\mathcal{S}}, \quad x_p = 0.$
    The proposed method takes into account the knowledge of a support ($\mathcal{S}$ is known and $\mathcal{S} \neq \mathcal{M}$) but remains also valid if $\mathcal{S} = \mathcal{M}$.

- (C_p): positivity
  $\forall p \in \mathcal{M}, \quad x_p \geq 0.$
  This information is taken to be valid in the following sections of this paper and all reconstructed maps will be positive.
- (C_t): template
  $\forall p \in \mathcal{M}, \quad t_p^- \leq x_p \leq t_p^+.$
  It is also possible account for a known template but it is not numerically investigated in the paper.

- Correlation structure. Here, we are concerned with the a priori correlation (ES) or non-correlation (PS) of the searched map. In the image plane, this information is naturally coded by penalization terms $R(\boldsymbol{x})$, as a sum of potential functions ϕ which addresses the pixels.
  - (P_c): the smooth map (ES) is favored by the introduction of interaction terms between pixels
    $$R_c(\boldsymbol{x}) = \sum_{p \sim q} \phi_c \left[x_q, x_p\right], \tag{5}$$
    where $p \sim q$ symbolizes neighbor pixels.
  - (P_s): on the other hand, separable terms favor PS
    $$R_s(\boldsymbol{x}) = \sum \phi_s \left[x_p\right]. \tag{6}$$
    These terms independently shrink the pixels to zero and therefore favor quasi-null maps.
  - (P_m): in the following section, we will also need to penalize the average level of the maps
    $$R_m(\boldsymbol{x}) = \phi_m \left[\sum x_p\right] \tag{7}$$
    so as to specifically compensate for the absence of Fourier coefficient at null-frequency.
  - (P_d): it is also possible account for a known default map $\bar{x}$ through a specific penalization term such as
    $$R_d(\boldsymbol{x}) = \sum \phi_d \left[x_p, \bar{x}_p\right] \tag{8}$$
    but this is not numerically investigated here.

A criterion J is then introduced as a combination of some penalization terms (5)−(8) and the data based one (4) according to the objective: PS component (Sect. 3.2), ES component (Sect. 3.3) and both of them simultaneously (Sect. 3.4). In every case, the solution $\widehat{\boldsymbol{x}}$ is defined as the minimizer of J under constraints C_p and C_s:

$$(\mathcal{P}) \begin{cases} \min J(\boldsymbol{x}) \\ \text{s.t.} \begin{cases} x_p = 0 & \text{for } p \in \bar{\mathcal{S}} \\ x_p \geq 0 & \text{for } p \in \mathcal{M} \end{cases} \end{cases} \tag{9}$$

that is to say, as the solution of problem ($\mathcal{P}$). One property then becomes crucial to the construction of J:

- (P_1): J is strictly convex and differentiable.

Indeed, under this hypothesis,

1. the problem ($\mathcal{P}$) possesses a unique solution $\widehat{\boldsymbol{x}}$, which allows the proper definition of the estimated map;
2. the solution in question is continuous with respect to the data and to the tuning parameter values;
3. a broad class of optimization algorithms is available.

As J^{LS} is itself (large sense) convex and differentiable, the property (P_1) can be assured if the potential functions are themselves convex and differentiable. Therefore, we resort to this kind of potential.

Remark 3. Non-convex potentials have been introduced in image reconstruction in the 1980s (Geman & Geman 1984; Blake & Zisserman 1987). As they are richer, they allow a sharper description of the searched images. For example, they can integrate binary variables, allowing contour *detection* to be carried out, at the same time as image reconstruction. As a counterpart, the involved criteria can possess numerous local minima. The computational cost for optimization then increases drastically, and sometimes without guarantee against local minima.

In Sect. 5, several optimization schemes have been investigated within the recommended convex framework. Various iterative algorithms solving ($\mathcal{P}$) are concerned, all of them converging to the unique solution $\widehat{\boldsymbol{x}}$ whatever the initialization. The only question at stake is computation time. An other property of J is therefore crucial.

- (P_2): J is quadratic and circular-symmetric.

This property allows fast optimization algorithms to be put into practice taking advantage of the FFT algorithm: fast criterion calculations, explicit intermediate solutions,... Since J^{LS} is itself quadratic and circulant, (P_2) is satisfied if the regularization terms are circulant and the potential functions ϕ are Quadratic (Q) or Linear (L).

Remark 4. Mixed convex potentials, generally quadratic about the origin and linear above a certain threshold, are used in image processing (Bouman & Sauer 1993) and especially in astronomical imaging (Mugnier et al. 2004) in order to *preserve* possible edges. From the optimization strategy stand point, recent works (Idier 2001b; Allain et al. 2004) allow to reduce the convex optimization problem to a partially quadratic one. This would make possible the development of an FFT and Lagrangian based algorithm for our PS+ES problem. We regard these forms as perspectives and we will see that forms Q and L are sufficiently rich and adapted to the envisaged contexts.

3.2. Point sources and separable linear penalty

This section is devoted to PS: the proposed penalization term is of type (6) where ϕ_s is a potential of $\mathbb{R}_+$ or $\mathbb{R}_+^*$ onto $\mathbb{R}$, to be specified.

Usual MEM (Nityananda & Narayan 1982; Narayan & Nityananda 1984, 1986; Komesaroff et al. 1981; Gull & Skilling 1984; Bhandari 1978; Le Besnerais et al. 1999) come into play, when, for example, $\phi_s[x] = -\log x$, $\phi_s[x] = x \log x$ or $\phi_s[x] = -x + \bar{x} + x \log x/\bar{x}$ where $\bar{x}$ is a default map (O'Sullivan 1995; Snyder et al. 1992). They have been widely used in the domain and in image reconstruction (Mohammad-Djafari & Demoment 1988). They have the advantage of ensuring the property (P_1) on $\mathbb{R}_+^*$, so the problem is properly regularized and ($\mathcal{P}$) possesses a unique solution. They also enjoy the advantage of ensuring (*strict*) positivity, thanks to the presence of an infinite derivative at the origin $\phi_s'(0^+) = -\infty$.

However, these functions prohibit null-pixels and this can be seen as a flaw when the searched maps are largely made up of null-pixels. On the other hand, null-pixels are favored by the introduction of a potential ϕ_s which possesses at its origin (Soussen 2000)

- a minimum value; and
- a strictly positive derivative.

Without loss of generality we set: $\phi_s(0) = 0$ and $\phi'_s(0^+) = 1$, while two possibilities allow property (P_2) to be respected: the form L and the more general form Q.

$$\text{L:}\quad \phi_s(x) = x$$
$$\text{Q:}\quad \phi_s(x) = \alpha x^2 + x.$$

The penalization is then written as:

$$R(\boldsymbol{x}) = \lambda_s \sum x_p + \varepsilon_s \sum x_p^2 . \tag{10}$$

The strict convexity property (P_1) imposes $\varepsilon_s > 0$: the L term ensures a positive derivative at the origin, while the Q term ensures strict convexity.

Remark 5. In order to favor high amplitude peaks, a least penalization function is desirable, i.e. $\varepsilon_s = 0$. In this case, it is possible that J remains unimodal or strictly convex, although we have no proof of this. This property could depend on the value of λ_s, on the knowledge and form of the support, on the (u, v)-plane coverage or on the data in each particular case.

3.3. Extended sources and correlated quadratic penalty

This section is devoted to ES: the penalty term of type (5) introduces interactions between neighboring pixels.

O'Sullivan (1995) proposes the use of an I-divergence: $\phi_c[x, x'] = -x + x' + x \log x/x'$or an Itakura-Saito distance: $\phi_c[x, x'] = -\log x/x' - 1 + x/x'$ in the symmetrized version. As in the case of Sect. 3.2, these allow property (P_1) and positivity to be ensured. However, they prohibit null-pixels and do not ensure property (P_2).

We resort to classical terms of image processing based on finite differences between neighboring pixels. In the simplest case, first order differences yield

$$\phi_c[x, x'] = \phi_c[x - x']$$

where ϕ_c is a potential of $\mathbb{R}$ onto $\mathbb{R}$ to be specified. In order to effectively favor smooth and correlated maps, and due to reasons of symmetry, ϕ_c is chosen to be minimal in 0 and even. In order to ensure property (P_2), we are led to choose ϕ_c in class Q and to reject class L: $\phi_c(x) = x^2$ and

$$R(\boldsymbol{x}) = \lambda_c \sum_{p=0}^{N} \left[x_{p+1} - x_p\right]^2$$

with the hypothesis $x_0 = x_N$ in order to ensure circularity.

We are here dealing with early regularization techniques, that appeared in the 1960s (Phillips 1962; Twomey 1963; Tikhonov 1963) and were developed in the mid-1970s in works by Tikhonov & Arsenin (1977) in a continuous context and by Hunt (1977) in a discrete context. They are also related to the well-known Wiener filter.

In this form, the strict convexity condition (P_1) is not respected. Indeed, J^{LS} is not sensitive to constant maps (since null-frequency is not observed) and neither is the regularization term (since it is only a function of the difference between pixels). Several options are available for dealing with this indetermination.

1. Support constraint C_s: as soon as the support constraint is valid, if at least one of the pixels is zero ($\mathcal{S} \neq \mathcal{M}$), J is strictly convex on $\mathbb{R}^{\mathcal{S}}$.
2. In the absence of support information, it is sufficient to penalize the mean of the map by a term such:

   $$R_m(\boldsymbol{x}) = \left[\sum x_p\right]^2 .$$

   Intuitively, it reduces the mean of the map towards 0 and is counterbalanced by the positivity constraint.
3. It is also possible to penalize the quadratic norm of the map by a term such as that introduced in Sect. 3.2.

The penalization thus reads

$$R(\boldsymbol{x}) = \lambda_c \sum \left[x_{p+1} - x_p\right]^2 + \varepsilon_m \left[\sum x_p\right]^2 . \tag{11}$$

Under this form, properties (P_1) and (P_2) are satisfied if ($\varepsilon_m > 0, \lambda_c > 0$) in the case $\mathcal{S} = \mathcal{M}$ and ($\varepsilon_m \geq 0, \lambda_c > 0$) in the case $\mathcal{S} \neq \mathcal{M}$.

3.4. Mixed model

The present paper is devoted to maps composed of both types of component simultaneously: ES and PS. Following (Magain et al. 1998) and (Pirzkal et al. 2000), we introduce two maps $\boldsymbol{x}_e$ and $\boldsymbol{x}_p$ which describe each component respectively. The direct model (1) becomes:

$$\boldsymbol{y} = \boldsymbol{TF}(\boldsymbol{x}_e + \boldsymbol{x}_p) + \boldsymbol{b} , \tag{12}$$

and the least-squares term

$$J^{LS}_{Mix}(\boldsymbol{x}_e, \boldsymbol{x}_p) = \|\boldsymbol{y} - \boldsymbol{TF}(\boldsymbol{x}_e + \boldsymbol{x}_p)\|^2,$$

where the subscript "Mix" stand for Mixed map. This form raises new indeterminates as it now concerns the estimation of $2N$ variables, still from a single set of M Fourier coefficients. However, it allows the explicit introduction of characteristic information about each map through two adapted regularization terms.

1. A separable term for $\boldsymbol{x}_p$, identical to that in Sect. 3.2

   $$R_s(\boldsymbol{x}_p) = \sum x_p(p),$$

   minimum at 0 and with a strictly positive derivative.
2. An interaction term between neighboring pixels of the map $\boldsymbol{x}_e$, identical to that in Sect. 3.3

   $$R_c(\boldsymbol{x}_e) = \sum \left[x_e(p+1) - x_e(p)\right]^2 .$$

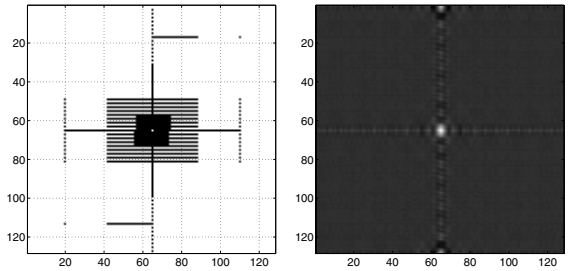

Fig. 2. Left figure shows instantaneous (u, v)-plane coverage (EW array is along vertical direction and NS array is along horizontal direction). Right figure gives the dirty beam, defined as the 2D Fourier transform of the (u, v)-plane coverage with a unitary weight for each visibility.

So as to ensure property (P_1), the same terms as in Sects. 3.2 and 3.3 are added, and the regularized criterion takes the form:

$$J^{\mathrm{Reg}}_{\mathrm{Mix}}(\boldsymbol{x}_{\mathrm{e}}, \boldsymbol{x}_{\mathrm{p}}) = J^{\mathrm{LS}}_{\mathrm{Mix}}(\boldsymbol{x}_{\mathrm{e}}, \boldsymbol{x}_{\mathrm{p}}) + \lambda_{\mathrm{s}} \sum x_{\mathrm{p}}(p) + \varepsilon_{\mathrm{s}} \sum x_{\mathrm{p}}(p)^2 + \lambda_{\mathrm{c}} \sum \left[x_{\mathrm{e}}(p+1) - x_{\mathrm{e}}(p)\right]^2 + \varepsilon_{\mathrm{m}} \left[\sum x_{\mathrm{e}}(p)\right]^2, \quad (13)$$

where superscript "Reg" stands for Regularized. Regularization parameters (hyperparameters) λ_{c} and λ_{s} tune the smooth and spiky character of maps $\boldsymbol{x}_{\mathrm{e}}$ and $\boldsymbol{x}_{\mathrm{p}}$.

In this form, properties (P_1)–(P_2) are satisfied if ($\lambda_{\mathrm{s}} \geq 0, \lambda_{\mathrm{c}} > 0, \varepsilon_{\mathrm{s}} > 0$) and $\varepsilon_{\mathrm{m}} > 0$ when $\mathcal{S} \neq \mathcal{M}$ or $\varepsilon_{\mathrm{m}} \geq 0$ when $\mathcal{S} = \mathcal{M}$. The couple of maps $(\widehat{\boldsymbol{x}_{\mathrm{e}}}, \widehat{\boldsymbol{x}_{\mathrm{p}}})$ is properly defined as the solution of problem $(\mathcal{P})$ and the next section (Sect. 4) gives the first practical results (simulated and real data processing). Section 5 is devoted to a fast optimization algorithm.

4. Computation results

4.1. Nançay radioheliograph

Radio emission of the Sun at meter wavelength is known since World War II. The Nançay radioheliograph (NRH) is a radio-interferometer dedicated to imaging the solar corona and it monitors the radio burst in solar atmosphere at such wavelengths with high temporal rate, adequate spatial resolution and high dynamic.

At such frequencies, mainly two kinds of structures are observed in the corona: (1) larger structures (ES) and (2) smaller structures (PS). The quiet Sun (1-*i*) is the largest structure, larger than the Sun size in the visible and slowly varying on long term scale (years) (Lantos & Alissandrakis 1996). Medium size structures (1-*ii*) are the radio counterpart of coronal holes and magnetic loops (*plateau*) (Alissandrakis & Lantos 1996), and are also observed simultaneously in soft X-rays. The time scale for such structures is days to weeks. They are clearly correlated to persistent structures observed in other wavelength (optical and X-rays) and rotate on the radio maps quasi simultaneously with their optical and X-rays counterparts. The small structures (2) with very high brightness, can often reach several tens of Millions Kelvin (Kerdraon & Mercier 1983); they usually have a small life time (few seconds) and are associated to energetic events in the magnetic loops in the Sun's atmosphere. Correlation with structures observed in other wavelengths is more difficult.

The NRH is composed by two arrays: one along Est-West (EW) direction with 23 antennas, the other along North-South (NS) with 19 antennas. The NRH is operating in the range 150–450 MHz at a time sampling rate of 1/10 s, about eight hours a day, with favorable signal to noise ratio. Since the refurbishing of the instrument (Kerdraon & Delouis 1997) cross-correlation between most of the antennas in both arrays are available. As a consequence: (*i*) 569 non redundant instantaneous visibilities are now available[2] (with unitary weights) and moreover; (*ii*) the instantaneous coverage of the (u, v)-plane (shown in Fig. 2) becomes much more uniform. Nevertheless, due to the structure of the arrays, the coverage is not uniform. The central part of the (u, v)-plane essentially consists of two rectangular domains: the central one is a 16×16 square and the larger one is a 32×46 rectangle. With this configuration 2D instantaneous imaging (without Earth rotation aperture synthesis) becomes possible despite strong sidelobes in the dirty beam (see also Fig. 2). As far as the dirty beam is concerned, the maximum value is normalized to 1 and located in the middle of the map at $(64, 64)$. A secondary important lobe partly around $(1, 64)$ and $(128, 64)$ referred to as the aliasing lobe has amplitude 0.70 and characterizes important aliased response. The first negative lobe is −0.10 around the central lobe and −0.23 around the aliasing lobe. Moreover, the first positive lobe is 0.14 near the central lobe and 0.12 near the aliasing lobe. In addition, the *FWHM* is 4.5 (resp. 4) pixels for the central (resp. aliasing) lobe.

At processed frequency (236 MHz), the field of view[3] (FOV) related to the shortest baseline (55 m in NS, 50 m in *EW*) is ∼1 ° 20 ′ and the size of the quiet sun is ∼40 ′, i.e. ∼1/2 FOV. Since at observed frequencies (150–450 MHz) the *FWHM* of the smallest antenna primary beam (few antennas are 15 m diameter) is much wider than the FOV, a unitary primary beam is appropriate. Moreover, the Shannon criterion is respected if the pixel number is ∼60 for a FOV of 1 °.

With the given characteristics, ES/PS separation must be achieved and reconstruction errors must be as small as possible for both maps, in order to strongly constrain physical models and to monitor position, amplitude and separation of bursts. But imaging the encountered context mixing PS and ES remains difficult and standard methods such as CLEAN and MEM (even in a multiresolution approach) are usually inefficient due to the large background and the intricate mixing of real structures and sidelobes (Coulais 1997). One possible outcome of the present work is to provide to the solar radio community accurate maps from NRH in order to achieve more detailed scientific studies. The following computation study

[2] Thanks to Hermitian symmetry 1138 Fourier coefficients are available. The computed (u, v)-plane and map are 128×128.

[3] For a declination 23 ° and null hour angle (the Sun at noon in summer), the FOV is 87 ′ in *EW* and 86 ′ in NS, and the resolution is 3.27 ′ in *EW* and 2.17 ′ in NS, since main *EW* arm is 1600 m with step 50 m and NS arm is 2640 m with step 55 m.

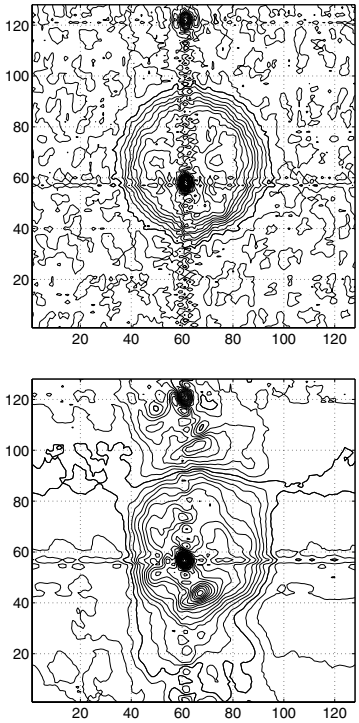

Fig. 3. Dirty maps typically encountered with NRH: simulated data (*top*) and real data (*bottom*). Contour levels are -10^{-2} to 5×10^{-2}, step 2.5×10^{-4} (they are used for all the shown maps).

(simulated and real data) is a typical case encountered with NRH and provides a first element in this sense.

4.2. Simulation results

Simulated data

The true ES map $\boldsymbol{x}_{\mathrm{e}}^{\star}$ (Fig. 4a), is ranging in amplitude (arbitrary units) from 0 to 5.5×10^{-3}. The true Sun lies in a disk centered in the middle of the image, i.e. $(64, 64)$ with a 64 pixels diameter. The outer part of the disk is zero and the mean of this component is 5.59×10^{-4}. The true PS map $\boldsymbol{x}_{\mathrm{p}}^{\star}$ (Fig. 4b) consists of two peaks: the first one is located at $(60, 61)$ with amplitude 5.0×10^{-2}, and the second one overlaps pixels $(57, 61)$ and $(57, 62)$ with respective amplitudes 5.0×10^{-2} and 4.5×10^{-2}. Data (in the (u, v)-plane) are simulated using the direct model Eq. (12), i.e. FFT and truncature, and corrupted by a white, zero-mean complex Gaussian noise with variance 2×10^{-7}. (This noise variance has been chosen in order to mimic real data.) The dirty map is shown in Fig. 3. It is clearly dominated by the PS, and the whole map is corrupted by side lobes. Moreover, the two close peaks at location $(60, 61)$ and $(57, 61)$–$(57, 62)$ are not resolved.

Reconstruction parameters

The supports have been deduced from the dirty map. It is a disk centered at $(64, 64)$ with a 70 pixels diameter for the ES map. Regarding the PS map, the support consists of one disk centered in $(58, 61)$ with a 10 pixels diameter.

In practice, two hyperparameters have to be tuned: λ_{c} and λ_{s} (ε_{s} is practically set to 10^{-10}). λ_{c} must be set in the order of magnitude of eigenvalues of the Hessian of the criterion and is set to $\lambda_{\mathrm{c}} = 2$. λ_{s} has been empirically selected after several trials in order to visually achieve separation of PS and ES: it has been set to $\lambda_{\mathrm{s}} = 10^{-3}$.

Reconstruction results

Figure 4 shows the reconstructed maps. A simple qualitative comparison with the references $\boldsymbol{x}_{\mathrm{e}}$ and $\boldsymbol{x}_{\mathrm{p}}$ shows that the two components $\widehat{\boldsymbol{x}_{\mathrm{e}}}$ and $\widehat{\boldsymbol{x}_{\mathrm{p}}}$ are efficiently separated and accurately reconstructed.

The two peaks of $\widehat{\boldsymbol{x}_{\mathrm{p}}}$ shown in Fig. 4d are precisely located at $(60, 61)$ and $(57, 61)$–$(57, 62)$ (overlapping). The estimated amplitudes are 0.051, 0.048 and 0.043 respectively, i.e. an error of less than 5%. Moreover, the two close peaks are separated whereas they are not in the dirty map. This illustrates the resolution capability of the proposed method resulting from both data and accounted information (positivity, support, and PS+ES hypothesis). It is also noticeable that the respective part of flux in overlapped pixels $(57, 61)$–$(57, 62)$ is correctly restored.

Figure 4c gives the estimated ES map $\widehat{\boldsymbol{x}_{\mathrm{e}}}$. Compared to the true one of Fig. 4a the main structures are accurately estimated. The contour lines of Fig. 4c are very similar to the one of Fig. 4a and the relative reconstruction error is less than 2%. Moreover, the mean of the estimated ES map $\widehat{\boldsymbol{x}_{\mathrm{e}}}$ is 5.57×10^{-4} while the true mean is 5.59×10^{-4}: the total flux is correctly estimated. The maximum value is 5.4×10^{-3} in $\widehat{\boldsymbol{x}_{\mathrm{e}}}$ whereas it is 5.5×10^{-3} in $\boldsymbol{x}_{\mathrm{e}}$: the dynamic is also correctly retrieved. Nevertheless, a slight distortion located around pixel $(65, 60)$ can be observed in the proposed ES map. It probably results from an imperfect separation of the two components: a slight trace of the dirty beam remains in the estimated ES map. Moreover, the sharp edges of the true Sun are slightly smoothed due to the lack of high frequencies in the available Fourier coefficients incompletely enhanced by accounted prior information (see Rems. 3 and 4).

4.3. Real data computations

This section is devoted to real data processing based on a data set from the NRH[4]. The coverage is identical to the one of simulated data of the previous section.

The dirty beam is shown in Fig. 2 and the dirty map is shown in Fig. 3. Both dirty beam and dirty map are typically encountered with NRH and are similar to the one simulated in the previous section. As expected, resolution is limited and the quality of the map is entirely contingented upon sidelobes around the brightest point sources (radio burst). Imaging such a complex context mixing PS and ES suffers from intricate mixing of real structures and sidelobes due the brightest ones.

The same supports have been used to compute the real data and the simulated ones. It is a disk centered in the middle of

[4] The eleventh of June, 2004, 13h00, at 236 MHz.

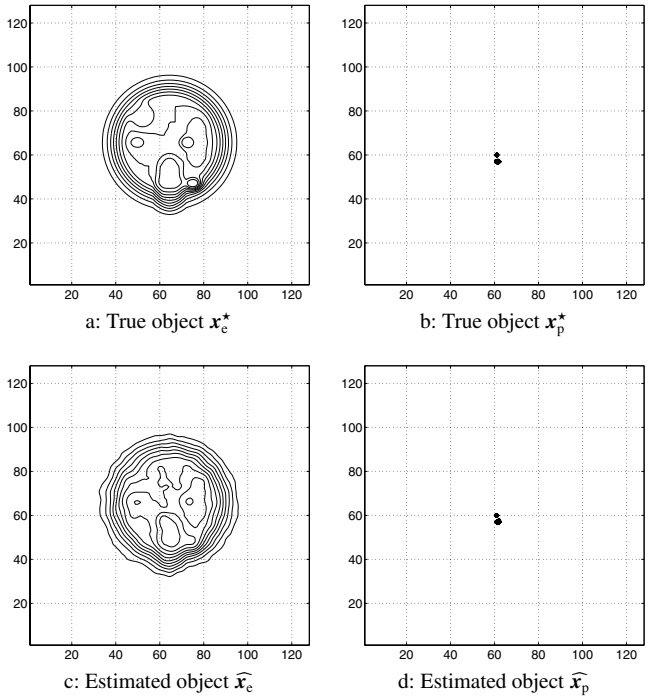

Fig. 4. Simulation results (see Sect. 4.2). Contour levels are the same than in Figs. 3 and 5 for all the maps: the true ES $\boldsymbol{x}_e^\star$ **a)** and the estimated one $\widehat{\boldsymbol{x}_e}$ **c)** as well as for the true PS $\boldsymbol{x}_p^\star$ **b)** and the estimated one $\widehat{\boldsymbol{x}_p}$ **d)**.

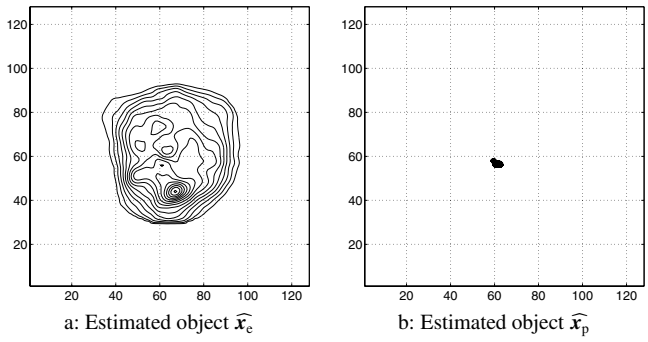

Fig. 5. NRH data processing from typical scientific observation at 236 MHz (see Sect. 4.3). Contour levels are the same than in Figs. 3 and 4. The two components $\widehat{\boldsymbol{x}_e}$ **a)** and $\widehat{\boldsymbol{x}_p}$ **b)** are clearly separated and deconvolution of both component is clearly achieved. Both maps are positive and the prescribed supports are respected.

the map with a 70 pixels diameter for the ES map and a disk centered in (58, 61) with 10 pixels diameter for the PS map. The same value of the parameters $\lambda_c = 2$ and $\lambda_s = 10^{-3}$ have been used to compute the real data and the simulated one (ε_s remains set to 10^{-10}).

Estimated maps are shown in Fig. 5a (ES component) and Fig. 5b (PS component). The two components $\widehat{\boldsymbol{x}_e}$ (Fig. 5a) and $\widehat{\boldsymbol{x}_p}$ (Fig. 5b) are clearly separated and both deconvolution is clearly achieved. Both maps are positive and the prescribed supports are respected. Moreover, the $\widehat{\boldsymbol{x}_e}$ map presents a similar structure to the usual one of the Sun at meter wavelengths without strong point sources (Coulais 1997; Lantos & Alissandrakis 1996).

5. Numerical optimization stage

The estimated maps are defined as the unique solution of the problem ($\mathcal{P}$) given by (9) which involves the quadratic criterion J given by (13). Up to an additive constant:

$$J(\boldsymbol{x}) = \frac{1}{2}\,\boldsymbol{x}^t\,\boldsymbol{Q}\,\boldsymbol{x} + \boldsymbol{q}^t\,\boldsymbol{x},$$

where $\boldsymbol{x} = [\boldsymbol{x}_e; \boldsymbol{x}_p]$ collects the two maps (Appendix C gives $\boldsymbol{Q}$ and $\boldsymbol{q}$). Thus, $(\mathcal{P})$ is a convex quadratic program:

$$(\mathcal{P}) \begin{cases} \min \dfrac{1}{2}\, \boldsymbol{x}^{\mathrm{t}} \boldsymbol{Q}\, \boldsymbol{x} + \boldsymbol{q}^{\mathrm{t}} \boldsymbol{x} \\ \text{s.t.} \begin{cases} x_p = 0 & \text{for } p \in \bar{\mathcal{S}} \\ x_p \geq 0 & \text{for } p \in \mathcal{M} \end{cases} \end{cases} \tag{14}$$

widely investigated in the optimization literature. The main difficulty is twofold. On the one hand, the non-separability of J together with positivity constraint prevents from explicit optimization. On the other hand, the number of variables is very large. We have investigated most of the proposed methods in the excellent reference book (Nocedal & Wright 2000):

- Constrained gradient.
- Gradient projection.
- Barrier and interior point.
- Relaxation (coordinate-by-coordinate).
- Augmented Lagrangian (method of multipliers),

and have selected the latter as the faster. It is based upon successive optimizations of a Lagrangian function $\mathcal{L}$ founded on Lagrange multipliers ℓ, slack variables s and quadratic penalty. It is computationally based on FFT and threshold, so it is, in addition, very simple to implement.

5.1. Lagrangian function

The equality constraint $x_p = 0$ ($p \in \bar{\mathcal{S}}$) is introduced by means of a usual Lagrangian term $-\ell_p x_p$ together with a penalty term $c x_p^2/2$. The entire term write:

$$-\sum_{p \in \bar{\mathcal{S}}} \ell_p x_p + \frac{1}{2}\, c \sum_{p \in \bar{\mathcal{S}}} x_p^2. \tag{15}$$

The inequality constraint $x_p \geq 0$ ($p \in \mathcal{S}$) is converted into the equality one $s_p - x_p = 0$ using the slack variable $s_p \geq 0$. Lagrange and penalty terms then write:

$$-\sum_{p \in \mathcal{S}} \ell_p (x_p - s_p) + \frac{1}{2}\, c \sum_{p \in \mathcal{S}} (x_p - s_p)^2. \tag{16}$$

In order to simultaneously process both equality (15) and inequality (16) constraints, we introduce extra slack variables $s_p = 0$ for $p \in \bar{\mathcal{S}}$. The Lagrangian then writes:

$$\mathcal{L}(\boldsymbol{x}, \boldsymbol{s}, \boldsymbol{\ell}) = J(\boldsymbol{x}) - \boldsymbol{\ell}^{\mathrm{t}}(\boldsymbol{x} - \boldsymbol{s}) + \frac{1}{2}\, c\, (\boldsymbol{x} - \boldsymbol{s})^{\mathrm{t}}(\boldsymbol{x} - \boldsymbol{s})$$

where $\boldsymbol{s}$ and $\boldsymbol{\ell}$ collect slack variables s_p and multipliers ℓ_p.

5.2. Algorithm

The algorithm then iterates three steps:

① unconstrained minimization of $\mathcal{L}$ w.r.t. $\boldsymbol{x}$;
② minimization of $\mathcal{L}$ w.r.t. $\boldsymbol{s}$, s.t. $s_p \geq 0$;
③ update $\boldsymbol{\ell}$ and c.

The efficiency of the proposed algorithm relies on both slack variables and property (P_2). Roughly speaking, positivity is transfered on slack variables, so, the non separable constrained problem $(\mathcal{P})$ is split in two subproblems: a non-separable but unconstrained one computable by FFT (step ①) and a constrained but separable one (step ②).

Step ① proceeds by fixing $\boldsymbol{\ell}$ and $\boldsymbol{s}$ to the current value and then computes the unconstrained minimizer $\widetilde{\boldsymbol{x}}$ of $\mathcal{L}$. It is an unconstrained convex quadratic problem, so its solution is explicit:

$$\widetilde{\boldsymbol{x}} = -(\boldsymbol{Q} + c\boldsymbol{I}_N)^{-1}\, (\boldsymbol{q} + [\boldsymbol{\ell} + c\boldsymbol{s}])\,,$$

and computable by means of FFT, thanks to circularity.

Step ② updates the slack variables s_p for $p \in \mathcal{S}$ (by construction, $s_p = 0$ for $p \in \bar{\mathcal{S}}$) as the minimizer $\widetilde{s}_p$ of $\mathcal{L}$, subject to $s_p \geq 0$.

$$\widetilde{s}_p = \begin{cases} \max\,(0, c x_p - \ell_p)/c & \text{for } p \in \mathcal{S} \\ 0 & \text{for } p \in \bar{\mathcal{S}}. \end{cases}$$

This step is constrained but separable: the constrained minimizer is the unconstrained one if positive and 0 if not.

Step ③ consists in updating the Lagrange multiplier ℓ:

$$\widetilde{\ell}_p = \begin{cases} \max\,(0, \ell_p - c x_p) & \text{for } p \in \mathcal{S} \\ \ell_p - c x_p & \text{for } p \in \bar{\mathcal{S}}. \end{cases}$$

This step can also include an update of c (e.g. $\widetilde{c} = 1.1c$). Practically, c is not updated (see next subsection).

Steps ① to ③ are iterated until stopping condition is met, e.g. relative variation smaller that 0.1%.

Remark 6. Constrained variables $x_p = 0$ for $p \in \bar{\mathcal{S}}$ can also be eliminated. This is a relevant strategy when using gradient based or relaxation methods. It does not prevent from computing J and its gradient by means of FFT. On the contrary, such a strategy is not relevant here: it would break circularity and prevent from using FFT in step ①.

5.3. Practical case and computations time

This section specializes the algorithm in the case of constant coefficient c. In this case, step ②-③ reduces to:

$$\widetilde{\ell}_p + c\widetilde{s}_p = \begin{cases} |\ell_p - c x_p| & \text{for } p \in \mathcal{S} \\ \ell_p - c x_p & \text{for } p \in \bar{\mathcal{S}}. \end{cases}$$

Moreover, $\boldsymbol{Q} + c\boldsymbol{I}_N$ can be inverted once for all and the algorithm then requires 4 FFT per iteration. The algorithm has been used in the previous computations with constant coefficient $c = 10^{-3}$. Convergence is achieved after about 1000 iterations and it takes half a minute[5].

[5] Algorithm has been implemented with the computing environments Matlab and IDL on a PC, with a 2 GHz AMD-Athlon CPU, and 512 MB of RAM. Both codes are ~50 lines long.

6. Conclusions

The problem of incomplete Fourier inversion is addressed as it arises in map reconstruction (deconvolution, spectral interpolation/extrapolation, Fourier synthesis). The proposed solution is dedicated to specific situations in which the imaged object involves two components: (*i*) an extended component together with (*ii*) a set of point sources. For this cases, new developments are given based on existing work of Magain et al. (1998) and Pirzkal et al. (2000).

The main part of the paper deals with inversion in the regularization framework. It essentially departs from usual strategies by the way it accounts for (1) noise and indeterminacies, (2) smoothness/sharpness prior and (3) positivity and support, in a unique coherent setting. The presented development can also include known template and default map. Thus, a new regularized criterion is introduced and estimated maps are properly defined as its unique minimizer. The criterion is iteratively minimized by means of an efficient algorithm essentially based on Lagrange multiplier which practically requires FFT and threshold only. The minimizer is shown to be both practically reachable and accurate. A first evaluation of the proposed method has been carried out using simulated and real data sets. We demonstrate ability to separate the two components, high resolution capability and high quality of each map. To our knowledge, such a development is an original contribution to the field of deconvolution.

Nevertheless, a further evaluation of the proposed method is desirable. Future work will include systematic evaluation of the capability of the proposed method as a function of (u, v)-plane coverage, PS amplitudes *versus* ES ones, PS position (especially in a subpixelic sense) and noise level. Such an assessment concerns both simulated and real data. Moreover evaluation of the potentiality of the method on large maps (e.g. VLA images), high dynamic imaging (e.g. WSRT images) and imaging using millimeter interferometers (e.g. IRAM PdBi and ALMA) or optical instruments will be considered.

A part of future work in the field of SP+ES imaging, will include convex non quadratic penalization of ES (see Rem. 4). Another part of future work will particularize the proposed method in order to produce maps of ES only and maps of PS only.

A Bayesian interpretation of the proposed method involve truncated Gauss-Markov models (ES component) and exponential white noise (PS component) and formally provides likelihood tools in order to achieve automatic tuning of the hyperparameters. This is a more delicate aspect but it will be addressed in future works.

Acknowledgements. The authors thank Anthony Larue and Patrick Legros for substantial contribution in optimization investigations. The authors are particularly grateful to François Viallefond, Alain Kerdraon, Christophe Marqué, Claude Mercier and Jérémie Leclère for useful discussions and for providing NRH data. We are grateful to Guy Le Besnerais and Éric Thiébaut for carefully reading the paper. Special thanks to the incredible, indescribable Grün.

Appendix A: Notations

In this paper, $\boldsymbol{I}_P$ denotes the $P \times P$ identity matrix and $\boldsymbol{M}^\dagger$ (resp. $\boldsymbol{M}^{\mathrm{t}}$) denotes the complex conjugate transpose (resp. transpose) of a given matrix $\boldsymbol{M}$.

Let us note $\boldsymbol{D}$ the (circulant) first order difference matrix and $\boldsymbol{\Lambda}_{\mathrm{D}} = \boldsymbol{F}\boldsymbol{D}\boldsymbol{F}^\dagger$ the diagonalized matrix. Let us also note $\mathbb{1}$ the ones column vector with N components and $\mathring{\mathbb{1}} = \boldsymbol{F}\mathbb{1}$ its FFT (non-null at null frequency only).

We introduce now two matrices $\boldsymbol{\Delta}_{\mathrm{E}}$ and $\boldsymbol{\Delta}_{\mathrm{P}}$ useful to compute ES and PS respectively:

$$\begin{cases} \boldsymbol{\Delta}_{\mathrm{E}} = \boldsymbol{\Delta}_{\mathrm{C}} + \lambda_{\mathrm{c}}\, \boldsymbol{\Delta}_{\mathrm{D}} + \varepsilon_{\mathrm{m}}\ \mathring{\mathbb{1}}^\dagger\, \mathring{\mathbb{1}} \\ \boldsymbol{\Delta}_{\mathrm{P}} = \boldsymbol{\Delta}_{\mathrm{C}} + \varepsilon_{\mathrm{s}}\, \boldsymbol{I}_N \end{cases}$$

where $\boldsymbol{\Delta}_{\mathrm{C}} = \boldsymbol{T}^{\mathrm{t}}\boldsymbol{T}$. The three sub-matrices $\boldsymbol{\Delta}_{\mathrm{E}}$, $\boldsymbol{\Delta}_{\mathrm{P}}$ and $\boldsymbol{\Delta}_{\mathrm{C}}$ are diagonal matrices.

Appendix B: Conventions and properties

This appendix gives several properties of $\boldsymbol{F}$ and $\boldsymbol{T}$ introduced in Sect. 2.

- $\boldsymbol{F}^\dagger\boldsymbol{F} = \boldsymbol{F}\boldsymbol{F}^\dagger = \boldsymbol{I}_N$: orthonormality of the normalized FFT.
- $\boldsymbol{T}$ is a truncation operator, $N \times M$, (eliminates coefficient outside the coverage).
- $\boldsymbol{T}^{\mathrm{t}}$ is a zero-padding operator, $M \times N$, (adds null coefficient outside the coverage).
- $\boldsymbol{\Delta}_{\mathrm{C}} = \boldsymbol{T}^{\mathrm{t}}\boldsymbol{T}$ is a projection matrix, $N \times N$, (nullifies coefficients outside the coverage).
- $\boldsymbol{T}\boldsymbol{T}^{\mathrm{t}} = \boldsymbol{I}_M$.

Appendix C: Gradient and Hessian calculi

This appendix is devoted to the vector $\boldsymbol{q}$ and the matrix $\boldsymbol{Q}$ involved in the minimized criterion.

$\boldsymbol{q}$ is a $2N$ components column vector based on the gradient of criterion J, at $\boldsymbol{x} = 0$. The first part is the dirty map and the second one is the dirty map minus a constant map equal to $\lambda_{\mathrm{s}}/2$. In the Fourier domain, $\boldsymbol{q}$ reads:

$$\mathring{\boldsymbol{q}} = \left.\frac{\partial\, \mathring{J}}{\partial\, \mathring{\boldsymbol{x}}}\right|_{\boldsymbol{x}=0} = \left[\begin{array}{c} \dfrac{\partial\, \mathring{J}}{\partial\, \mathring{\boldsymbol{x}}_{\mathrm{e}}} \\[2ex] \dfrac{\partial\, \mathring{J}}{\partial\, \mathring{\boldsymbol{x}}_{\mathrm{p}}} \end{array}\right]_{\boldsymbol{x}=0} = -2\left[\begin{array}{c} \bar{\boldsymbol{y}} \\ \bar{\boldsymbol{y}} - \lambda_{\mathrm{s}}\, \mathring{\mathbb{1}}\ /2 \end{array}\right].$$

$\boldsymbol{Q}$ is a $2N \times 2N$ matrix based on the Hessian of J. The two anti-diagonal elements are the Hessian of the LS term and rely on the dirty beam only. The diagonal elements are the Hessian of J w.r.t. each map $\boldsymbol{x}_{\mathrm{p}}$ and $\boldsymbol{x}_{\mathrm{e}}$. In the Fourier domain, $\boldsymbol{Q}$ reads:

$$\mathring{\boldsymbol{Q}} = \frac{\partial^2\, \mathring{J}}{\partial\, \mathring{\boldsymbol{x}}^2} = \left[\begin{array}{cc} \dfrac{\partial^2\, \mathring{J}}{\partial\, \mathring{\boldsymbol{x}}_{\mathrm{e}}^2} & \dfrac{\partial^2\, \mathring{J}}{\partial\, \mathring{\boldsymbol{x}}_{\mathrm{e}}\ \partial\, \mathring{\boldsymbol{x}}_{\mathrm{p}}} \\[2ex] \dfrac{\partial^2\, \mathring{J}}{\partial\, \mathring{\boldsymbol{x}}_{\mathrm{p}}\ \partial\, \mathring{\boldsymbol{x}}_{\mathrm{e}}} & \dfrac{\partial^2\, \mathring{J}}{\partial\, \mathring{\boldsymbol{x}}_{\mathrm{p}}^2} \end{array}\right] = \left[\begin{array}{cc} \boldsymbol{\Delta}_{\mathrm{E}} & \boldsymbol{\Delta}_{\mathrm{C}} \\ \boldsymbol{\Delta}_{\mathrm{C}} & \boldsymbol{\Delta}_{\mathrm{P}} \end{array}\right].$$

Table C.1. Functions, gradients and Hessian of encountered criteria (given as a function of map and their FFT).

$\rho(\boldsymbol{x})$	$\mathring{\rho}\,(\mathring{\boldsymbol{x}})$	$\partial\rho/\partial\boldsymbol{x}$	$\partial\,\mathring{\rho}\,/\partial\,\mathring{\boldsymbol{x}}$	$\partial^2\rho/\partial\boldsymbol{x}^2$	$\partial^2\,\mathring{\rho}\,/\partial\,\mathring{\boldsymbol{x}}^2$
$\lVert\boldsymbol{y}-\boldsymbol{T}\boldsymbol{F}\boldsymbol{x}\rVert^2$	$\lVert\boldsymbol{y}-\boldsymbol{T}\,\mathring{\boldsymbol{x}}\,\rVert^2$	$-2\,\boldsymbol{F}^\dagger\boldsymbol{T}^\mathrm{t}(\boldsymbol{y}-\boldsymbol{T}\boldsymbol{F}\boldsymbol{x})$	$-2\,\boldsymbol{T}^\mathrm{t}(\boldsymbol{y}-\boldsymbol{T}\,\mathring{\boldsymbol{x}})$	$2\,\boldsymbol{F}^\dagger\boldsymbol{T}^\mathrm{t}\boldsymbol{T}\boldsymbol{F}$	$2\,\boldsymbol{T}^\mathrm{t}\boldsymbol{T}$
$\boldsymbol{x}^\mathrm{t}\boldsymbol{D}^\mathrm{t}\boldsymbol{D}\boldsymbol{x}$	$\mathring{\boldsymbol{x}}^\dagger\,\boldsymbol{\Lambda}_\mathrm{D}^\dagger\boldsymbol{\Lambda}_\mathrm{D}\,\mathring{\boldsymbol{x}}$	$2\,\boldsymbol{D}^\mathrm{t}\boldsymbol{D}\boldsymbol{x}$	$2\,\boldsymbol{\Lambda}_\mathrm{D}^\dagger\boldsymbol{\Lambda}_\mathrm{D}\,\mathring{\boldsymbol{x}}$	$2\,\boldsymbol{D}^\mathrm{t}\boldsymbol{D}$	$2\,\boldsymbol{\Lambda}_\mathrm{D}^\dagger\boldsymbol{\Lambda}_\mathrm{D}$
$\boldsymbol{x}^\mathrm{t}\boldsymbol{x}$	$\mathring{\boldsymbol{x}}^\dagger\,\mathring{\boldsymbol{x}}$	$2\,\boldsymbol{x}$	$2\,\mathring{\boldsymbol{x}}$	$2\,\boldsymbol{I}_N$	$2\,\boldsymbol{I}_N$
$(\mathbb{1}^\mathrm{t}\boldsymbol{x})^2$	$\mathring{\boldsymbol{x}}\,(0)^2$	$2\,\mathbb{1}\mathbb{1}^\mathrm{t}\boldsymbol{x}$	$2\,\mathring{\mathbb{1}}\,\mathring{\mathbb{1}}^\dagger\,\mathring{\boldsymbol{x}}$	$2\,\mathbb{1}\mathbb{1}^\mathrm{t}$	$2\,\mathring{\mathbb{1}}^\dagger\,\mathring{\mathbb{1}}$
$\mathbb{1}^\mathrm{t}\boldsymbol{x}$	$\mathring{\boldsymbol{x}}\,(0)$	$\mathbb{1}$	$\mathring{\mathbb{1}}$	$\mathbf{0}$	$\mathbf{0}$

Appendix D: Object updates

The present subsection gives details about the step ① of the proposed algorithm (Sect. 5): the unconstrained minimization of $\mathcal{L}$ w.r.t. $\boldsymbol{x}$, i.e. the update of $\boldsymbol{x}_\mathrm{e}$ and $\boldsymbol{x}_\mathrm{p}$. Let us introduce the two vectors

$$\begin{cases} z_\mathrm{e} = \bar{\boldsymbol{y}} + (\mathring{\boldsymbol{\ell}}_\mathrm{e} \;+c\;\mathring{s}_\mathrm{e})/2 \\ z_\mathrm{p} = \bar{\boldsymbol{y}} + (\mathring{\boldsymbol{\ell}}_\mathrm{p} \;+c\;\mathring{s}_\mathrm{p})/2 - \lambda_\mathrm{s}\;\mathring{\mathbb{1}} \end{cases}$$

based on observed data $\bar{\boldsymbol{y}}$ and FFT of slack variables and Lagrange multipliers $\mathring{s} = \boldsymbol{F}\boldsymbol{s}$ and $\mathring{\boldsymbol{\ell}} = \boldsymbol{F}\boldsymbol{\ell}$ (for each map ES and PS). Let us also introduce two diagonal matrices

$$\begin{cases} \boldsymbol{M}_\mathrm{E} = \boldsymbol{\Delta}_\mathrm{E} + c\,\boldsymbol{I}_N/2 \\ \boldsymbol{M}_\mathrm{P} = \boldsymbol{\Delta}_\mathrm{P} + c\,\boldsymbol{I}_N/2. \end{cases}$$

The update reads:

$$\begin{cases} \mathring{\boldsymbol{x}}_\mathrm{e} = \left(\boldsymbol{M}_\mathrm{E}\,\boldsymbol{M}_\mathrm{P} - \boldsymbol{\Delta}_\mathrm{C}^2\right)^{-1}\left(\boldsymbol{M}_\mathrm{P}\,z_\mathrm{e} - \boldsymbol{\Delta}_\mathrm{C}\,z_\mathrm{p}\right) \\ \mathring{\boldsymbol{x}}_\mathrm{p} = \left(\boldsymbol{M}_\mathrm{E}\,\boldsymbol{M}_\mathrm{P} - \boldsymbol{\Delta}_\mathrm{C}^2\right)^{-1}\left(\boldsymbol{M}_\mathrm{E}\,z_\mathrm{p} - \boldsymbol{\Delta}_\mathrm{C}\,z_\mathrm{e}\right) \end{cases}$$

easily implemented since $\boldsymbol{M}_\mathrm{E}\,\boldsymbol{M}_\mathrm{P} - \boldsymbol{\Delta}_\mathrm{C}^2$ is diagonal.

References

Ables, J. G. 1974, A&AS, 15, 383
Alissandrakis, C. E., & Lantos, P. 1996, Sol. Phys., 165, 61
Allain, M., Idier, J., & Goussard, Y. 2004, IEEE Transactions on Image Processing, submitted
Bhandari, R. 1978, A&A, 70, 331
Blake, A., & Zisserman, A. 1987, Visual reconstruction (Cambridge, MA: The MIT Press)
Bontekoe, T. R., Koper, E., & Kester, D. J. M. 1994, A&A, 284, 1037
Bouman, C. A., & Sauer, K. D. 1993, IEEE Transactions on Image Processing, 2, 296
Buck, B., & Macaulay, V. A. 1989, in Maximum Entropy and Bayesian Methods, ed. J. Skilling (Dordrecht: Kluwer Academic Publishers)
Ciuciu, P., Idier, J., & Giovannelli, J.-F. 2001, IEEE Transactions on Signal Processing, 49, 2201
Coulais, A. 1997, Ph.D. Thesis, Université de Paris VII
Daniell, G. J., & Gull, S. F. 1980, Proceedings of the IEE, 127E, 170
Demoment, G. 1989, IEEE Transactions on Acoustics, Speech and Signal Processing, ASSP-37, 2024
Dixon, D. D., Johnson, W. N., Kurfess, J. D., et al. 1996, A&AS, 120, 683
Fomalont, E. B. 1973, Proc. IEEE, Special issue on radio and radar astronomy, 61, 1211
Geman, S., & Geman, D. 1984, IEEE Transactions on Pattern Analysis and Machine Intelligence, PAMI-6, 721
Gull, S. F. 1989, in Maximum Entropy and Bayesian Methods, ed. J. Skilling (Dordrecht: Kluwer Academic Publishers), 53
Gull, S. F., & Daniell, G. J. 1978, Nature, 272, 686
Gull, S. F., & Skilling, J. 1984, Proceedings of the IEE, 131-F, 646
Hogbom 1974, A&AS, 15, 417
Hunt, B. R. 1977, IEEE Transactions on Communications, C-26, 219
Idier, J., ed. 2001a, Approche bayésienne pour les problèmes inverses (Paris: Traité IC2, Série traitement du signal et de l'image, Hermès)
Idier, J. 2001b, IEEE Transactions on Image Processing, 10, 1001
Kerdraon, A., & Delouis, J. 1997, in Coronal Physics from Radio and Space Observations, 192
Kerdraon, A., & Mercier, C. 1983, A&A, 127, 132
Komesaroff, M., Narayan, R., & Nityananda, R. 1981, A&A, 93, 269
Lannes, A., Anterrieu, E., & Maréchal, P. 1997, A&AS, 123, 183
Lantos, P., & Alissandrakis, C. E. 1996, Sol. Phys., 165, 83
Le Besnerais, G., Bercher, J.-F., & Demoment, G. 1999, IEEE Transactions on Information Theory, 45, 1565
Macaulay, V. A., & Buck, B. 1985, in Maximum Entropy and Bayesian Methods, ed. C. R. Smith, & W. T. J. Grandy
Macaulay, V. A., & Buck, B. 1994, in Maximum Entropy and Bayesian Methods, ed. J. Skilling (Dordrecht: Kluwer Academic Publishers), 59
Magain, P., Courbin, F., & Sohy, S. 1998, ApJ, 494, 472
Mohammad-Djafari, A., & Demoment, G. 1988, Traitement du Signal, 5, 235
Mohammad-Djafari, A., Giovannelli, J.-F., Demoment, G., & Idier, J. 2002, Int. J. Mass Spectrometry, 215, 175
Mugnier, L., Fusco, T., & Conan, J.-M. 2004, J. Opt. Soc. Am., 21, 1841
Narayan, R., & Nityananda, R. 1984, in Indirect Imaging, ed. J. Roberts, URSI, Australia 1983, 281
Narayan, R., & Nityananda, R. 1986, A&A, 24, 127
Nityananda, R., & Narayan, R. 1982, JA&A, 3, 419
Nocedal, J., & Wright, S. J. 2000, Numerical Optimization, Series in Operations Research (New York: Springer Verlag)
O'Sullivan, J. A. 1995, IEEE Transactions on Image Processing, 4, 1258
Pantin, E., & Starck, J.-L. 1996, A&AS, 118, 575
Phillips, D. L. 1962, J. Ass. Comput. Mach., 9, 84
Pirzkal, N., Hook, R. N., & Lucy, L. B. 2000, in ASP Conf. Ser., Astronomical Data Analysis, Software, and Systems IX, ed. N. Manset, C. Veuillet, & D. Crabtree, 216, 657
Puetter, R. C., & Yahil, A. 1999, in ADASS VIII, ASP Conf. Ser., 172, 307
Samson, V., Champagnat, F., & Giovannelli, J.-F. 2003, Detection of Point Objects with Random Subpixel Location and Unknown Amplitude, Applied Optics, Special Issue on Image processing for EO sensors

Schwartz, U. J. 1978, A&A, 65, 345
Snyder, D. L., Schulz, T. J., & O'Sullivan, J. A. 1992, IEEE Transactions on Signal Processing, 40, 1143
Soussen, C. 2000, Ph.D. Thesis, Université de Paris–Sud, Orsay, France
Starck, J.-L., Bijaoui, A., Lopez, B., & Perrier, C. 1994, A&A, 283, 349
Starck, J.-L., Murtagh, F., Querre, P., & Bonnarel, F. 2001, A&A, 368, 730
Starck, J.-L., Pantin, E., & Murtagh, F. 2002, PASP, 114, 1051
Tarantola, A. 1987, Inverse problem theory: Methods for data fitting and model parameter estimation (Amsterdam: Elsevier Science Publishers)
Thompson, A. R., Moran, J. M., & Swenson, G. W. J. 2001, Interferometry and Synthesis in Radio-astronomy (New York: Wiley (Interscience))
Tikhonov, A. 1963, Soviet. Math. Dokl., 4, 1624
Tikhonov, A., & Arsenin, V. 1977, Solutions of Ill-Posed Problems (Washington, DC: Winston)
Twomey, S. 1963, J. ACM, 10, 97
Wakker, B. P., & Schwarz, U. J. 1988, A&A, 200, 312
Weir, N. 1992, in ASP Conf. Ser., Astronomical Data Analysis, Software, and Systems I, ed. D. Worral, C. Biemesderfer, & J. Barnes, 25, 186

G. Rochefort, F. Champagnat, G. Le Besnerais et **J.-F. Giovannelli**, « Super-resolution from a sequence of undersampled images under affine motion », en révision pour *IEEE Trans. Image Processing*, 2005.

A New Observation Model for Super-Resolution under Affine Motion

Gilles Rochefort, Frédéric Champagnat, Guy Le Besnerais, and Jean-François Giovannelli

***Abstract*— Super-resolution (SR) techniques make use of sub-pixel shifts between frames in an image sequence to yield higher-resolution images. We propose an original observation model devoted to the case of non isometric inter-frame motion as required, for instance, in the context of airborne imaging sensors. First, we explicit how the main observation models used in the SR literature deal with motion, and we explain why they are not suited for non isometric motion. Then, we propose a novel observation model adapted to affine motion. This model is based on a decomposition of affine transforms into successive shear transforms, each one efficiently implemented by row-by-row or column-by-column 1-D affine transforms.**

We demonstrate on synthetic and real sequences that our observation model incorporated in a SR reconstruction technique leads to better results in the case of variable scale motions whereas it provides equivalent results in case of isometric motion.

***Index Terms*— Super-Resolution, affine motion, multi-pass interpolation, bspline, L_2 approximation, projection, inverse problems, convex regularization.**

I. Introduction

SUPER-RESOLUTION (SR) techniques aim at estimating a high-resolution image with reduced aliasing, from a sequence of low-resolution (LR) frames. The literature on the subject is abundant, see [1–6] and [7] for a recent review.

Our contribution deals with the class of "Reconstruction Based" SR techniques [8], which can be split in three steps: (1) estimation of inter-frame motion; (2) computation of a linear observation model including motion; (3) regularized inversion of the linear system.

We are interested in aerial imaging applications which often imply non isometric motion, as in the case of an airborne imager getting closer to the observed scene, see Sec. VI-C. Such non isometric motion fields can be estimated using various registration algorithms [9, 10]. Hence, step (1) is not the main issue in this context. On the other hand, the SR literature is rather allusive about step (2): most published methods implicitly assume translational motion [1, 4, 6, 8, 11–19]. To the best of our knowledge, if some former contributions apply to affine [**?**, 20] or even homographic [9][21] warps none of them explicitly deals with variable distance from scene to imager in step (2)[1]. We focus on the construction of a proper observation model for affine motions with consistent scale changes.

Section II proposes a bibliographical survey of the SR literature, with respect to the observation model. It is shown that published methods are not adapted to the context that we consider: the main difficulty is to account for non translational motion in a tractable discrete model.

Section III is devoted to the proposed new observation model that extends the popular one due to Elad and Feuer [5] by replacing traditional pointwise interpolation by techniques based on L_2 approximations [22] and shifted bspline basis. We show that our model leads to a more precise prediction of LR frame pixel values, in the case of combined zoom and rotation motion.

Further comparisons are performed on SR reconstruction results. Section IV briefly introduces the convex regularization framework that we use for SR reconstruction. Such techniques are customary in various inverse problems, including restauration and SR [2, 5, 23].

We use the resulting SR reconstruction technique to compare various observation models on synthetic (section V) and real (section VI) datasets. These experiments consistently show that our model is more accurate and reliable for sequences combining rotation and important scale changes, at the expense of a moderate increase of computational load.

II. Analysis of previous works

This section describes several published observation models different by the way they account for motion through numerical approximations.

A. Notations

Uppercase letters (resp. boldface letters) refer to matrices (resp. vectors). $\boldsymbol{n} = [n, l]^{\mathrm{t}} \in \mathbb{Z}^2$ and $\boldsymbol{i} = [i, j]^{\mathrm{t}} \in \mathbb{Z}^2$ denote discrete positions of LR and SR pixels and $\boldsymbol{u} = [u, v]^{\mathrm{t}} \in \mathbb{R}^2$ denotes real positions on the image plane. An image x can be described by a continuous field $x(\boldsymbol{u})$, or by a sequence of discrete coefficients $x[\boldsymbol{i}]$ and as lexicographycally ordered vector $\boldsymbol{x}$.

B. General observation model

Let $x(.)$ be the input irradiance field and $y[.]$ be the observed LR image. y is a sampled version of the convolution of x with an optical point spread function (PSF) h_o integrated by a box function I corresponding to the collecting surface of the detector:

$$y[\boldsymbol{n}] = \int_{\mathbb{R}^2} (h_o * x)(\boldsymbol{n}\Delta - \boldsymbol{v})\, I(\boldsymbol{v})\, \mathrm{d}\boldsymbol{v}\,,$$

with $\boldsymbol{n} \in \mathcal{G}_\Delta$. $\mathcal{G}_\Delta \subset \mathbb{Z}^2$ is the set of discrete detectors positions on a grid with step Δ. Let us denote $N = \mathrm{Card}(\mathcal{G}_\Delta)$ the number of LR pixels in frame y.

[1] It is addressed formally in [3] but not implemented nor demonstrated.

It is customary to define a joint optics-plus-detector PSF $h = h_o * I$ so that $y[\boldsymbol{n}] = h * x(\boldsymbol{n}\Delta)$.

SR methods rely on the usual "brightness constancy" assumption which is the basis of many motion estimation techniques, in particular intensity-based techniques [10]. In this framework, SR methods assume that temporally neighboring frames originate from a unique input x up to a warp modeling relative sensor / scene motion.

Let y_k $(k = 1, \ldots, K)$ denotes a neighboring frame of y, then (*i*) y_k derives from an irradiance field x_k through sensor h: $y_k[\boldsymbol{n}] = h * x_k(\boldsymbol{n}\Delta)$ and (*ii*) there is a warp w_k, such that $x_k(\boldsymbol{u}) = x(w_k(\boldsymbol{u}))$. Combination of both equalities yields

$$y_k[\boldsymbol{n}] = h * (x \circ w_k)(\boldsymbol{n}\Delta) \ . \tag{1}$$

The next step is discretization of x for the sake of numerical computations. The irradiance field x is decomposed on a shifted kernel basis:

$$x(\boldsymbol{u}) = \sum_{\boldsymbol{i} \in \mathcal{G}_{\Delta'}} x[\boldsymbol{i}]\, \varphi(\boldsymbol{u} - \boldsymbol{i}\Delta') \ . \tag{2}$$

$\mathcal{G}_{\Delta'}$ is the SR grid, with step Δ' and $M = \mathrm{Card}(\mathcal{G}_{\Delta'})$ is the number of SR pixels. The ratio $L = \Delta/\Delta'$ defines the practical magnification factor (PMF) of the SR process: it is usually greater than two. Note that it does not imply that the actual resolution improvement is as high as the PMF.

φ may be any classical interpolation kernel (box function, bilinear, ...). In the sequel, we use bspline basis, which encompass most classical interpolation schemes [24–26]. Then φ is a separable bspline kernel of order m: $\varphi(\boldsymbol{u}) = \beta^m(u)\,\beta^m(v)$, where $\beta^m(u)$ is the $(m+1)$-fold convolution of a box function.

Let us rewrite (1) as:

$$y_k[\boldsymbol{n}] = \int_{\mathbb{R}^2} x(w_k(\boldsymbol{v}))\, h(\boldsymbol{n}\Delta - \boldsymbol{v})\, \mathrm{d}\boldsymbol{v} \ . \tag{3}$$

Injecting (2) yields:

$$y_k[\boldsymbol{n}] = \sum_{\boldsymbol{i} \in \mathcal{G}_{\Delta'}} a_k[\boldsymbol{n}, \boldsymbol{i}]\, x[\boldsymbol{i}] \ ,$$

$$a_k[\boldsymbol{n}, \boldsymbol{i}] = \int_{\mathbb{R}^2} \varphi(w_k(\boldsymbol{v}) - \boldsymbol{i}\Delta')\, h(\boldsymbol{n}\Delta - \boldsymbol{v})\, \mathrm{d}\boldsymbol{v} \ . \tag{4}$$

Using lexicographically ordered vector representation of images, a matrix formulation writes:

$$\boldsymbol{y}_k = \mathrm{A}_k \boldsymbol{x} \ .$$

The whole matrix $\mathrm{A} = [\mathrm{A}_1 \ldots \mathrm{A}_K]^{\mathrm{t}}$ is huge with dimensions $KN \times M$, $M \approx NL^2$. For instance, a sequence of $K = 10$ frames, with dimensions $N = 128^2$ and a PMF $L = 2$ leads to about 43 billion elements. Of course, A_k is a sparse matrix with a band structure, as practical PSF h spreads over two or three LR pixels at most and φ is a separable bspline kernel, whose support is $(m+1)\Delta'$ wide. However, the cost of computing all non zero elements of A remains formidable for general warps w_k.

In the following, we review landmark SR papers with respect to the way they compute A. We discuss three main approaches:

1) Exact computation for special cases of $\boldsymbol{w}_k, h$ and φ
2) Approximate computation
   a) Convolve-then-Warp
   b) Warp-then-Convolve

C. Exact computation

Exact computation is tractable only in two special cases:

- motion is a global translation;
- φ and h are both box functions and motion is affine.

1) Global translation: When w_k is a global translation, (1) leads to a simple convolution. Indeed, replacing $w_k(\boldsymbol{u}) = \boldsymbol{u} - \boldsymbol{\tau}_k$ inside (4) yields:

$$a_k[\boldsymbol{n}, \boldsymbol{i}] = \varphi * h(\boldsymbol{n}\Delta - \boldsymbol{i}\Delta' - \boldsymbol{\tau}_k) \ ,$$

and the observation equation writes:

$$y_k[\boldsymbol{n}] = \sum_{\boldsymbol{i}} \varphi * h(\boldsymbol{n}L\Delta' - \boldsymbol{i}\Delta' - \boldsymbol{\tau}_k)\, x[\boldsymbol{i}] = g_k * x[\boldsymbol{n}L]$$

with $g_k(\boldsymbol{u}) = (\varphi * h)(\boldsymbol{u}\Delta' - \boldsymbol{\tau}_k)$. For integer L, each LR frame appears as a subsampled version of the discrete convolution of x with kernel g_k.

Most of the early SR literature is devoted to this case. It naturally leads to either Fourier techniques [1, 11, 12] or equivalent multi-channel filtering techniques [13] based on the generalized Papoulis theorem [27].

2) φ and h are box funtions: When φ and h are box functions [2, 3, 28], (4) is the common area between each detector and each warped SR pixel (see Fig. 1).

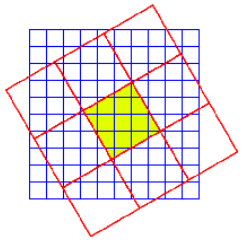

Fig. 1. φ and h are assumed box functions and motion is a rotation. The fine grid represents the grid of SR pixels, while the coarse one is the grid of detectors. Common areas between the middle detector and each SR pixel are colored.

Such an observation model has been proposed by Stark and Oskoui for rotational warps [28]. No indication is provided in their paper about the numerical computation of the relevant intersections.

Assuming affine motion, each warped SR pixel is a convex polygon, and computation of the intersection of two convex polygons can be performed by a "clipping" algorithm such as [29]. However, this technique is not suitable for SR purpose due to its high computational burden.

D. Convolve-then-Warp

Let us start back from (3). In practice, h scarcely spreads over two or three LR pixels, thus integral (3) extends on a

neighborhood $\mathcal{V}(\boldsymbol{n}\Delta)$ around $\boldsymbol{n}\Delta$. Let us assume that $w_k(\boldsymbol{u})$ can be locally approximated by a translation:

$$w_k(\boldsymbol{u}) \approx w_k(\boldsymbol{n}\Delta) + \boldsymbol{u} - \boldsymbol{n}\Delta\,, \qquad \boldsymbol{u} \in \mathcal{V}(\boldsymbol{n}\Delta)\,.$$

Then (3) can be approximated by a convolution:

$$y_k[\boldsymbol{n}] \approx (h * x)(w_k(\boldsymbol{n}\Delta))\,. \tag{5}$$

Such an approximation is depicted in Fig. 2. The center of each detector is well positioned, but the integration area is a rough approximation. Such an approximation leads to errors in the integration step for large rotations and scale variations.

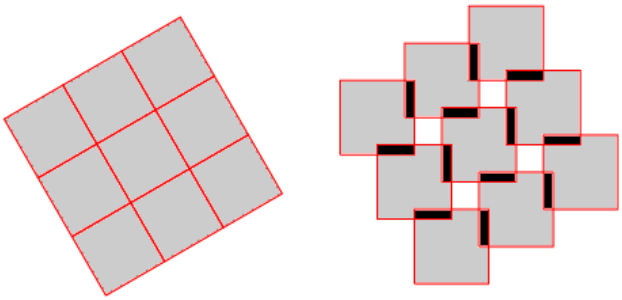

(a) Correct detector integration area.

(b) Local translation approximation of the warp and resulting detector area.

Fig. 2. llustration of the Convolve-then-Warp approximate model (5): white regions are not accounted for, gray ones are integrated once while black regions are incorrectly integrated in two detectors output.

The discretization of this model is much easier than the general model (1), because it is an irregular sampling of a convolution. The simple model of Schultz and Stevenson [2] is a special case of this approach when h and φ are both box functions and detector center positions are rounded to integer multiples of Δ'. Then, components $a_k[\boldsymbol{n},\boldsymbol{i}]$ are binary, with $a_k[\boldsymbol{n},\boldsymbol{i}] = 1$ if the $\boldsymbol{i}$-th SR pixel is inside the $\boldsymbol{n}$-th detector area, approximated as in Fig. 2(b). A refined version of this model is used in [30].

As a conclusion, this model appears computationnaly attractive but is clearly unable to correctly account for non-translational warp because of the fixed detector geometry (see Fig. 2).

E. Warp-then-Convolve

This approach consists in using the convolution relationship (1) between the data $\boldsymbol{y}_k$ and the warped SR image $x_k(\boldsymbol{u}) = x(w_k(\boldsymbol{u}))$. If a discretized version $\hat{x}_k$ of x_k over the Δ'-shifted basis functions φ is available, (1) can easily be discretized as:

$$\boldsymbol{y}_k = \mathrm{DH}\hat{\boldsymbol{x}}_k$$

where D is a down-sampling matrix, and H is the convolution matrix associated to the optical-plus-detector response.

Now the main problem is to construct $\hat{\boldsymbol{x}}_k$ using the discretized SR image coefficients $x[.]$ defined by (2). A first approach may be to enforce equality on the grid nodes:

$$\sum_{\boldsymbol{i}\in\mathcal{G}_{\Delta'}} \hat{x}_k[\boldsymbol{i}]\,\varphi((\boldsymbol{l}-\boldsymbol{i})\,\Delta') = \sum_{\boldsymbol{j}\in\mathcal{G}_{\Delta'}} x[\boldsymbol{j}]\,\varphi(w_k(\boldsymbol{l}\Delta') - \boldsymbol{j}\Delta')\,.$$

If φ is a bspline of order $m = 0$ or $m = 1$, it satisfies $\varphi((\boldsymbol{l}-\boldsymbol{i})\,\Delta) = \delta(\boldsymbol{l}-\boldsymbol{i})$, and we get:

$$\hat{x}_k[\boldsymbol{l}] = \sum_{\boldsymbol{j}\in\mathcal{G}_{\Delta'}} x[\boldsymbol{j}]\,\varphi(w_k(\boldsymbol{l}\Delta) - \boldsymbol{j}\Delta)\,. \tag{6}$$

In other words, the discrete coefficient $\hat{x}_k[\boldsymbol{l}]$ is the interpolation of x at point $w_k(\boldsymbol{l}\Delta)$. If φ is a box function ($m = 0$), (6) reduces to nearest neighbor interpolation and if φ is a triangle function ($m = 1$), (6) is bilinear interpolation.

Interpolation (6) leads to the definition of a warping matrix W_k, which summarizes all motion information. The complete image formation model is then:

$$\boldsymbol{y}_k = \mathrm{DHW}_k\boldsymbol{x}\,. \tag{7}$$

This is exactly the formulation proposed by Elad and Feuer [5, 20] referred to as "E&F" model in the following.

Fig. 3 summarizes this method: starting from the sought SR image Fig. 3(a), an intermediate high-resolution image Fig. 3(b) is constructed with a pixel grid aligned with the detector grid using either bilinear of nearest neighbor interpolation. Integration and subsampling are then straightforward.

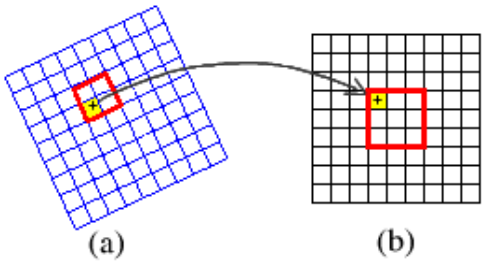

Fig. 3. Illustration of the E&F model: starting from SR image Fig. 3(a) an intermediate high-resolution image Fig. 3(b) is constructed with a pixel grid aligned with the y_k data detector grid using either bilinear of nearest neighbor interpolation.

Compared to the previous approach, the E&F model seems much more precise for rotation warps. However, one can foresee aliasing problems in the case of scale changes due to the pointwise interpolation step (6).

III. Proposed observation model

This Section introduces an original observation model extending the E&F model, by replacing pointwise interpolation (6) by a technique based on L_2 function approximation.

Dealing with variable scale using L_2 approximation technique is not easy in 2D. In this context, Catmull and Smith [31] introduced an efficient decomposition of 2D affine transforms into separable 1D transforms.

First, we will introduce such decomposition into our observation model. Next, we focus on the 1D operations in order

to achieve a L_2 approximation on a bspline basis. Finally, we will compare observation models and point out improvements provided by the proposed model.

A. Warping decomposition

Thevenaz and Unser have shown that 2D invertible affine transforms can be handled by two-shear or three-shear decompositions [22]. Each shear is a vertical or horizontal coordinate transform such as:

$$S_u(\boldsymbol{u}) = \begin{pmatrix} \alpha_2 & \beta_2 \\ 0 & 1 \end{pmatrix} \begin{pmatrix} u \\ v \end{pmatrix} + \begin{pmatrix} \varepsilon_2 \\ 0 \end{pmatrix} . \tag{8}$$

$$S_v(\boldsymbol{u}) = \begin{pmatrix} 1 & 0 \\ \beta_1 & \alpha_1 \end{pmatrix} \begin{pmatrix} u \\ v \end{pmatrix} + \begin{pmatrix} 0 \\ \varepsilon_1 \end{pmatrix} . \tag{9}$$

Both are one-dimensional affine transforms separably applied row-by-row or column-by-column. As an example, Fig. 4 provides the intermediate images resulting of each shear of the following affine motion and decomposition:

$$\begin{pmatrix} 1 & 1/4 \\ -1/4 & 7/16 \end{pmatrix} = \begin{pmatrix} 1 & 0 \\ -1/4 & 1/2 \end{pmatrix} \begin{pmatrix} 1 & 1/4 \\ 0 & 1 \end{pmatrix} . \tag{10}$$

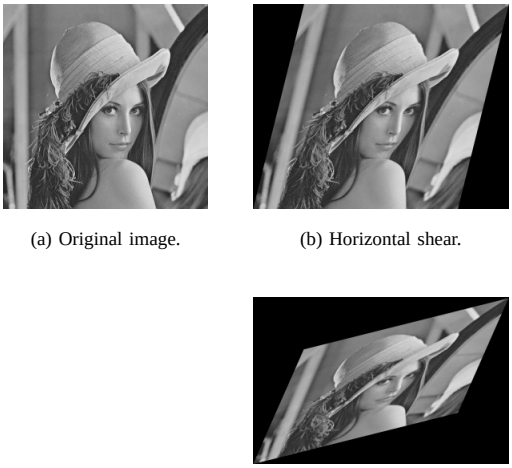

(a) Original image. (b) Horizontal shear. (c) Vertical shear.

Fig. 4. Example: the affine transform of (10) is decomposed in two steps. Each step is a shear along one coordinate image axe.

This decomposition is not unique, and the choice of one particular decomposition impacts the transformed image quality. Catmull and Smith [31] mentioned the bottleneck problem resulting from a down-scaling in one pass followed by up-scaling in the next pass, resulting in a loss of resolution.

Many approaches have been proposed to minimize image degradation, depending on the considered transform. For intance, Paeth [32] has proposed a three-shear decomposition well-suited for rotation. Other authors refer to N-pass decomposition [33].

Multi-pass interpolation techniques and their limitations are outside the scope of this article, the reader can refer to [33] for deeper insight. In the sequel, we consider only two-shear decompositions. In this case, there are two possibilities, and one selects the decomposition which reduces the involved scale variations [22, 34, 35].

B. 1D affine transform approximation

Let us consider an 1D affine transform with parameters (a, τ): $f(u) \to f((u-\tau)/a)$. With this notation, $a < 1$ yields a signal reduction and $a > 1$ yields a signal magnification. It is clear that signal reduction may result in important discretization errors (as naive subsampling undergoes a frequency aliasing).

In the line of Thevenaz *et al.* [22], let us decompose f on the 1D shifted bspline basis:

$$f(u) = \sum_{k \in \mathcal{G}_Q} f[k]\, \beta^m (u-k) , \tag{11}$$

where $\mathcal{G}_Q \subset \mathbb{Z}$ denotes the set of Q discrete samples (for instance the set of pixels of a row of the image). We search for coefficients $g[k]$, $k \in \mathcal{G}_Q$ such that g, defined by

$$g(u) = \sum_{k \in \mathcal{G}_Q} g[k]\, \beta^m (u-k) , \tag{12}$$

achieves the best approximation of $f((u-\tau)/a)$ in the L_2 sense, *i.e.* minimization of $\int [f((u-\tau)/a) - g(u)]^2 \, du$. The approximation is the orthogonal projection, and the optimal coefficients satisfy the orthogonality equations

$$\left\langle g(u) - f\left(\frac{u-\tau}{a}\right), \beta^m (u-k) \right\rangle = 0 , \tag{13}$$

for $k \in \mathcal{G}_Q$. Replacing (11) and (12) in (13) yields:

$$\sum_j g[j]\, \beta^{2m+1}[j-k] = \sum_l f[l]\, a\, \xi_a^m (k-\tau-al) ,$$

with $\beta_a^m(u) = \beta^m(u/a)/a$ and $\xi_a^m = \beta_a^m * \beta^m$. The so-called bi-kernel ξ_a^m encodes the geometric transform of a sample to a different scale space [35], and actually provides an optimal anti-aliasing filter [36]. If $a \neq 1$, ξ_a^m is not a bspline kernel, but remains a piecewise polynomial. A closed form expression of ξ_a^m is provided in [34].

Finally, the sought coefficients $g[k]$ writes:

$$g[k] = \left(\beta^{2m+1}\right)^{-1} * \left(a \sum_{l \in \mathcal{G}_Q} f[l]\, \xi_a^m (k-\tau-al) \right) , \tag{14}$$

and the inverse filter $\left(\beta^{2m+1}\right)^{-1}$ can be efficiently implemented through recursive filtering [26].

To sum up the process, given a sequence of signal samples $f(k)$ and 1D affine transform parameters (a, τ) the approximation goes through four steps:

1) compute bspline coefficients $f[k]$;
2) compute the bi-kernel function ξ_a^m;
3) compute $g[k]$ with (14) and
4) post-filter coefficients $g[k]$ to get samples values $g(k)$.

Remark 1 — *The first and the last steps are not required when the bspline representation order m is 0 or 1. Indeed,*

for these particular orders, bspline coefficients are identical to image samples.

Remark 2 — *In case of translation motion ($a = 1$), $\xi_a^m(u) = \beta^{2m+1}(u)$. The L_2 approximation then turns to a mere bspline interpolation with a higher-order kernel.*

C. A two-shear observation model

In the proposed model, the k-th observed frame $\boldsymbol{y}_k$ (in vector notation) writes:

$$\boldsymbol{y}_k = \mathrm{DHS}_1\mathrm{S}_2\hat{\boldsymbol{x}}\,,$$

where S_1 and S_2 are shear operators. Each operator is an 1D row-by-row (or column-by-column) affine transform, which is implemented as described in the previous section. In the sequel, we use an order-0 bpline kernel. Thus, as a consequence of Remark 2, our model is identical to that of Elad and Feuer with bilinear interpolation for translation motion. The resulting model is denoted TS0 for Two-Shear model with 0-order bspline basis.

D. Comparing observation models

In this section we illustrate the quality of each observation model compared to exact computation in the special case of h and φ chosen as box functions and affine motion, see Sec. II-C.

We represent the components of the observation matrix $a_k[\boldsymbol{n}, \bullet]$ for a unique LR pixel in the form of an image patch. This patch displays the weighting coefficients actually applied on SR image pixels for computing one LR detector output. The first rows of the following three arrays of patches show the exact components for rotation angles $\{0, 15, 30, 45\}$ degrees, scale variations of 1 (Fig. 5(a)), 1.2 (Fig. 5(b)) and 1.6 (Fig. 5(c)) and a PMF of 5.

The remaining patches show the approximated components obtained using Elad and Feuer models with nearest neighbor interpolation (E&F0) or with bilinear interpolation (E&F1) and the proposed model (TS0).

The Convolve-then-Warp model is not presented, but would lead to the same image patch made of a fixed size square pattern, whatever rotation and zoom factor.

Fig 5 shows that E&F0 is always incorrect even with limited rotation and/or scale variations. It is noticeable that in Fig. 5(a), some coefficients value reach two: some SR pixels (white colored) contribute twice to the detector. Such a behavior has been previously observed for the "Convolve-then-Warp" approach, see Fig. 2(b). In the same time several SR pixels do not contribute at all to the detector.

E&F1 provides a better approximation. Still, contributions of SR pixels are not uniform inside the detector footprint. This is already observed in Fig. 5(a) with rotations, and take more importance in Fig. 5(b) and Fig. 5(c) with scale factor and rotations. As E&F1 contributions appear as a smoothed version of E&F0 ones, one wonders if a bicubic interpolation (E&F3) would give correct contributions. This is not the case, as shown by Fig. 6. Moreover, as bicubic interpolation does not preserve positivity, the E&F3 model exhibits negative contributions.

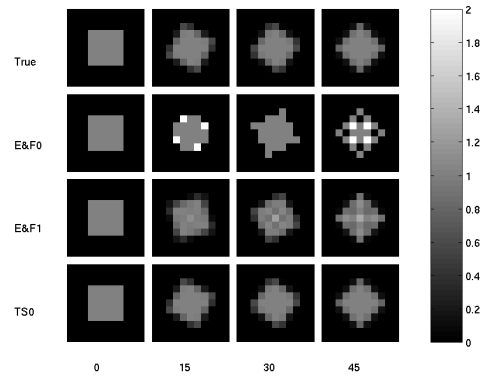

(a) scale factor 1.

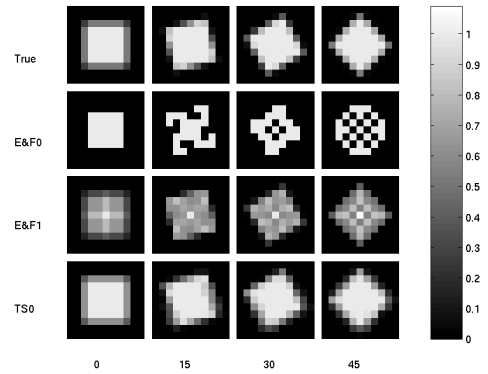

(b) scale factor 1.2.

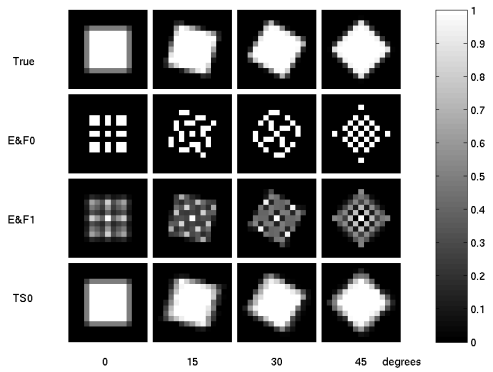

(c) scale factor 1.6.

Fig. 5. Comparing observation models: SR pixels contributions to one detector. Scale factor 1.0 5(a), 1.2 5(b) and 1.6 5(c), rotation up to 45 degrees. Models being compared came from E&F methods with order 0 (E&F0) and order 1 (E&F1) interpolation. Last line shows the proposed TS0 model, while the first line shows the true contributions.

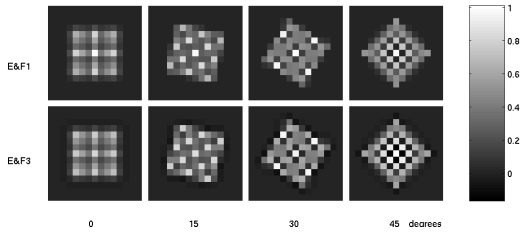

Fig. 6. Comparing E&F1 model with an Elad and Feuer model with bicubic interpolation (E&F3), Scale factor 1.6 and rotation up to 45 degrees.

Whatever the interpolation method, Elad and Feuer models become inaccurate for rotations as low as 15° and zooming factor as low as 20%.

In contrast, the TS0 observation model ensures that the contributions of SR pixels are uniform inside the detector footprint whatever rotation and/or scale factor being applied. Remaining differences between exact contributions and TS0 ones are located on the detector boundaries: TS0 contributions spread on slightly more than true ones.

IV. Regularization framework

The inversion step is tackled within a classical convex regularization framework [23] as in many other SR methods [2, 5]. The estimated SR image is the (eventually constrained) minimizer of a regularized criterion based on observation model and convex edge-preserving penalty:

$$J_\lambda(\boldsymbol{x}) = \sum_k \left\| \boldsymbol{y}_k - \mathrm{A}_k^{\mathrm{model}} \boldsymbol{x} \right\|^2 + \lambda \sum_{c \in \mathcal{C}} \psi_s\left(\boldsymbol{v}_c^t \boldsymbol{x}\right) . \quad (15)$$

The first term of criterion (15) is a least squares discrepancy between data and model output: $\mathrm{A}_k^{\mathrm{model}}$ stands for the observation model which is to be inverted and derives either from Elad and Feuer approach or from the proposed model of Sec. III. The second term is a convex penalization term [23]. $\mathcal{C}$ is the set of cliques: it consists of all subsets of three adjacent pixels either horizontal, vertical and diagonal. $\boldsymbol{v}_c$ denotes a second-order difference operator within clique c. The regularization parameter λ balances the trade-off between the two terms of the criterion. The potential ψ_s is chosen as a $\mathrm{L}_2 - \mathrm{L}_1$ hyperbolic function:

$$\psi_s(u) = 2s\left(\sqrt{s^2 + u^2} - s\right) .$$

Parameter s sets the threshold between the quadratic behavior ($u \ll s$), which allows small pixel differences smoothing and the linear behavior ($u \gg s$) aimed at preserving edges. The latter part produces a lower penalization of large differences compared to a pure quadratic function. ψ has the same qualitative behaviour as the Huber function of [2].

Finally, for a given observation model, four solutions are computed, based on:

- quadratic penalty
- quadratic penalty and positivity constraint
- hyperbolic penalty
- hyperbolic penalty and positivity constraint.

The criterion is convex by construction and has a unique global minimizer. The optimization can be achieved by iterative gradient-like techniques [37] and we resort to a limited memory BFGS algorithm[2]. It belongs to the Quasi-Newton class of algorithms which only requires evaluation of the criterion and its gradient (no second order derivative are explicitly needed) and it is known to have better convergence properties than gradient algorithms.

V. Experiments with synthetic sequences

This section presents the experiments conducted on synthetic sequences. Using synthetic sequences has two main advantages:

- Sequences are built from a reference HR image which will later be used as a reference to compare with reconstructed SR images;
- We control all parameters such as PSF, etc. Motion is known exactly too.

A. Synthetic data

To generate a sequence of LR frames, the observation matrices A_k are computed exactly according to assumptions of Sec. II-C that φ and h are box functions. As previously said, such a technique is very time consuming.

We simulate a smooth motion that is a up to 20 degrees maximum rotation, and 1.6 maximum zoom. Each frame is 128×128 and is built from a 256×256 HR reference image. In Fig. 7(a), we show the first, middle and last frame generated from reference HR image *Lena*.

(a) Lena.

(b) Mire.

Fig. 7. We show the first, middle and last frame of sequences *Lena* 7(a) and *Mire* 7(b).

[2]The implementation named VMLMB, have been provided by Éric Thiébaut (thiebaut@obs.univ-lyon1.fr).

We also generate another sequence from a bitonal calibration pattern named *Mire*. The first, middle and last image of the sequence are shown in Fig. 7(b).

B. Results

Four regularized solutions and three observation models (E&F0, E&F1 and TS0) are then available. Hence, we finally compare performances of 12 SR settings with respect to the reference HR image, by means of the PSNR (Peak Signal-to-Noise Ratio, PSNR$= 20\log_{10}(255/\sqrt{e})$, with e the mean square error). For each setting, the presented result is obtained with the best regularization parameter (*i.e.*, selected to get the highest reachable PSNR).

Let us first deal with the "Lena" sequence of Fig. 7(a). Fig. 8(a) sums up the performance levels which have been achieved. First note that, on these relatively smooth images, various regularization settings lead to similar performances, and unconstrained quadratic regularization suffices to obtain good results. On the other hand, we observe strong differences between observation models. On the average, there is an improvement from 4 dB (noisy case) up to 6 dB (no noise) between E&F0 and E&F1 models. Moreover, there is also a gain between 1 to 6 dB between E&F1 model and TS0 model.

Fig. 10 illustrates the differences between reconstructed SR images, using $\mathrm{L}_2 - \mathrm{L}_1$ regularization and positivity constraint, depending on the chosen observation model. Once again, the reconstructed images shown on the first row of Fig. 10 have been obtained with the best regularization parameters. E&F reconstructions are slightly more blurred than the SR image obtained from the proposed TS0 model. This is confirmed in the lower row which shows image error with respect to the reference HR image: TS0 observation model yields better reconstruction on high frequency areas, like the feather on the hat or the eyes.

We have also measured CPU time on a Pentium 4 at 2.66GHz. For this particular sequence, one iteration duration is respectively 2.0 and 4.6 seconds, for E&F0 and E&F1 methods. Our model requires 5.9 seconds per iteration. All methods converge roughly with the same number of iterations. Hence our method is 30% more time consuming than E&F1.

We now consider the bitonal "Mire" sequence shown in Fig. 7(b). Results are reported in Fig. 9 in terms of PSNR. As expected, this high-frequency sequence lead to much stronger differences between regularization terms and constraints.

As previously, strong differences are observed between observation models. On the average, there is a gain improvement from 5 dB (noisy case) up to 10 dB (no noise) between E&F1 model and TS0. Such improvement is due to the high contrast in *Mire* image. Indeed, we know from Sec. III-D that our observation model does not induce non homogeneous contributions in case of variable scale motion. The induced errors in the reconstructions are very much visible in high contrast areas, as shown in Fig. 11.

We also note that, in the noiseless case, hyperbolic regularization does not improve performances of E&F methods, whereas we notice a gain up to 1 dB on the average, with the TS0 model.

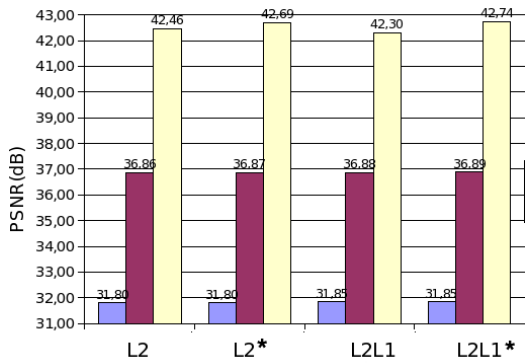

(a) No additional noise.

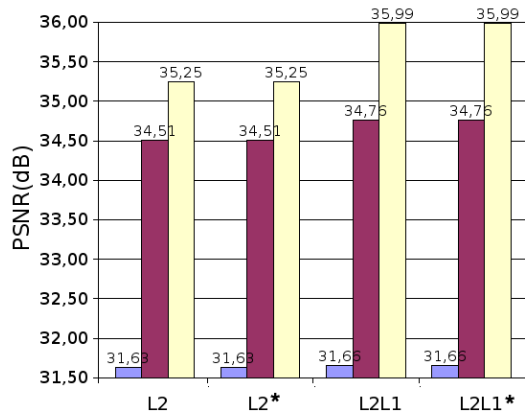

(b) Additive Gaussian noise of variance 2.

Fig. 8. SR performances on the *Lena* sequence. Three observation models (E&F0 (cyan), E&F1 (magenta) and TS0 (yellow)) and four criteria are compared. Solutions which use a positivity constraint are labelled with a star.

E&F reconstructions are much more noisy than the one obtained with the TS0 model. Let us recall that these reconstruction are obtained with a regularization parameter adjusted to get the better PSNR w.r.t. the reference HR image. The selected regularization parameter is lower (10^{-4}) with the TS0 model than with E&F models (10^{-3}). It might indicate that the more precise the model is the less it is necessary to regularize. In other words, regularization compensate for model errors which are lower with the proposed TS0 model.

By using synthetic sequences with rotational and variable scale motion, we have shown that the TS0 observation model leads to better reconstructed SR images than E&F methods, whatever the regularization involved.

As a general comment, it should be emphasized that performances are much more sensitive to a change of observation model than to a change of regularization. In other words, a good choice of the observation model leads to much higher improvement than changing the regularization term, at least in

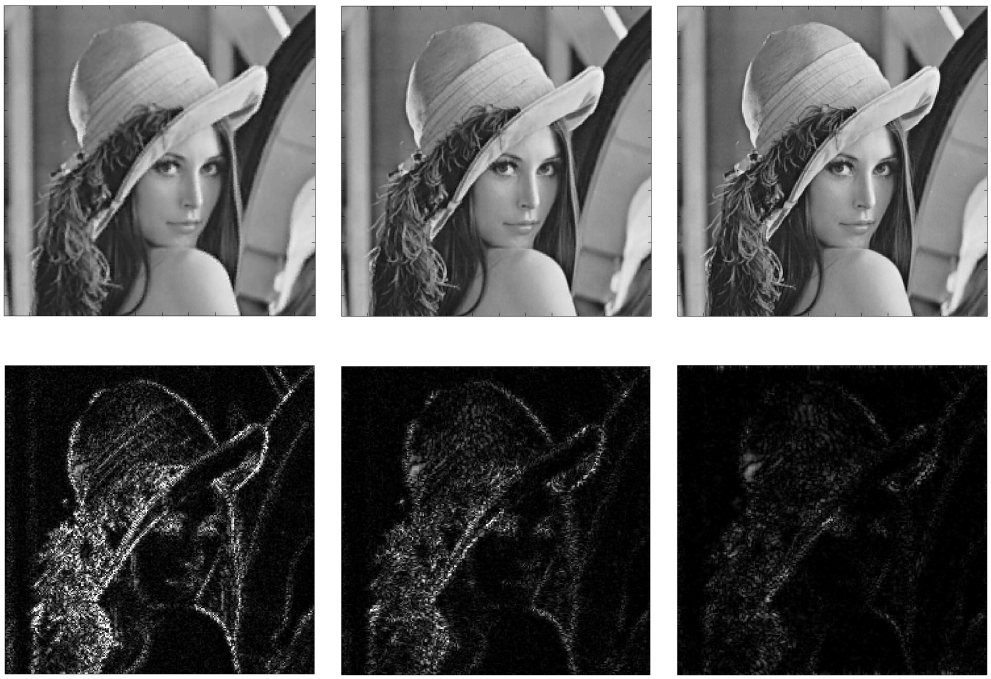

Fig. 10. First row, reconstructed SR images. From left to right: E&F0, E&F1 and TS0 observation model. All reconstructions are performed with a hyperbolic regularization and positivity constraint. Second row: differences between HR reference image and reconstructed SR images.

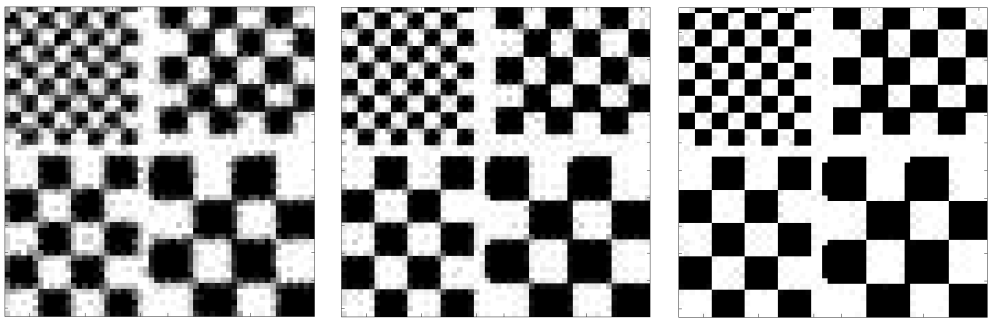

(a) E&F0. (b) E&F1. (c) TS0.

Fig. 11. Top-left parts of SR reconstructed images with hyperbolic regularization and positivity constraint. 11(a): E&F0 model, 11(b): E&F1, and 11(c): proposed TS0 model. Parameters have been adjusted to get the best PSNR w.r.t. HR reference image.

the context of rotation and scale variation explored here.

VI. Experiments on real sequences

In this section, we compare observation models on real sequences. We first discuss prior assumptions on the sequences with an emphasis on motion modelization and estimation, then we present the results obtained on two real datasets.

A. General assumptions and motion estimation

SR requires knowledge of the sensor response and of the motion field between frames. We use the common box function model for the PSF. Note that all tested observation models can accomodate more general PSF.

We restrict our experiments to affine motions between frames, since the proposed TS0 model is limited to these motion fields. Affine model accurately describes the motion of a planar scene through orthographic projection [38]. Such assumptions are usually not valid on the whole field of view (except in special purpose experiments, see VI-B), nevertheless the affine motion model is often a good local approximation of complex motion fields [9], valid in a restricted part of the image support (see an example in the aerial sequence of

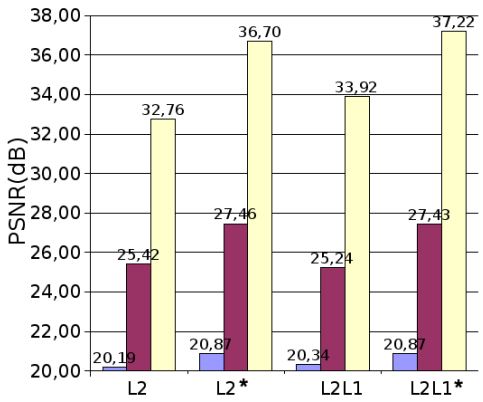

(a) No additional noise.

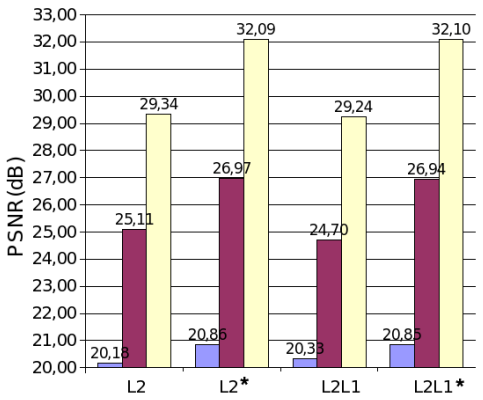

(b) Gaussian noise of variance 2.

Fig. 9. SR Performances on sequence *Mire*. Three observation models (E&F0 (cyan), E&F1 (magenta) and TS0 (yellow)) and four criteria are compared. Positivity constraint is labelled with a star.

Sec. VI-C).

We focus on sequences which exhibit large affine motions, with total zoom factor greater than 1.4 and rotations higher than 20 degrees (with inter-frame zoom up to 1.2 and rotation 5 degrees). Note that such experimental settings are not considered in the previous papers on SR, even those which address the non translational context [9, 21].

The first problem is to register each image of the sequence with respect to the reference image (usually the more resolved one). In this context, direct intensity based methods, which minimizes a DFD (displaced frame difference) criterion are subject to false local minima, even using a multiresolution approach. This is due to the sensitivity of DFD criterion with respect to large rotational and scale changes. Hence, we use a two-step approach:

1) compute a rough affine motion from scale-invariant keypoints matching;
2) refine the affine model using multiresolution DFD minimization on a restricted part of the image.

The first step uses Scale-Invariant Fast Transform (SIFT) keypoints of D. Lowe [39]. We match hundreds of keypoints between the considered frame and the reference one by SIFT descriptor correlation, then we robustly fit an affine model on selected matches using a crude rejection threshold. The second step is essentially a domestic version of the pyramidal image registration method of Thevenaz *et al.* [10].

B. Lab tests

We have made several SR experiments by using sequences of a bitonal resolution chart printed on an A4 paper sheet observed with a AVT-046B SVGA Marlin B/W camera. We acquired image sequences with variable inter-frames translation, rotation and zoom factor: some examples are shown in figure 12. Each frame of a sequence is registered with respect to the reference frame as explained in the previous section. We have run SR reconstructions with the three concurrent observation models and quadratic or hyperbolic regularization, subject to positivity constraint. For each setting, several values of the regularization parameter have been tried. Indeed, most of the time there is a certain range of (low) values of the parameter where differences between methods can easily be observed, whereas above some regularization strength, all methods become equivalent and yield an oversmoothed result.

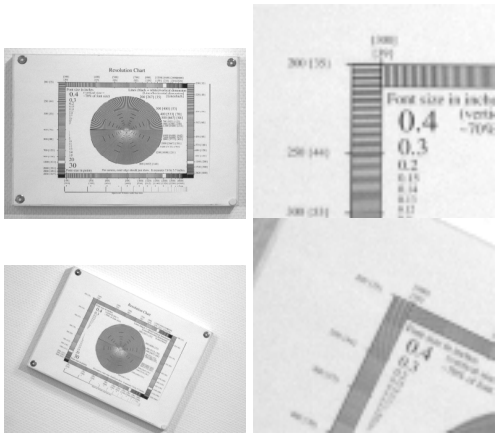

Fig. 12. A sample of frames of the resolution chart, for various rotations and zoom factors, left column shows a zoom on the region used for further SR comparison. Up: reference frame, which is the most resolved one.

As a first example, we process a purely translational sequence, using 7 frames with a PMF $L = 3$ and a quadratic regularization: comparison on a small (240×240) region is shown in figure 13, for a low value of $\lambda = 7.10^{-3}$. As expected, in this case E&F1 and TS0 lead to quasi-identical results (PSNR = 68dB) whatever the parameter λ, while E&F0 shows some instability for low λ.

Fig. 14 and Fig. 15 show compared SR results on 7 frames of a sequence with both rotation (up to 25 degrees) and zoom (there is a factor 1.5 between the reference image and the farthest view). We use either quadratic regularization

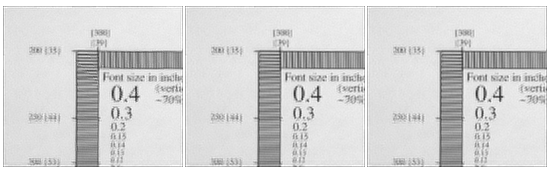

Fig. 13. Reconstruction results with PMF $L = 3$ using 7 frames with global translation motion, in an under-regularized quadratic setting, $\lambda = 7.10^{-3}$. From left to right: E&F0, E&F1 and TS0 models.

(upper part of the figures) or hyperbolic regularization with a threshold parameter $s = 10$ (lower part).

For a low value of the regularization parameter ($\lambda = 10^{-3}$ with quadratic term and $\lambda = 3.10^{-3}$ with hyperbolic regularization), see Fig. 14, E&F0 and E&F1 suffer from artifacts in the form of a pseudo-periodic texture, which is of high amplitude in E&F0 and less important, but manifest, in E&F1. Not surprisingly, this phenomenon is amplified by the hyperbolic regularization. For the same regularization parameter, TS0 does not encounter such instabilities, but exhibits ripples which are typical of an under-regularized quadratic solution, and appear amplified by the hyperbolic edge-preserving potential.

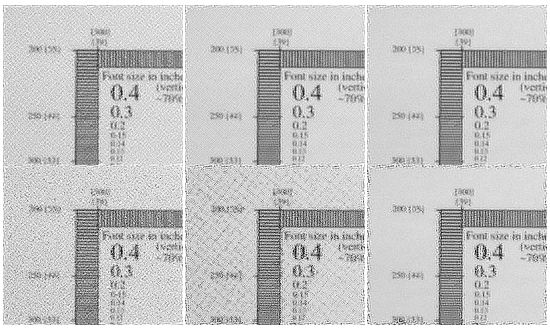

Fig. 14. Reconstruction results with PMF $L = 3$ using 7 frames with zoom and rotations, in an under-regularized setting. Up: quadratic regularization, $\lambda = 10^{-3}$; Down: hyperbolic regularization, $s = 10$, $\lambda = 3.10^{-3}$. From left to right: E&F0, E&F1 and TS0 models.

For a more balanced value of the regularization parameter, see Fig. 15, E&F0 is still clearly degraded by instabilities. E&F1 and TS0 are now very close, but a careful examination of both solutions reveals that small amplitude artifacts remain in the E&F1 reconstruction.

C. Aerial sequence

Fig. 16 displays the first and the last frames of an infrared sequence captured by an array sensor mounted on an airborne platform. As the plane gets closer to the scene, the last frame is the most resolved one and is chosen as the reference frame. The scene is a harbour with the sea and waterfront in the foreground, a building with a vertical antenna in the middle and a series of cans lined up in the background. Two ships are present in the right low part of the last frame. Because of perspective effects – the lowest part of the frame is closer to

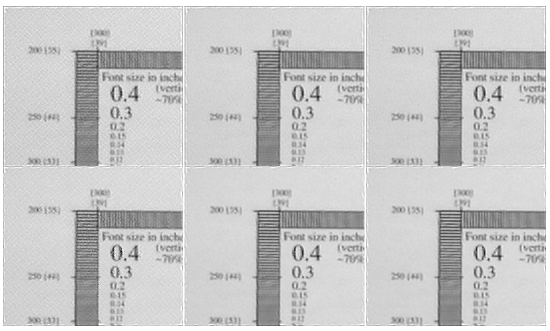

Fig. 15. Reconstruction results with PMF $L = 3$ using 7 frames with zoom and rotations, using a balanced regularization strength. Up: quadratic regularization, $\lambda = 10^{-2}$; Down: hyperbolic regularization, $s = 10$, $\lambda = 3.10^{-2}$. From left to right: E&F0, E&F1 and TS0 models.

(a) First frame. (b) Last frame.

Fig. 16. IR sequence captured by an airborne sensor, motion resuts from variable distance and small rotation.

the sensor than the upper part – apparent motion is closer to an homography than an affinity. From first frame to the refence one, the low part (resp. upper part) of the field of view is magnified with a factor about 1.4 (resp. 1.6). Therefore our method can only be applied to small regions of the frames.

Two regions are considered in the sequel: *(i)* in the upper part of the scene, the lined-up cans that remain unresolved in the reference frame (see Fig. 17) and *(ii)* in the right low part of the scene, the waterfront and the ships, see Fig. 20.

Fig. 17. Detail of the last (reference) frame. Lined-up cans zoomed up twice using bilinear interpolation. The cans are not resolved. The black vertical line in the low middle of the image is the antenna on the building seen in Fig. 16.

We considered five frames of the sequence, Fig. 16 displays two of them. As already described, motion is estimated using SIFT on the whole sequence then the intensity based method of [10] is used to refine the SIFT estimate in each region.

SR reconstruction is performed with the algorithms of

Sec. V-A, with quadratic regularization ($s = \infty$) and positivity constraint. PMF $L = 2$ along both image axis.

D. Upper region

The observation models are compared through the SR reconstructions in Fig. 18.

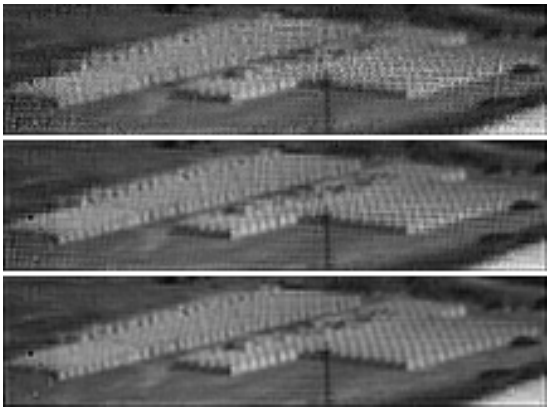

Fig. 18. Reconstructions obtained through E&F0 (top image) , E&F1 (middle image) and TS0 (bottom image) observation model. $\lambda = 5.10^{-3}$.

The image quality in Fig. 18 gradually increases from the top image (E&F0) to the bottom image (TS0 model). Even if the latter is still not a high quality image, the improvement in resolution enables the count of the right block of cans in the bottom image, whereas it is less obvious in the middle image and even impossible in the upper image. The results of Fig. 18 look somewhat oversmooth. So a lower regularization parameter has been tested, results are displayed in Fig. 19.

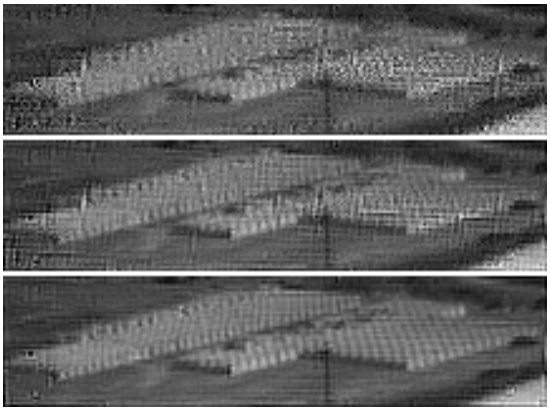

Fig. 19. Reconstructions obtained through E&F0 (top image) , E&F1 (middle image) and TS0 (bottom image) observation model. $\lambda = 1.10^{-3}$.

Fig. 19 reveals that E&F0 and E&F1 models are severely affected by the decrease of regularization parameter, whereas our model seems more robust: artifacts appear in the right top part of the scene, but cans can still be counted.

E. Right lower region

Fig. 21 proposes similar results for the ships at the right low part of the scene. The ships appear in bright contrast. A bicubic interpolation of the last observed frame is provided in Fig. 20. The top image (E&F0 model) in Fig. 21 has many

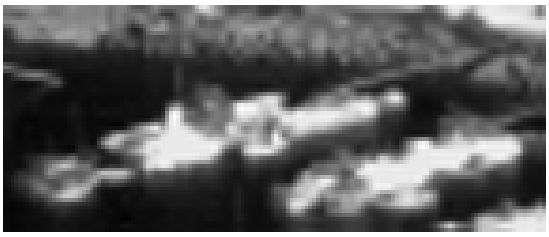

Fig. 20. Detail of the last frame of Fig. 16. Low right part of the scene: waterfront and ships zoomed up twice using bicubic interpolation.

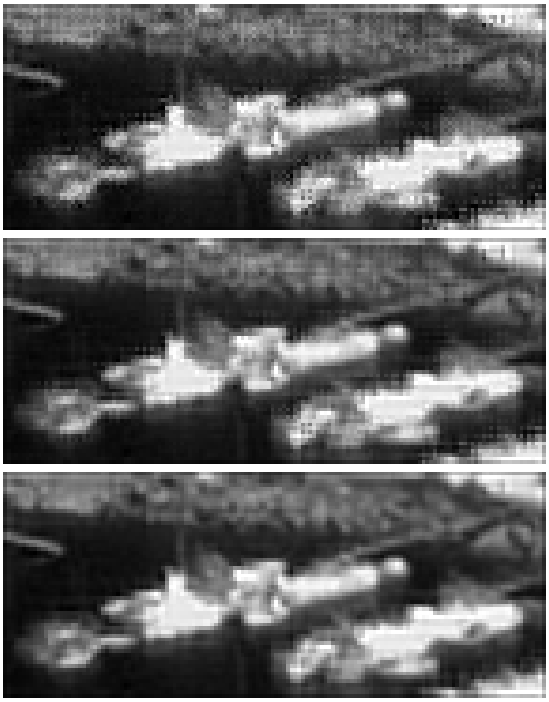

Fig. 21. Reconstructions have been performed using E&F0 (top image), E&F1 (middle image) and TS0 (bottom image) observation model. $\lambda = 10^{-2}$.

localized high frequency artifacts, part of them are absent in the middle image (E&F1 model). These artifacts are not present in the bottom image (proposed TS0 model). In the same time, comparison of SR results and Fig. 20 shows that resolution has indeed been increased.

VII. Conclusion

The presented paper deals with SR techniques in the field of aerial imagery. The proposed work focuses on the observation model in the case of an affine motion whereas the main part

of SR literature deals with the inversion process or motion estimation.

We analyzed the existing observation models used in SR reconstruction and emphasized their underlying assumptions, so as to clarify their limitations. As a result, it is shown that these observation models fall into three cateories:

- exact computation
- convolve-then-warp
- warp-then-convolve

The exact computation is not tractable for general motions. The convolve-then-warp approach is numerically efficient but is unable to capture large rotations and scale variations. So, only the third approach, due to Elad and Feuer is relevant in our framework. However, we have observed inaccuracies for rotations as low as 15° and zooming factor as low as 20%. We succeeded in extending the E&F model to cover a more important range of affine transforms with high accuracy, for about 30% more computation time. Pointwise interpolation stage in E&F method has been replaced by L_2 functional approximation techniques. This technique combines a two-shear decomposition for the affine transform and a 1D L_2 projection on a shifted bspline basis.

The proposed model has been compared with various E&F-like models. These models have been associated to several regularization settings to be tested for SR reconstruction purposes using synthetic and real image sequences.

These tests have stressed the importance of the observation model in SR reconstruction when dealing with large zoom and rotation effects. In particular the choice of a bilinear interpolation instead of a nearest-neighbor one within an Elad and Feuer setting dramatically improves the reconstructions. Moreover, the proposed model consistently achieves even better results.

Further research should be conducted to accurately deal with homographic motion, or piecewise parametric motion. It should unlock SR techniques to a larger application field.

ACKNOWLEDGMENT

The authors would like to thank Éric Thiébaut for providing an implementation of the VMLMB algorithm (see Sec. IV), used to optimize the constrained regularized criteria.

REFERENCES

[1] R. Tsai and T. Huang, "Multiframe image restoration and registration," in *Advances in Computer Vision and Image Processing*, vol. 1. JAI, 1984, pp. 317–339.

[2] R. Schultz and R. Stevenson, "Extraction of high-resolution frames from video sequences," *IEEE Transactions on Image Processing*, vol. 5, no. 6, pp. 996–1011, June 1996.

[3] A. Patti, M. Sezan, and A. Murat Tekalp, "Superresolution video reconstruction with arbitrary sampling lattices and nonzero aperture time," *IEEE Transactions on Image Processing*, vol. 6, no. 8, pp. 1064–1076, August 1997.

[4] R. C. Hardie, K. J. Barnard, and E. E. Armstrong, "Joint MAP registration and high-resolution image estimation using a sequence of undersampled images," *IEEE Transactions on Image Processing*, vol. 6, no. 12, pp. 1621–1633, December 1997.

[5] M. Elad and A. Feuer, "Restoration of a single superresolution image from several blurred, noisy, and undersampled measured images," *IEEE Transactions on Image Processing*, vol. 6, no. 12, pp. 1646–1658, Dec 1997.

[6] S. Farsiu, M. Robinson, M. Elad, and P. Milanfar, "Fast and robust multiframe super-resolution," *IEEE Transactions on Image Processing*, vol. 13, no. 10, pp. 1327–1343, October 2004.

[7] S. C. Park, M. K. Park, and M. G. Kang, "Super-resolution image reconstruction: A technical overview," *IEEE Signal Processing Magazine*, vol. 20, no. 3, pp. 21–36, May 2003.

[8] S. Baker and T. Kanade, "Limits on super-resolution and how to break them," *IEEE Transactions on Pattern Analysis and Machine Intelligence*, vol. 24, no. 9, pp. 1167–1183, September 2002.

[9] S. Mann and R. W. Picard, "Virtual bellows: Constructing high quality stills from video," in *IEEE Int. Conf. on Image Processing*, Austin, TX, 1994, pp. 363–367.

[10] P. Thévenaz, U. Ruttimann, and M. Unser, "A pyramid approach to subpixel registration based on intensity," *IEEE Transactions on Image Processing*, vol. 7, no. 1, pp. 27–41, Jan. 1998.

[11] S. Kim, N. Bose, and H. Valenzuela, "Recursive reconstruction of high resolution image from noisy undersampled multiframes," *IEEE Transactions on Acoustics, Speech and Signal Processing*, vol. 38, no. 6, pp. 1013–1027, June 1990.

[12] S. Kim and W. Su, "Recursive high-resolution reconstruction of blurred multiframe images," *IEEE Transactions on Image Processing*, vol. 2, no. 4, pp. 534–539, October 1993.

[13] H. Ur and D. Gross, "Improved resolution from sub-pixel shifted pictures." *CVGIP : Graph,Models, Image Processing*, vol. 2, no. 54, pp. 181–186, March 1992.

[14] M. Elad and Y. Hel-Or, "A fast super-resolution reconstruction algorithm for pure translationnal motion and common space-invariant blur," *IEEE Transactions on Image Processing*, vol. 10, no. 8, pp. 1187–1193, October 2001.

[15] B. C. Tom and A. K. Katsaggelos, "Reconstruction of a high-resolution image by simultaneous registration, restoration, and interpolation of low-resolution images," in *Proceedings of the International Conference on Image Processing*, Washington, D.C., 1995, pp. 2539–2542.

[16] A. Tekalp, M. Ozkan, and M. Sezan, "High-resolution image reconstruction from lowerresolution image sequences and space-varying image restoration," *IEEE Transactions on Acoustics, Speech and Signal Processing*, vol. 3, pp. 169–172, March 1992.

[17] E. Lee and M. Kang, "Regularized adaptive high-resolution image reconstruction considering inaccurate subpixel registration," *IEEE Transactions on Image Processing*, vol. 12, no. 7, pp. 526–837, July 2003.

[18] A. J. Patti and Y. Altunbasak, "Artifact reduction for set theoretic super resolution image reconstruction with edge adaptative constraints and higher-order interpolants," *IEEE Transactions on Image Processing*, vol. 10, no. 1, pp. 179–186, January 2001.

[19] N. Woods, N. Galatsanos, and A. Katsaggelos, "EM-based simultaneous registration, restoration, and interpolation of super-resolved images," in *IEEE Int. Conf. on Image Processing*, Barcelona, Spain, 2003.

[20] M. Elad and A. Feuer, "Superresolution restoration of an image sequence: Adaptive filtering approach," *IEEE Transactions on Image Processing*, vol. 8, no. 3, pp. 387–395, March 1999.

[21] S. Lertrattanapanich and N. K. Bose, "High resolution image formation from low resolution frames using delaunay triangulation," *IEEE Transactions on Image Processing*, vol. 11, no. 12, pp. 1427–1441, Dec. 2002.

[22] P. Thévenaz and M. Unser, "Separable least-squares decomposition of affine transformations," in *Proceedings of the 1997 IEEE International Conference on Image Processing (ICIP'97)*, Santa Barbara CA, USA, October 1997.

[23] J. Idier, "Convex half-quadratic criteria and interacting auxiliary variables for image restoration," *IEEE Transactions on Image Processing*, vol. 10, pp. 1001–1009, July 2001.

[24] H. Curry and I. Schoenberg, "On spline distributions and their limits: The polya distribution functions," *Bull. Amer. Math. Soc.*, vol. 53, no. 1114, 1947.

[25] M. Unser, A. Aldroubi, and M. Eden, "B-Spline signal processing: Part I—Theory," *IEEE Transactions on Signal Processing*, vol. 41, no. 2, pp. 821–833, February 1993.

[26] ——, "B-Spline signal processing: Part II—Efficient design and applications," *IEEE Transactions on Signal Processing*, vol. 41, no. 2, pp. 834–848, February 1993.

[27] A. Papoulis, *Signal Analysis*. New-York: McGraw-Hill, 1977.

[28] H. Stark and P. Oskoui, "High-resolution image recovery from image-plane arrays, using convex projections," *JOSA*, vol. 6, no. 11, pp. 1715–1726, Novembre 1989.

[29] I. Sutherland and G. Hodgman, "Reentrant polygon clipping," *Communication of the ACM*, vol. 17, pp. 32–42, 1974.

[30] M. Irani and S. Peleg, "Improving resolution by image registration," *Computer Vision and Graphics and Image Processing*, vol. 52, no. 3, pp. 231–239, May 1991.
[31] E. Catmull and A. Smith, "3D-transformations of images in scanline order," *Computer Graphics (SIGGRAPH '80 Proceedings)*, vol. 14, no. 3, pp. 279–285, July 1980.
[32] A. Paeth, "A fast algorithm for general raster rotation," *Proc. Graphics Interface*, pp. 77–81, 1986.
[33] D. Fraser and R. Schowengerdt, "Avoidance of additional aliasing in multipass image rotations," *IEEE Transactions on Image Processing*, vol. 6, no. 3, pp. 721–735, November 1994.
[34] S. Horbelt, "Spline and wavelets for image warping and projection," Ph.D. dissertation, Swiss Federal Institute of Technology Lausanne (EPFL), May 2001, EPFL Thesis no. 2397 (2001), 131 p.
[35] A. Muñoz Barrutia, T. Blu, and M. Unser, "Least-squares image resizing using finite differences," *IEEE Transactions on Image Processing*, vol. 10, no. 9, pp. 1365–1378, September 2001.
[36] M. Unser, A. Aldroubi, and M. Eden, "Enlargement or reduction of digital images with minimum loss of information," *IEEE Transactions on Image Processing*, vol. 4, no. 3, pp. 247–258, March 1995.
[37] J. Nocedal and S. J. Wright, *Numerical Optimization*. New York: Springer-Verlag, 1999.
[38] J. L. Mundy and A. Zisserman, Eds., *Geometric Invariants in Computer Vision*. Cambridge (MA), USA: MIT Press, 1992.
[39] D. G. Lowe, "Distinctive image features from scale invariant keypoints," *International Journal of Computer Vision*, vol. 60, no. 2, pp. 91–110, 2004.

R. Boubertakh, **J.-F. Giovannelli**, A. De Cesare et A. Herment, « Regularized reconstruction of MR images from sparse acquisitions », à paraître dans *Signal Processing* janvier 2004.

Regularized Reconstruction of MR Images from Spiral Acquisitions

R. Boubertakh[a,c], J-.F. Giovannelli[b], A. De Cesare[a] and A. Herment[a]

[a] *U494 INSERM, CHU Piti-Salptrire, 91 boulevard de l'Hpital, F-75634 Paris Cedex 13, France.*

[b] *Laboratoire des Signaux et Systmes, Suplec, Plateau de Moulon, 91192 Gif-sur-Yvette Cedex, France.*

[c] *Division of Imaging Sciences, Thomas Guy House Guy's Hospital, Kings College London, London, SE1 9RT, United Kingdom.*

Abstract

Combining fast MR acquisition sequences and high resolution imaging is a major issue in dynamic imaging. Reducing the acquisition time can be achieved by using non-Cartesian and sparse acquisitions. The reconstruction of MR images from these measurements is generally carried out using gridding that interpolates the missing data to obtain a dense Cartesian k-space filling. The MR image is then reconstructed using a conventional Fast Fourier Transform (FFT). The estimation of the missing data unavoidably introduces artifacts in the image that remain difficult to quantify.

A general reconstruction method is proposed to take into account these limitations. It can be applied to any sampling trajectory in k-space, Cartesian or not, and specifically takes into account the exact location of the measured data, without making any interpolation of the missing data in k-space. Information about the expected characteristics of the imaged object is introduced to preserve the spatial resolution and improve the signal to noise ratio in a regularization framework. The reconstructed image is obtained by minimizing a non-quadratic convex objective function. An original rewriting of this criterion is shown to strongly improve the reconstruction efficiency. Results on simulated data and on a real spiral acquisition are presented and discussed.

Key words: Fast MRI, Fourier synthesis, inverse problems, regularization, edge-preservation.

1 Introduction

In Magnetic Resonance Imaging (MRI) the acquired data are samples of the Fourier transform of the imaged object [1]. Acquisition is often discussed in terms of location in k-space and most conventional methods collect data on a regular Cartesian grid. This allows for a straightforward characterization of aliasing and Gibbs artifacts, and permits direct image reconstruction by means of 2D-Fast Fourier Transform (FFT) algorithms. Other acquisition sequences, such as spiral [2], PROPELLER [3], projection reconstruction, *i.e.* radial [4], rosette [5], collect data on a non-Cartesian grid. They possess many desirable properties, including reduction of the acquisition time and of various motion artifacts. The gridding procedure associated to an FFT is the most common method for Cartesian image reconstruction from such irregular k-space acquisitions.

Preprint submitted to Elsevier Science *12 October 2005*

Re-gridding data from non-Cartesian locations to a Cartesian grid has been addressed by many authors. O'Sullivan [6] introduced a convolution-interpolation technique in computerized tomography (CT) which can be applied to magnetic resonance imaging [2]. He suggested not to use a direct reconstruction, but to perform a convolution-interpolation of the data sampled on a polar pattern onto a Cartesian k-space. The final image was obtained by FFT. The stressed advantage of this technique was the reduction of computational complexity compared to the filtered back-projection technique. Moreover, it can be applied to any arbitrary trajectory in k-space.

More generally, the reconstruction process is four steps:

(1) data weighting for nonuniform sampling compensation,
(2) re-sampling onto a Cartesian grid, using a given kernel,
(3) computation of the FFT,
(4) correction for the kernel apodization.

Jackson *et al.* [7] precisely discussed criteria to choose an appropriate convolution kernel. This is necessary for accurate interpolation and also for minimization of reconstruction errors due to uneven weighting of k-space. Several authors have suggested methods for calculating this sampling density. Numerical solutions have been proposed that iteratively calculate the compensation weights [3]. But, for arbitrary trajectories, the weighting function is not known analytically and must somehow be extracted from the sampling function itself. A possible solution is to use the area of the Voronoi cell around each sample [8].

The gridding method is computationally efficient. However, convolution-interpolation methods unavoidably introduce artifacts in the reconstructed images [8]. Indeed, for a given kernel the convolution modifies data in k-space and it is difficult to know the exact effect of gridding in the image domain. Moreover, this method tends to correlate the noise in the measured samples and lacks solid analysis and design tools to quantify or minimize the reconstruction errors.

The principle of regularized reconstruction has been described by several authors for parallel imaging: [9], [10] and more recently [11] proposed the use of a general reconstruction method for sensitivity encoding (SENSE) [12] which has been applied with a quadratic regularization term and a Cartesian acquisition scheme. In this paper, we extend this work by: 1) giving a more general formulation of the reconstruction term for Non Cartesian trajectories, 2) specifically using the exact non-uniform locations of the acquired data in k-space, without the need for gridding the data to a uniform Cartesian grid and, 3) incorporate a non–quadratic convex regularization term in order to maintain edge sharpness compared to a purely quadratic term. The regularization term represents the prior information about the imaged object that improves the signal to noise ratio (SNR) of the reconstructed image as well as the spatial resolution.

In section 2, we recall the basis of MRI signal acquisition and the modelling of the MR acquisition process. Then we address the image reconstruction methods for different acquisition schemes and develop the proposed method, in section 3. The reconstruction is based on the iterative optimization of a Discrete Fourier Transform (DFT) regularized criterion. Rewriting this criterion allows to reduce the complexity of the computation and to decrease the reconstruction time. Finally, section 4 compares the proposed method and the gridding reconstruction for simulated and real sparse data acquired along interleaved spiral trajectories.

2 Direct model

MRI theory [1] indicates that the acquired signal s is related to the imaged object f through:

$$s(\boldsymbol{k}(t)) = \iint_D f(\boldsymbol{r})\, \mathrm{e}^{i2\pi \boldsymbol{k}(t)^{\mathrm{t}} \boldsymbol{r}}\, \mathrm{d}\boldsymbol{r}\,, \qquad (1)$$

in a 2D context. D is the field of view, *i.e.*, the extent of the imaged object, $\boldsymbol{r}$ is the spatial vector and $\boldsymbol{k}(t) = [k_x(t), k_y(t)]^{\mathrm{t}}$ ("t" denotes a transpose) is the k-space trajectory. Thus, the received signal can be thought as the Fourier transform of the object, along a trajectory $\boldsymbol{k}(t)$ determined by the magnetic gradient field $\boldsymbol{G}(t) = [G_x(t), G_y(t)]^{\mathrm{t}}$:

$$\boldsymbol{k}(t) = \gamma \int_0^t \boldsymbol{G}(t')\, \mathrm{d}t'.$$

The modulus of $f(\boldsymbol{r})$ is proportional to the spin density function and the phase factor is influenced by spin motions and magnetic field inhomogeneities.

Remark 1 — *Eq. (1) presents a model for an ideal signal. Actual signals also include terms for the relaxation of the magnetic moments which will cause the signal amplitude to decrease, as well as a term for inhomogeneity within the image. By the way, they could be easily incorporated in (1), but for our purposes here we will ignore these effects.*

Practically, the acquired signal is not a continuous function of time but made of a finite number of samples. This introduces the discretization of the data, and the measured data set writes $\boldsymbol{s} = [s_0, s_1, \ldots, s_{L-1}]^{\mathrm{t}} \in \mathbb{C}^L$, *i.e.*, consists of L data sampled along the discrete trajectory $[\boldsymbol{k}_0, \boldsymbol{k}_1, \ldots, \boldsymbol{k}_{L-1}]$, where $\boldsymbol{k}_l = [k_x^l, k_y^l]^{\mathrm{t}}$. For a single sample, Eq. (1) then reads:

$$s_l = \iint_D f(\boldsymbol{r})\, \mathrm{e}^{i2\pi \boldsymbol{k}_l^{\mathrm{t}} \boldsymbol{r}}\, \mathrm{d}\boldsymbol{r}\,.$$

Generally the object f is not reconstructed as a continuous function of the spatial variables $\boldsymbol{r}$ but is also discretized for practical considerations: to use image visualization and also to perform fast reconstruction techniques by means of FFT. This introduces a discretization of the unknown object and a common choice is a Cartesian grid of size $N \times N$. We note $f_{n,m}$ the unknown discretized object evaluated at locations $\boldsymbol{r}_{nm} = [n, m]^{\mathrm{t}}$ with $n, m = 0, 1, \ldots, N-1$.

The discrete model is then given by an approximation of the integral of Eq. (1):

$$s_l = \frac{1}{N} \sum_{n,m=0}^{N-1} f_{n,m}\, \mathrm{e}^{i2\pi\left(k_x^l m/F_x + k_y^l n/F_y\right)}$$

where $\boldsymbol{F} = [F_x, F_y]^{\mathrm{t}}$ is the spatial sampling frequency of the object. To comply with the Shannon sampling frequency, $\boldsymbol{F}$ must be chosen such as $F_x \geq 2/D_x$ and $F_y \geq 2/D_y$, where D_x and D_y are the dimensions of the field of view. For sake of simplicity we assume here that $\boldsymbol{F} = [1, 1]^{\mathrm{t}}$ and the spatial frequencies k_x^l and k_y^l are normalized and lie in $[-0.5, +0.5]$.

In practice the acquired samples are corrupted by a complex valued noise, denoted $\boldsymbol{b} = [b_0, \ldots, b_{L-1}]^{\mathrm{t}} \in \mathbb{C}^L$, which can be assumed to be additive white and Gaussian [13].

We can then write, for one datum, the final discretized model as:

$$s_l = \frac{1}{N} \sum_{n,m=0}^{N-1} f_{n,m}\, \mathrm{e}^{i2\pi(k_x^l m + k_y^l n)} + b_l \qquad (2)$$

for $l = 0, \ldots, L-1$ or, more simply as

$$s_l = \boldsymbol{h}_l \boldsymbol{f} + b_l\,,$$

with $\boldsymbol{f}$ being a column vector, collecting the $f_{n,m}$ rearranged column by column in one vector, and $\boldsymbol{h}_l$ a row vector

$$\boldsymbol{h}_l = \frac{1}{N}\left[\mathrm{e}^{i2\pi \boldsymbol{k}_l^{\mathrm{t}} \boldsymbol{r}_{00}}, \mathrm{e}^{i2\pi \boldsymbol{k}_l^{\mathrm{t}} \boldsymbol{r}_{01}}, \ldots, \mathrm{e}^{i2\pi \boldsymbol{k}_l^{\mathrm{t}} \boldsymbol{r}_{N-1,N-1}}\right].$$

The whole data vector then writes:

$$\boldsymbol{s} = H\boldsymbol{f} + \boldsymbol{b}, \qquad (3)$$

where H is the inverse Fourier matrix:

$$H = \begin{pmatrix} \boldsymbol{h}_0 \\ \hline \boldsymbol{h}_1 \\ \hline \vdots \\ \hline \boldsymbol{h}_{L-1} \end{pmatrix},$$

depending on the acquisition locations.

Eq. (3) is a linear model with additive Gaussian noise. It has been extensively studied in literature [14]. The aim of the reconstruction process is to compute an estimate $\widehat{\boldsymbol{f}}$ of the unknown object $\boldsymbol{f}$ from the discrete, incomplete and noisy k-space samples $\boldsymbol{s}$. The problem is referred to as a Fourier synthesis problem and consists of inversion of the model (3).

3 Model inversion

A usual inversion method relies on a Least Squares (LS) criterion, based on Eq. (3):

$$\mathcal{J}_{\mathrm{LS}}(\boldsymbol{f}) = ||\boldsymbol{s} - H\boldsymbol{f}||^2 = \sum_{l=0}^{L-1} |s_l - \boldsymbol{h}_l \boldsymbol{f}|^2\,. \qquad (4)$$

The reconstructed image is the minimizer of $\mathcal{J}_{\mathrm{LS}}$:

$$\widehat{\boldsymbol{f}}_{\mathrm{LS}} = \arg\min_{\boldsymbol{f}} \mathcal{J}_{\mathrm{LS}}(\boldsymbol{f})\,,$$

and minimizes the quadratic error between the measured data and the estimated ones generated by the direct model (3). The solution writes:

$$\widehat{\boldsymbol{f}}_{\mathrm{LS}} = (H^{\dagger}H)^{-1}H^{\dagger}\boldsymbol{s}\,,$$

if $H^{\dagger}H$ is invertible, property that depends on the acquisition scheme.

3.1 Cartesian and complete acquisitions

In *Complete Cartesian (CC)* acquisitions H is the $N \times N$ inverse Fourier transform matrix, evaluated on an uniform grid. We then have $H^{\dagger}H = I$ and the LS solution simplifies to

$$\widehat{f} = H^{\dagger}\boldsymbol{s}. \tag{5}$$

It is efficiently computed by the FFT of the raw data and the compromise between acquisition time and image characteristics depends only on the acquisition scheme.

This inversion method directly holds as long as a complete Cartesian k-space is available as for the conventional line by line acquisitions where one line is acquired for each successive radio-frequency (rf) excitation. It holds also for multi-shot acquisitions when more than a single k-space line is acquired for each rf excitation. It can finally be applied to EPI sequences when only one excitation is used to sample the whole k-space domain.

The method remains convenient for time segmented acquisitions that update only partially k-space, such as keyhole, BRISK or TRICKS techniques [15–18] provided that a convenient filling of k-space data has been made previously.

3.2 Incomplete and non Cartesian acquisitions

Other acquisition schemes have been proposed in order to reduce acquisition time. They can be divided in two groups: *Incomplete Cartesian (IC)* ones and *Non Cartesian (NC)* ones.

IC - Partial Cartesian filling of a k-space such as the widely used "half Fourier" method [19] or variable density phase encoding technique [20] allow to reduce the number of acquired data and thus the acquisition time. In this case, H is a partial matrix and can still be computed with the FFT.

NC - Non Cartesian k-space filling (interleaved spirals, PROPELLER sequence, radial, concentric circles, rosettes...) conjugate a variable, non–uniform density encoding with specific gradient sequences with the same objective of acquisition time reduction. These acquisition schemes often require a small number of rf pulses, take advantage of the available gradient strength and rising time, reduce motion artifacts and lessen sensitivity to off-resonances and field inhomogeneities [2].

From a mathematical stand point, the main difficulty of the Non Cartesian acquisition schemes is that (5) cannot be computed using the FFT algorithm, since the samples are no longer on a uniform grid. Current strategies force the re-use of FFT reconstruction (5) by means of data pre-processing.

IC - The missing data are completed beforehand using Fourier symmetry properties of the k-space [19] (see also the Margosian reconstruction [21]), or a zero-padding extrapolation. Conventional zero padding used to construct a square image from a rectangular acquisition matrix also belongs to this category.

NC - The acquired data are interpolated and resampled by means of a gridding method.

Thus a complete Cartesian k-space is pre-computed from the acquired data and the final image is obtained by FFT. The wide availability of high-speed FFT routines and processors have made the method by far the most popular. But, such methods do not rely on the physical model (3) nor on the true acquired data: they introduce interpolated data resulting in inaccuracies in the reconstructed images. On the contrary, the proposed method accounts for exact locations of the data in k-space. The methodology is applicable for both *IC* and *NC* acquisition scheme and we concentrate on the *NC* case *i.e.* the non-uniform DFT model.

Other strategies rely on true DFT and LS framework. The main problem here is that $H^{\dagger}H$ is not invertible: the unknown image pixels usually outnumber

the acquired data and the problem is indeterminate, *i.e.*, $\mathcal{J}_{\text{LS}}$ does not have a unique minimizer. From basic inverse problem theory, several regularization approaches have been proposed. Among the earliest are the Truncated Singular Value Decomposition (TSVD) and the Minimum Norm Least Squares (MNLS). They properly regularize the problem, alleviate the indeterminacy and define a solution to (3). The TSVD and the MNLS approaches have been proposed in MRI by [20] for *IC* acquisition and by [22,23] for *NC* acquisitions, respectively. Practically they both can be extended for *IC* and *NC* acquisitions and behave similarly.

In any case (TSVD, MNLS, gridding, zero-padding), it is difficult to control the information accounted for, in order to regularize the problem. Moreover they cannot incorporate more specific information such as pixel correlation, and edge enhancement. The proposed method, described below, accounts for known common information about the expected images and exact locations of the data in the k-space.

3.3 Regularized Method

The proposed method relies on Regularized Least Squares (RLS) criterion:

$$\mathcal{J}_{\text{Reg}}(\boldsymbol{f}) = \mathcal{J}_{\text{LS}}(\boldsymbol{f}) + \mathcal{R}(\boldsymbol{f}).$$

It is based on the LS term and a *prior* one $\mathcal{R}$, that only depends upon the object $\boldsymbol{f}$. The proposed solution writes:

$$\widehat{\boldsymbol{f}}_{\text{Reg}} = \arg\min_{\boldsymbol{f}} \mathcal{J}_{\text{Reg}}(\boldsymbol{f}) \,.$$

The choice of $\mathcal{R}$ depends on the information to be introduced. In MR, there are a great variety of image kinds, but at least two common characteristics are observed.

(1) The structure have usually smooth variations and a good contrast compared to the surrounding organs, more particularly when contrast agents are used. These regions are separated by sharp transitions representing the edges.
(2) The regions outside the imaged object *i.e.* the background is a region where $\boldsymbol{f}$ is expected to be zero.

The proposed regularization term accounts for these information and takes the following form:

$$\mathcal{R}(\boldsymbol{f}) = \lambda_1 \Omega_1(\boldsymbol{f}) + \lambda_0 \Omega_0(\boldsymbol{f}).$$

λ_1 and λ_0 are the regularization parameters (hyperparameters) that balance the trade-off between the fit to the data and the prior. One can clearly see that $\lambda_1 = \lambda_0 = 0$ gives the LS criterion, and no information about the object is accounted for. On the contrary, when $\lambda_1, \lambda_0 \to \infty$ the solution is only based on the *a priori* information.

The first term $\Omega_1(\boldsymbol{f})$ is an edge-preserving smoothness term based on the first order pixel differences in the two spatial directions:

$$\begin{aligned}\Omega_1(\boldsymbol{f}) &= \sum_{n,m} \varphi_{\alpha_1}(f_{n+1,m} - f_{n,m}) \\ &\quad + \sum_{n,m} \varphi_{\alpha_1}(f_{n,m+1} - f_{n,m}) \,,\end{aligned}$$

and the second one $\Omega_0(\boldsymbol{f})$ introduces the penalization for the image background:

$$\Omega_0(\boldsymbol{f}) = \sum_{n,m} \varphi_{\alpha_0}(f_{n,m}) \,.$$

The penalization functions φ_α parametrized by the coefficient α (discussed below) determine the characteristics of the reconstruction and has been addressed by many authors [24–28].

Interesting edge-preserving functions are those with a flat asymptotic behaviour towards infinity, such as the Blake and Zisserman function [27] or Geman and McClure [28]. However these functions are not convex and the resulting regularized criterion may present numerous local minima. Its optimization therefore requires complex and time-consuming techniques. On the contrary, the quadratic function proposed by Hunt [25]: $\varphi(x) = x^2$ is best suited to fast optimization algorithms. Nevertheless, it tends to introduce strong penalizations for large transitions (see Fig. 1), which may over-smooth discontinuities. An interesting trade-off can be achieved by using a combination between a quadratic function (L_2) to smooth small pixel differences and a linear function (L_1) for large pixel differences beyond a defined threshold α. The latter part produces a lower penalization of large differences

compared to a pure quadratic function. So, we chose the Huber function [29] (see Fig. 1)

$$\varphi_\alpha(x) = \begin{cases} x^2 & \text{if } |x| \leq \alpha \\ 2\alpha|x| - \alpha^2 & \text{elsewhere} \end{cases}$$

which is convex and gives an acceptable modeling of the desired image properties. The α parameter tunes the trade-off between the quadratic and the linear part of the function.

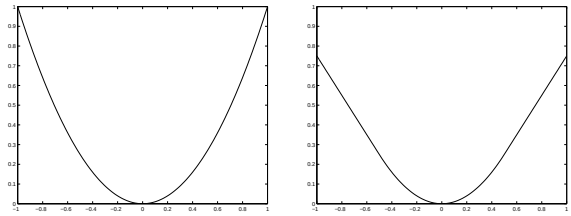

Fig. 1. Penalization functions φ: quadratic (lhs) and Huber (rhs).

The criterion $\mathcal{J}_{\text{Reg}}$ is convex by construction and presents a unique global minimum: the optimization can be achieved by iterative gradient-like optimization techniques and we have implemented a pseudo-conjugate gradient procedure with a Polak-Ribiéres correction method [30].

3.4 Optimization Stage

The optimization process requires numerous evaluation of $\mathcal{J}_{\text{Reg}}$ and its gradient hence numerous non-uniform DFT computations. In order to avoid these computations, $\mathcal{J}_{\text{LS}}$ is rewritten, without changing the formulation of the problem. The new expression is founded on Toeplitz property of $H^\dagger H$ and reads (see Appendix for details):

$$\mathcal{J}_{\text{LS}}(\boldsymbol{f}) = \sum_{l=0}^{L-1} |s_l|^2 - 2\Re\left\{\sum_{n,m=0}^{N-1} f^*_{n,m}\, D_{n,m}\right\} + \sum_{u,v=1-N}^{N-1} C_{u,v}\, G_{u,v} \tag{6}$$

where C is the image correlation matrix, computable by FFT. D and G are given by:

$$D_{n,m} = \frac{1}{N}\sum_{l=0}^{L-1} s_l\, \mathrm{e}^{-i2\pi(k_x^l m + k_y^l n)} \tag{7}$$

$$G_{u,v} = \frac{1}{N^2}\sum_{l=0}^{L-1} \mathrm{e}^{i2\pi(k_x^l u + k_y^l v)} \tag{8}$$

for $n, m = 0, \cdots, N-1$ and $u, v = 1-N, \cdots, N-1$ and can be precomputed before the optimization stage.

The $2N-1 \times 2N-1$ matrix G depends on the k-space trajectory only and can be computed once for all, given a trajectory. Moreover, it has a Hermitian symmetry, $G^\dagger = G$, which allows to compute only one half of the matrix. The $N \times N$ matrix D depends on the k-space trajectory and on the measured data. It can then be precomputed, but must be recomputed with each new data set.

The new expression allows to reduce the computational complexity of the optimization stage: instead of one DFT computation at each iteration, only one precomputed DFT is required, the criterion and its gradient can be computed from D and G by means of usual products and FFT.

The gradient using a matrix formulation, is given then as (see also Appendix for details):

$$\frac{\partial \mathcal{J}_{\text{LS}}(\boldsymbol{f})}{\partial \boldsymbol{f}} = 2f \star G - 2D.$$

where $\star$ is a bidimentional convolution efficiently computed by FFT.

4 Simulation and acquisition results

In this section the proposed reconstruction method is compared to the gridding method on a mathematical model and a real phantom both acquired using a spiral sequence.

4.1 Simulated model

The simulated model is a 128×128 complex valued image and mimics two vessels on a variable background. The magnitude image includes homogeneous

regions and sharp transitions, while the phase image, related to the velocity image, corresponds to a parabolic and a blunt flow profi le on a zero phase background (see Fig. 2).

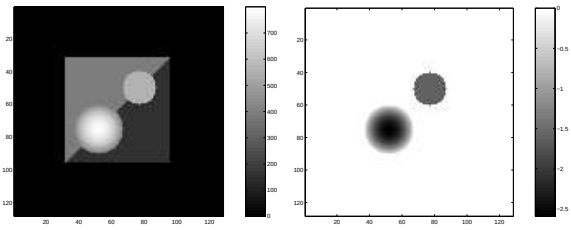

Fig. 2. Simulated phantom: magnitude image on the left-hand side (lhs) and phase image on the right-hand side (rhs). We have selected two ROIs: ROI1 is the central square and ROI2 is the blunt fbw area (upper right circle).

For the direct problem, *i.e* simulating the acquired data, the exact model has been used without any approximation, which allows to compute the value of the k-space data along any sampling trajectory. A data set of 6 spiral arms of 512 samples each have been simulated, thus the number of samples (6×512) was 5 folds less than the number of pixels (128×128). The reduced number of samples and their very irregular density makes the reconstruction problem non invertible and thus allowed to test the quality of the regularized reconstruction in the case of sparse data.

The hyperparameters, chosen empirically to obtain the best possible reconstruction, have been set to following values: $\lambda_1 = 0.1$, $\alpha_1 = 20$, $\lambda_0 = 0.5$ and $\alpha_0 = 10$ and were then also used for the phantom reconstruction. A 7×7 Kaiser-Bessel kernel, as introduced in [6], was used for the gridding reconstruction.

It can be observed that the regularized reconstruction offers a better visual quality than the gridding (Fig. 4) and that it is closer to the reference image. Sharp edges are maintained and enhanced while at the same time the noise level is smoothed throughout the image. This trade-off is achieved by the properties of the selected penalization function. The reconstruction presents less artifacts inside and outside the inner part of the image while the spatial resolution is preserved. These aliasing artifacts due to the undersampling are greatly reduced but their structure is more complex to analyze than for a Cartesian acquisition due to the characteristics of the spiral sampling trajectory [31].

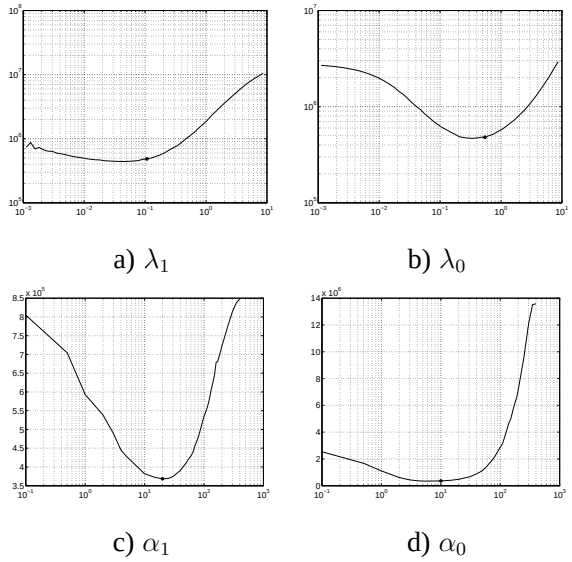

Fig. 3. Sensitivity to hyperparameters around the chosen values $\lambda_1 = 0.1$, $\alpha_1 = 20$, $\lambda_0 = 0.5$ and $\alpha_0 = 10$: reconstruction errors when one hyperparameter is varied at a time. Case for 6 spirals and 512 samples/spiral (noise free), selected values are indicated (as dots) on each curve.

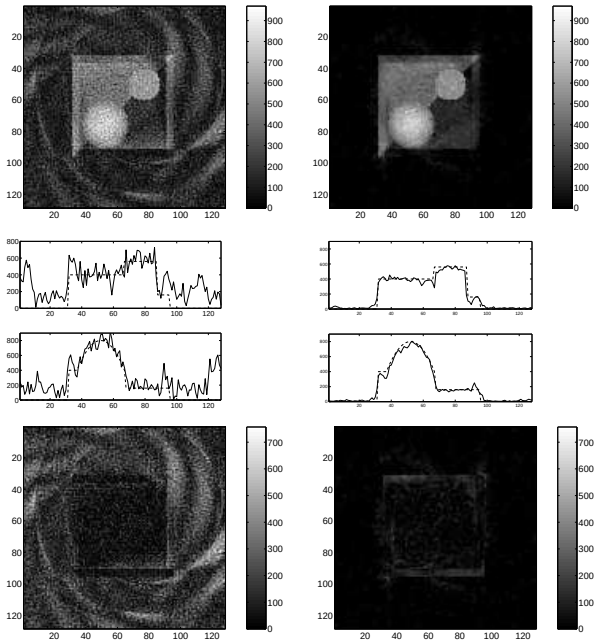

Fig. 4. Reconstruction for noisy data (30 dB): 6 spirals and 512 samples/spiral: re-gridding method (lhs) and proposed one (rhs). The top part shows the modulus images, middle part shows rows 50 and 75 and bottom one shows difference images with the reference.

The examination of the k-space of the reconstructed images (FFT of the reconstructed images), shown in Fig. 5, allows to compare the frequency content of the two reconstructed images versus the reference one. The proposed method restores a k-space very close to the reference one, while the gridding reconstruction still lets appear the underneath sampling trajectory. This shows that the *a priori* introduced by the regularization is more pertinent and helps to restore an image closer to the original object.

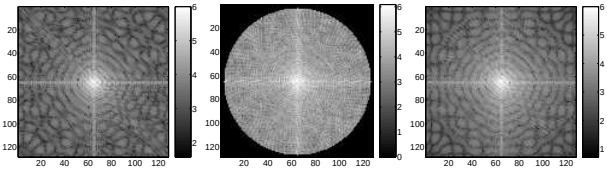

Fig. 5. From left to right : reference k-space, gridding k-space and reconstructed k-space (6 spirals and 512 samples/spiral).

Figure 6 presents a quantitative validation of the method, varying the number of spirals, the number of samples per spiral and the SNR, using the following criteria.

- The quadratic reconstruction error in ROI1 (see Fig. 2) which gives a measure of the distance between the reconstruction and the reference.
- The variance for the constant gray level region of ROI2 (see Fig. 2) [13].

These figures confirm the former qualitative results. The proposed method gives a quadratic error 5 to 300 folds lower than the gridding, while the variance is improved 3 to 10 folds whatever the sampling or noise level.

Figure 3 presents a quantitative evaluation of the hyperparameter sensitivity computed as the variations of the squared reconstruction error in a defined region of interest (ROI1). We note that the selected values are very close to the ones that minimize the errors when only one hyperparameter is varied at a time. The intervals where these parameters can be chosen are relatively large: this ensures that the solution is robust with respect to the hyperparameter values.

This results show that the quality of the image can be maintained while using acquisition sequences that sample a smaller number of data and then reduce the acquisition time, proportionally to the number of acquired spirals.

4.2 Phantom acquisition

The method was then tested on the GEMS test phantom with a 1.5 Tesla Signa system [1]. The sampling trajectory consisted in 24 interleaved spirals each of 2048 samples and a 16 cm FOV.

Figure 7 presents the reconstructed magnitude images (256×256) for the gridding and the regularized methods as well as a zoom in the comb like ROI for the genuine acquisition geometry (24 spirals). Fig. 8 presents the corresponding results when one spiral over two has been discarded, providing a gain of two in the acquisition time.

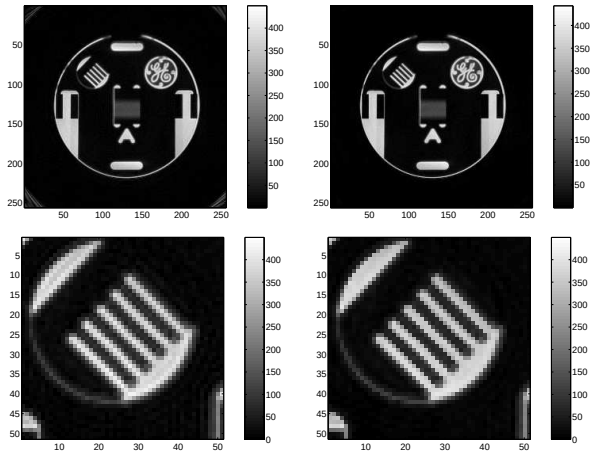

Fig. 7. Reconstruction with 24 spirals and 2048 samples/spiral. From top to bottom : modulus image, ROI. On the left the gridding reconstruction and on the right the proposed method.

For the genuine acquisition geometry (Fig. 7) the regularized image is very close to the gridding reconstruction and it even shows a slight reduction of the noise level in the background.

Undersampling strongly degrades the gridding reconstruction (Fig. 8): only a small central region remains free of all artifacts. As has been shown for simulated

[1] Acquisition are provided by M.J. Graves, University of Cambridge and Addenbrooke's Hospital, Cambridge, UK.

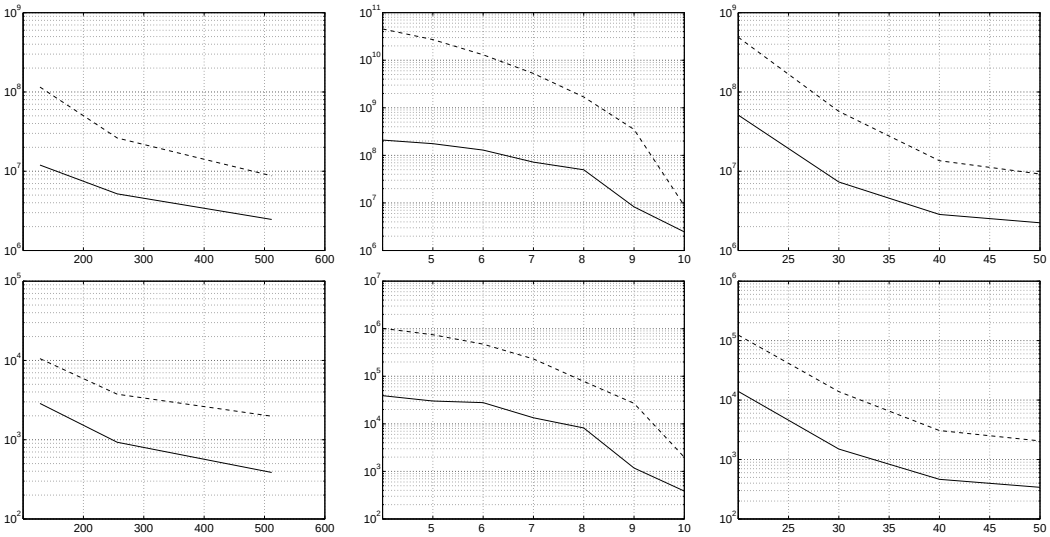

Fig. 6. First row: quadratic reconstruction error in ROI1 and second row : variance in ROI2. The gridding method results are plotted with a dotted line and the proposed method results with a solid line. From left to right: 10 spirals, variable number of samples (128, 256 et 512), no noise; variable number of spirals (4 to 10), 512 samples/spiral, no noise; 10 spirals, 512 samples/spiral, variable noise level (20 to 50 dB).

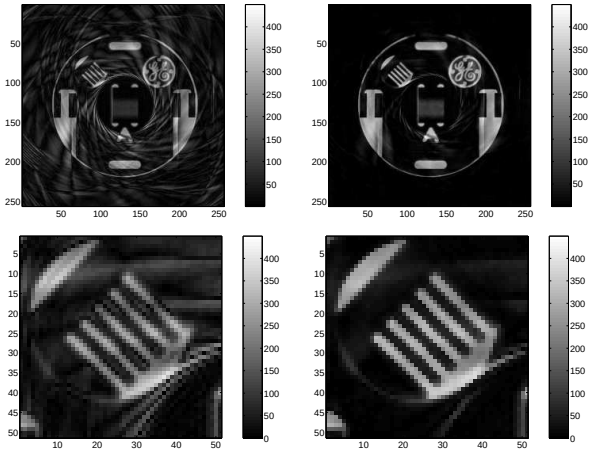

Fig. 8. Reconstruction with 12 spirals and 2048 samples/spiral. From top to bottom: modulus image, ROI. On the left the gridding reconstruction and on the right the proposed method.

data, our method applied to actual measurements gives an image where the aliasing artifacts are strongly reduced inside the object and where a very homogeneous background is preserved. The two comb-like ROIs (Fig. 8) show more clearly the improvement provided by the proposed method. The regularization also provides an image with well defi ned edges, illustrating that the chosen prior is well suited to achieve the compromise between noise smoothing and contour preservation constraints.

Characterization of aliasing artifacts can be approached by studying the structure of the matrix G which can be interpreted as the point spread function of the imaging system: the observed image being the convolution of the true object with G. Fig. 9 shows this matrix for the two sampling schemes. The central white spot (resp. peak in the 1D fi gures) introduces a blurring effect proportional to its diameter (resp. width), while the outer circles (resp. peaks) are responsible for aliasing. The closer these circles to the center the more important the aliasing artifacts. The undersampling that shrinks these circles was partially inverted by the proposed method while it was kept unchanged by the gridding reconstruction.

Beforehand computation of matrices D and G considerably speeds up the optimization procedure. However, if G can be computed once for all for a given acquisition sequence, D must be computed for each data set. The computational complexity that arises in computing D is not a drawback for clinical use of the method: it takes 30 sec to compute matrix D (12 spirals, 2048 samples per spiral, image 256×256) using a C-Program on a PC computer with an AMD-Athlon 2.1 GHz processor.

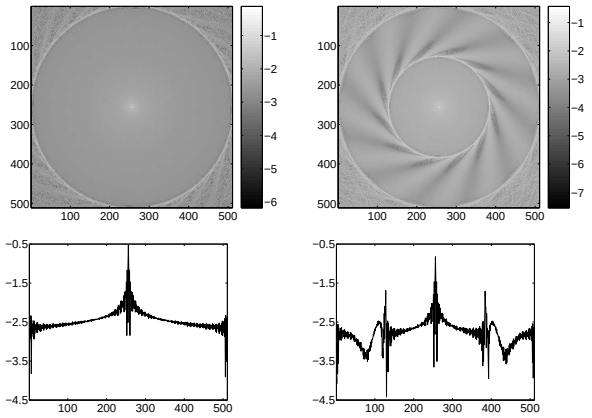

Fig. 9. Matrix G for 24 spirals (lhs) and 12 spirals (rhs) (Log scale). Sharp peaks denoted by arrows cause aliasing.

The optimization was performed using the computing environment *Matlab* in 3 minutes, and 50 iterations were needed to converge to an accurate solution. Each iteration requires one gradient and three criterion calculations. The calculations of the FFTs represent the main computational burden during the minimization: every iteration involves six 512×512 2D-FFTs for the criterion and two 768×768 2D-FFTs for the gradient. This time could be considerably reduced by implementing the algorithm on a dedicated processor. Indeed, given the characteristics of the Texas Instruments TMS320C64x series DSP, all of the FFTs could, theoretically, be performed in about 18 sec, leading to an important decrease in the total optimization time.

Moreover the computation of the criterion, the gradient and the matrix D are highly amenable to parallelization, and with a sufficient number of processing elements, the reconstruction could be done even faster, which could allow the use of the method in a wide variety of clinical applications.

5 Discussion / Conclusion

The proposed method differs from more conventional ones insofar as it does not involve any regridding of the acquired data and accounts for edge preserving smoothing penalties. Utilization of only the acquired data and integration of smoothness and edge preservation penalization in the reconstruction opens the way to strong improvement in MRI.

From a computational stand point, the original formulation leads to the awkward situation of an optimization algorithm permanently shifting from Fourier to image domains requiring for numerous heavy non-uniform Fourier transform computations. Rewriting the criterion allowed to perform the whole optimization in the image domain providing the pre-computation of two matrices. The first one characterizes the geometry of acquisitions in k-space and gives interpretation of aliasing structures; the second can be seen as a discrete Fourier transform of the acquired data.

Moreover, alternatives exist to still improve the reconstruction efficiency of the method: substituting non-uniform FFT algorithms for the non-uniform Fourier transform in the pre-computations [32]; calculating a solution corresponding to a small ROI only; substituting a Newton like [33] or a dual optimization [34] method to the conjugate gradient could dramatically reduce the computational cost and make the method available for clinical applications.

Finally, the inverted model could be improved by integrating an exponential term that takes into account the relaxation of the magnetic moments. A Laplace inversion framework should then be substituted for the present Fourier framework but the overall inversion procedure will remain valid.

Acknowledgement — *The authors express their gratitude to M.J. Graves, University of Cambridge and Addenbrooke's Hospital, Cambridge, UK, for providing the acquisitions, fundamental for proposed evaluations.*

Appendix

The appendix gives detailed calculi for the new form of the fit to the data term $\mathcal{J}_{\text{LS}}$ and its gradient, required for efficient numerical optimization.

A Criterion calculus

We have:

$$\mathcal{J}_{\text{LS}}(\boldsymbol{f}) = \sum_{l=0}^{L-1} |s_l - y_l|^2 = \sum_{l=0}^{L-1} |s_l|^2 + |y_l|^2 - 2\Re\{s_l\, y_l^*\}\,. \tag{A.1}$$

where $y_l = \boldsymbol{h}_l \boldsymbol{f}$ is the noise free model output given by Eq (2). It is the sum of quadratic terms over the whole acquired data. The first term is simply the norm of the data, the second one is developed in subsection A.1 and the last one in subsection A.2.

A.1 Term involving model output y_l

Expansion of $|y_l|^2$, given model (2) yields:

$$|y_l|^2 = \frac{1}{N^2} \left| \sum_{p,q=0}^{N-1} f_{p,q}\, \mathrm{e}^{i2\pi(k_x^l p + k_y^l q)} \right|^2 = \frac{1}{N^2} \sum_{q,q,p',q'=0}^{N-1} f_{p,q}\, f^*_{p',q'}\, \mathrm{e}^{i2\pi[k_x^l (p-p') + k_y^l (q-q')]} \,.$$

A change of the summation variable : $u = p - p'$ and $v = q - q'$ gives:

$$|y_l|^2 = \frac{1}{N^2} \sum_{u,v=1-N}^{N-1} \sum_{\substack{p=\mathrm{m}(u)\\ q=\mathrm{m}(v)}}^{\substack{q=\mathrm{M}(v)\\ p=\mathrm{M}(u)}} f_{p,q}\, f^*_{p-u,q-v}\, \mathrm{e}^{i2\pi(k_x^l u + k_y^l v)}$$

where $\mathrm{m}(\cdot)$ and $\mathrm{M}(\cdot)$ are the index summation bounds:

$$\mathrm{m}(w) = \begin{cases} |w| & \text{if } w \geq 0 \\ 0 & \text{if } w \leq 0 \end{cases}$$

and

$$\mathrm{M}(w) = \begin{cases} N-1 & \text{if } w \geq 0 \\ N-1-|w| & \text{if } w \leq 0 \end{cases}$$

We then introduce the image correlation matrix :

$$C_{u,v} = \sum_{\substack{p=\mathrm{m}(u)\\ q=\mathrm{m}(v)}}^{\substack{q=\mathrm{M}(v)\\ p=\mathrm{M}(u)}} f_{p,q}\, f^*_{p-u,q-v}$$

which can be computed by FFT. So, $|y_l|^2$ simply writes:

$$|y_l|^2 = \frac{1}{N^2} \sum_{v,u=1-N}^{N-1} C_{u,v}\, \mathrm{e}^{i2\pi(k_x^l u + k_y^l v)} \,.$$

The summation over l yields

$$\sum_{l=0}^{L-1} |y_l|^2 = \frac{1}{N^2} \sum_{l=0}^{L-1} \sum_{v,u=1-N}^{N-1} C_{u,v}\, \mathrm{e}^{i2\pi(k_x^l u + k_y^l v)} = \frac{1}{N^2} \sum_{v,u=1-N}^{N-1} C_{u,v} \sum_{l=0}^{L-1} \mathrm{e}^{i2\pi(k_x^l u + k_y^l v)}$$

after rearrangement of the summations. Let us state for $u, v = 1-N, \ldots, N-1$:

$$G_{u,v} = \frac{1}{N^2} \sum_{l=0}^{L-1} \mathrm{e}^{i2\pi(k_x^l u + k_y^l v)} \tag{A.2}$$

which only depends upon the k-space trajectory. We finally have:

$$\sum_{l=0}^{L-1} |y_l|^2 = \sum_{v,u=1-N}^{N-1} C_{u,v}\, G_{u,v} \,. \tag{A.3}$$

A.2 Term involving model output y_l and observed data s_l

Using (2), the involved term writes:

$$s_l\, y_l^* = s_l \frac{1}{N} \sum_{p,q=0}^{N-1} f^*_{p,q}\, \mathrm{e}^{-i2\pi(k_x^l p + k_y^l q)}$$

and summation over l yields:

$$\sum_{l=0}^{L-1} s_l\, y_l^* = \frac{1}{N} \sum_{l=0}^{L-1} s_l \sum_{p,q=0}^{N-1} f^*_{p,q}\, \mathrm{e}^{-i2\pi(k_x^l p + k_y^l q)} = \frac{1}{N} \sum_{p,q=0}^{N-1} f^*_{p,q} \sum_{l=0}^{L-1} s_l\, \mathrm{e}^{-i2\pi(k_x^l p + k_y^l q)}$$

after rearrangement. We then introduce the DFT, for $p, q = 0, \ldots, N-1$:

$$D_{p,q} = \frac{1}{N} \sum_{l=0}^{L-1} s_l\, \mathrm{e}^{-i2\pi(k_x^l p + k_y^l q)} \tag{A.4}$$

which depends upon observed data and k-space trajectory. The current term then simply writes:

$$\sum_{l=0}^{L-1} s_l\, y_l^* = \sum_{p,q=0}^{N-1} f^*_{p,q}\, D_{p,q} \,. \tag{A.5}$$

Substitution of (A.5) and (A.3) in (A.1) yields the announced form of Eq. (6).

B Gradient of the Criterion

The partial derivative of (A.5) with respect to f_{nm} clearly writes:

$$\frac{\partial}{\partial f_{nm}} \sum_{l=0}^{L-1} s_l \, y_l^* = \frac{\partial}{\partial f_{nm}} \sum_{p,q=0}^{N-1} f_{p,q}^* \, D_{p,q} = D_{n,m}$$

The partial derivative of (A.3) with respect to f_{nm} is more complicated.

$$\begin{aligned}
&\frac{\partial}{\partial f_{nm}} \sum_{v,u=1-N}^{N-1} C_{u,v} \, G_{u,v} \\
&= \frac{2}{N^2} \sum_{l=0}^{L-1} \mathrm{e}^{-i2\pi(k_x^l m + k_y^l n)} \sum_{n',m'=0}^{N-1} f_{n',m'} \, \mathrm{e}^{i2\pi(k_x^l m' + k_y^l n')} \\
&= \frac{2}{N^2} \sum_{l=0}^{L-1} \sum_{n',m'=0}^{N-1} f_{n',m'} \, \mathrm{e}^{i2\pi[k_x^l (m'-m) + k_y^l (n'-n)]}
\end{aligned}$$

Finally, we can write, using the expressions of the matrices D and G:

$$\begin{aligned}
&\frac{\partial}{\partial f_{nm}} \sum_{v,u=1-N}^{N-1} C_{u,v} \, G_{u,v} \\
&= \frac{2}{N^2} \sum_{l=0}^{L-1} \sum_{u,v=1-N}^{N-1} f_{n-v,m-u} \, \mathrm{e}^{-i2\pi(k_x^l u + k_y^l v)} \\
&= 2 \sum_{u,v=1-N}^{N-1} f_{n-v,m-u} \, G_{v,u}^*.
\end{aligned}$$

where G^* is the conjugate of G.

The total gradient using a matrix formulation, is given then as:

$$\frac{\partial \mathcal{J}_{\mathrm{LS}}(\boldsymbol{f})}{\partial \boldsymbol{f}} = 2 f \star G - 2D.$$

where $\star$ is a bidimentional circular-convolution that can be effi ciently computed by FFT.

References

[1] Z. H. Cho, H. S. Kim, H. B. Song, and J. Cumming, "Fourier Transform Nuclear Magnetic Resonance Tomographic Imaging," *Proc. IEEE*, vol. 70, no. 10, pp. 1152–1173, 1982.

[2] H. Meyer, Craig, B. S. Hu, D. G. Nishimura, and A. Macovski, "Fast Spiral Coronary Artery Imaging," *Magn. Reson. Med.*, vol. 28, pp. 202–213, 1992.

[3] J. G. Pipe and P. Menon, "Sampling Density Compensation in MRI: Rationale and an Iterative Numerical Solution," *J. Magn. Reson. Imaging*, vol. 41, pp. 179–186, 1999.

[4] G. H. Glover and J. M. Pauly, "Projection reconstruction techniques for reduction of motion effects in MRI," *Magn. Reson. Med.*, vol. 28, pp. 275–289, 1992.

[5] H. Azhari, O. E. Denisova, A. Montag, and E. P. Shapiro, "Circular Sampling : Perspective of a Time-Saving Scanning Procedure," *J. Magn. Reson. Imaging*, vol. 14, no. 6, pp. 625–631, 1996.

[6] J. D. O'Sullivan, "A Fast Sinc Function Gridding Algorithm for Fourier Inversion in Computer Tomography," *IEEE Transactions on Medical Imaging*, vol. MI-4, no. 4, pp. 200–207, 1985.

[7] J. I. Jackson, C. H. Meyer, D. G. Nishimura, and A. Macovski, "Selection of a Convolution Function for Fourier Inversion Using Gridding," *IEEE Trans. Medical Imaging*, vol. 10, no. 3, pp. 473–478, 1991.

[8] N. G. Papadakis, C. T. Adrian, and L. D. Hall, "An Algorithm for Numerical Calculation of the k-space Data-Weighting for Polarly Sampled Trajectories: Application to Spiral Imaging," *J. Magn. Reson. Imaging*, vol. 15, no. 7, pp. 785–794, 1997.

[9] K. F. King, and L. Angelos, "SENSE Image Quality Improvement Using Matrix Regularization," *Proceedings of the 9th Annual Meeting of ISMRM*, pp. 1771, 2001.

[10] R. Bammer , M. Auer, S. L. Keeling, M. Augustin, L. A. Stables, R. W. Prokesch, R. Stollberger, M. E. Moseley, and F. Fazekas, " Diffusion Tensor Imaging Using Single-Shot SENSE-EPI," *Magn. Reson. Med.*, vol. 48, pp. 128–136, 2002.

[11] F.-H. Lin, K. K Kwong, J. W. Belliveau, and L. L. Wald, "Parallel Imaging Reconstruction Using Automatic Regularization," *Magn. Reson. Med.*, vol. 51, pp. 559–567, 2004.

[12] K. P. Pruessmann, M. Weiger, M. B Scheidegger, and P. K. Boesiger, "SENSE: Sensitivity Encoding for Fast MRI," *Magn. Reson. Med.*, vol. 42, pp. 952–962, 1999.

[13] R. M. Henkelman, "Measurement of signal intensities in the presence of noise in MR images," *Med. Phys*, vol. 12 (2) Mar/Apr, pp. 232–233, 1985.

[14] G. Demoment, "Image reconstruction and restoration: Overview of common estimation structure and problems," *IEEE Trans. Acoust. Speech, Signal Processing*, vol. ASSP-37, pp. 2024–2036, December 1989.

[15] C. Oesterle and J. Hennig, "Improvement of Spatial Resolution of Keyhole Effect Images," *Magn. Reson. Med.*, vol. 39, pp. 244–250, 1998.

[16] M. Doyle, G. E. Walsh, E. R. Foster, and M. G. Pohost, "Block Regional Interpolation Scheme for *k*-Space (BRISK): A Rapid Cardiac Imaging Technique," *Magn. Reson. Med.*, vol. 33, pp. 163–170, 1995.

[17] M. Doyle, G. E. Walsh, E. R. Foster, and M. G. Pohost, "Rapid Cardiac Imaging with Turbo BRISK," *Magn. Reson. Med.*, vol. 37, pp. 410–417, 1997.

[18] F. R. Korosec, R. Frayne, T. M. Grist, and C. A. Mistretta, "Time-resolved contrast-enhanced 3D MR angiography.," *Magn. Reson. Med.*, vol. 36(3), pp. 345–351, 1996.

[19] Y. Cao and D. N. Levin, "Using Prior Knowledge of Human Anatomy to Constrain MR Image Acquisition and Reconstruction: Half k-space and Full k-space Techniques," *J. Magn. Reson. Imaging*, vol. 15, No. 6, pp. 669–676, 1997.

[20] I. Dologlou, D. van Ormondt, and G. Carayannis, "MRI scan time reduction through non-uniform sampling and SVD-based estimation," *Signal Processing*, vol. 55, pp. 207–219, 1996.

[21] G. McGibney, M. R. Smith, S. T. Nichols, and A. Crawley, "Quantitative Evaluation of Several Partiel Fourier Reconstruction Algorithms Used in MRI," *Magn. Reson. Med.*, vol. 30, pp. 51–59, 1993.

[22] R. Van de Walle, H. H. Barrett, K. J. Myers, M. I. Altbach, B. Desplanques, A. F. Gmito, J. Cornelis, and I. Lemahieu, "Reconstruction of MR images from data acquired on a general nonregular grid by pseudoinverse calculation," *IEEE Trans. Medical Imaging*, vol. 19, no. 12, pp. 1160–1167, 2000.

[23] Y. Gao and S. J. Reeves, "Optimal k-space sampling in MRSI for images with a limited region of support," *IEEE Trans. Medical Imaging*, vol. 19, no. 12, pp. 1168–1178, 2000.

[24] A. Tikhonov and V. Arsenin, *Solutions of Ill-Posed Problems*. Washington, DC: Winston, 1977.

[25] B. R. Hunt, "Bayesian methods in nonlinear digital image restoration," *IEEE Trans. Communications*, vol. C-26, pp. 219–229, March 1977.

[26] S. Geman and D. Geman, "Stochastic relaxation, Gibbs distributions, and the Bayesian restoration of images," *IEEE Trans. Pattern Anal. Mach. Intell.*, vol. PAMI-6, pp. 721–741, November 1984.

[27] A. Blake and A. Zisserman, *Visual reconstruction*. Cambridge, MA: The MIT Press, 1987.

[28] S. Geman and D. McClure, "Statistical methods for tomographic image reconstruction," in *Proceedings of the 46th Session of the* ICI, *Bulletin of the* ICI, vol. 52, pp. 5–21, 1987.

[29] H. R. Künsch, "Robust priors for smoothing and image restoration," *Ann. Inst. Stat. Math.*, vol. 46, no. 1, pp. 1–19, 1994.

[30] W. H. Press, S. A. Teukolsky, W. T. Vetterling, and B. P. Flannery, *Numerical recipes in C, the art of scientific computing*. New York: Cambridge Univ. Press, 2nd ed., 1992.

[31] H. Sedarat, A. B. Kerr, J. M. Pauly, and D. Nishimura, "Partial-FOV Reconstruction in Dynamic Spiral Imaging," *Magn. Reson. Med.*, vol. 43, pp. 439–439, 2000.

[32] B. Dale, M. Wendt, and J. L. Duerk, "A rapid look-up table method for reconstructing MR images from arbitrary k-space trajectories," *IEEE Trans. Medical Imaging*, vol. 20, no. 3, pp. 207–217, 2001.

[33] D. P. Bertsekas, *Nonlinear programming*. Belmont, MA: Athena Scientific, 2nd ed., 1999.

[34] J. Idier, "Convex half-quadratic criteria and interacting auxiliary variables for image restoration," *IEEE Trans. Image Processing*, vol. 10, pp. 1001–1009, July 2001.